Seismic structure, gas hydrate, and slumping studies on the Northern Cascadia margin using multiple migration and full waveform inversion of OBS and MCS data

by

Subbarao Yelisetti
M.Sc. (Physics), University of Hyderabad, Hyderabad, India 2006
M.Tech. (Mineral Exploration), University of Hyderabad, Hyderabad, India 2008

A Dissertation Submitted in Partial Fulfillment of the
Requirements for the Degree of

DOCTOR OF PHILOSOPHY

in the School of Earth and Ocean Sciences

Seismic structure, gas hydrate, and slumping studies on the Northern Cascadia margin using multiple migration and full waveform inversion of OBS and MCS data

by

Subbarao Yelisetti
M.Sc. (Physics), University of Hyderabad, Hyderabad, India 2006
M.Tech. (Mineral Exploration), University of Hyderabad, Hyderabad, India 2008

Supervisory Committee

Dr. George D. Spence, Supervisor
(School of Earth and Ocean Sciences)

Dr. Michael Riedel, Departmental Member
(School of Earth and Ocean Sciences)

Dr. Roy D. Hyndman, Departmental Member
(School of Earth and Ocean Sciences)

Dr. Joanne Wegner, Outside Member
(Department of Mechanical Engineering)

Supervisory Committee

Dr. George D. Spence, Supervisor
(School of Earth and Ocean Sciences)

Dr. Michael Riedel, Departmental Member
(School of Earth and Ocean Sciences)

Dr. Roy D. Hyndman, Departmental Member
(School of Earth and Ocean Sciences)

Dr. Joanne Wegner, Outside Member
(Department of Mechanical Engineering)

ABSTRACT

The primary focus of this thesis is to examine the detailed seismic structure of the northern Cascadia margin, including the Cascadia basin, the deformation front and the continental shelf. The results of this study are contributing towards understanding sediment deformation and tectonics on this margin. They also have important implications for exploration of hydrocarbons (oil and gas) and natural hazards (submarine landslides, earthquakes, tsunamis, and climate change).

The first part of this thesis focuses on the role of gas hydrate in slope failure observed from multibeam bathymetry data on a frontal ridge near the deformation front off Vancouver Island margin using active-source ocean bottom seismometer (OBS) data collected in 2010. Volume estimates (~ 0.33 km^3) of the slides observed on this margin indicate that these are capable of generating large ($\sim 1-2$ m) tsunamis. Velocity models from travel time inversion of wide angle reflections and refractions recorded on OBSs and vertical incidence single channel seismic (SCS) data were used to estimate gas hydrate concentrations using effective medium modeling. Results indicate a shallow high velocity hydrate layer with a velocity of $2.0 - 2.1$ km/s that corresponds to a hydrate concentration of 40% at a depth of 100 m, and a bottom simulating reflector (BSR) at a depth of $265 - 275$ m beneath the seafloor (mbsf). These are comparable to drilling results on an adjacent frontal ridge. Margin perpendicular normal faults that extend down to BSR depth were also observed on SCS and bathymetric data, two of which coincide with the sidewalls of the slump indicating that the lateral extent of the slump is controlled by these faults. Analysis of bathymetric data indicates, for the first time, that the glide plane occurs at the same depth as the shallow high velocity layer (100 ± 10 mbsf). In contrast, the glide plane coincides with the depth of the BSR on an adjacent frontal ridge. In either case, our results suggest that the contrast in sediments strengthened by hydrates and overlying or underlying sediments where there is no hydrate is what causing the slope failure on this margin.

The second part of this dissertation focuses on obtaining the detailed structure of the Cascadia basin and frontal ridge region using mirror imaging of few widely spaced OBS data. Using only a small airgun source (120 cu. in.), our results indicate structures that were previously not observed on the northern Cascadia margin. Specifically, OBS migration results show dual-vergence structure, which could be related to horizontal compression associated with subduction and low basal shear stress resulting from over-pressure. Understanding the physical and mechanical properties of the basal layer has important implications for understanding earthquakes on this margin. The OBS migrated image also clearly shows the continuity of reflectors which enabled the identification of thrust faults, and also shows the top of the igneous oceanic crust at $5 - 6$ km beneath the seafloor, which were not possible to identify in single-channel and low-fold multi-channel seismic (MCS) data.

The last part of this thesis focuses on obtaining detailed seismic structure of the Vancouver Island continental shelf from MCS data using frequency domain visco-acoustic full waveform inversion, which is first of its kind on this margin. Anelastic velocity and attenuation models, derived in this study to subseafloor depths of ~ 2 km, are useful in understanding the deformation within the Tofino basin sediments, the nature of basement structures and their relationship with underlying accreted terranes such as the Crescent and the Pacific Rim terranes. Specifically, our results indicate a low-velocity zone (LVZ) with a contrast of 200 m/s within the Tofino basin sediment section at a depth $600 - 1000$ mbsf over a lateral distance of 10 km. This

LVZ is associated with high attenuation values ($0.015 - 0.02$) and could be a result of over pressured sediments or lithology changes associated with a high porosity layer in this potential hydrocarbon environment. Shallow high velocities of $4 - 5$ km/s are observed in the mid-shelf region at depths > 1.5 km, which is interpreted as the shallowest occurrence of the Eocene volcanic Crescent terrane. The sediment velocities sharply increase about 10 km west of Vancouver Island, which probably corresponds to the underlying transition to the Mesozoic marine sedimentary Pacific Rim terrane. High attenuation values of $0.03 - 0.06$ are observed at depths > 1 km, which probably corresponds to increased clay content and the presence of mineralized fluids.

Contents

List of Tables

List of Figures

ACKNOWLEDGEMENTS

First and foremost, I would like to extend my sincere and heartfelt thanks to my supervisor, Prof. George Spence for giving me this wonderful opportunity to do Ph.D. under his able guidance at the University of Victoria (UVic). I'm grateful for his constant support, brilliant ideas, enthusiasm, giving freedom to think independently, patience during difficult times, encouragement and funding throughout my Ph.D. program, and more importantly for giving me chance to work on three major research projects. Thank you very much for giving me an excellent opportunity to participate in both on-land and offshore seismic data acquisition, and for supporting all the conferences that I have attended and presented. I very much appreciate your support in starting the SEG student chapter at UVic and for your help in organizing many SEG and CSEG lectures. It was a great pleasure working with you and playing badminton with you. Apart from the subject, I have learnt many things from you which would go a long way. I will never forget the moment that I first met you on Jan 25^{th} in Victoria airport at midnight when you came to receive me.

My warmest thanks also goes to my wonderful committee members Dr. Michael Riedel, Prof. Roy Hyndman and Dr. Joanne Wegner (now unfortunately deceased) for helpful discussions, suggestions and encouragement all the way through my Ph.D. I'm grateful to my external examiner Dr. Andrew Gorman for his constructive comments on my thesis and Dr. Stan Dosso for quickly reading my thesis and providing feedback. I thank Dr. Kalachand Sain and Dr. Satyavani from National Geophysical Research Institute, India for writing reference letters for my Ph.D. program at UVic.

I would also like to thank Natural Sciences and Engineering Research Council of Canada (NSERC) for funding the projects and UVic for providing fellowship to me. I thank JAMSTEC and WHOI for providing OBS instruments for the SeaJade project. I appreciate all the technicians from GSC and JAMSTEC, the Captain and crew of C.C.G. Research Vessel J. P. Tully for acquiring the OBS data used in this thesis. Many thanks to SEG, EAGE, UVic and CGU for providing travel grants to attend the conferences. Thank you to the editor and reviewers of Geophysical Journal International for constructive comments that greatly improved the quality of my manuscript on slope failure.

Many thanks to Dr. Colin Zelt for providing travel time inversion routines, RAY-INVR & FAST and Dr. Gerhard Pratt for providing waveform tomography code. I also thank the developers and supporters of GMT and Seismic Unix softwares which have been used for processing and preparing most of the figures in this thesis. I appreciate the license and support provided by GLOBE Claritas for their processing software. Many thanks to Brendan Smithyman (UBC), Eric Takam Takougang (SFU), Michael Afanasiev (UWO), Rie Kamei (UWO), Rajesh Vayavur (SFU) and Dibakar Ghosal (IPGP) for helpful discussions on waveform inversion. I would also like to thank Ranjan Dash (Chevron) for his suggestions on mirror imaging. I take this opportunity to thank share journal group comprising friends scattered across the globe for providing articles which I dont have access at UVic.

Very special thanks to all my colleagues from SEOS, particularly, Andy Stephenson, Angela Schlesinger, Martin Scherwath, Rongwen Guo, Mei Sato, Tian Sun, Romina Gehrman and Ayodeji Kuponiyi for their friendship, countless discussions for long hours, all the fun, and for proving support to start the SEG student chapter and the Victoria Geoscience Society at UVic. I would also like to thank SEOS staff, particularly Allison, Kimberly and Kathleen for providing all the necessary administrative support over the years.

Dear Sunny and Rose, a big thank you to both of you for hours and hours of cross-country and cross-continental talks over the years. My stay in Victoria wouldnt have been easier without the support of Archana, Prashant, Suma, Divya, Sharada aunty & Prasad uncle, Vijay uncle & Gayatri aunty and all other friends. I won't forget all the fun, many wonderful dinners and your support in difficult times which made my stay memorable in Victoria.

Last but not least, I'm deeply indebted to my family, my parents Janardhanarao Yelisetti and Lakshmi Yelisetti and my sisters, Ramadevi and Urmila for all their tireless hard work in sun & rain, love, support and many sacrifices over the years. Your struggles, perseverance and hard work to support my education have been my BIGGEST motivation over the years. I'm very grateful for your understanding and patient waiting for my return home. Without your emotional support, this thesis wouldn't have been possible. Very special thanks to my great-grandmother, who was responsible for my existence on this planet!

DEDICATION

For their hard work, constant support and concern, I dedicate this thesis
to my parents, Janardhanarao Yelisetti and Lakshmi Yelisetti &
to my great-grandmother, Subbamma Yelisetti
for taking care of me during my childhood while my parents were working in the field.

"It must have appeared almost as improbable to the earlier geologists, that the laws of earthquakes should one day throw light on the origin of mountains, as it must to the first astronomers, that the fall of an apple should assist in explaining the motions of the moon."

Sir Charles Lyell
English Geologist
(1797-1875)

Chapter 1

Introduction

Over the years, seismic migration, raytracing and traveltime tomography have been widely used in controlled source seismology for imaging the Earth's crust and uppermost mantle. But only in recent years, have advanced techniques like full waveform inversion and multiple migration been used in seismic imaging of the Earth's upper lithosphere. These computationally intensive techniques not only provide high quality images of the Earth's subsurface structure, but also provide information about the subsurface elastic parameters and lithological discontinuities. Both these techniques were implemented in this thesis to identify the subsurface geological structures of the northern Cascadia subduction zone. These were applied to multi-channel and ocean bottom seismometer (OBS) data collected off Vancouver Island. The results of this study are useful in understanding the sediment deformation and tectonics on this margin. They also have important implications for exploration of hydrocarbons (oil and gas) and natural hazards (submarine landslides, earthquakes, tsunamis, and climate change).

1.1 Motivation

The study area extends approximately from 100 km off Vancouver Island to about 10 km from the coast (Fig. 1.1). This region is characterized by uniform sedimentation in the Cascadia basin and by heavily deformed accreted frontal ridge sediments with large frontal thrusts in the lower continental slope region near the deformation front (*Hyndman et al.*, 1990; *Spence et al.*, 1991b). Landward dipping thrust faults that separate the accretionary wedge sediments, the Crescent terrane and the Pacific Rim terrane are observed in the continental shelf region (Figs. 1.2 & 1.3).

Societal issues associated with this region are the possibility of earthquakes and tsunamis. According to Earthquakes Canada database, about fourteen earthquakes of magnitude ≥ 5 have been observed in the study area over the last three decades. Multibeam bathymetry data have revealed several slope failure features near the deformation front that may have produced tsunamis. Previous work in the frontal ridge area (*Lopez et al.*, 2010) investigated a large sediment slump that appears to have failed at the base of the gas hydrate stability zone. The primary focus of this thesis is to examine the detailed geological structure of this complex region, using modern geophysical imaging techniques such as full waveform inversion and multiple migration, and so contribute to our understanding of geological hazards on the margin.

1.1.1 Frontal ridge structure and slope failures

The first part of this thesis focuses on OBS seismic analysis at Cascadia frontal ridge, looking at hydrates and slides using recently collected active source OBS data from the SeaJade (Seafloor Earthquake Array Japan Canada Cascadia Experiment) project.

As a result of subduction of the Juan de Fuca plate beneath the North American plate (Fig. 1.1), sediments are scraped off from the downgoing plate and near the deformation front they form a series of anticlinal accretionary frontal ridges, which are as high as 700 m above the seafloor (*Hyndman et al.*, 1990). Associated with these frontal ridges, several slope failure features are observed near the foot of the continental slope. Volume estimates of these failures indicate that some of these are capable of generating tsunamis (*Lopez et al.*, 2010). The cause of these features is not clear, although several studies indicate potential connection between mass failures and the occurrence of gas hydrates on this margin (*Lopez et al.*, 2010; *Scholz*, 2014). Since hydrates may prevent normal sediment compaction, their destabilization may decrease the sediment strength, potentially facilitating landslides on the continental slopes. Hydrate destabilization could be caused by changing the pressure and temperature conditions. These changes could be caused by an earthquake (*Berndt et al.*, 2005; *Goldfinger et al.*, 2003), by an upward migration of warm fluids into the gas hydrate stability zone (GHSZ) (*Riedel et al.*, 2010a) or by sea-level change caused by bottom water warming (*Vogt and Jung*, 2002). Given the fact that the Cascadia margin is one of the seismically most active regions in the world (14 earthquakes of M $\geq$ 5 were recorded within a 200 km radius of the study area between 1986 and 2013

(Earthquakes Canada database)), tectonic triggering of hydrate destabilization may occur quite regularly on this margin. Although the Cascadia megathrust is currently fully locked (*Hyndman*, 2013), a future megathrust earthquake on this margin could potentially trigger many landslides near the foot of the continental slope and possibly lead to a tsunami.

1.1.2 Vergence structure on north Cascadia margin

The second part of this thesis focuses on understanding the vergence structure on the north Cascadia margin through the application of multiple migration techniques to active source OBS data collected near the deformation front.

The rheology of the basal layer at depth depends on shear strength, fluid flow patterns associated with compressional faults and sediment deformation within the accreted wedge. A previous megathrust earthquake on this margin occurred in 1700. According to *Hyndman* (2013), the recurrence interval between megathrust earthquakes is $\sim 500 - 600$ years. The viscoelastic basal layer beneath the accretionary wedge is capable of rupturing during the megathrust event. Analysis of multichannel seismic (MCS) data from Vancouver Island continental margin indicates that sediment deformation varies along the margin, which could be related to localized variations in fluid pressure (*Spence et al.*, 1991b). Previous studies on the southern Cascadia margin off Oregon and Washington indicate that the vergence structure changes along the margin (Fig. 1.1) (*MacKay et al.*, 1992; *MacKay*, 1995). The change in vergence is associated with variation in shear strength of the basal layer at depth (*Gutscher et al.*, 2001), which has direct implications for understanding natural hazards on this margin.

1.1.3 Continental shelf seismic structure

The third part of this thesis focuses on continental shelf seismic analysis off Vancouver Island margin using traveltime tomography and full waveform inversion of marine MCS reflection data.

As a result of subduction of the Juan de Fuca Plate, sediments are scraped off and accreted to the margin forming the accretionary wedge, the Crescent and the Pacific Rim terranes on top of which lies the Tofino forearc basin under the continental shelf off Vancouver Island margin (Figs. 1.2 & 1.3) (*Hyndman et al.*, 1990). Several studies were conducted to estimate the hydrocarbon potential of this basin (*Shouldice*, 1971;

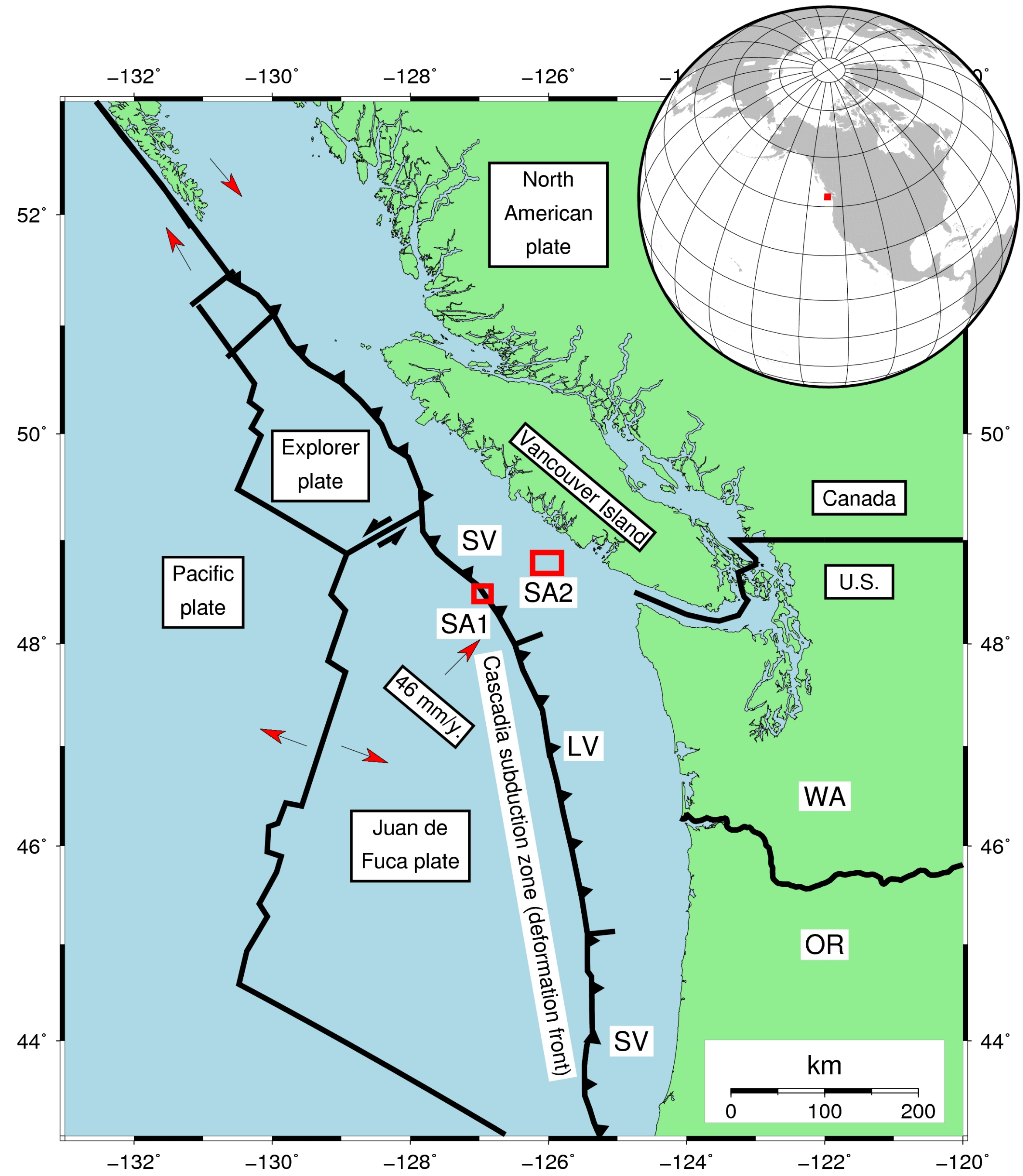

Figure 1.1: Tectonic setting of west-central coast of North America. Red rectangle boxes SA1 and SA2 are the study areas investigated in this study. SV: Seaward vergence and LV: landward vergence are based on *MacKay* (1995).

Hannigan et al., 1998; *Schuemann et al.*, 2010). According to *Hannigan et al.* (1998), Tofino basin has a single defined play with a potential of 266 x 10^9 m^3 (9.4 TCF) of in-place gas and thirty eight fields with gas volume of 3000 x 10^6 m^3 are predicted to occur. Mesozoic source rocks in the basin may be a potential target for hydrocarbon exploration in future (*Schuemann et al.*, 2010). Previous studies using conventional processing and tomography of MCS data provide information about the subsurface fault structures (*Spence et al.*, 1991b; *Hayward and Calvert*, 2007), but there remains ambiguity over the boundary between the Crescent terrane and Pacific Rim terrane and the shallowest occurrence of the volcanic Crescent terrane (Fig. 1.3).

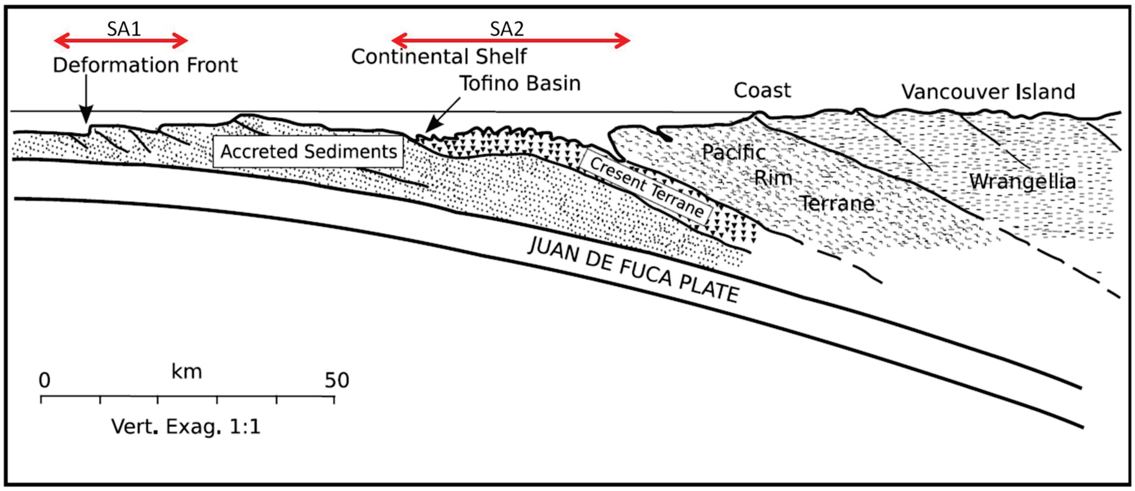

Figure 1.2: Cross section across the continental margin off Vancouver Island (After *Hyndman et al.*, 1990). SA1 and SA2 indicate the location of present study areas.

1.2 Detailed thesis objectives

The objective of the first part of the study is to determine gas hydrate concentrations and distribution in the frontal ridge region, and to investigate possible links of gas hydrate occurrence to slope stability. Emphasis is on seismic inversion methods to quantify gas hydrate concentrations, and to image the ridge structure and submarine slides using high resolution velocity models from traveltime tomography. This study has large societal significance as mass failures on the margin are of comparable size (e.g., $1-3$ km^3) to others that have generated large tsunamis specifically Papua New Guinea in 1998 with loss of $\sim$ 2000 lives. Results of this study provide well constrained velocity models that act as "ground truth" for development of ambient noise tomography methods (Honn Kao, pers. comm.). These methods will be applied at the crustal scale where they will help our understanding of the seismic locked zone which will eventually unlock in the next inevitable megathrust earthquake on the Cascadia margin.

The second part of this thesis which deals with multiple migration of the OBS data will be useful in understanding sediment deformation within the accreted wedge sediments and the Cascadia basin sediment section, fluid flow patterns associated with compressional faults and the vergence structures on the northern Cascadia subduction zone. This study has important implications for the understanding of megathrust earthquakes on this margin.

In the last part of this study, high resolution seismic velocity and attenuation models from travel time tomography and full waveform inversion were used to determine the correlations between seismic velocities and structures interpreted from the MCS data (Fig. 1.3). The data are devoid of low-frequency components, which are critical for successful application of waveform inversion. Furthermore, steep dips are present in the study area and lateral changes in velocity are apparent along the length of the line (Fig. 1.3). Therefore, this study aims to develop an effective inversion strategy to mitigate the non-linear and ill-posed nature of the inversion process. This is the first 2D full waveform inversion study on this margin, with a primary objective to supplement the structural information obtained from previous studies by applying waveform inversion to MCS data. In particular, this study aims to illuminate deformation within accretionary wedge and Tofino basin sediments and the nature of basement structures. The estimation of velocities from MCS data using inversion methods will provide background or regional seismic velocity trends that are useful to the hydrocarbon exploration industry for planning of possible new seismic exploration in Tofino basin.

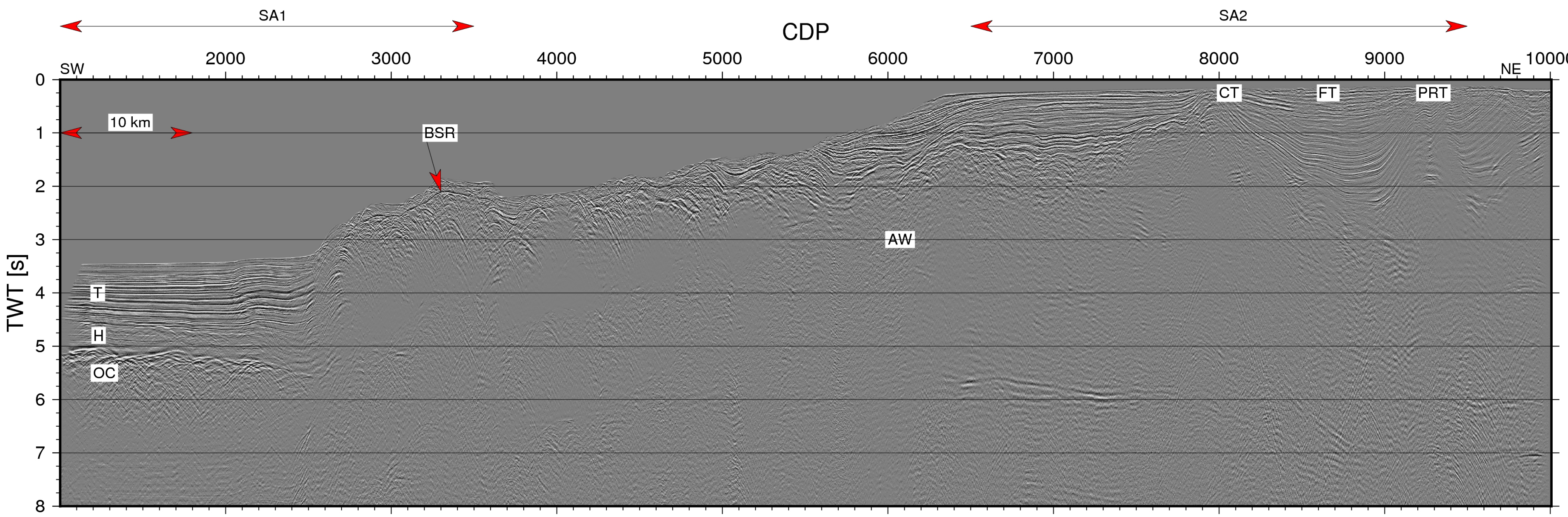

Figure 1.3: Accretionary prism structure from multichannel seismic line 89-06 across the continental slope. Labels T: Turbidites, H: Hemipelagic, OC: Oceanic crust, BSR: Bottom simulating reflector, AW: Accretionary wedge, CT: Crescent terrane, FT: Fossil trench, and PRT: Pacific Rim terrane are based on previous multichannel line interpretations by *Hyndman et al.* (1990) and *Spence et al.* (1991b). SA1 and SA2 indicate the location of present study areas. Seismic section was processed by Digicon.

1.3 Background geology and geophysics

1.3.1 Regional geology and tectonic history

Vancouver Island is part of the Insular Belt, which is the westernmost of five north-westerly trending subdivisions (Foreland, Omineca, Intermontane, Coast and Insular) of the Canadian Cordillera. The Insular Belt is a product of collisions (about 100 Ma) between the ancient western edge of North America and exotic pieces of earth's crust, called Wrangellia, which comprises Devonian through Lower Jurassic igneous sequences and sedimentary successions (*Muller*, 1977; *Monger et al.*, 1982). At the western Canadian convergent margin, the Juan de Fuca and Explorer plates subduct beneath and converge towards the North American plate at about 47 and 20 mm/year and diverge from the Pacific plate along the Dellwood, Explorer and Juan de Fuca ridges at rates up to 59 mm/y (Fig. 1.1) (*Riddihough*, 1977; *Keen and Hyndman*, 1979; *Riddihough*, 1991).

The Cascadia accretionary wedge has formed above the down-going oceanic plate by deformation, off-scraping and underplating of rocks beneath the overriding continental plate. In southernmost Vancouver Island, major westerly trending faults partition the crust into two narrow zones, the Pacific Rim terrane and Crescent terrane (Fig. 1.2) (*Clowes et al.*, 1987; *Hyndman et al.*, 1990). These terranes extend beneath the continental shelf and provide a landward dipping backstop to the accretionary wedge sediments (*Spence et al.*, 1991b). The deformation front is characterized by mainly landward dipping thrust faults that cut close to basement (*Davis and Hyndman*, 1989).

The Pacific Rim terrane and Crescent terrane were accreted to Vancouver Island in late Eocene time, between 55 and 42 million years ago. The Pacific Rim terrane, which is exposed along the west coast of Vancouver Island, consists of a melange of intensely disrupted mudstone, chert, sandstone, and conglomerate (*Brandon*, 1985). The Crescent terrane, which consists of Eocene ophiolitic basalt and gabbro, lies above and landward of the accretionary wedge under the continental shelf and occurs in the footwalls of the Leech River and Tofino faults, respectively (*Yorath et al.*, 1985; *Clowes et al.*, 1987; *Hyndman et al.*, 1990).

Previous interpretations of MCS line 89-06 (Fig. 1.3) by *Spence et al.* (1991b) indicate that Crescent terrane has a maximum thickness of 12 km and reaches down to the top of the subducting oceanic plate. *Hayward and Calvert* (2007) provide a more in-depth interpretation of this line (and others). They interpret the formation of the sub-basin (fossil trench as interpreted by *Hyndman et al.* (1990)) at the boundary between the Crescent and Pacific Rim terranes along the margin by roll back of the subducting plate together with the reactivation of the terrane bounding Tofino fault. Alternatively, this could have been formed by the removal of parts of the lower forearc crust by subduction erosion.

1.3.2 Previous geophysical studies

The oceanic crust at the Northern Cascadia subduction zone is well imaged by marine and land multichannel seismic data to depths of 40 km beneath Vancouver Island. Previous seismic interpretations indicate that the oceanic lithosphere subducts at a shallow angle of 3 degrees or less at the continental slope, with dip increasing to $14-16$ degrees below the continental shelf (*Spence et al.*, 1985; *Hyndman et al.*, 1990). The dip is substantially less beneath the Olympic Peninsula (*Taber and Smith*, 1985; *Davis and Hyndman*, 1989). The decollement slope beneath Tofino basin is greater than the critical angle (11 degrees) for upward growth of an accretionary prism, and hence subsidence occurred to form Tofino sedimentary basin (*Davis et al.*, 1983; *Davis and Hyndman*, 1989; *Wang and Hu*, 2006).

The oceanic crust entering the subduction zone carries a sediment section comprising of pre-Pleistocene, mainly hemipelagic sediments and a thicker section of rapidly deposited, highly reflective Pleistocene turbidites (Fig. 1.3). The turbidites fill the basin and even completely fill the basement trench of this subduction zone. Mass balance studies show that the volume of the accretionary sedimentary prism is roughly equal to the estimated volume of sediments brought from the Juan de Fuca plate since the Eocene (*Davis and Hyndman*, 1989; *Hyndman et al.*, 1990). This supports other arguments that, since the Eocene, most of the incoming sediment has been scraped off rather than subducted (Fig. 1.3). According to *Hyndman et al.* (1990) and *Spence et al.* (1991b), landward dipping thrusts at the deformation front cut through the sediment section to near the base of the oceanic crust resulting in fewer sediments that are available for underplating in the mantle. This is in contrast to many subduction zones where substantial amounts of sediment are subducted to great depths (e.g., *von Huene and Scholl*, 1991).

Multichannel reflection data from 1984, 1985 and 1989 indicate that Juan de Fuca plate is clearly observed below the Cascadia basin sediments, but it is discontinuously imaged below the continental slope, shelf and Vancouver Island (*Clowes et al.*, 1987). These data also show three distinct reflective bands (C, D, E) beneath Wrangellia. The C band corresponds to the Olympic subduction complex, while the high velocity reflective band D corresponds to detached slab of oceanic lithosphere or imbricated package of mafic rocks. According to *Calvert* (1996), the E band which occurs extensively over this margin corresponds to a former subduction decollement where one or two mafic units were underplated beneath the overlying continent.

Some studies identified a low velocity zone (LVZ) corresponding to the E reflection band and interpreted it as the plate boundary (*Bostock et al.*, 2002; *Nedimović et al.*, 2003; *Audet et al.*, 2009, 2010). Recent studies show that the LVZ represent a shear zone or over pressured sediments and that the top of the downgoing plate is about $6 - 8$ km deeper than the LVZ (*Ramachandran et al.*, 2005; *Calvert et al.*, 2011; *Calkins et al.*, 2011; *McCrory et al.*, 2012).

Analysis of multichannel data from 1985 reveals strong seismic reflection amplitudes in the accreted wedge sediment section (*Calvert and Clowes*, 1991). These were associated with low seismic velocities. Furthermore, amplitude analysis of these reflections show high Poisson's ratio indicating that much of the high reflectivity is related to elevated pore pressure. Some of these reflections are associated with thrust faults that indicate upward migration of fluids. According to *Davis and Hyndman* (1989), sediments within the accretionary prism contain elevated pore pressure as a result of dehydration of the subducting slab and compaction of the lower accreted sediments.

Thermal structure of the margin indicate that heat flow decreases landward across the continental margin from as high as 120 mW/m^2 in the Cascadia basin to 90 mW/m^2 over the lower continental slope and 50 mW/m^2 over the continental shelf. The low heat flow indicates the tectonic thickening of accretionary wedge sediments and ongoing subduction of cold crust and sediments beneath the margin (*Davis et al.*, 1990; *Hyndman and Wang*, 1993).

Despite the considerable amount and diversity of research, and ensuing development in resolution and understanding of the northern Cascadia subduction zone structure, competing and contradictory theories regarding the depth of the subducting crust, the location of the inter-plate plate boundary (*Spence et al.*, 1991b; *Calvert*, 2004; *Nicholson et al.*, 2005; *Hayward and Calvert*, 2007), and the continuation of major terrane boundaries at depth (*Hyndman et al.*, 1990; *Calvert*, 1996) are still present.

1.4 Gas hydrate studies

Certain low-molecular-weight gases (< 0.9 nm), such as methane, ethane, and carbon dioxide, can combine with water to form ice-like substances at moderate pressures (> 0.6 MPa) and temperatures (< 300 K) (*Sloan*, 1998b, 2003). These compounds, commonly called gas hydrates or clathrates, concentrate gas in solid form. They occur naturally in sediments beneath the Arctic permafrost and in the sediments of the continental slope (*Shipley et al.*, 1979; *Hyndman and Spence*, 1992; *Kvenvolden*, 1993). In general, gas hydrate studies shed light on the global understanding of the role of gas hydrates as a potential future energy resource (*Kvenvolden*, 1993; *Collett and Ladd*, 2000; *Milkov*, 2004), their role in past and future climate change (*Haq*, 2003; *Andersen et al.*, 2004), and their potential as a geologic hazard in areas with active offshore/onshore industry activities (*Mienert et al.*, 2005).

Hydrates are commonly observed in seismic data by the occurrence of a bottom simulating reflection (BSR), which marks the contrast between hydrate-bearing sediments above and gas-saturated sediments below. The BSR closely follows the seafloor reflection and has opposite polarity to that of seafloor. Compared to the background P-wave velocity profile, the seismic velocity is typically $100 - 200$ m/s higher above the BSR and is lower below the BSR.

1.4.1 Stability field of gas hydrates

The stability of gas hydrate depends mainly on temperature, pressure, gas composition and saturation, and pore-water composition. Gas hydrate nucleation and growth also depend on sediment grain size, shape, and composition (*Clennell et al.*, 2000). Figure 1.4 indicates the gas hydrate stability field for the frontal ridge region assuming a seawater-methane system (100% methane gas and a geothermal gradient of $0.06\,^{\circ}$C/m based on Integrated Ocean Drilling Program (IODP) X311 results, *Riedel et al.* (2006a)). The phase boundary curve is calculated using CSMHYD program (*Sloan*, 1998a) assuming a three-phase equilibrium condition with a salinity of 35‰ as inhibitor.

Several authors indicated that sea-level change and bottom water temperature increase could affect the stability of gas hydrates (*Canals et al.*, 2004; *Wong et al.*, 2003; *Maslin et al.*, 1998; *Rothwell et al.*, 1998; *Kayen and Lee*, 1991). Some studies also show the occurrence of double BSRs. In a recent review, *Spence et al.* (2010) compared the occurrence of double BSRs in various tectonic environments. Mecha-

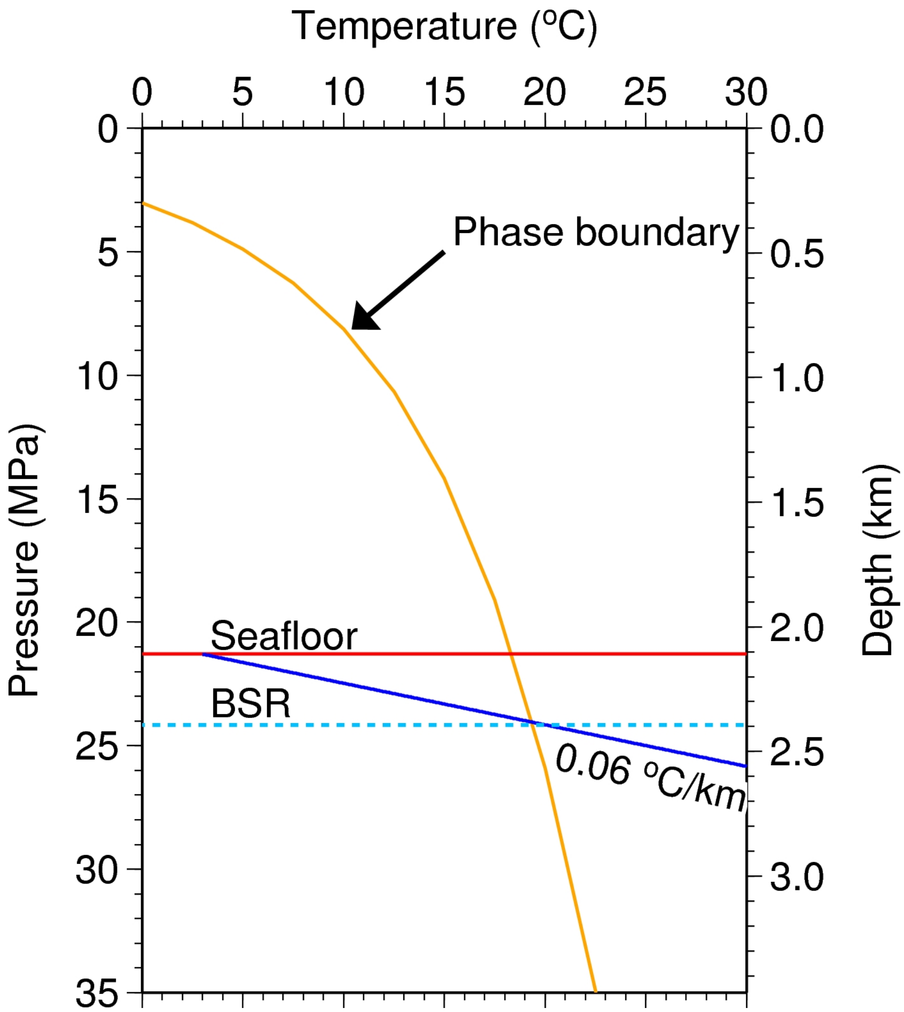

Figure 1.4: Methane hydrate stability diagram for seawater. Orange line indicates the phase boundary curve calculated using CSMHYD program (*Sloan*, 1998a) assuming a three-phase equilibrium condition with a salinity of 35‰ as inhibitor.

nisms that cause double BSRs include tectonic uplift (*Matsumoto et al.*, 2004; *Foucher et al.*, 2002), bottom water warming (*Popescu et al.*, 2006; *Bangs et al.*, 2005; *Bünz and Mienert*, 2004), sea-level rise, sedimentation, different gas composition and erosion (*Hornbach et al.*, 2003). *Popescu et al.* (2006) noticed up to five BSR's in the Black Sea region. They interpreted these as diagenetic signatures caused by successive stages of stable climatic episodes. These paleo BSR's continue to exist as long as the time since the last warming event is less than the gas-zone depletion time, which is typically of the order of $10^5 - 10^6$ years (*Haacke et al.*, 2008).

Finite difference models of slope failure associated with gas hydrate suggest that a bottom water temperature increase of $\sim 1\,^{\circ}$C could lead to an increase in pore-pressure that is sufficiently large to reduce the stability of a slope (*Kwon and Cho*, 2012). According to this study it requires over $10,000$ years for the heat to transfer from seafloor to the base of the hydrate stability zone (BHSZ), which is at 450 mbsf for the case of Blake Ridge region.

Several studies in the past have reported a disrupted BSR associated with active faulting and mud diapirism (*Berndt et al.*, 2005; *De Batist et al.*, 2002; *Dillon et al.*, 1998). For example, seismic observations in the Lake Baikal gas hydrate province indicate that the BSR is strongly disrupted in the 10 km vicinity of small antithetic faults and shallows to depths of 150 mbsf (meters below seafloor) in contrast to $300-350$ mbsf in the adjoining areas. Further, the BSR is vertically displaced along a major fault with an offset as large as 110 m compared to the actual fault throw of only 75 m (*De Batist et al.*, 2002). Anomalously high heat flow values of up to ~ 165 mW/m^2 were reported over the disrupted BSR region as opposed to $\sim 55-90$ mW/m^2 in the surrounding areas, which indicate that the irregular morphology of the BSR is mostly temperature controlled in this region.

1.4.2 Models for gas hydrate formation and dissociation

Gas hydrates usually form at water depths greater than 400 m and at sub-seafloor depths of 100 m to 600 m. The origin of the methane in a hydrate can be either thermogenic or biogenic. Several models have been proposed to describe the formation of gas hydrate and the development of BSRs. In one such model, methane is assumed to be generated microbiologically from organic matter within the gas hydrate stability zone (*Claypool and Kaplan*, 1974). Hydrate then forms concurrent with sedimentation. The significance of this model is that hydrates should present throughout the stability zone and free gas may or may not occur beneath the BSR.

Hyndman and Davis (1992) proposed a model for the formation of hydrates in accretionary margins. According to this model hydrates form by removal of methane from regional diffusive upward fluid flow as they pass from below into the hydrate stability zone. A consequence of this model is that hydrates should be concentrated at the base of the stability zone, i.e., at the BSR, and free gas is not to be expected beneath the BSR.

According to *Xu and Ruppel* (1999), hydrates form by methane advection and diffusion and the base of the hydrate occurrence may be above the base of the hydrate stability field and top of free gas may be below the stability field. *Haeckel et al.* (2004)

proposed another hydrate formation model in which gas bubbles from deeper sources rise up to the seafloor to form shallow hydrate deposits. When the bubbles reach the seafloor through migration pathways such as faults, they form seafloor hydrate deposits.

In the continental slope sediments, after the formation of gas hydrates, the sediments are carried landward into the prism where water depths become shallow due to tectonic uplift and ongoing sediment deposition. As a consequence, the stability field moves upward because of less pressure. The hydrate just above the BSR is therefore progressively moved out of the stability field and dissociates into free gas, which in turn will migrate upward to form a shallower BSR (e.g., *Paull et al.*, 1994). This successive accumulation of methane just above the BSR will lead to an increase in concentration of hydrate not far above the BSR (e.g., *Zatsepina and Buffett*, 1998; *Xu and Ruppel*, 1999). The thickness and concentration of the free gas layer depends on the permeability of sediments and the rate of fluid expulsion.

1.4.3 Gas hydrate studies on the northern Cascadia margin

The first gas hydrate study on the Cascadia margin goes back to 1985 (*Davis and Hyndman*, 1989; *Davis et al.*, 1990), where a multichannel seismic survey imaged the BSR. Since then the region has been the subject of numerous geological and geophysical studies, which include multichannel seismic reflection, shallow seismic profiling, seismic refraction, seafloor compliance, and piston coring, plus geothermal, seismicity, gravity, magnetic and electromagnetic surveys. These studies have inferred the presence of methane hydrate in the continental slope sediments in a 30 km wide band at water depths ranging from $800 - 2200$ m.

Results from ODP site 889 together with regional seismic velocities initially suggested that the pore space contains $20 - 30\%$ of hydrate. Geochemical core analysis and wireline log results shows the presence of hydrates at $\sim 127 - 228$ mbsf.

The continental margin gas hydrates are highly concentrated at cold seepage sites, where large amounts of gas are vented into the water column (*Spence and Hyndman*, 2001; *Riedel et al.*, 2001). *Riedel et al.* (2006b) integrated geophysical and geochemical studies to develop a vent model incorporating all constraints. Results from IODP Expedition 311 show that by far the largest concentrations of gas hydrate ($> 80\%$ of the pore volume in sections several tens of meters thick) occur at a shallow depths of less than 100 mbsf (e.g., at Sites U1326 and U1327) (Expedition 311 Scientists, *Riedel* *et al.* (2006a)). Furthermore, in regions of focused fluid/gas flow associated with fault-related conduits within active cold vent fields, gas hydrate concentration is highest in the near-surface (e.g., Site U1328). Massive hydrate was recovered at shallow depths by piston coring (*Riedel et al.*, 2006b), and this massive layer was found to be $40-50$ m thick by IODP drilling at Site U1328 (*Riedel et al.*, 2006a). The geophysical logs and core chlorinities indicated only low underlying concentrations (*Malinverno et al.*, 2008), consistent with the seismic data interpretations.

Numerous other studies on the margin have used MCS data to derive P-wave velocities up to BSR depths; methods included normal move out velocity analysis (*Yuan et al.*, 1996), 1D full waveform inversion (*Singh et al.*, 1993; *Singh and Minshull*, 1994; *Yuan et al.*, 1999) and AVO studies (*Yuan et al.*, 1999; *Chen*, 2006). Initial BSR analysis suggested that above the BSR is a 10 to 30 m thick high velocity layer with about 30% of its pore space filled with gas hydrate (*Hyndman and Spence*, 1992). Waveform inversion results from *Singh et al.* (1993) near ODP site 889/890 showed that sediment pores beneath the BSR contain free methane gas in a layer approximately 30 meters thick with a P-wave velocity of 1.58 km/s, an S-wave velocity of 0.723 km/s (Poisson's Ratio of 0.4) and a density of 1.6 g/cc. Their velocity values and Poisson's Ratios correspond to hydrate saturation of less than 10% and a free gas saturation of probably less than 1%. Estimates of *Yuan et al.* (1996) showed that about 2/3 of the BSR impedance contrast comes from high-velocity hydrate and about 1/3 from the low-velocity methane, relative to a no-hydrate no-gas reference velocity.

Multi-frequency analysis of seismic data in the vicinity of ODP site 889 indicated that BSR reflection coefficients are slightly larger for 30 Hz frequency data than for 75 Hz or 150 Hz data (*Fink and Spence*, 1999). BSR reflection waveform modeling showed high reflection coefficients of BSR $(0.15-0.18)$ beneath topographic highs, while that of the seafloor $(0.5-0.6)$ were found on the flanks of the topographic highs. This suggests that topography provides a major control on the flow of methane-bearing fluids.

Deployments of OBSs have been carried out in the vicinity of ODP Site 889 and IODP 1327, in 1993, 1999, and 2005. These data have allowed travel-time inversion studies to provide 2-D or 3-D velocity models in the region of the drill site (*Spence et al.*, 1995; *Hobro et al.*, 1998; *Hobro*, 1999; *Hobro et al.*, 2005; *Zykov*, 2006; *Dash*, 2007). According to these studies, velocities directly above the BSR range from 1.87 to 1.96 km/s. The higher velocities relative to a no-hydrate reference appear to be correlated to an increase in the reflection strength of the BSR.

1.4.4 Slope failures on a frontal ridge

Several slope failure features are observed near the deformation front off Vancouver Island (Fig. 1.5). The most prominent among these are Orca slide and Slipstream slide (Fig. 1.5). Possible causes for the frontal ridge slope failures are hydrate dissociation, high pore pressure, contrasting sediment physical properties, salinity elevation in faults and earthquakes. The presence of hydrates increases the sediment strength. But this increase depends on hydrate concentration and how the hydrates are distributed within the sediments.

Enkin et al. (2010) suggested that contrasting sediment physical properties (glacial vs deglacial vs inter-glacial) may provide glide plane for failure. Coring results conducted on the frontal ridge slope failures show that the bottom of the core contains much older sediments, much stiffer and stronger than overlying sediments found everywhere else, which are likely weak de-glacial deposits (14 ky). This suggests that the top of the older sediments may provide the glide plane.

Marine gas hydrates have been identified in many areas of the accretionary prism of the Northern Cascadia subduction zone at the frontal ridge. A previous study (*Lopez et al.*, 2010) on the frontal ridge region near a slope failure (Orca slide) observed BSR at $\sim 250-260$ m depth beneath the ridge crest and on its seaward slope. The velocity structure above the BSR shows anomalously high velocities of about 1.95 (± 0.05) km/s at shallow depths of $80-110$ m. They also observed a series of normal faults on the migrated stack section which are perpendicular to the strike of the ridge and the direction of plate convergence. Furthermore, the depth of the BSR coincides with the estimated depth of the glide plane beneath the slide, which indicates that the base of the slope failure is associated with the contrast between hydrated sediments above the BSR and underlying gas saturated sediments.

The presence of hydrates strengthens the sediments and their dissociation increase the pore pressure and cause the failure of over-steepening slopes. In a recent study, *Scholz* (2014) estimated pore-pressure generated from hydrate dissociation on this margin using empirical relations. The results of this study indicate that sediments with a permeability of $10^{-17}m^2$ or lower can generate excess pore-pressure that is sufficient to cause slope failure on this margin. As well, the results showed that the top of gas hydrate occurrence zone is more susceptible to pressure changes than the

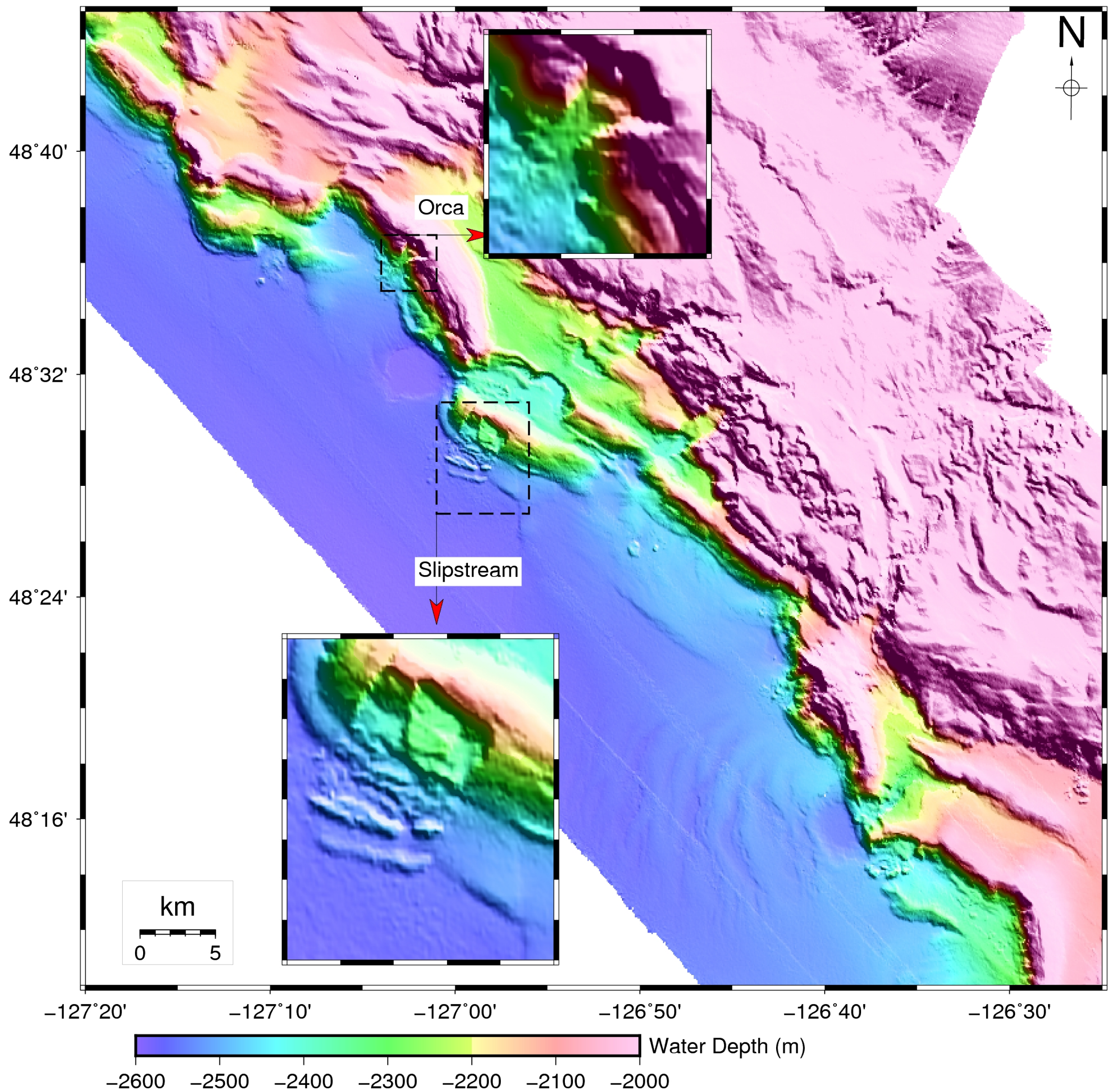

Figure 1.5: Multibeam bathymetry map of Vancouver Island continental slope showing mass failure events. Insets show enlarged figures of Slipstream and Orca slides. High resolution swath bathymetry data was acquired by University of Washington in 2004 (*Kelley and Delaney*, 2005).

BSR.

1.5 Seismic imaging and full waveform inversion

Seismic reflection imaging which is widely used in the oil and gas industry typically involves dense source and receiver arrays, with relatively short offsets that typically do not exceed $5 - 6$ km; this geometry therefore provides information about the small wave length (large wave number) features beneath the subsurface (*Yilmaz*, 2001). Refraction imaging, on the other hand, recovers long wavelength components or large scale structures by using large source-receiver distances; it is often used in deep crustal investigations (*Levander et al.*, 2007). Waveform imaging uses full wave form information that includes both reflections and refractions and therefore recovers both small and large wave number components (*Tarantola*, 1984; *Pratt et al.*, 1996; *Virieux and Operto*, 2009). However, this requires both densely sampled and large offset data.

The resolution of traveltime tomography is limited to the first Fresnel zone width, since it uses the high frequency approximation of asymptotic ray theory (*Woodward*, 1992; *Williamson and Worthington*, 1993). Full waveform inversion on the other hand uses a complete numerical solution of the wave equation (*Tarantola*, 1988; *Pratt et al.*, 1998). It is highly non-linear in nature, so that the solution depends strongly on the initial model, which is commonly obtained by first arrival tomography. The inversion tries to minimize the misfit between the observed and forward modelled waveform by iteratively updating the initial model. It forms the gradient of the objective function by utilizing the Born approximation (*Lailly*, 1983; *Tarantola*, 1984; *Pratt*, 1990; *Pratt and Worthington*, 1990). The model gradient is calculated using the adjoint method in either time domain (*Lailly*, 1983; *Tarantola*, 1984) or frequency domain (*Pratt and Worthington*, 1990; *Pratt*, 1990) by correlating the forward propagated wavefields with back propagated data residuals. The gradient-based methods (conjugate gradient and steepest descent) are more computationally efficient due to adjoint computation as opposed to Newtonian methods which require the computation of more expensive Fréchet derivatives. In the conjugate gradient method, the gradient is preconditioned by filtering it in some way to improve the convergence.

According to *Pratt et al.* (1998), the gradient of the objective function (E) with respect to a model parameter (m) is given by

$$\nabla_{m(r)}E = -\sum_{\omega} u^T(\omega) \left[\frac{\partial S}{\partial m(r)}\right]^T \left[S^{-1}\right]^* \delta d \tag{1.1}$$

where u is the frequency domain forward propagated wavefield, S is the impedance matrix, δd is the data residuals, ^{T} is the Hermite conjugate and * is the complex conjugate. The term $[S^{-1}]^* \delta d$ represents the back propagated wavefield which is weighted by $\frac{\partial S}{\partial m(r)}$ before correlating with the forward propagated wavefield in gradient computation.

The smallest recoverable anomaly in waveform tomography is half a wavelength in contrast to $\sqrt{\lambda L}$ in traveltime inversion, where L is the propagation length (*Williamson and Worthington*, 1993).

Although the theory of full waveform inversion was developed three decades ago, it is only in recent years that it was applied to real data in hydrocarbon exploration (*Brenders*, 2011; *Sears et al.*, 2010; *Plessix and Cao*, 2011; *Sirgue et al.*, 2010; *Vigh and Starr*, 2008), near-surface engineering studies (*Smithyman et al.*, 2009; *Gao et al.*, 2005, 2006), and crustal-scale studies (*Shipp and Singh*, 2002; *Dessa and Pascal*, 2003; *Ravaut et al.*, 2004; *Operto et al.*, 2006; *Bleibinhaus et al.*, 2007; *Malinowski et al.*, 2011; *Takougang and Calvert*, 2011; *Arnulf et al.*, 2012). While most studies only obtained P-wave velocity structure using waveform inversion, some studies also explored other elastic parameters such as S-wave velocities (*Mora*, 1987; *Tarantola*, 1988; *Shipp and Singh*, 2002; *Brossier et al.*, 2009a), P-wave attenuation (*Tarantola*, 1988; *Song et al.*, 1995; *Malinowski et al.*, 2011; *Takougang and Calvert*, 2011), density (*Choi et al.*, 2008; *Jeong et al.*, 2012), and anisotropic parameters (*Barnes et al.*, 2008; *Gholami et al.*, 2011a,b).

1.6 Multiple imaging

Unlike full waveform inversion, which requires dense source receiver sampling, multiple imaging of downgoing waves recorded on OBS data is a useful technique when the receiver interval is large. It provides information about a much larger area than is possible using primary signals alone (*Godfrey et al.*, 1998; *Ronen et al.*, 2005; *Grion et al.*, 2007; *Dash et al.*, 2009; *Wong et al.*, 2011, 2012a). This method is less sensitive to near seabed inhomogeneities and provides detailed information about shallow subseafloor targets, which are poorly resolved using upgoing primaries alone. It is also easy to implement using existing migration algorithms by simply changing the receiver depth. Recent developments of this technique (*Wong et al.*, 2011, 2012b) show that joint inversion of primaries and multiples would provide better subsurface illumination with enhanced resolution, more balanced amplitude information and fewer migration artifacts.

1.7 Thesis outline

Chapter 2 presents the application of traveltime inversion to the OBS data set acquired near the deformation front on a frontal ridge of the northern Cascadia subduction zone. This chapter is published as a manuscript in Geophysical Journal International in 2014 as “Role of gas hydrates in slope failure on a frontal ridge of the northern Cascadia margin” by Subbarao Yelisetti, George D. Spence and Michael Riedel. This chapter describes data acquisition, processing and P-wave velocity modeling of wide-angle reflections and refractions recorded on OBS data and vertical incidence reflections recorded on SCS data. Glide plane analysis, volume estimates of the slide from multi-beam bathymetry data and a brief description of fluid flow, possible double BSR and BSR uplift is presented in this chapter. Furthermore, glide plane analysis results were compared to seismic structure obtained by estimating gas hydrate concentrations from shallow velocity structure using effective medium modelling. The tsunamigenic marine landslide and debris flow documented in this chapter has large societal impact.

Chapter 3 presents the application of mirror imaging to the OBS data described in chapter 2. This chapter is intended for publication in Geophysics as “Dual-vergence structure from multiple migration of widely spaced OBSs from the northern Cascadia margin” by Subbarao Yelisetti, George D. Spence, Martin Scherwath, Michael Riedel and Volkhard Spiess. A brief description of seismic data acquisition, processing and wavefield separation are presented in this chapter. Mirror imaging results are compared to coincident single channel and multichannel data in the region. The high-quality multiple migration image shows a dual-vergence structure that was not previously seen on the northern Cascadia margin, and could be associated with low shear stress resulting from over pressure and has important implications for understanding natural hazards in the Cascadia margin.

Chapter 4 deals with the application of frequency domain visco-acoustic full waveform inversion to multichannel seismic data from Vancouver Island continental shelf. This is the first 2D full waveform inversion study on this margin. This chapter is intended for publication in Canadian Journal of Earth Sciences as “Seismic velocity and attenuation structure beneath the Vancouver Island continental shelf using frequency domain visco-acoustic fullwaveform inversion of multichannel seismic data” by Subbarao Yelisetti and George D. Spence. This chapter describes the successful application of waveform inversion to challenging data that are devoid of low-frequency components. Furthermore, the structure is complex in the accretionary wedge region with the presence of steep dips and large lateral changes in seismic velocity. Strong emphasis was laid on developing very good starting velocity model that is required for waveform inversion. A brief description of data preparation through inversion strategy and extensive quality control tools are presented in this chapter. Geological implications of waveform inversion results are discussed towards the end of the chapter, which are useful for possible future exploration in the Tofino basin and to understand the regional tectonics of the margin.

The final chapter, chapter 5 summarizes the results presented in Chapters 2-4, and discusses possible future directions of this study.

Chapter 2

Role of gas hydrates in slope failure

A version of this chapter was published in Geophysical Journal International as: Subbarao Yelisetti, George D. Spence and Michael Riedel, 2014. Role of gas hydrates in slope failure on frontal ridge of northern Cascadia margin, Geophysical Journal International, 199(1), 441-458, doi:10.1093/gji/ggu254.

Author contribution: The author of this thesis is responsible for design of the research program, analysis of the data and composition of the manuscript. My supervisor, George Spence, provided guidance with the research plan, feedback and editorial supervision throughout the development of this manuscript. Coauthor Michael Riedel gave feedback on the final version of the manuscript. All the above authors were part of the data acquisition.

2.1 Introduction

Continental margin submarine landslides play an important role in the development and understanding of accretionary complexes. They are also important geologic hazards as they may cause tsunamis, and possibly release methane into the atmosphere in regions of gas hydrate (*Mienert et al.*, 2005; *Nisbet and Piper*, 1998). The mass failures and associated tsunamis can thus result in damage to coastal communities and seafloor infrastructure. For example, in 2006 a submarine landslide off Taiwan caused failure of subsea cables (*Hsu et al.*, 2009) and disrupted network communication between Taiwan, China, South Korea, Thailand, Vietnam, Malaysia and Singapore. A submarine landslide off Papua New Guinea in 1998, likely triggered by a magnitude 7.1 earthquake, caused a tsunami resulting in 2200 deaths (*Synolakis et al.*, 2002). In

1979 a slide with volume 0.15 km^3 off Nice airport generated a tsunami that killed 11 people (*Nisbet and Piper*, 1998).

Many studies have examined the relationship between slope failure and the presence of gas hydrate. Some studies support a potential connection based on the coincidence of a bottom-simulating reflector (BSR) depth to the depth of the glide plane (e.g., *Lopez et al.*, 2010; *Berndt et al.*, 2005). The presence of hydrate strengthens the sediments, and in addition, gas hydrate dissociation produces a zone of weakness at the BSR, which then may act as a glide plane for failure. The collapse structure on the crest of the Blake Ridge (off south-eastern United States) was first interpreted as a result of gas hydrate dissociation and resulting overpressure (*Dillon et al.*, 1998) and later as a long-lived, periodically reactivated structure (*Holbrook*, 2001). The dissociation of gas hydrate may also cause fluid and sediment liquefaction during or immediately after a slide event (*Berndt et al.*, 2005). In contrast, results from recent studies on the Storegga slide off the Norwegian continental margin (*Brown et al.*, 2006) and Cape Fear slide off the U.S. Atlantic margin (*Hornbach et al.*, 2007) suggest that gas hydrate dissociation played no role in slide initiation based on the evidence that the BSR is deeper than the glide plane at those sites.

The main objective of the present study is to examine possible connections between sedimentary slide features and the presence of gas hydrate beneath frontal anticlinal ridges on the seismogenic Cascadia margin off Vancouver Island. Recently, *Lopez et al.* (2010) studied a frontal ridge slide, informally called Orca slide and located near Site U1326 of the Integrated Ocean Drilling Program (IODP) Expedition 311, and found evidence that the failure glide plane occurred at the same depth as the base of hydrate stability. There are many similar slides on this portion of the Cascadia margin, and we wish to determine if other slides are also associated with gas hydrate. Specifically, we focus on a prominent slide just to the southeast, informally called Slipstream slide. We present evidence from multi-beam bathymetry, single-channel seismic reflection, and wide-angle seismic refraction data to show that the failure glide plane on Slipstream slide matches not with the BSR but with a much shallower high-velocity layer, which we interpret as a gas hydrate layer.

2.2 Gas hydrate studies on the Cascadia margin

As a result of the subduction of the Juan de Fuca plate beneath the North American plate, sediments are scraped off the downgoing plate and attached to the continental plate forming the accretionary wedge and frontal anticlinal ridges (*Davis and Hyndman*, 1989). Gas hydrates are widely inferred in this region from seismic reflection data, mainly by the observation of a BSR, which occurs at depths of 200 − 300 m below the seafloor (*Hyndman and Spence*, 1992). The BSR represents the base of the hydrate stability zone and marks the boundary between sediments containing gas hydrate and sediments containing free gas. Gas hydrate has been recovered directly from shallow piston coring and from drilling by Integrated Ocean Drilling Program Expedition 311 (*Riedel et al.*, 2006a). Analysis of resistivity and sonic logs, as well as pore-water chlorinity, indicate low average hydrate concentrations of ∼4-10% of the pore space in the gas hydrate occurrence zone (*Malinverno et al.*, 2008; *Riedel et al.*, 2010b). However, over some specific depth ranges, very high concentrations are inferred from the downhole logs of resistivity and sonic velocity. The drilling results show that by far the largest concentrations of gas hydrate (> 80% of the pore volume in sections several tens of meters thick) occur at a shallow depths of less than 100 mbsf (e.g., at Sites U1326 and U1327, *Riedel et al.*, 2006a, 2010b). Furthermore, in regions of focused fluid/gas flow associated with fault-related conduits within active cold vent fields (Site U1328), a near-surface massive hydrate plug was found with previous piston coring, and with IODP drilling the layer was found to be 40 − 50 m thick (*Riedel et al.*, 2006a,b).

2.3 Slipstream slide characteristics and timing

Modern northern Cascadia slope failures are mainly limited to the frontal ridge region near the foot of the continental slope. Slipstream slide is observed on one of these frontal ridges near the deformation front. The ridge rises approximately 500 m above the abyssal plain. The detailed morphology of Slipstream slide is determined from EM300 multi-beam bathymetry data (Fig. 2.1), collected in 2004 during University of Washington cruise TN175. The slide scar has a series of en echelon box-like features bounded by normal faults that cross-cut the frontal ridge. It has a steep headwall of height ∼ 100 m and rotational slump blocks. The slide extends 3.3 km in length and 2.5 km in width. Based on bathymetry profiles through the slide, slope angles as large as 25° were observed. The debris field lying on sediments of the ocean basin contains outrunner blocks and ridges within 1 − 2 km of the base of the slope, but finer sediments extend much farther (Fig. 2.1).

Sedimentological analyses of piston core data from 2008 indicate that slide debris in the proximal toe region contains hemipelagic clay and silty sand of age 14 ka and post-slump headwall debris contains stiff interglacial microfossil ooze of age 30 ka with episodic occurrence of turbidite sands/silts (*Enkin et al.*, 2010). The presence of post-gas-hydrate diagenetic minerals (pyrite, gregite, carbonates and chlorite) was noted in the slide material and post-slide turbidites spawned from the slide scar.

2.4 Seismic data acquisition and processing

A grid of five ocean bottom seismometers (OBSs) was deployed on the ridge, mostly near its crest with a spacing of 500 m, and two additional OBSs were deployed in the deep ocean basin with a spacing of 5 km (Fig. 2.1). These short period OBSs, with a bandwidth of $1 - 50$ Hz, contain a hydrophone and a three-component geophone (Mark Products L-28LB with natural frequency 4.5 Hz). These were provided as part of a larger seismicity project (SeaJade) in a collaboration among the University of Victoria, the Geological Survey of Canada, and the Japan Agency for Marine-Earth Science and Technology. The OBSs recorded wide-angle reflections and refractions from a 120 cubic inch Bolt airgun that was fired every 7 s, which corresponded to a nominal shot spacing of 15 to 20 m. Refraction line-4, about 22 km in length, was located along the crest of the ridge parallel to the deformation front, and a linked set of three refraction lines (hereafter combined and called line-1), nearly 20 km in length, was nominally perpendicular to the ridge and deformation front (Fig. 2.1). Two single-channel seismic (SCS) reflection lines (line-4a and line-1a) were recorded coincident with the refraction lines. Six additional single-channel reflection lines, approximately 5 km in length, were also recorded to obtain the detailed structure of the frontal ridge.

2.4.1 SCS data

The vertical incidence data were recorded on a single-channel Teledyne streamer with a 1 ms sample rate and a record length of 5 s using the same airgun source. On line-4a, strong reflections are seen at times of $230 - 280$ ms below the seafloor (Fig. 2.2a). Below this depth, the data quality is poor, particularly beneath the flanks of the ridge on line-1a (Fig. 2.2b). We applied predictive deconvolution with a operator length of 800 ms and prediction gap of 6 ms to suppress the bubble pulse, followed by bandpass filtering with frequencies $10 - 20 - 80 - 120$ Hz to suppress the high

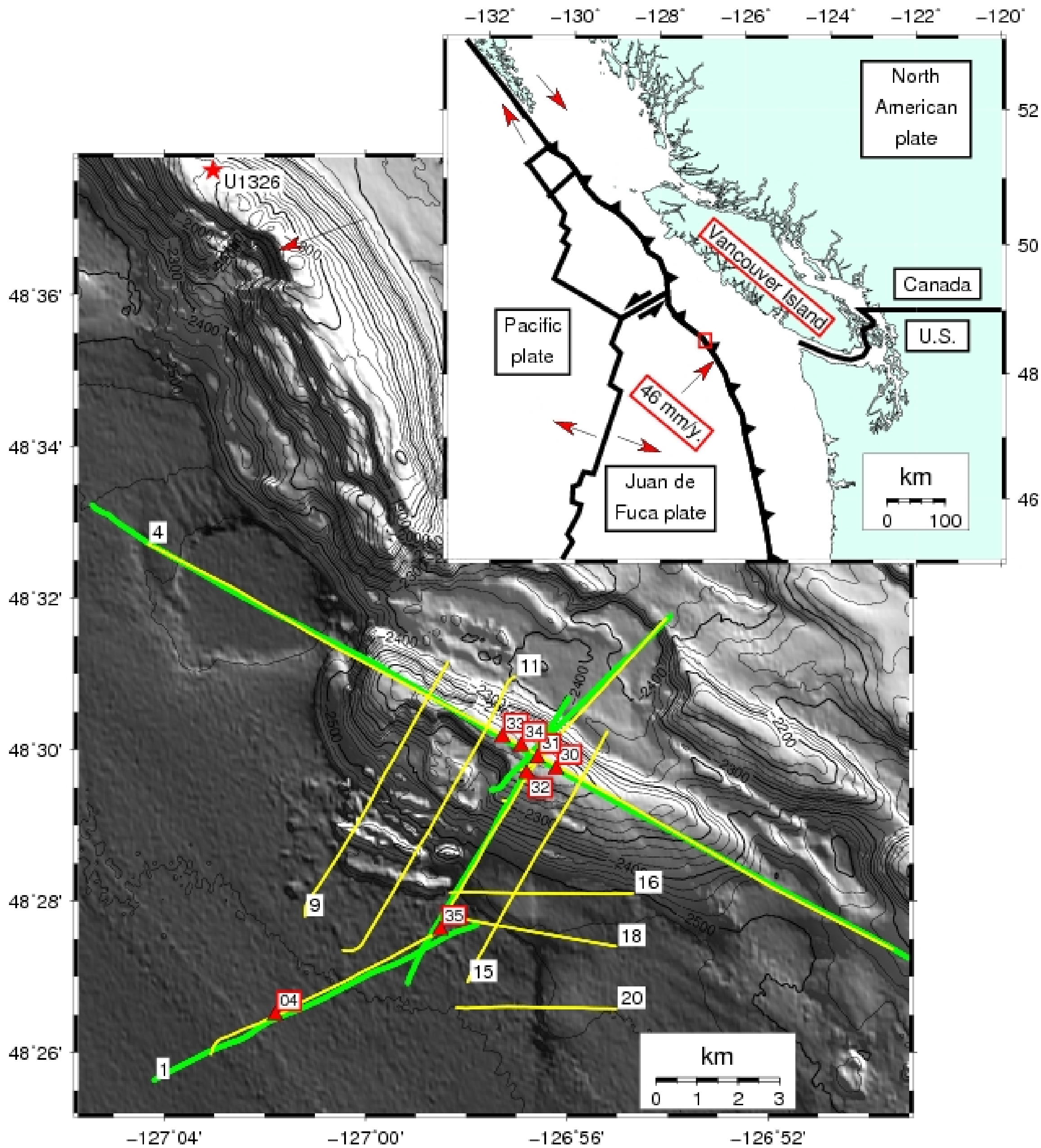

Figure 2.1: Bathymetry map showing the location of all OBSs (red triangles). OBS 33, 34, 31, 30 and 32 were deployed on the frontal ridge adjacent to Slipstream slide. OBS 04 and 35 were deployed in the deep basin where water depths are around 2500 m. Green lines represent refraction lines. Yellow lines correspond to single channel reflection lines; line-4a and line-1a are mostly coincident with refraction line-4 and line-1, respectively. Red star corresponds to Site U1326 from IODP X311. Arrow indicates Orca slide discussed in the text. Inset shows tectonic setting with convergence at 46 mm/yr.

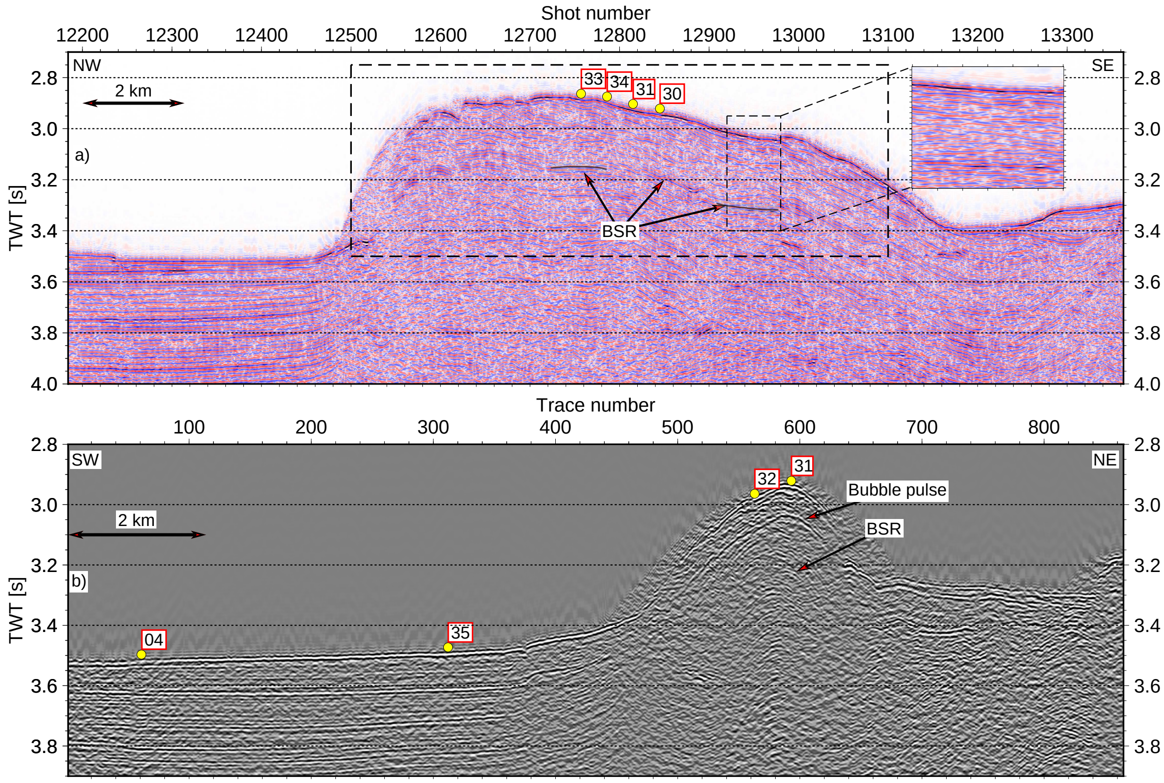

Figure 2.2: Migrated seismic section of (a) single channel line-4a parallel to the margin (passes through OBS 33, 34, 31 and 30), which coincides with refraction line-4 shown in Fig. 2.1 and (b) single channel line-1a perpendicular to the margin (passes through OBS 4, 35, 32 and 31), which coincides with refraction line-1 shown in Fig. 2.1. BSR is observed at $\sim$ 280 ms below the seafloor and is indicated by black arrows. Gray bars in (a) indicate the travel time picks used in inversion. The thickness of this line indicates the pick uncertainty. The approximate locations of the OBS units on the seafloor are shown by yellow circles. Data within the black dashed rectangle in figure (a) are expanded in Figure 2.14a. Inset figure in (a) enable the clear identification of the BSR.

frequency noise. After this, a finite difference time migration routine with a linear velocity field from 1.48 km/s at seafloor to 2.1 km/s at BSR depth (based on sonic log velocities at site U1326 of IODP X311) was applied. The migration assumed a constant trace spacing of 17.5 m. The migration was highly successful in removing diffractions near sharp offsets or scarps on the seafloor (Fig. 2.2a) and in correctly repositioning dipping reflections. The sedimentary structure is uniform in the deep basin and strong reflections can be seen to times of 4.0 s and more, in contrast to the weak reflectivity beneath the ridge crest (Fig. 2.2b).

2.4.2 OBS data

The OBS data were recorded up to 30 s with a sampling interval of 10 ms and a maximum offset of nearly 12 km on margin-parallel line-4 and 14 km on margin-perpendicular line-1. The data were resampled to 4 ms from the original 10 ms sample rate using a quadratic interpolation technique. The data quality was severely impacted by the occurrence of a strong bubble pulse sequence, which occurred with a time period of 100 ms. A gapped deconvolution was applied to the pressure component to remove the bubble pulse; this was only partially successful for the first bubble, but significantly reduced the amplitudes of later bubbles. Subsequently, bandpass filtering with frequencies 5 to 35 Hz was applied to remove the high frequency noise (Fig. 2.3 & 2.5). It was necessary to apply a static time correction to the OBS data, since the vertical-incidence travel times did not match the times expected from the well-constrained bathymetry (or from the single-channel data); a maximum shift of 150 ms was required for OBS30, while typical shifts ranging from $20-50$ ms were applied to other OBSs. The processed data show reasonable reflections including the BSR. Clear refractions are observed out to distances of up to $5-9$ km with an apparent velocity ranging from $2-4$ km/s (Fig. 2.3 & 2.5).

2.4.3 OBS relocation

The deployment location of an OBS is well determined from the ship's differential global positioning system. But the actual location of the OBS on the seafloor is not known as it can drift several hundred meters from the deployment position due to ocean currents. The total drift also depends on water depth, particularly on a frontal ridge where the depth changes rapidly. To obtain the accurate location of an OBS on the seafloor, we applied an inversion algorithm (Dalhousie University Matlab program 'obsloc') which uses the travel time of the direct arrival, a water velocity profile, an initial assumed water depth for the OBS and an initial location based on sea-surface deployment and recovery positions. For a given OBS, it positions the OBS at each node within the uniform grid, and calculates the distance to each shot. Since water velocity is known and for each shot the observed direct arrival traveltime is measured, the corresponding true shot-receiver distance can be calculated. The routine then sums the total distance residual (calculated node-distance minus true distance) over all shots for that given OBS position, and the minimal distance residual gives the best position. Water depths are constrained only from the high resolution multi-

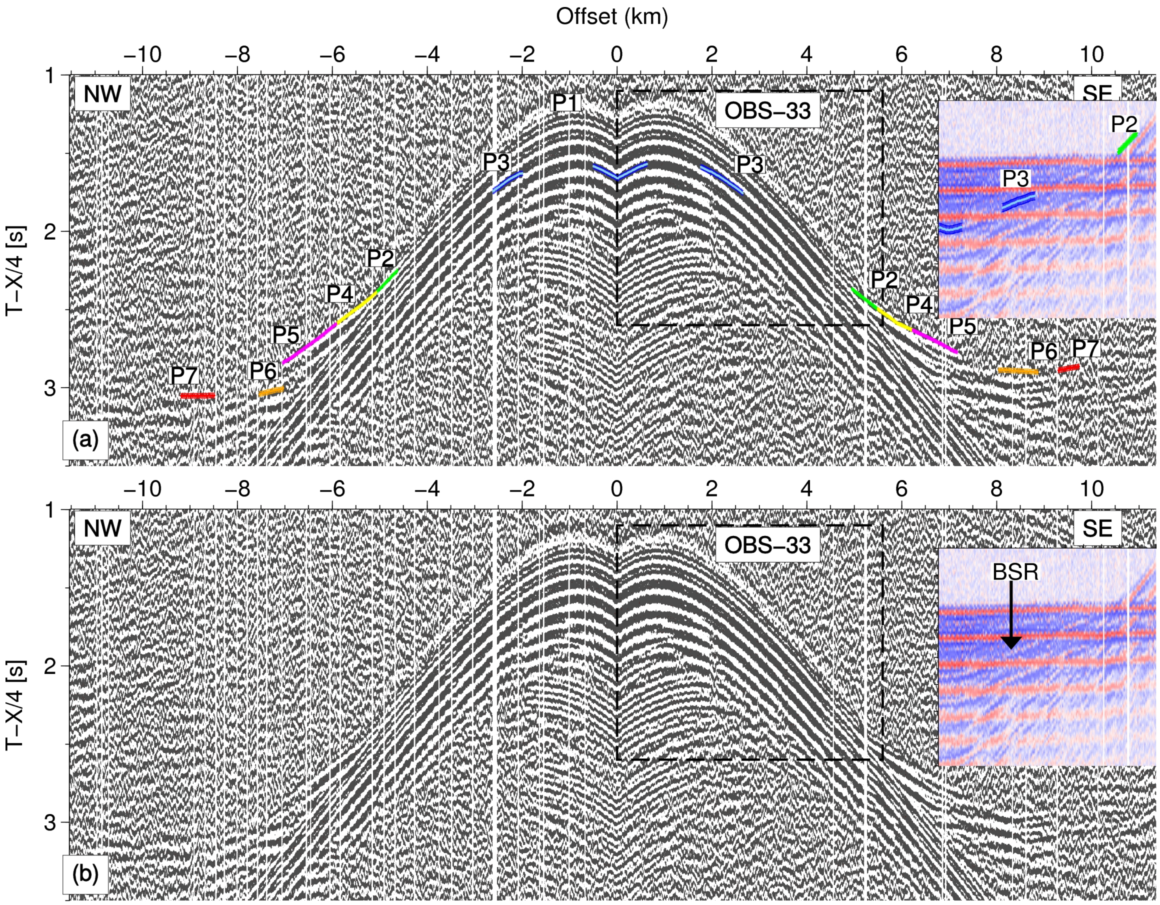

Figure 2.3: Hydrophone component of OBS-33 data along SCS Line 4a with (a) travel time picks (vertical colour bars) for the reflection and refraction events used in velocity modeling and (b) without travel time picks. The width of the colour bar indicates the travel time uncertainty. The colour scheme used in this figure to identify different arrivals is followed in figures 2.4, 2.5 and 2.6. The OBS times are plotted with a reduction velocity of 4 km/s. The inset figures in both (a) and (b) enable the clear identification of event P2 and the BSR; a normal-moveout velocity of 1.482 km/s is applied to flatten the direct arrival. Black dashed rectangles in (a) and (b) indicate approximate locations of the inset figures.

beam bathymetry data; after an OBS location shift is determined, the corresponding new water depth is selected and a new iteration of the inversion is run. We also assumed that the clock time drift is small and linear over the 33 hour period of airgun operation; this assumption is a possible source of error. Another uncertainty is the maximum distance to which one can pick the direct arrival, before a sub-seafloor refraction emerges as the first arrival. This distance is typically about $4 - 6$ km.

The distance residual tended to increase at farther offsets, and also at locations just over the OBS. Provided that an accurate water velocity model is used, rays from distant sources arrive more parallel to the seafloor and hence provide good constraints on the horizontal position, but lack vertical resolution. Rays from sources directly above an OBS arrive at near-vertical angles, provide good constraints on the depth of the OBS, but lack horizontal resolution. The residuals for these OBSs average 12 m, which correspond to time shifts of 8 ms. This time shift is close to the picking uncertainity of ± 10 ms. The average drift in position of the OBSs was about 50 m for water depths of $2.0 - 2.5$ km in the frontal ridge region. For additional details on OBS relocation see Appendix A.

2.5 P-wave velocity modeling

We used refractions and wide-angle reflections recorded on the OBSs and vertical incidence reflections recorded on coincident single-channel data to determine the velocity structure. Wide-angle reflections and refractions provide good constraints on the velocity structure, while the vertical incidence data control the layer depth.

2.5.1 Event identification

Single-channel seismic data from line-4a that passes through OBSs 33, 34, 31 and 30 were used for the velocity analysis. On the SCS data section, only two reflection segments were identified as BSR (Fig. 2.2a); these apparently have polarity opposite to the seafloor (Fig. 2.2a, inset), and they occur at very similar sub-seafloor depths as a continuous and more easily identifiable BSR across Orca ridge just to the north (*Lopez et al.*, 2010). To facilitate the event identification, the wide-angle data and the vertical incidence data were plotted together to match the seafloor and the BSR. Reflection events corresponding to the BSR that originated from the same interface in both the data sets were identified and picked (Fig. 2.2, 2.3, & 2.5). Hydrophone (pressure) components were selected for picking. To maintain consistency, only refraction and reflection events that were observed on all four OBSs were selected and picked, except in cases where a strong event is obvious. On wide-angle data, seven distinct events were identified (Fig. 2.3); the most important events include (i) an early event (P2) from top of Layer L2 at shallow depths of < 100 m with an apparent velocity of $\sim 2.0 - 2.1$ km/s, (ii) the wide-angle reflection from the bottom of Layer L3 or the BSR (P3), (iii) refractions (P4-P7) from interfaces below the BSR, with apparent velocities varying from 2.3 km/s to > 4.0 km/s. Events P2 and P3 are more clearly identified when a normal-moveout velocity of 1.482 km/s is applied to the data (Fig. 2.3, inset). The signal-to-noise ratios of the refraction events were quite similar, and so a common uncertainty of $\pm 10 - 15$ ms was assigned. For vertical incidence data (BSR arrivals or P3), an uncertainty of $\pm 10 - 20$ ms was assigned based on the greater difficulty in picking the BSR.

The identification of the shallow high velocity layer (corresponding to P2 event) and BSR (corresponding to P3 event) was difficult on single-channel line-1a that passes through OBSs 04, 35, 32 and 31. Hence only wide-angle refraction events (P4 - P7), similar to the ones observed above, were identified and picked (Fig. 2.5).

2.5.2 Modeling

The seismic velocity structure at the frontal ridge was obtained using the two-dimensional (2D) travel time inversion program of (*Zelt and Smith*, 1992). In traveltime tomography, the inversion is carried out by finding a model that predicts the measured arrival times, usually by iterative ray trace methods. In the forward problem, travel times are computed using a reference velocity model. The inverse problem tries to minimize the difference between the observed travel times and calculated travel times by updating the reference velocity model. A starting model was carefully constructed by first modelling a subset of the travel times using a ray-tracing approach in a block model with interfaces. The final velocity model was interactively constructed by using both forward and inverse modeling. Two-point ray tracing was used in this modeling. A layer-stripping approach was followed in which the top layer was modelled first and held fixed for modelling subsequent layers. For this model only P-waves were analyzed; no converted S-waves were included in the modeling. The BSR phase was modeled as reflected waves, while wide-angle refractions were modeled as pure head waves as these are observed over a small offset range and hence contain little information about velocity gradients. Therefore, most of the layers are constrained only at the top, but some constraints on velocity gradients are available from drillhole sonic log data on the adjacent frontal ridge (*Riedel et al.*, 2006a) and from previous studies which used detailed semblance analyses on nearby multichannel seismic lines (*Yuan et al.*, 1994).

2D velocity models were determined along line-4 and line-1. On line-4, the model was constrained by simultaneous inversion of travel times from wide-angle reflections and refractions on the OBSs, and from vertical-incidence reflections recorded on the single channel seismic line. For the picked phases from the four OBSs on line-4, the final ray tracing through the velocity model is shown in Fig. 2.4.

On line-1, only wide-angle refractions were used for modeling as there is ambiguity in identifying reflection events. This line is crooked, which implies that the model distance is larger (or shorter - depending on how the 2D model was set up) than the shot-receiver offset when there is a bend in the line. Hence, we projected the shot and relocated OBS positions onto a straight line by keeping the shot-receiver offset intact. The projected line is a linear fit of the actual shot locations. The starting velocity model for this line is based on the line-4 velocity model. Velocities were fixed at the intersection point where line-4 intersects line-1, and so the model contains a shallow high velocity layer and BSR layer beneath the ridge crest. However, there is no evidence for hydrates away from the ridge in the deep ocean, so layers L1 to L4 were assigned a common velocity gradient and there were no velocity contrasts between the layers. For the four OBSs on line-1, the final ray trace through the velocity model is shown in Fig. 2.6.

Inversion was continued until the travel time residual reduced to the order of picking uncertainty and χ^2 normalized misfit parameter approached 1. For the final velocity model on line-4, an RMS travel time residual of 13 ms with a normalized χ^2 misfit of 0.96 was achieved. On line-1, an RMS travel time residual of 9 ms with a normalized χ^2 misfit of 0.76 was achieved.

Finally, to estimate uncertainty in the model parameters, a sensitivity analysis was performed by perturbing the model parameters, i.e. depth and velocity (*Katzman et al.*, 1994). Uncertainty of a model parameter was determined by perturbing its value from the final model and holding it fixed while allowing the other parameters to vary during inversion. In this method the depth and velocity of layers L2 and L3 were examined (Fig. 2.7). While estimating velocity uncertainty, the velocity gradient within the layer was fixed at the final model value while allowing lateral variations in velocity. Assuming an RMS residual uncertainty of 1 ms, typical depth errors for these layers were ±20 m and ±15 m, respectively (Fig. 2.7a,c). However, there is no formal criterion as such in choosing this uncertainty value of 1 ms. But if we assume an RMS residual uncertainty of 2 ms, typical depth errors for these layers increase to only ±25 m and ±20 m, respectively. Similarly, by assuming ±3% uncertainty in velocity estimates would give a velocity error of ±58 m/s for Layer 2 and ±57 m/s for Layer 3, respectively (Fig. 2.7b,d).

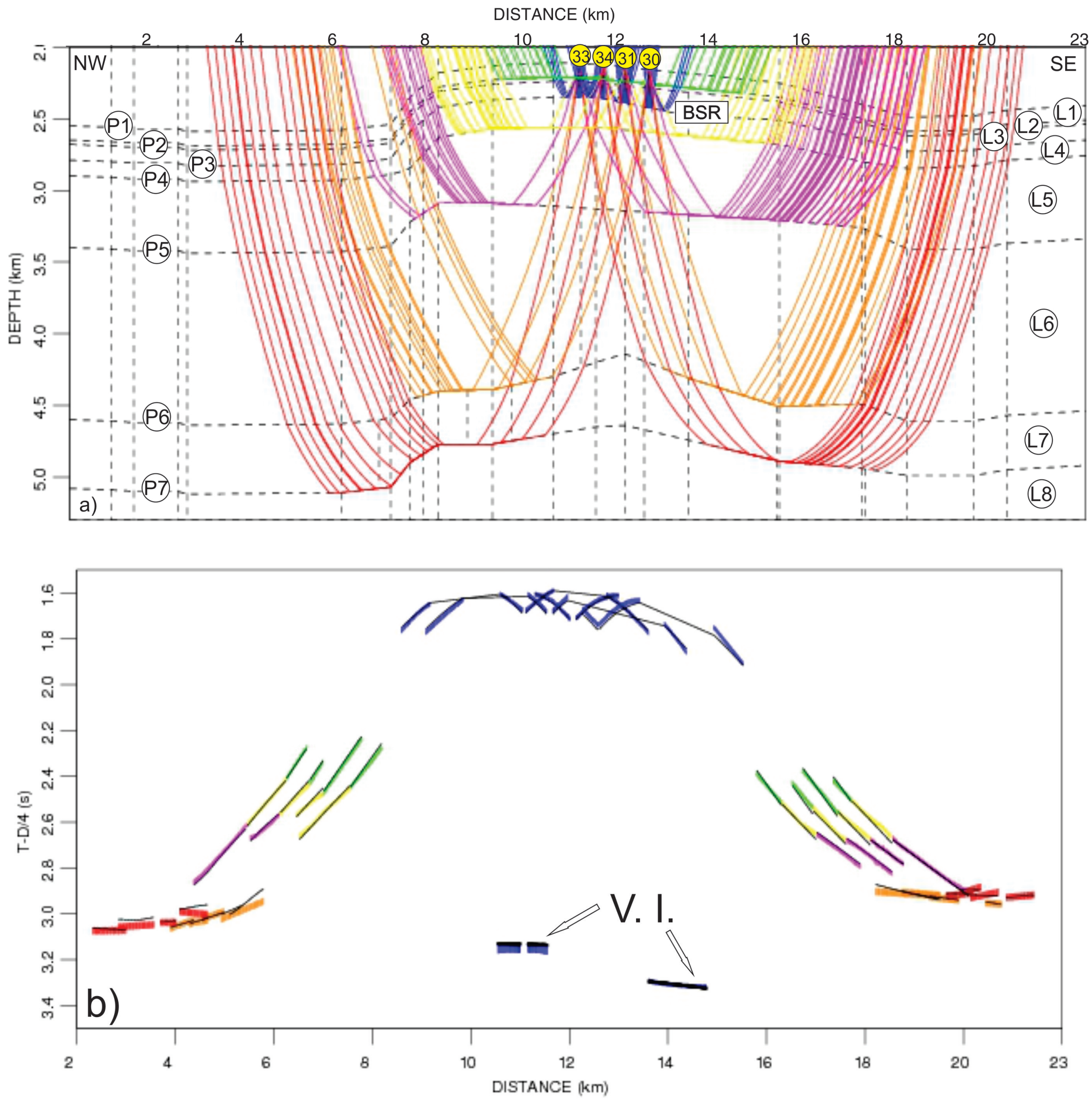

Figure 2.4: (a) Reflected and refracted rays traveling along a profile (Line-4) through OBS 33, 34, 31, and 30. Green rays correspond to refractions from just below Layer1/Layer2 interface, and blue rays are wide-angle reflections from the base of layer 3 (BSR); other refractions are yellow rays below Layer4/Layer5 interface, magenta rays below Layer5/Layer6 interface, orange rays below Layer6/Layer7 interface and red rays below Layer7/Layer8 interface. For clarity, vertical incidence rays, based on single-channel seismic arrivals, are not shown. (b) Observed travel times (coloured vertical bars) compared with calculated travel times (black solid lines) for wide-angle data with the same colour scheme as for the rays in (a); label V.I. indicates vertical incidence travel times.

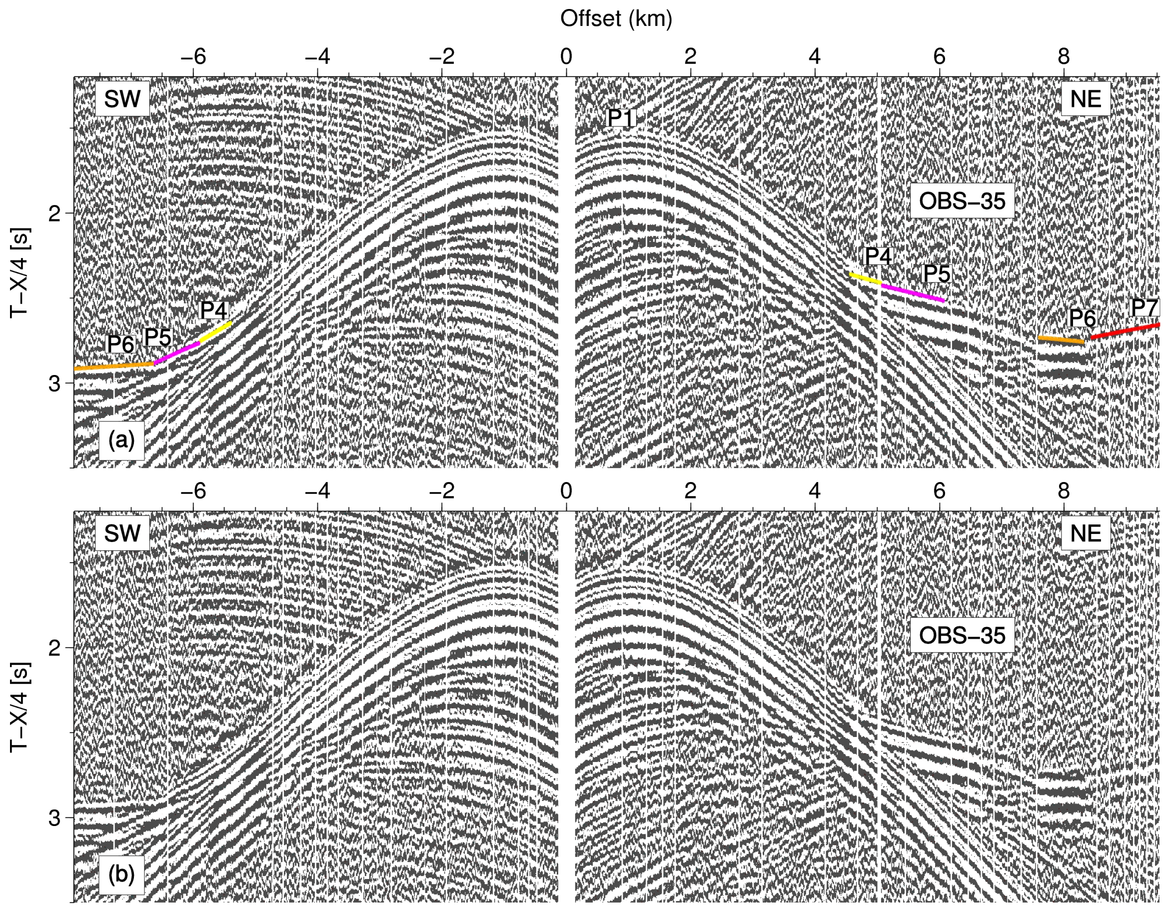

Figure 2.5: a) Hydrophone component of OBS-35 data along SCS Line 1a with (a) travel time picks (vertical colour bars) for the refraction events used in velocity modeling and (b) without travel time picks. The width of the colour bar indicates the travel time uncertainty. The colour scheme used in this figure to identify different arrivals is followed in figure 2.6. The OBS times are plotted with a reduction velocity of 4 km/s.

2.6 P-wave velocity model

The final velocity models beneath line-4 and line-1 are shown in Fig. 2.8.

2.6.1 Margin parallel line-4

This line consists of eight layers corresponding to seven different phases (Fig. 2.8a). Perhaps the most significant feature of this model is a shallow high velocity structure (1.9 – 2.0 km/s) observed in layer L2 at a depth of 100 m below the seafloor. The velocity is constrained by event P2, but no events are observed to constrain the

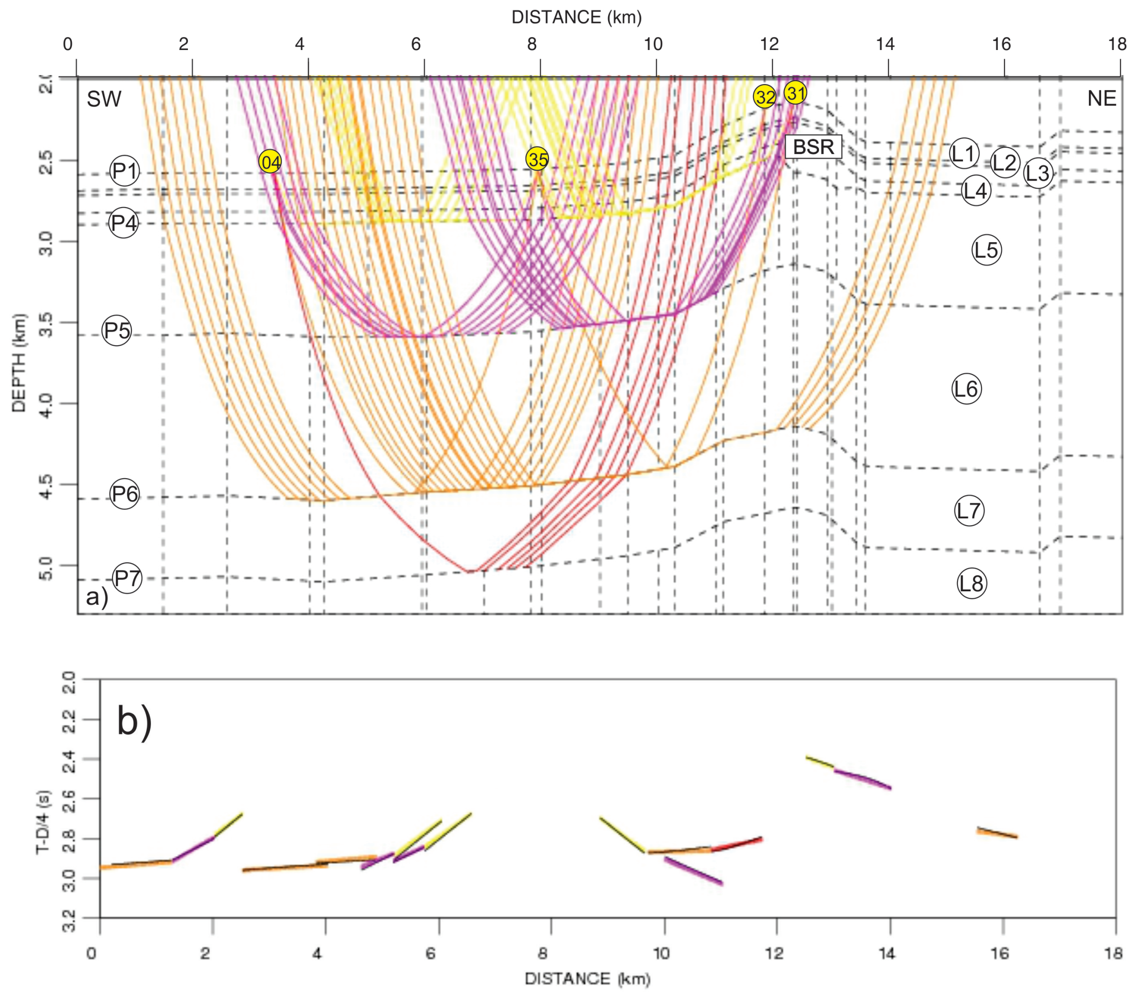

Figure 2.6: (a) Refracted rays traveling along a profile (Line-1) through OBS 4, 35, 32, and 31. Yellow rays correspond to refractions from just below Layer4/Layer5 interface, magenta rays to Layer5/Layer6 interface, orange rays to Layer6/Layer7 interface and red rays to Layer7/Layer8 interface. Shallow velocities (L1-L3) are constrained by line 4 velocities beneath the ridge and sonic velocities from Site 888 of ODP Leg 146 in the deep ocean. (b) Observed travel times (coloured vertical bars) compared with calculated travel times (black solid lines) for wide-angle data with the same colour scheme as for the rays in (a).

thickness of this layer. The thickness of this layer is assumed to be 30 m, based on IODP (Integrated Ocean Drilling Program) drilling results at Site U1326 where velocities of 1.75 km/s to > 2.6 km/s, and high resistivities, were observed from 72 – 107 mbsf (*Riedel et al.*, 2006a).

The BSR is modelled at a depth of 265 – 275 m below the seafloor, which is constrained by vertical incidence and wide-angle reflections (P3). These results agree

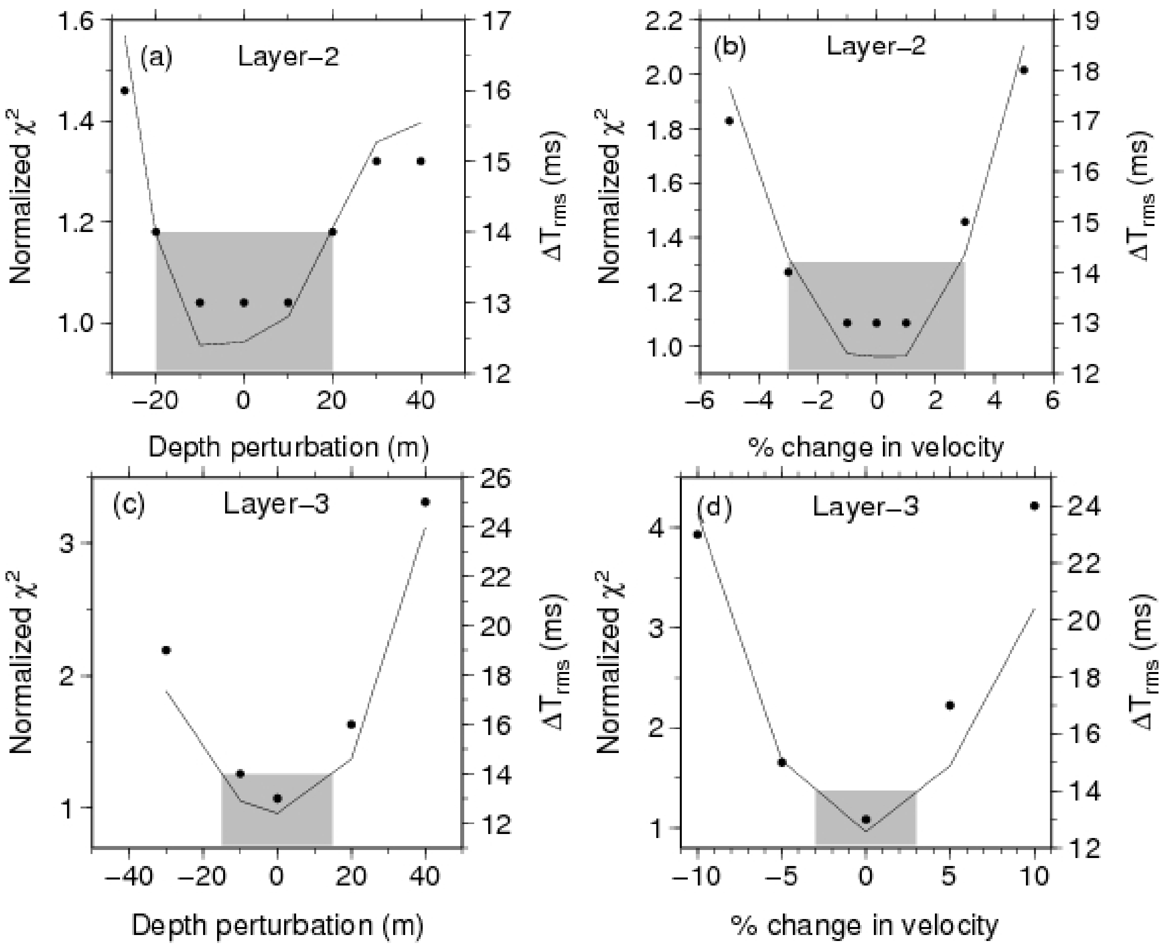

Figure 2.7: Sensitivity analysis of the best fitting velocity model for margin parallel line (Line-4). Normalized χ^2 misfit (line) and RMS travel time residual (dots) with respect to change of (a) the depth to the top of Layer 2, (b) velocity within Layer 2, (c) BSR depth and (d) velocity above the BSR.

with IODP drilling measurements as well as MCS velocities measurements of *Chen* (2006) (Fig. 2.9a). Layers L4-L8 extend from just below the BSR to depths of more than 2.5 km below the seafloor (Fig. 2.8a).

2.6.2 Margin perpendicular line-1

Four layers corresponding to five different events were modelled in ocean basin for this line. However, beneath the ridge the structure (Fig. 2.8b) is constrained to be similar to line-4. Specifically, there are four shallow layers (L1 to L4) beneath the ridge, while away from the ridge there is only a single shallow layer (labelled L1-L4). The average velocity for layer L1-L4 is 1.75 km/s and the thickness is about 300 m.

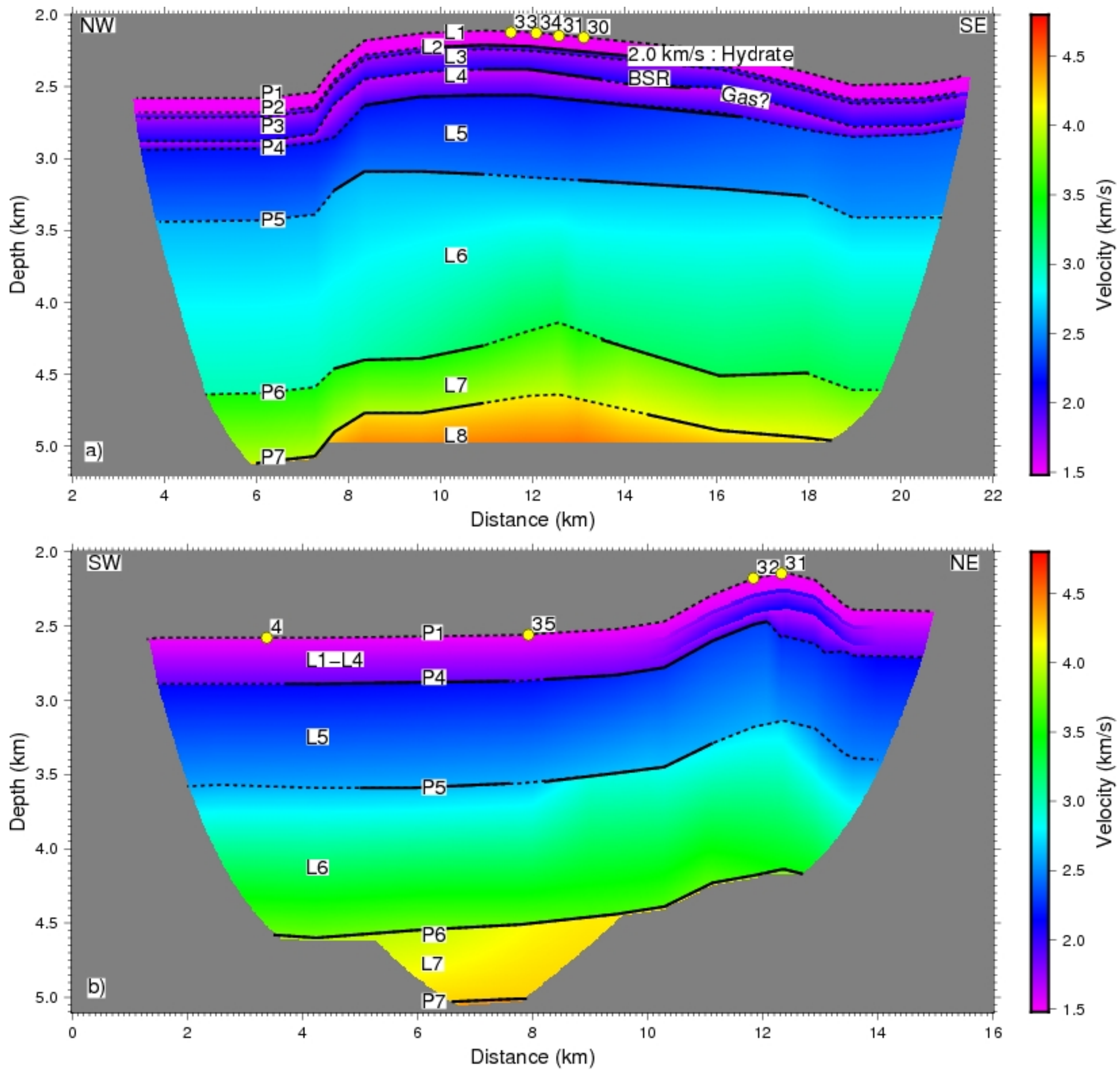

Figure 2.8: (a) Final velocity model along margin-parallel line 4 and (b) final velocity model along margin-perpendicular line 1. The yellow circles indicate the location of OBSs along the line. Solid boundary lines indicate regions where ray coverage constrains the boundary. Layers (L1-L7) and boundaries corresponding to travel time events (P1-P7) are labeled for ease of interpretation.

Layer L5 has a thickness of approximately 700 m with an average velocity of 2.2 km/s, which increases up to 2.4 km/s below the ridge. Layers L6 and L7 have thicknesses of about 1 km and 0.5 km, respectively.

2.7 Interpretation and discussion

2.7.1 Shallow velocity structure and gas hydrate concentrations

Shallow OBS velocities from this study are compared to sonic log velocities (*Riedel et al.*, 2006a; *Westbrook et al.*, 1994) and MCS interval velocities from line 89-08 (*Chen*, 2006) at Site U1326 (Fig. 2.9a and 2.10b). The reference no-hydrate velocity profile based on the rock physics modeling approach of *Helgerud et al.* (1999) is also plotted in Fig. 2.9a to compare with our velocity estimates. In general, our velocities are in good agreement with previous estimates.

The depth of the BSR varies laterally beneath the ridge crest. This is evident from the single channel seismic section shown in Fig. 2.2a and the velocity model shown in Fig. 2.8a. The BSR depth increases towards southeast along the ridge. Also, the identification of BSR is ambiguous on the northwest side beneath the ridge. Particularly, the occurrence of double reflections between 3.1−3.2 s (near shot number 12650 in Fig. 2.2a) indicates an apparent double BSR. In the deep basin, the sub-horizontal bedded sediments obscure the BSR or it is not present.

The shallow velocity structure obtained from travel time inversion is then used to estimate gas hydrate concentrations. The same method was applied by *Chen* (2006) and *Lopez et al.* (2010), who also used the Site U1326 drilling results of IODP Expedition 311 (*Riedel et al.*, 2006a). These estimates are based on expected P-wave velocity vs. depth profiles for various gas hydrate saturations using the gas hydrate "in-frame" model, in which gas hydrate is assumed to form a load-supporting part of the sediment matrix. The effective medium model requires the porosity and elastic properties of sediment constituents. The porosity is taken as the smoothed porosity-depth profile from Site U1326, and the average mineralogy is taken to be 85% clay and 15% quartz based on the smear slide analyses undertaken for Site U1326 (see Lithostratigraphy Chapters of the Initial results volume for IODP Expedition 311, *Riedel et al.*, 2006a). The elastic parameters of the sediment constituents used in this study are summarized in Table 1. The sediment matrix is modeled as packed spheres, each with eight grain contacts. We used a critical porosity value of 0.36 as suggested by *Nur et al.* (1998). Velocity-depth profiles calculated for various gas hydrate saturations are shown in Fig. 2.10c. As expected, the reference no-hydrate velocity profile calculated by this method shows good correlation with previously

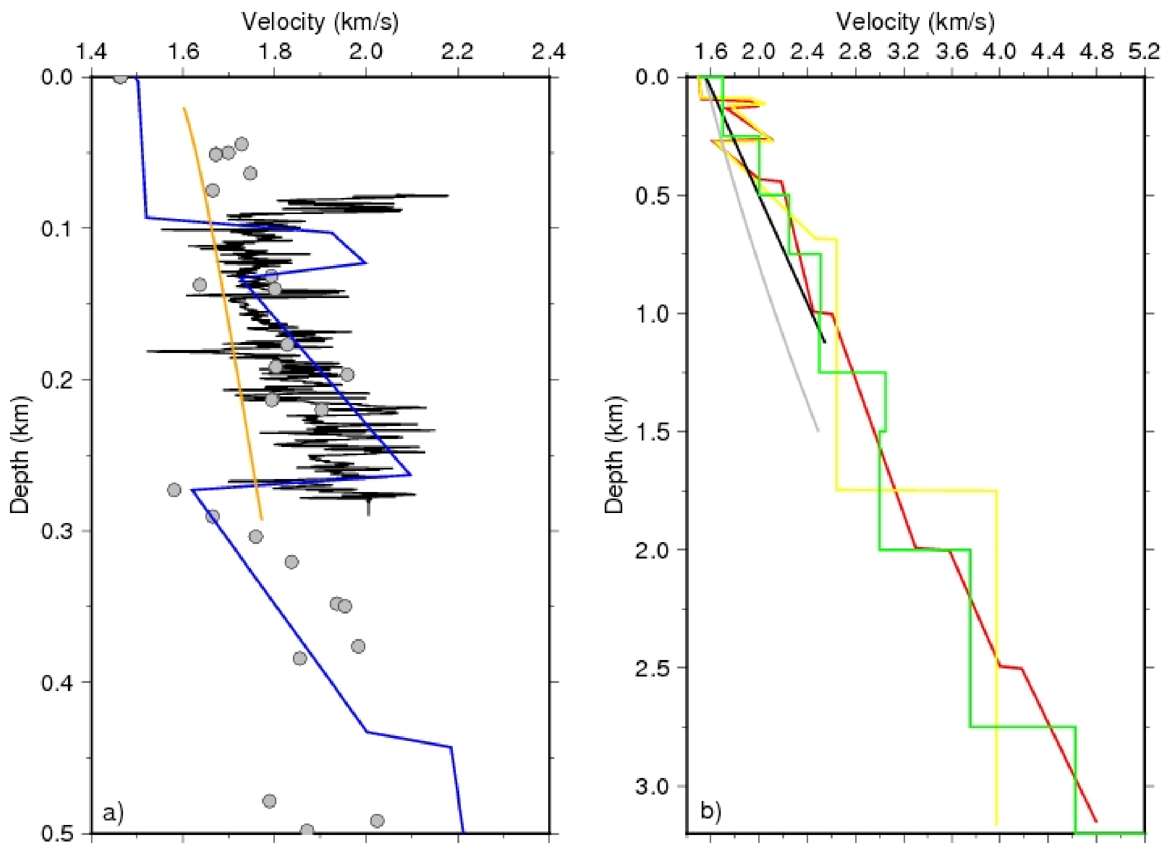

Figure 2.9: (a) OBS-31 seismic velocities from current study (blue line), compared with sonic log velocities from U1326 (black line). Solid gray circles show MCS interval velocities near U1326 (*Chen*, 2006). Orange line indicates reference velocity profile from rock physics modeling of (*Helgerud et al.*, 1999). (b) OBS-31 velocities from current study (red line) compared with OBS-D velocities (yellow line) from an adjacent ridge (*Lopez*, 2008) and MCS interval velocities (green line) from the seaward of the deformation front (*Yuan et al.*, 1994). Gray and black lines indicate MCS interval velocity trend from the mid-slope region of the accretionary prism and the Cascadia basin, respectively (*Chen*, 2006).

calculated velocity trends for site U1326 (*Chen*, 2006; *Lopez et al.*, 2010).

The anomalous high velocity layer (L2) beneath the ridge crest at shallow depths of $\sim 80 - 126$ mbsf, with velocities up to 2.0 km/s, indicates gas hydrate saturations of up to 40% in this shallow region (Fig. 2.10c). These high velocities provide concentrations that are in reasonable agreement with those from sonic velocity and resistivity measurements at Site U1326, which also suggest that high concentrations of gas hydrate are present beneath the frontal ridge region at shallow depths. Therefore, layer L2 is interpreted as a gas hydrate layer.

Table 2.1: Elastic properties of sediment constituents used in this study (after *Helgerud et al.*, 1999).

Sediment constituent	Bulk Modulus (GPa)	Shear Modulus (GPa)	Density (g/cm^3)	P-wave Velocity (km/s)	S-wave Velocity (km/s)
Clay	20.9	6.85	2.58	3.41	1.63
Quartz	36.6	45.0	2.65	6.04	4.12
Pore Water	2.4	0	1.03	1.5	0
Methane Hydrate	8.7	3.5	0.92	3.8	2.0
Methane Gas	0.1245	0	0.25	0.71	0

In the depth interval $130 - 263$ mbsf, saturation increases from 20% to nearly 50% at BSR depth (Fig. 2.10c). This rather high concentration estimate, which is based on OBS-31 velocities alone, indicates local high velocities. We note that velocities at OBS-30 are comparatively lower than those at OBS-31 (Fig. 2.10c), which suggests that the velocity structure just above the BSR varies laterally. Based on the sensitivity analysis (Fig. 2.7), the velocity structure just above the BSR shows a broad range from $2.00 - 2.15$ km/s, which indicates a corresponding uncertainty range for gas hydrate saturations of $30 - 40$%. Previous saturation estimates at U1326 indicate values of 20-30% at U1326 (*Lopez et al.*, 2010; *Riedel et al.*, 2006a; *Chen*, 2006). This discrepancy in concentration estimates on the frontal ridges suggests variation in gas hydrate concentration along the Northern Cascadia margin.

2.7.2 Depth of glide plane and comparison with seismic structure

The depth of the glide plane at Slipstream slide was estimated by analysing the swath bathymetry data. A set of depth profiles approximately parallel to the contour lines was extracted throughout the slide region and outside of the slide to obtain details of the current bathymetry (Fig. 2.11). Profiles were constructed every 50 m and bathymetry was extracted every 50 m along the profile length. The bathymetry was then interpolated across the slide from sidewall to sidewall to obtain the original bathymetry before the slide (Fig. 2.12). Based on this analysis, the estimated depth of the glide plane was about 100 m below the seafloor (Fig. 2.13a). This depth is equivalent to the depth of the observed shallow high velocity layer on the margin-

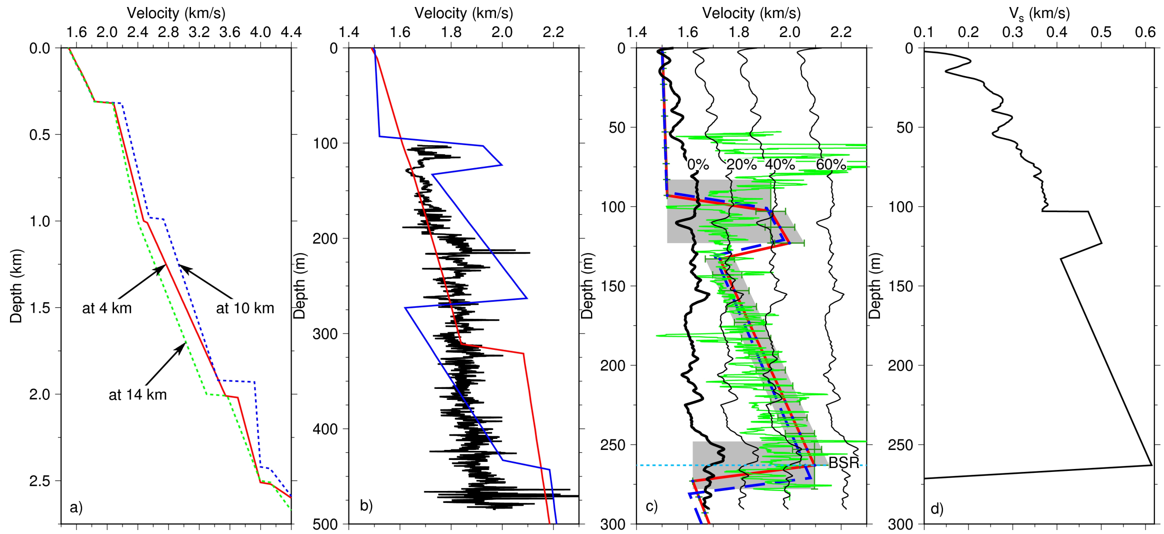

Figure 2.10: (a) 1D velocity profiles from margin-perpendicular line at three different locations (4, 10 and 14 km model distance), showing landward increase in sediment velocity up to the ridge and then decrease afterwards. (b) OBS velocities compared with sonic log velocities (black line) from Site 888 of ODP leg 146. Red line indicates OBS-04 velocities from the deep ocean while blue line indicates OBS 31 velocities from the top of the ridge. (c) Gas hydrate concentration estimates from rock physics modeling based on gas hydrate in-frame model (*Helgerud et al.*, 1999). Red line represents OBS-31 velocity profile beneath the ridge crest and gray shaded regions with error bars indicate uncertainty in velocity and BSR layer depth, based on sensitivity analyses (Fig. 2.7). Green line shows sonic log velocities from U1326 of IODP X311, which is 50 km away from the study area. Solid black line is the reference sediment velocity (no hydrate) from rock physics modeling, while light black lines correspond to sediment velocities with hydrate concentration of 20%, 40% and 60%, respectively. BSR is indicated with dotted light blue line. Dashed blue line indicates OBS-30 velocities. (d) Shear wave velocity profile from rock physics modeling based on gas hydrate in-frame model (*Helgerud et al.*, 1999).

parallel line, and much shallower than the $\sim 265-275$ m depth of the BSR beneath the ridge (Fig. 2.9a). This is in contrast to Orca slide where the depth of the glide plane matches with that of the BSR (Fig. 2.13b). We note that on both ridges the depths of the high velocity layer and the BSR are mainly constrained from OBS and SCS data near the top of the ridges, on the corresponding margin-parallel lines; it is very difficult to image ridge structures on margin-perpendicular SCS lines due to steep slopes, although an indication of the BSR across Orca ridge can be seen (Fig. 2b in *Lopez et al.*, 2010).

At Slipstream slide, the formation of the glide plane observed here could be

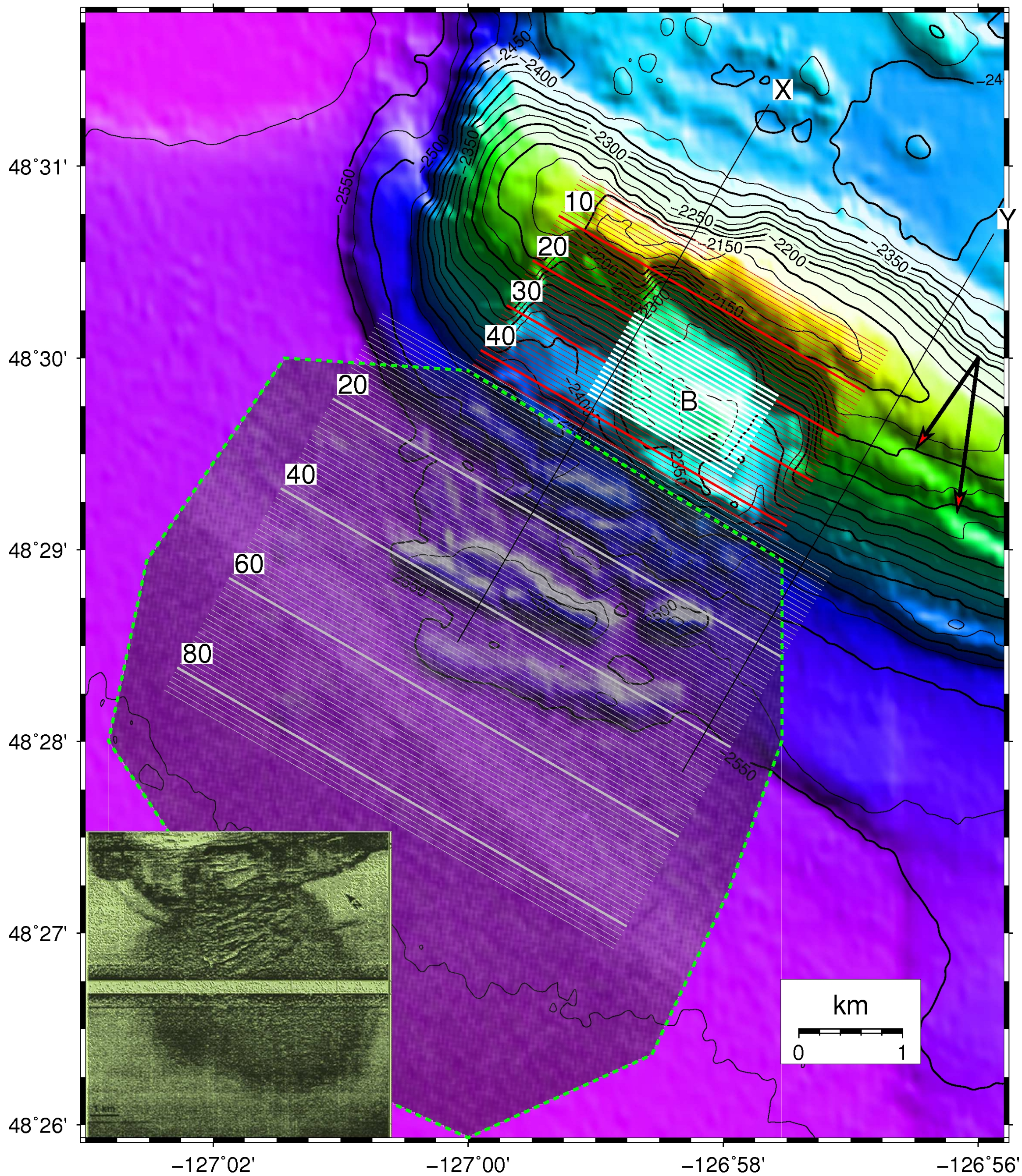

Figure 2.11: Multi-beam bathymetry map showing the extent of the slide region. White lines marked as B within the slide indicate a big block of slide material whose volume is 0.03 km^3. Outlined region in gray indicate the approximate location of the sidescan debris shown in inset figure (digitized from *Davis and Hyndman*, 1989). Solid black lines marked as X, Y indicate the location of current and pre-failure bathymetry profiles shown in Fig. 2.13a. Red and grey lines indicate the location of depth profiles shown in Fig. 2.12a and 2.12b, respectively. Arrows indicate incipient headwall discussed in text.

due to the strength contrast between normal non-hydrated sediments and sediments strengthened by large amounts of hydrate. This is indicated by the predicted shear velocity profile (Fig. 2.10d), based on effective medium modelling. Concentrations from Fig. 2.10c were used while estimating the shear velocity profile. We also assumed zero hydrate concentration above 100 m depth. Assuming that shear velocity is a reasonable proxy for sediment strength, we see a significant increase in strength at 100 m depth, where the shear velocity increases from 367 m/s to 501 m/s. Furthermore, massive hydrate is more likely to form in sand-prone layers (as seen in the same depth ranges of Site U1326 near Orca Slide), and so the top of the sand layer at 100 m depth may also represent a lithology contrast that also contributes to a strength contrast.

The Orca ridge region also has a similar high-velocity layer at 100 m depth, also interpreted as a layer with large hydrate concentrations (*Lopez et al.*, 2010). We do not have an explanation at this time as to why the glide plane localizes at the BSR for the Orca slide, whereas it localizes at the top of the massive hydrate layer for the Slipstream slide. Speculatively, the reason could be related to different distances that the high-velocity layer or the BSR extend downdip from the top of the ridge, but we do not have sufficiently detailed seismic data to confirm this. As well, a much more detailed comparison with other slides on the north Cascadia margin could provide additional hints about the different mechanisms; this is underway (*Scholz*, 2014).

2.7.3 Volume estimates of the slide from bathymetry analysis

The amount of material removed during the slide was estimated by finding the volume between the pre-failure surface and current bathymetric surface (Fig. 2.12a, 2.13a). From this analysis, the amount of material removed during the slide was 0.30$\pm$ 0.06 km^3, assuming a 20% uncertainty in estimates. This is probably an underestimate as not all the material is moved out of slide area and subsequent sedimentation would reduce the current bathymetry value. A large block of material is present within the slide, marked as 'B' in Fig. 2.11. We constructed similar depth profiles across this block to estimate its volume, which was calculated to be 0.03 km^3. Assuming that the slide occurred as a single event, the estimate for the sediment volume mobilized during the Slipstream slide is about one-third the minimum volume estimate for the 1998 Papua New Guinea slide, which produced a devastating tsunami (*Synolakis et al.*, 2002).

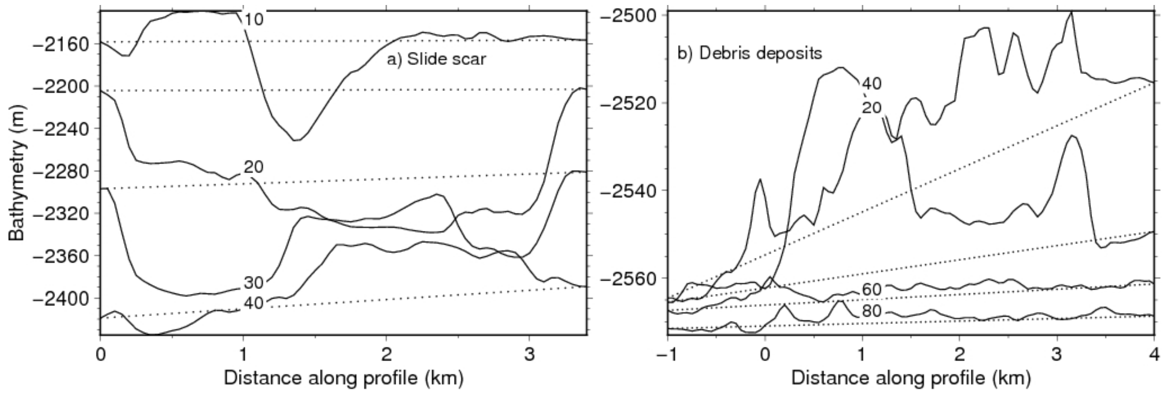

Figure 2.12: (a) Depth profiles along different ridge-parallel transects through the slide region were used to estimate the amount of material mobilized in the slide. Dotted lines represent pre-failure bathymetry and solid lines represent the current bathymetry. See Figure 2.11 for location of the depth profiles, which were separated by 50 m. (b) The amount of material removed or present as debris is calculated by finding the volume between the pre-failure and current bathymetric surfaces.

The actual amount of debris material that was deposited on the deep ocean basin was calculated by constructing similar bathymetric profiles across the debris material, interpolating from flat ocean floor on one side of the debris field to flat ocean floor on the other side. The amount of debris material was calculated by finding the volume between the depositional surface and current surface (Fig. 2.12b). The estimates indicate a volume of 0.24 km^3, which is smaller than the amount of material removed by 0.06 km^3. This may be due to error in the two measurements, but the difference is consistent with not all the debris material being accounted for (Fig. 2.11). That is, the debris is most likely spread over a larger area than the region with anomalous bathymetry, which extends over an area of approximately 3 km by 2.5 km. This is clearly evident from the sidescan image (Fig. 2.11), which shows an area of high backscatter of approximately 25 km^2. We assume that the missing material is mostly fine sediments, with a thickness below the resolution available from the bathymetry profiles. If the missing 0.06 km^3 is spread over the entire 25 km^2 area of high backscatter, the crudely estimated thickness of the fine material distributed over this area is about 2 ± 1 m.

In this estimation, we assume that pre-failure bathymetry was linear across the slide and that our interpolated surfaces are accurate. We also assume that the current bathymetry represents either the failure surface for the slide, or the top of debris for the ocean basin. The uncertainty on these assumptions is probably at least 10%

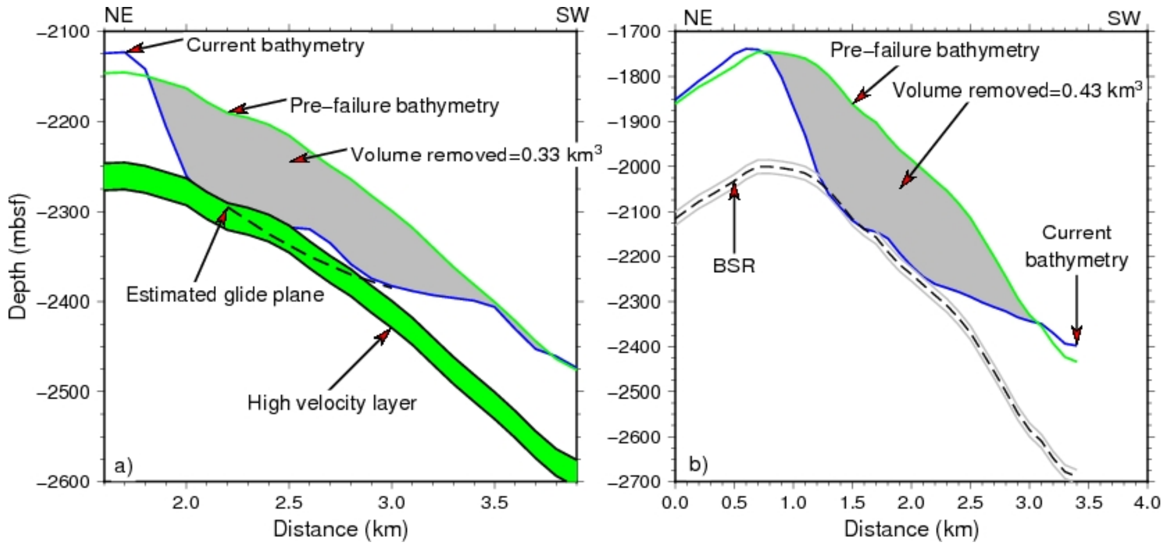

Figure 2.13: (a) Estimates of the depth of the glide plane. Original pre-failure surface (dark green) is estimated by interpolating across slide. Present water depths down the slide are shown by the blue line. The estimated depth of the glide plane (thick black dash-dot line) is approximately (100$\pm$10) mbsf, which coincides closely with the 30-m-thick high velocity layer (light green shading) observed (Figure 2.8) at about $\sim$ 100 m beneath the seafloor. Location of the depth profiles is shown in Figure 11, marked as X and Y. (b) Depth of the glide plane matches closely with the depth of the BSR on an adjacent slide (Orca slide), just 50 km north of the current study area. Location of this slide is shown in Fig. 2.1 and the BSR depth is taken from *Lopez et al.* (2010).

(e.g., based on the calculation of the 0.03 km^3 for the slump block still within the slide area).

2.7.4 Deeper velocity structure

The sedimentary section entering the Cascadia basin comprises 2.0 to 2.5 km rapidly deposited probably Pleistocene turbidites which are underlain by 0.8 to 1.0 km thick pre-Pleistocene hemipelagic deposits (*Davis and Hyndman*, 1989). Seismic structure is mostly uniform in the turbidite section on the seaward side of the ridge. However, very few reflections are seen beneath the ridge crest on line-4a and line-1a (Fig. 2.2a & b), likely due to increased deformation. The topmost sediment reflections are primarily from clayey silts and fine sands (*Riedel et al.*, 2006b). Layers L4 and L5 represent the upper turbidite sequence. Both layers L6 and L7 are likely compacted accreted wedge sediments (Fig. 2.8a,b). With the base of layer L6 at 2.0 km beneath the seafloor and the velocity increase from 3.0 km/s in layer L6 to 3.8 km/s in layer L7, the L6/L7 interface likely represents the boundary between the turbidites and the hemipelagic deposits. However, we note that the ray coverage is sparse in the deeper parts of the model (Figs. 2.4, 2.6) and so the structures are poorly constrained; however, velocity gradients are consistent with previous MCS and OBS studies (*Lopez*, 2008; *Yuan et al.*, 1994, see Fig. 2.9b).

We compared OBS-31 velocities from the top of the ridge with i) MCS-based interval velocities from Cascadia basin, ii) MCS velocities just seaward of the deformation front, iii) MCS velocities in the mid-slope region and iv) OBS velocities on an adjacent ridge (50 km northwest). Consistent with previous estimates (*Lopez*, 2008; *Chen*, 2006; *Yuan et al.*, 1994), sediment velocities increase in the horizontally layered Cascadia Basin section toward the deformation front and then decrease on the landward side of the ridge (Fig. 2.8b & 2.10a). For example, at a depth of 2.9 km, there is about 500 m/s increase in velocity over a distance of about 10 km from the deep ocean to the frontal ridge. *Yuan et al.* (1994) also observed an equivalent increase in velocity ($\sim$ 29%) from deep ocean to the deformation front based on a nearby multichannel seismic line. This probably indicates sediment over-consolidation and horizontal compression as a result of ongoing subduction, as the sediments are scraped off the oceanic plate, deformed, and compressed in the processes that form the frontal ridge. Farther landward, a decrease in velocity in the mid-slope region, indicated by the gray line in Fig 2.9b, probably indicates high porosities and under-consolidation, perhaps due to rapid thickening of the accretionary wedge sediments (*Yuan et al.*, 1994).

2.7.5 Theoretical BSR depth estimation

The hydrate phase boundary curve for the seawater-methane system is calculated using the CSMHYD program (*Sloan*, 1998b), assuming hydrostatic conditions with a water density of 1.03 g/cm^3 (*Hyndman et al.*, 2001). Seafloor temperature ($T_\circ$=3 °C) and geothermal gradient $\left(\frac{\partial T}{\partial z} = 0.06\,^\circ\mathrm{C/m}\right)$ were taken from IODP drilling results (*Riedel et al.*, 2006a). The estimated base of gas hydrate stability zone (BGHSZ) is at 273 m below the seafloor for a water depth of 2110 m on the ridge crest. This depth increases by 17.5 m for one degree decrease in seafloor temperature. Similarly, for every 100 m increase in water depth, the BGHSZ increases by $5 - 6$ m; so for the increase in water depth to the southeast by 125 m (a slope of $\sim 2^\circ$), the theoretical

BGHSZ depth increases by only ~ 8 m. By considering the uncertainties in pressure and temperature estimates (*Koh et al.*, 2011), the uncertainty in BGHSZ depths is approximately ± 12 m.

Theoretically predicted BGHSZ and seismically determined BSR depths (assuming the BSR is at the BGHSZ) are plotted on the migrated, depth-converted seismic section (Fig. 2.14a). Below the seafloor a 2D velocity model, based on smoothed travel time inversion velocities, was used for migration and depth conversion. It is evident from Fig. 2.14a that the theoretically estimated BGHSZ matches reasonably well with the BSR depth obtained from the velocity model, which uses vertical-incidence traveltimes from two BSR segments (SP 12700-12780 and SP 12900-12960 in Fig. 2.14a). Similar agreement was found in the Orca slide region (*Lopez et al.*, 2010). The good agreement between observed and theoretical BSR could be fortuitous, given uncertainties that could move the BSR either deeper (e.g., on the ridge crest due to 3D heat losses from the flanks of the ridge, or lithostatic pressure instead of hydrostatic; see *Ganguly et al.*, 2000) or shallower (e.g., focussed fluid flow; see *Xu and Ruppel*, 1999).

2.7.6 Fluid flow, a possible double BSR, and BSR uplift

A discontinuous BSR is visible on the margin-parallel single-channel seismic line (line-4a) crossing Slipstream Ridge. Additionally, some prominent reflection-packages interpreted to be anomalous BSR reflections (labelled BSR_a as indicated by arrows in Fig. 2.14a), are significantly shallower than the theoretical BSR curve (Fig. 2.14a), which assumes a geothermal gradient of $0.06\,^{\circ}\mathrm{C/m}$. The most likely cause for BSR uplift is localized fluid flow that also carries heat upwards. Assuming the BSR is the base of the gas hydrate stability zone, the observed shallowing of $50-80$ m would require a temperature gradient of $0.073-0.083\,^{\circ}\mathrm{C/m}$, which corresponds to a increase of $\sim 20-40\%$ relative to the measured thermal gradient nearby at U1326.

On the northwest side of the section of line-4a (SP 12620-12700), two distinct reflection packages are interpreted as a possible double BSR (Fig. 2.14a). The reflections, which have opposite polarity to that of the seafloor, are parallel to each other and sub-parallel to the seafloor. One possible cause of a shallower BSR is a bottom warming pulse produced by ocean warming at the end of the Last Glacial Maximum (LGM). It is possible that the deeper reflector is a former or transient BSR, which still has reflectivity since a significant amount of time is required for the

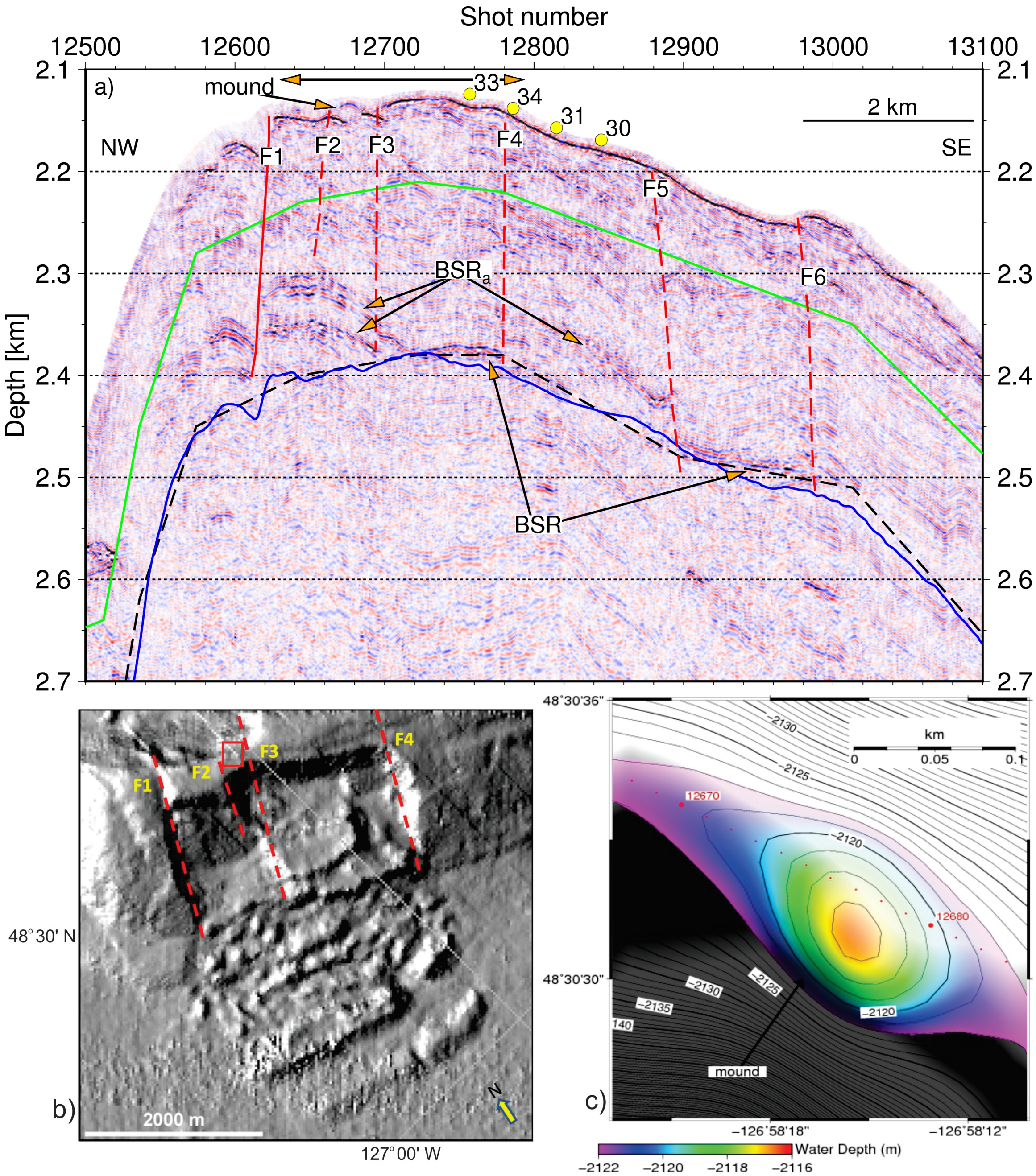

Figure 2.14: (a) Migrated single-channel seismic section along margin-parallel line-4a, converted to depth using the smoothed tomography velocity model. The double-headed arrow indicates the downdip location of Slipstream slide. The section shows the depth extent of the normal faults identified in (b). The faults are generally aligned with clear offsets in the bright reflector near the BSR depth. Green line indicates the top of Layer 2, while the blue and black dashed lines indicate the theoretically and seismically inferred BSR depths. Yellow circles indicate the location of OBS's on the seafloor. Label BSR$_a$ indicates segments interpreted to be anomalous BSR reflections. This figure is an enlargement of the region indicated in Fig. 2.2a. (b) Swath bathymetry map showing the surface features of margin-perpendicular normal faults. (c) Bathymetric image showing the mound feature indicated in (a). Red dots indicate the location of shot positions shown in (a). Approximate location of this figure is shown in (b) as red rectangle.

dissociated free gas to disperse by advection or diffusion (e.g., *Popescu et al.*, 2006). We speculate that the shallower reflection could represent upward migration of the BSR produced mostly by bottom water warming since the LGM (see Appendix B), with the amount reduced slightly by the associated increase in water depth. However, a general problem with a change of the BGHSZ from bottom-warming and pressure changes from sea level rise during the Holocene is that it should uniformly occur all along the margin, if not at least across the Slipstream Ridge. But on the ridge, the observed "double BSR" only occurs over a short fragment of the Slipstream Ridge and is especially apparent where slope failure has occurred. We note also that rapid sedimentation rates are another possible cause of BSR uplift, but the rates in the north Cascadia region (10-40 cm/kyr; *Riedel et al.*, 2006a) are too small and would only produce a maximum uplift of about 4 m (see *Martin et al.*, 2004, for a more complete analysis). Also, sedimentation would be more uniform across the margin, and not vary on a local scale to create such short-wavelength BSR discontinuities.

A series of margin-perpendicular normal faults (F1 - F6) were interpreted on the time-migrated section along the margin-parallel line-4a (Fig. 2.14a) on the frontal ridge. These faults were also observed on the bathymetry data shown in Fig. 2.14b. The faults extend from seafloor to below the current BSR depth. Fault F1 cuts through the seafloor and has a large seafloor scarp with a height of approximately $\sim 40 \pm 5$ m. The reflector packages referred to as BSR_a are disrupted by these northeast-southwest trending faults. For example, at faults F1, F3, F4 and F5, these reflections are offset with a vertical displacement as large as ~ 40 m. Further, the faults F1 and F4 coincide with the sidewalls of the slide. In a similar fashion, a set of 13 seafloor scarps, interpreted as margin-perpendicular normal faults, were observed on an adjacent frontal Orca Ridge (*Lopez et al.*, 2010). These faults also extend down to below BSR depth and the two largest faults, with seafloor vertical displacement up to ~ 75 m, coincide with the sidewalls of the slide. These structures on both frontal ridges suggest that the collapse features observed in the multibeam bathymetry data and in seismic reflection data are fault controlled.

The origin of these faults is associated with stresses in the central uplift region of the ridge, with extension most easily accommodated in the direction of least compressive stress, parallel to the ridge orientation and generally perpendicular to the direction of compression produced by ongoing subduction. Several of these faults appear to be active since they offset the seafloor, and any further displacement associated with uplift and flexural extension could potentially trigger future failures on this margin. As an example, the arrows in Fig. 2.11 probably indicate incipient head walls of the next generation of slumping.

Although the faults clearly control the lateral extent of the slide features, it is not obvious how the faults are related to the depth extent of the slides. If fluid flow is increased by migration of fluids along the faults, it is possible that the associated increase in heat flow, and upward migration of the phase boundary, would release methane gas to migrate upward and contribute to increasing the concentration of methane hydrate in the shallow high-velocity layer. However, such a large increase of thermal gradient and speculated fluid flow, with faults penetrating to the seafloor, should result in some seafloor manifestation of venting. While a small mound-like structure was seen in the bathymetry (Fig. 2.14c), we have no direct heat flow measurements on the ridge, and the repeated seismic expeditions have never revealed any evidence for fluid or gas discharge at the seafloor, as e.g. observed at other vent-like features at this margin (e.g. *Riedel et al.*, 2010a, 2006b; *Zyla*, 2012). More work would be required to verify that fluid flow along faults is present at Slipstream and Orca Ridge.

2.8 Conclusions

Mass failure features observed on the frontal ridges of the Northern Cascadia margin in the vicinity of gas hydrates indicate that the gas hydrate reservoir is dynamic in this region. At Slipstream slide on the frontal ridge, the presence of gas hydrate is indicated by the occurrence of a BSR at $265 - 275$ m below the seafloor, and by shallow high velocities of 2.0 km/s, based on wide-angle and vertical incidence seismic data. Gas hydrate concentrations as large as 40% of the pore space were interpreted from these high seismic velocities at shallow depths of ~ 100 m below the seafloor in the vicinity of the slide. Comparable seismic velocities, layer depths and hydrate concentrations were observed from previous seismic and sonic log studies at Orca slide on the adjacent frontal ridge, where high gas hydrate concentrations exceeding 40% of the pore space were observed by logging and coring at IODP Site U1326 over the same depth range within sediments containing a stack of sand-rich turbidites. The coincident occurrence of these high velocity layers at both ridges points towards a regional occurrence of the sand-rich interval with high gas hydrate concentration, which has not been appreciated before.

The depth of the glide plane at Slipstream slide (100 ± 10 mbsf) coincides with the top of this shallow high velocity layer. We suggest that the contrast between sediments with little or no-hydrate above, and the sediments containing gas hydrate provided the glide plane for failure as it represents a plane of weakness due to, not only the change in sediment strength from gas hydrates, but also from the change in general lithology from fine to coarse grained sediment. This result points to a different origin of the failure than previously postulated occurring at the Cascadia margin: At Orca slide, the depth of the glide plane coincides with the depth of the BSR, where the plane of failure is the surface between gas hydrate bearing sediment above and hydrate-free sediments (with some free gas) underneath. That is, both glide planes at Slipstream and Orca slides are potentially related to the presence of hydrate. The actual triggering for the two slumps is still unresolved, but failure is "promoted" (or made easier) by the presence of gas hydrates.

Acknowledgments

The authors are grateful to Shuichi Kodaira and Koichiro Obana for use of the JAMSTEC ocean bottom seismometers (OBSs), and to their technical team for OBS operations. We also thank Peter Neelands and Greg Middleton of the Geological Survey of Canada, and the captain and crew of Canadian Coast Guard Research Vessel John P. Tully for their help in our OBS deployment and recovery. Part of the funding for this project was provided through grants to G. Spence from the Natural Science and Engineering Research Council. Figures and maps were prepared with GMT software (*Wessel et al.*, 2013) and seismic data were processed and plotted using the Seismic Unix software. This is Natural Resources Canada, Earth Science Sector publication # 20130502.

Chapter 3

Multiple migration of OBS data

A version of this chapter is intended for publication in Geophysics as: "Dual-vergence structure from multiple migration of widely spaced OBSs from northern Cascadia margin" by Subbarao Yelisetti, George D. Spence, Martin Scherwath, Michael Riedel and Volkhard Spiess.

Author contribution: The author of this thesis is responsible for design of the research program, analysis of the data and composition of the manuscript. My supervisor, George Spence, provided guidance with the research plan, feedback and editorial supervision throughout the developement of this manuscript. Coauthor Martin Scherwath provided and assisted in running the migration code of D. Klaeschen. Coauthor Michael Riedel gave feedback on the final version of the manuscript. All the above authors are part of the data acquisition. Coauthor Volkhard Spiess provided a version of Figure 3.16c which we modified and presented in this manuscript.

3.1 Introduction

Ocean bottom multiple imaging techniques have increasingly become popular in recent times. Earlier multiples were treated as noise and were separated from the seismic data during the data processing stage. But recent studies (for example, *Godfrey et al.*, 1998; *Ronen et al.*, 2005; *Grion et al.*, 2007; *Dash et al.*, 2009; *Wong et al.*, 2011, 2012a) show that multiples contain enormous information about the structure beneath the seafloor.

Data from an ocean bottom seismometers (OBS) provide wide-azimuth illumination and shear wave recording, and in addition the fixed OBS position on the seafloor provides a quiet recording environment and better repeatability for time-lapse seismic surveys (4D) (*Grion et al.*, 2007). OBS nodes record four-component seismic data, with one hydrophone component recording pressure and three geophone components recording ground velocity in three perpendicular directions. The pressure and velocity components can be decomposed to form upgoing (primaries) and downgoing (multiples) waves. This helps to attenuate water column reverberations and improves first-break picking (*Barr and Sanders*, 1989). As well, *Ronen et al.* (2005) presented a method of imaging the downgoing waves recorded on the seafloor and showed that the illumination is better particularly for shallow targets when compared to images produced using conventional migration of upgoing waves. The main advantage of multiple imaging is that it provides information about a much larger area than imaging with the primary signal alone. Furthermore, it can be easily adapted to existing migration algorithm by simply changing the receiver depth. OBS node geometry is sometimes sparse due to large costs associated with OBS deployment. Therefore, shallow reflectors are often poorly imaged, particularly when the reflector depth is smaller than the node separation. This problem is handled efficiently by using downgoing multiples for imaging, which bounce from the same reflectors as the primary waves, but the subsurface reflection points of multiple are much farther away from the OBS than for the primary, because of the additional sea-surface reflection point.

This method can be applied to other data types as well. For example, *Godfrey et al.* (1998) applied a multiple imaging method to ocean bottom cable data, but without wavefield decomposition. *Yu* (2004) developed a crosscorrelogram migration method to image the ghost reflections recorded on VSP data and showed better illumination coverage than standard migration routines.

Processing and imaging of OBS data are sometimes complex. For example, standard processing routines are inadequate when applied to OBS data acquired from the deep ocean with large separation between nodes (*Pacal*, 2012). Downward continuation is sometimes used to remove the contribution of the large water column by bringing the shot and receiver positions to a common datum such as the seafloor. However, this method is uncertain because it assumes continuity of the wavefield and potentially gives error when there are anomalies present above the common datum. Furthermore, conventional imaging gives poor resolution at shallow subsurface depths when the receiver interval is large. In this scenario, the mirror migration technique is quite useful. In a recent study, *Wong et al.* (2010) showed that joint least-squares inversion of upgoing and downgoing signals from OBS data provides better subsurface illumination with enhanced resolution and more balanced amplitude information. In a later study, *Wong et al.* (2012b) also showed that joint inversion of OBS and streamer data in a linearized inversion scheme provides a better subsurface image with fewer migration artifacts and is useful in correctly imaging dipping reflectors.

On the Cascadia margin, *Dash et al.* (2009) applied a multiple imaging technique using down-going waves to image the shallow subsurface structures, at depths as great as $300 - 400$ m below the seafloor (mbsf), with the gas hydrate bottom simulating reflector being the main target. In the present study, we used a similar technique to image the downgoing signal with a large trace length ($\sim$ 12 s) and a large receiver separation (up to 5 km). Our results indicate for the first time that a multiple imaging technique provides a significantly better image of deep subsurface structure than the simultaneously recorded near-vertical single-channel seismic image. Specifically, using only a small airgun source, our results image the downgoing oceanic crust at $5 - 6$ km beneath the seafloor in water depths of over $2.0 - 2.5$ km near the deformation front of the Northern Cascadia margin off Vancouver Island.

3.2 Data acquisition

Seismic data presented in this thesis were collected in 2010 as part of the SeaJade project, a joint Japanese-Canadian program with recording of seismicity as its main focus (*Riedel et al.*, 2014). Only a brief description of the data acquisition and processing is described here; for a more complete description, please see Chapter 2 of this thesis. A grid of five ocean bottom seismometers (OBSs) was deployed on the ridge, mostly near its crest with a spacing of 500 m, and two additional OBSs were deployed in the deep ocean basin with a spacing of 5 km (Fig. 3.1). These short period OBSs, with a bandwidth of 150 Hz, contain a hydrophone and a three-component geophone (Mark Products L-28LB with natural frequency 4.5 Hz). The OBSs recorded wide-angle reflections and refractions from a 120 cubic inch Bolt airgun that was fired every 7 s, which corresponded to a nominal shot spacing of 15 m to 20 m. Refraction line-4, about 22 km in length, was located along the crest of the ridge parallel to the deformation front, and a linked set of three refraction lines (hereafter combined and called line-1), nearly 20 km in length, was nominally perpendicular to the ridge and deformation front (Fig. 3.1). Two single-channel seismic (SCS) reflection lines (line-4a and line-1a) were recorded coincident with the refraction lines. Six additional single-channel reflection lines, approximately 5 km in length, were also recorded to obtain the detailed structure of the frontal ridge.

We also compared our OBS and SCS data with a nearby margin-perpendicular multi-channel seismic line (MCS-395; see Fig. 3.1) that was collected in 2001 by IFM-GEOMAR, Germany (*Spiess and cruise participants*, 2001). One standard GI-gun (Sodera) with normal chamber volume (2 x 1.7 L, for a total volume of $\sim$ 207.5 cubic inch; $30-200$ Hz) as well as a second GI-gun with reduced chamber volume (2 x 0.41 L, for a total of $\sim$ 48.8 cubic inch; $100-500$ Hz) were used to collect these data. The multichannel seismic streamer (Syntron) contained 48 channels with a group spacing of 12.5 m for a total cable length of 600 m. Each gun was fired every $18-26$ s, and the corresponding shot spacing was approximately $25-34$ m. Data were recorded up to 6 s with a sample interval of 0.25 ms.

3.3 Data processing

3.3.1 SCS data

The vertical incidence data were recorded on a single-channel Teledyne streamer with a 1 ms sample rate and a record length of 5 s. On line-4a, strong primary reflections are seen at times of $230-280$ ms below the seafloor (Fig. 3.2a). Below this depth, the data quality is poor, particularly beneath the flanks of the ridge on line-1a (Fig. 3.2b). We applied predictive deconvolution with a filter length of 800 ms and gap length of 6 ms to suppress the bubble pulse, followed by trapezoidal bandpass filtering with frequencies $10-20-80-120$ Hz to suppress the high frequency noise. After this, a finite difference time migration routine was applied using tomographic velocities derived from travel time inversion of wide-angle reflections, refractions and vertical incidence reflections (*Yelisetti et al.*, 2014). The migration assumed a constant trace spacing of 17.5 m. The migration was highly successful in removing diffractions near sharp offsets or scarps on the seafloor (Fig. 3.2a) and in correctly repositioning dipping reflectors. The sedimentary structure is very uniform in the deep basin and strong reflections can be seen to times of 4.0 s and more, in contrast to the weak reflectivity beneath the ridge crest (Fig. 3.2b).

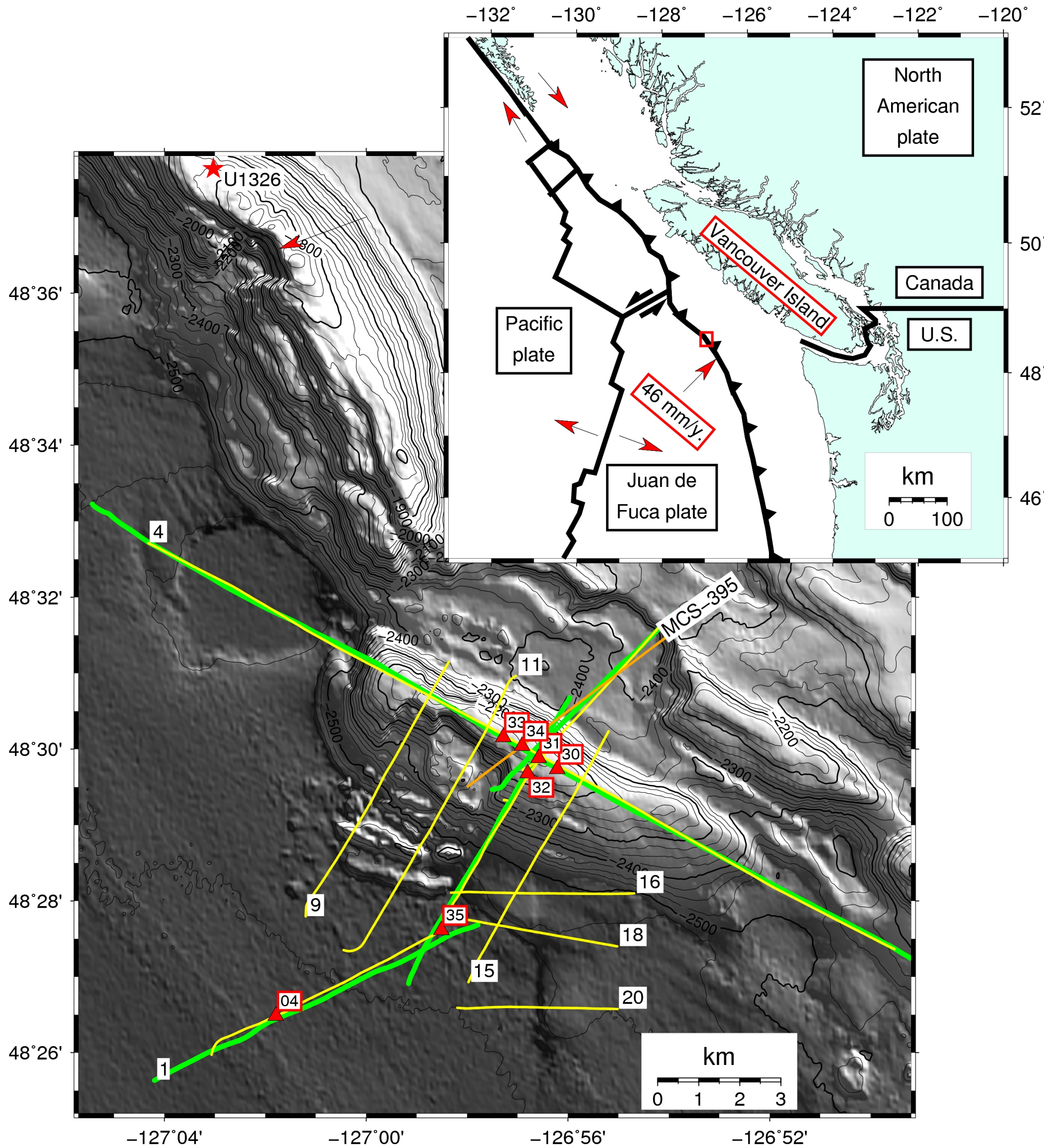

Figure 3.1: Bathymetry map showing the location of all OBSs (red triangles). OBS 33, 34, 31, 30 and 32 were deployed on the frontal ridge adjacent to Slipstream slide. OBS 04 and 35 were deployed in the deep basin where water depths are around 2500 m. Green lines represent refraction lines. Yellow lines correspond to single channel reflection lines; line-4a and line-1a are mostly coincident with refraction line-4 and line-1, respectively. Orange line corresponds to approximate location of MCS line 395 collected by IFM-GEOMAR, Germany. Red star corresponds to Site U1326 from IODP X311. Arrow indicates Orca slide discussed in the text. Inset shows tectonic setting with convergence at 46 mm/yr.

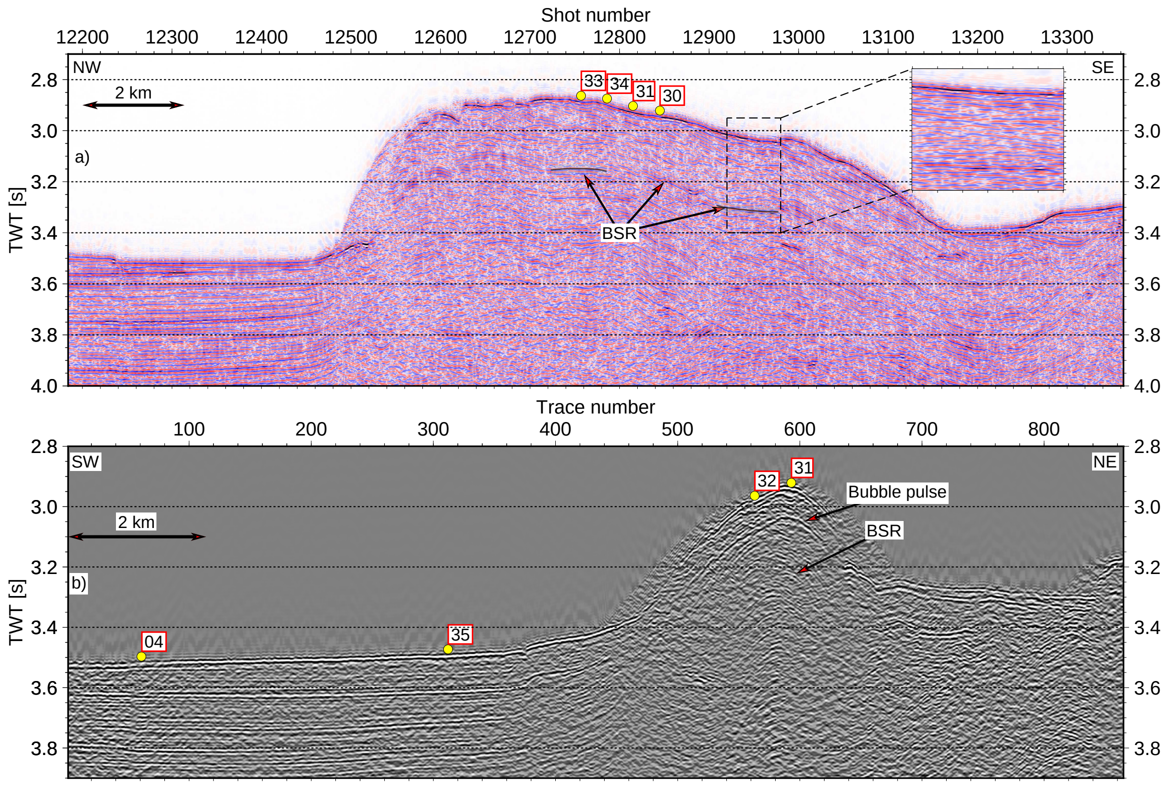

Figure 3.2: Migrated seismic section of (a) single channel line-4a parallel to the margin (passes through OBS 33, 34, 31 and 30), which coincides with refraction line-4 shown in Fig. 3.1 and (b) single channel line-1a perpendicular to the margin (passes through OBS 4, 35, 32 and 31), which coincides with refraction line-1 shown in Fig. 3.1. BSR is observed at $\sim$ 280 ms below the seafloor and is indicated by black arrows. Gray bars in (a) indicate the travel time picks used in inversion (*Yelisetti et al.*, 2014). The thickness of this line indicates the pick uncertainty. The approximate location of the OBS on the seafloor is shown by yellow circles. Inset figure in (a) enable the clear identification of the BSR.

3.3.2 OBS data

The OBS data were recorded up to 30 s with a sampling interval of 10 ms and a maximum offset of nearly 12 km on margin-parallel line-4 and 14 km on margin-perpendicular line-1. The data were resampled to 4 ms from the original 10 ms sample rate. Each OBS recorded four- component data with one hydrophone component, one vertical geophone component and two perpendicular horizontal components. Only hydrophone and vertical geophone components were used in this study. Examples of hydrophone and vertical geophone data recorded along the margin-parallel line on OBS's 33, 34, 31 and 30 are shown in figures 3.3 and 3.4.

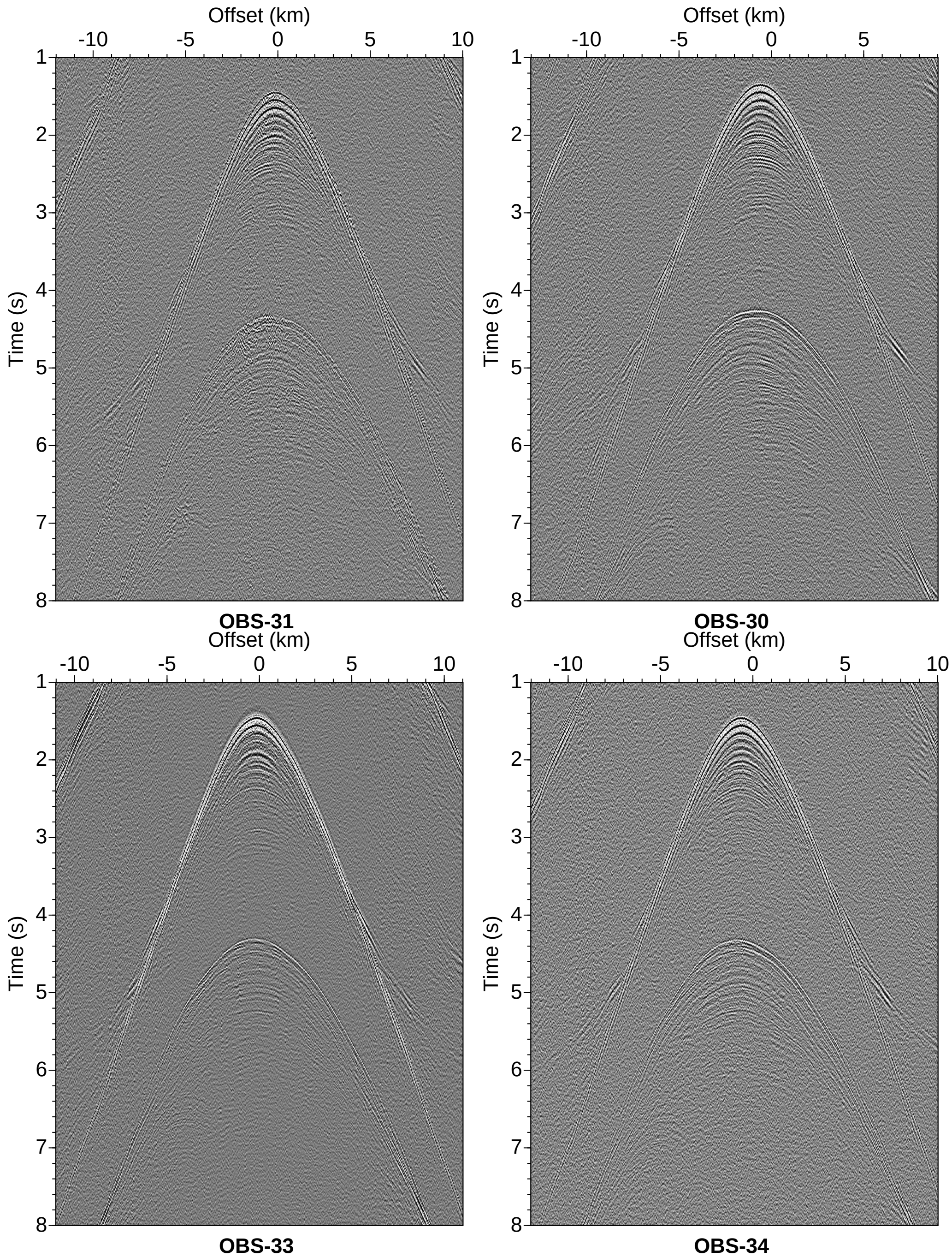

Figure 3.3: Hydrophone component of OBS data recorded on OBS 33, 34, 31 and 30 along margin parallel line-4. Deconvolution with filter length of 300 ms and gap length of 15 ms plus bandpass filtering with frequencies 5-10-30-40 Hz were applied to remove the bubble pulse and high frequency noise.

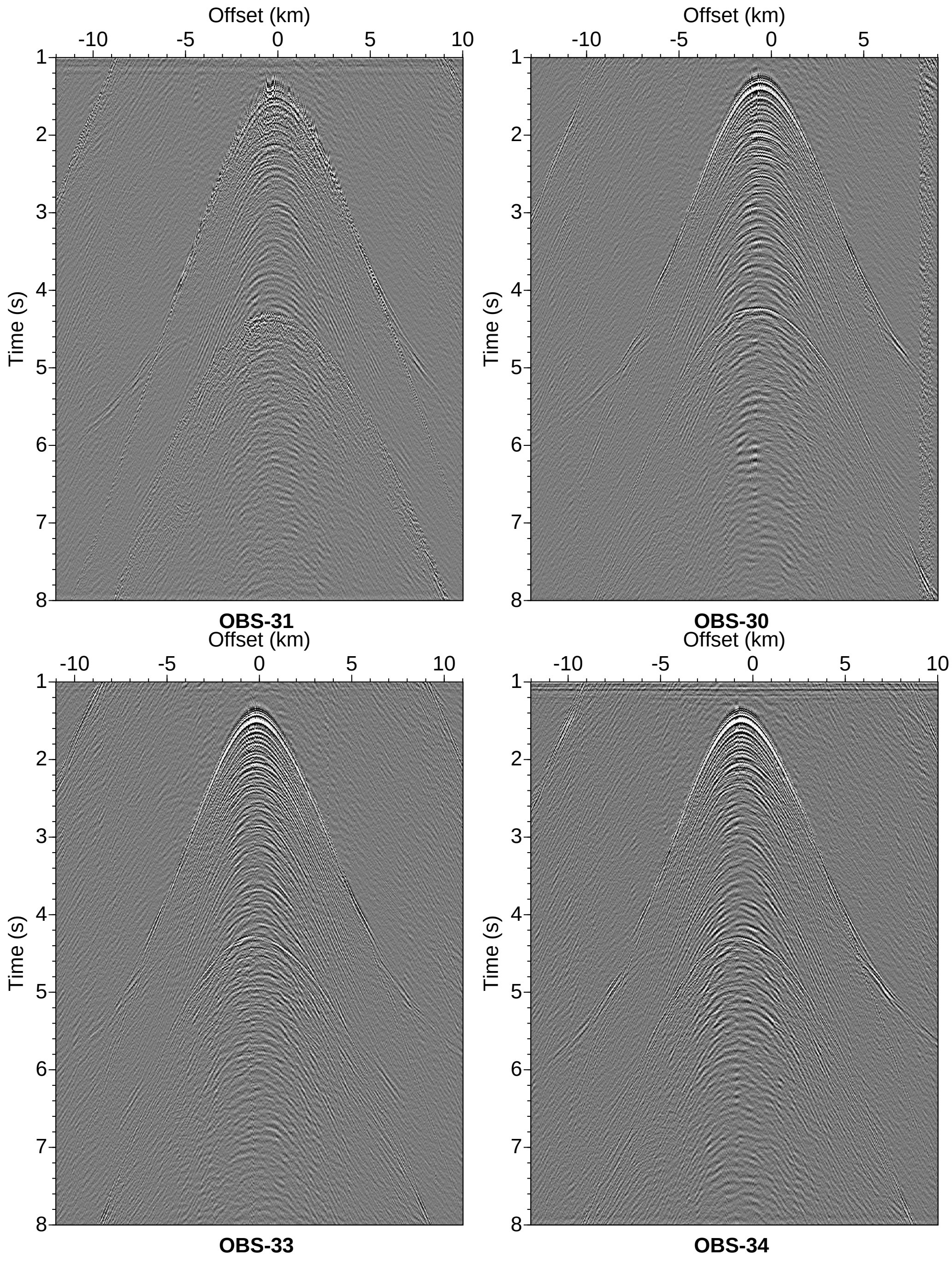

Figure 3.4: Geophone component of OBS data recorded on OBS 33, 34, 31 and 30 along margin parallel line-4. Deconvolution with filter length of 300 ms and gap length of 15 ms plus bandpass filtering with frequencies 5-10-30-40 Hz were applied to remove the bubble pulse and high frequency noise.

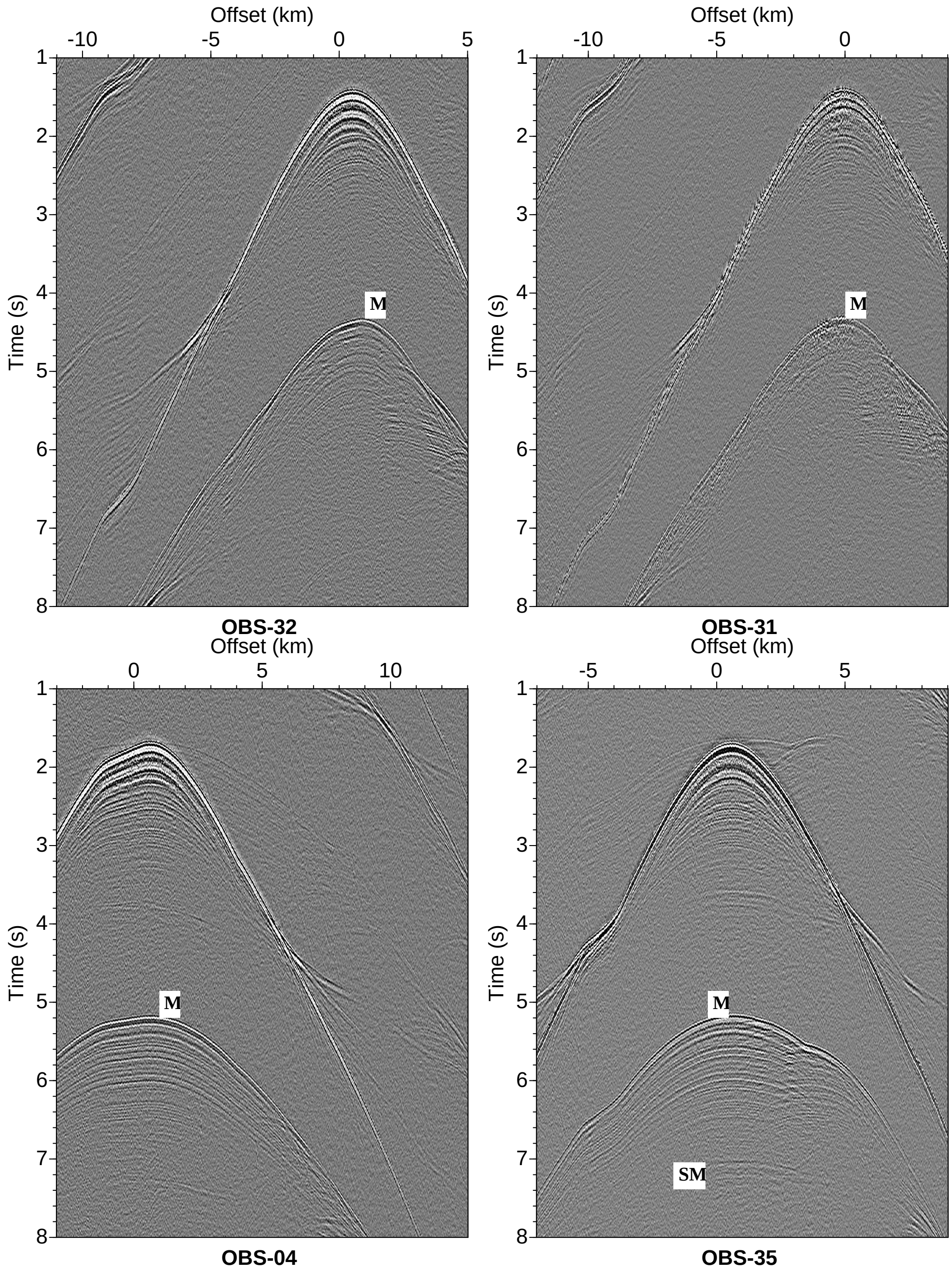

Figure 3.5: Hydrophone component of OBS data recorded on OBS 4, 35, 32 and 31 along margin perpendicular line-1. Deconvolution with filter length of 300 ms and gap length of 12 ms plus bandpass filtering with frequencies 2-7-22-35 Hz were applied to remove the bubble pulse and high frequency noise. M and SM indicate primary and secondary multiples.

The hydrophone component of OBS data recorded along the margin-perpendicular line on OBS's 4, 35, 32 and 31 is shown in Fig. 3.5. A clear dipping reflection package is seen beneath the seafloor multiple at times $5.2-6.4$ s and trace numbers $840-1040$ on OBS 32 along the margin-perpendicular line-1 (Fig. 3.5). A similar reflection package is also seen on OBS 31 on the same line (Fig. 3.5). NMO correction with the water velocity of 1480 m/s was applied to see the wide azimuth information contained in the multiples (Fig. 3.6 and 3.7). NMO corrected data along line-1 also clearly show the dipping reflection package seen above that cross cuts the frontal ridge sedimentary layering structure (Fig. 3.7 on OBS's 32 and 31).

Clear refractions are observed out to distances of up to $5-9$ km with an apparent velocity ranging from $2-4$ km/s (Fig. 3.3, 3.4, 3.5). These were used in a tomographic velocity analysis to obtain detailed velocity models along line-1 and line-4 (Chapter 2; *Yelisetti et al.* (2014)). Primary and secondary multiples are seen at approximately three and five times the seafloor time (Fig. 3.5).

3.4 Wavefield separation

Marine seismic reflection data are often contaminated with ghost reflections from the air-water interface and water-bottom reverberations or multiples. Unfortunately, at large water depths, deconvolution alone is unsuccessful in removing these sources of noise in reflection data. *Barr and Sanders* (1989) proposed a method in which pressure and velocity signals recorded on the ocean bottom are combined to eliminate the ghosts and multiples. Specifically, both pressure (P(t)) and velocity (V(t)) signals have the same polarity for upward traveling waves, while they have opposite polarity for downward traveling ghost reflections and multiples after reflection from the sea surface. Therefore, the combined signal for upward ($U(t)_+$) and downward ($D(t)_+$) traveling waves above seafloor is given by

$$U(t)_+ = P(t) + \frac{\rho\alpha}{cos\,\gamma_p}V(t) \tag{3.1}$$

$$D(t)_+ = P(t) - \frac{\rho\alpha}{cos\,\gamma_p}V(t) \tag{3.2}$$

Similarly, the combined signal for upward ($U(t)_-$) and downward ($D(t)_-$) traveling waves below seafloor is given by

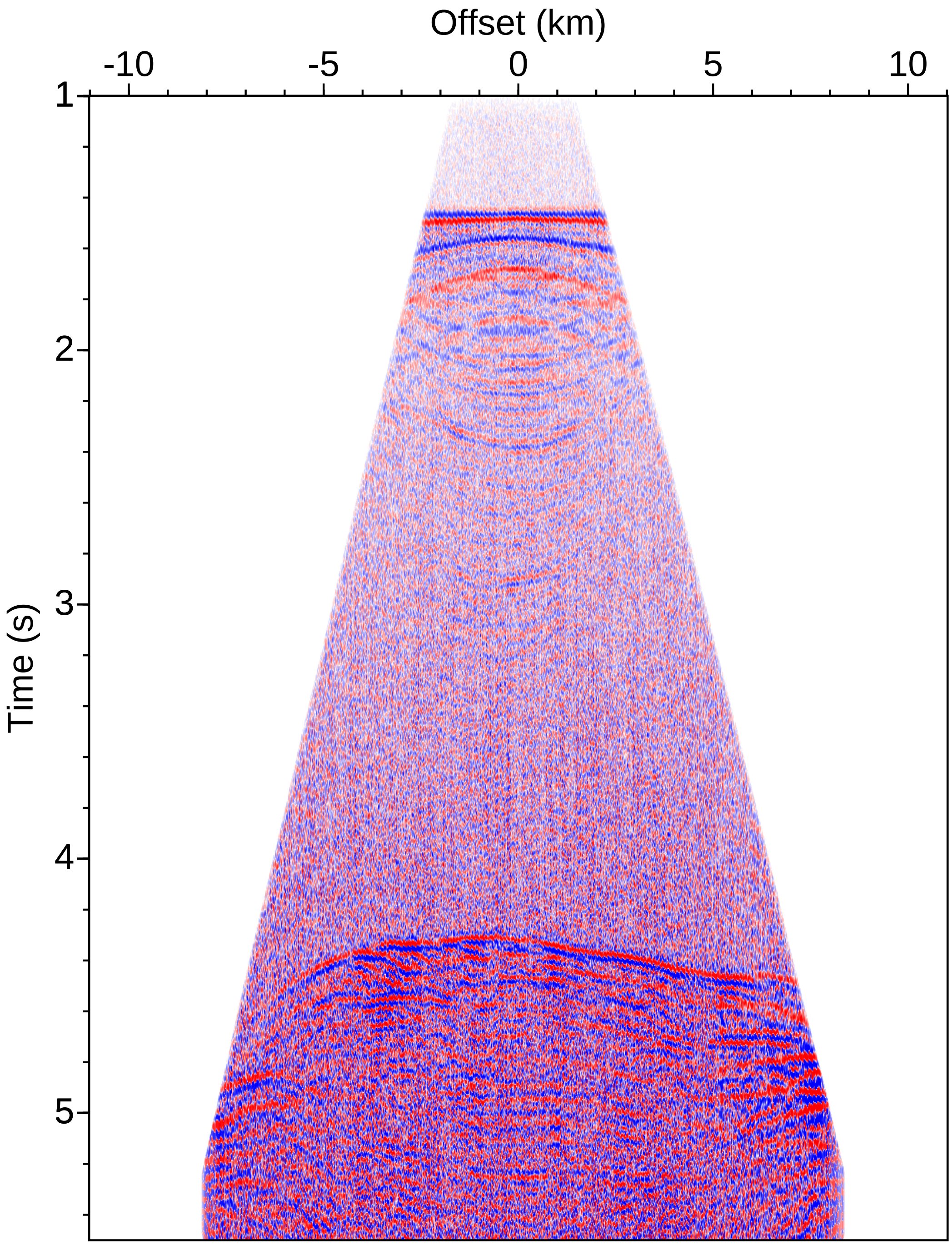

Figure 3.6: Hydrophone component of OBS-33 along margin parallel line-4 showing the structural information contained in the primaries and multiples. Normal moveout (NMO) correction with the water velocity of 1480 m/s was applied to flatten the seafloor reflection.

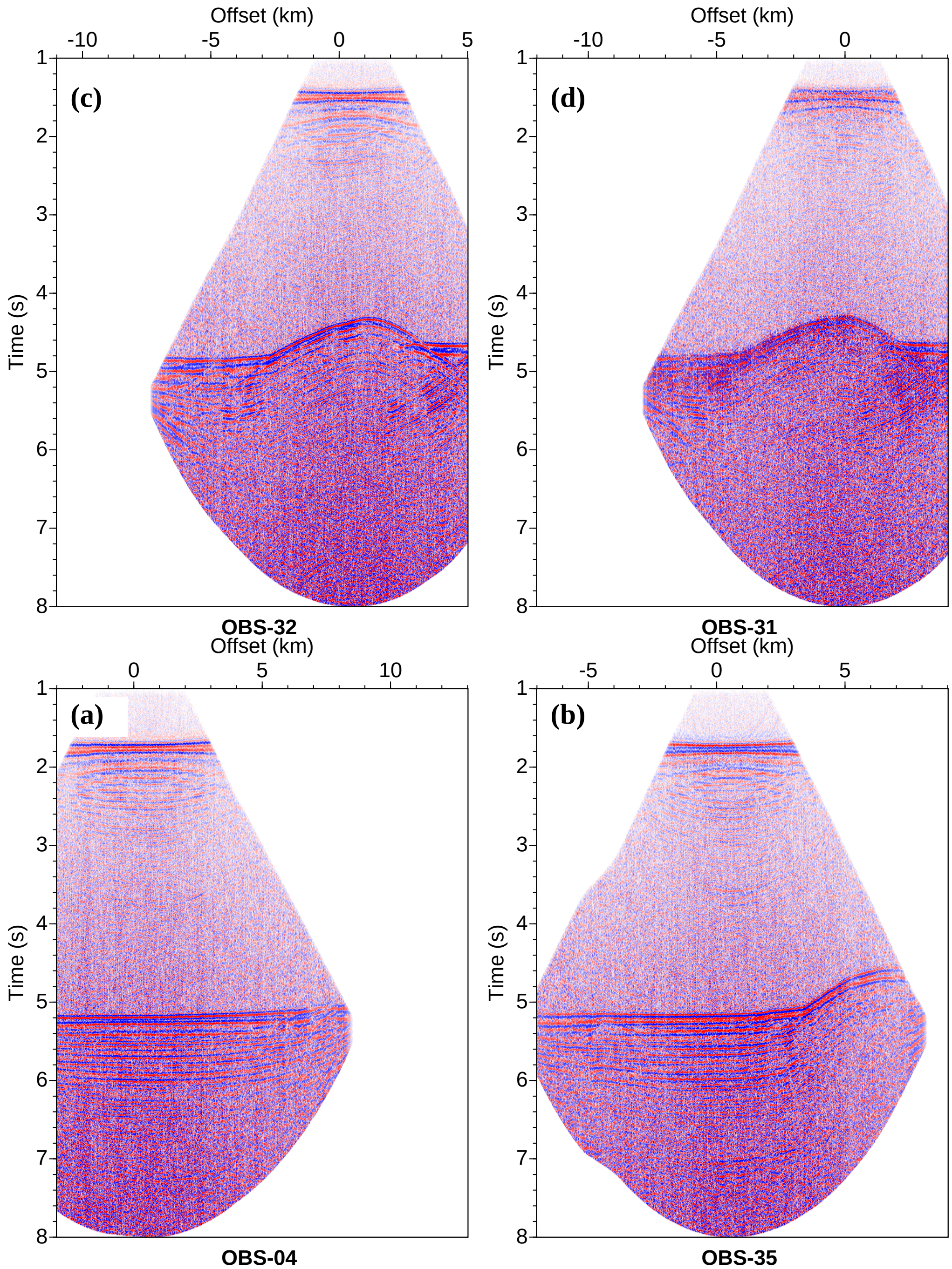

Figure 3.7: Hydrophone component of OBS 4, 35, 32 and 31 along margin perpendicular line-1 showing the structural information contained in the primaries and multiples. Normal moveout (NMO) correction with the water velocity of 1480 m/s was applied to flatten the seafloor reflection.

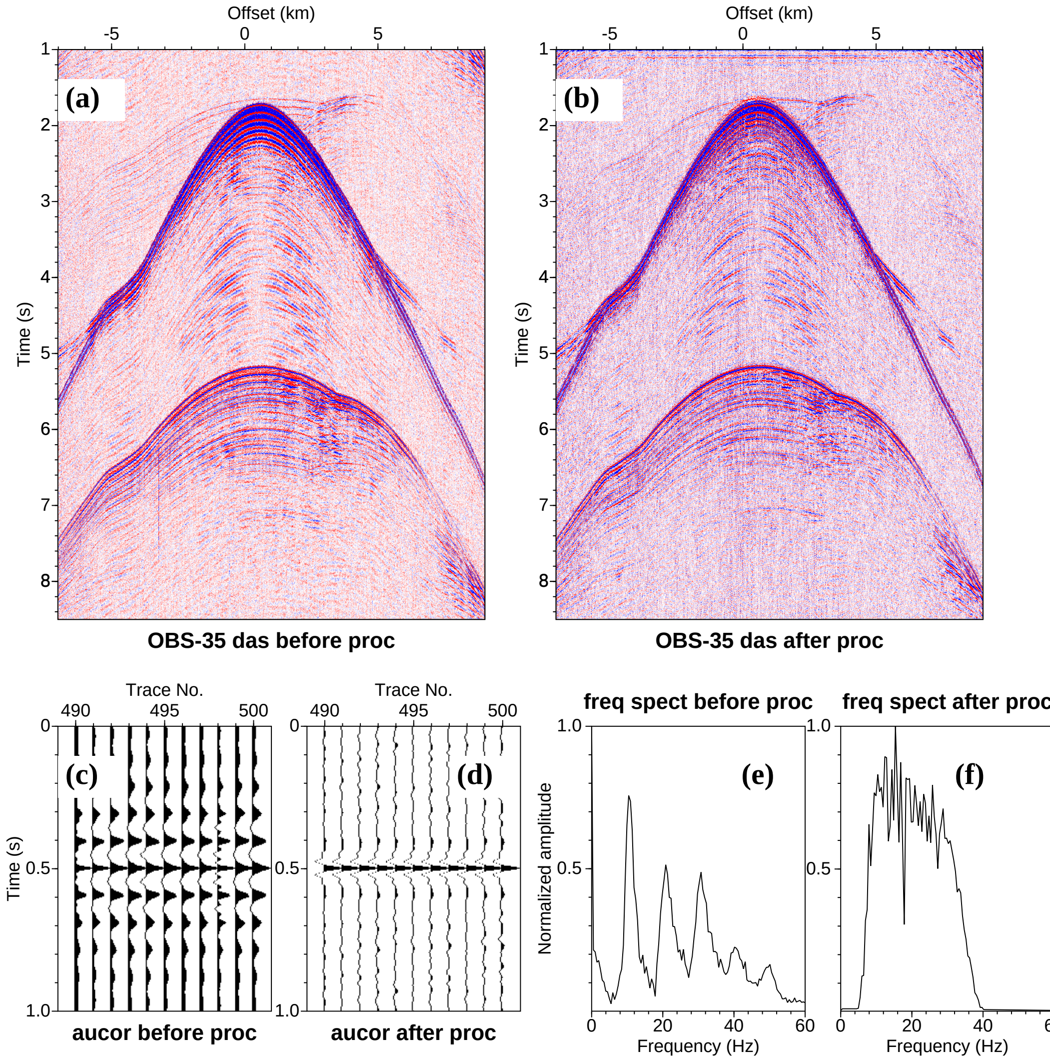

Figure 3.8: Down going wavefield above seafloor (das) from OBS-35 showing (a) before processing and (b) after deconvolution and band pass filtering. (c) and (d) show autocorrelograms before and after processing, while (e) and (f) show frequency spectrum before and after processing corresponding to trace number 490 in the time window 1-3 s.

$$U(t)_- = P(t) + \frac{\rho\alpha}{cos\,\gamma_p}\frac{1+K_r}{1-K_r}V(t) \tag{3.3}$$

$$D(t)_- = P(t) - \frac{\rho\alpha}{cos\,\gamma_p}\frac{1+K_r}{1-K_r}V(t) \tag{3.4}$$

where $\rho\alpha$ is acoustic impedance of water, γ_p is angle of refraction of the P-wave in water and K_r is seafloor reflection coefficient. It is very difficult to obtain a well-calibrated absolute velocity from a geophone, since geophone amplitudes can vary significantly due to variable geophone-ground coupling and to highly-variable near-surface velocities. Hence, in these equations, we did not use the quantity $\frac{\rho\alpha}{cos\,\gamma_p}$ as a scale factor, but rather we determined an empirical factor for a downward propagating wavefield as the absolute amplitude ratio of the pressure phone and velocity phone signals (*Barr and Sanders*, 1989). Specifically, we found the maximum absolute amplitudes at the near-offset within a time window ($\sim$ 20 ms) that includes mainly the direct arrival waveform. These were averaged over $\sim$ 50 traces to eliminate any potential errors from noisy spikes. The ratio of average amplitude of hydrophone to geophone component gives the velocity scaling factor, which is typically around $5-25$ for OBSs used in this study.

As with the raw data, the data quality of the downgoing wavefield component was severely impacted by the occurrence of a strong bubble pulse sequence, which occurred with a time period of 100 ms. Wiener gapped deconvolution with a filter length of 300 ms and gap length of 15 ms (chosen based on auto-correlograms shown in Fig. 3.8c,d) was applied to the downgoing waves above the seafloor to remove the bubble pulse. Subsequently, bandpass filtering with frequencies $5-10-30-40$ Hz was applied to remove the high frequency noise (Fig. 3.8e,f). The processed data including deconvolution (Fig. 3.8b) show less ringing compared to the unprocessed data (Fig. 3.8a). In the downgoing wavefield above seafloor (Fig. 9a) the multiples are enhanced, while in the upgoing wavefield above seafloor (Fig. 3.9b) the multiples are reduced but the primaries are enhanced. Unlike *Barr and Sanders* (1989), who dealt with MCS reflection data, we are not treating the multiples as noise that needs to be eliminated, but rather we wish to enhance them because they are a rich source of valuable information as seen from the NMO-corrected data (Fig. 3.6 and 3.7).

3.5 Migration of OBS data

Kirchhoff time migration was used for migrating the OBS data. This technique involves summing the amplitudes along the diffraction hyperbolas and then placing them at the apex, and the curvature of the diffraction hyperbola for amplitude summation depends on the velocity function used. The migration aperture width (the lateral extent of diffraction hyperbolae) and the maximum dip to migrate are two main important factors in Kirchhoff migration. Since a small aperture size causes

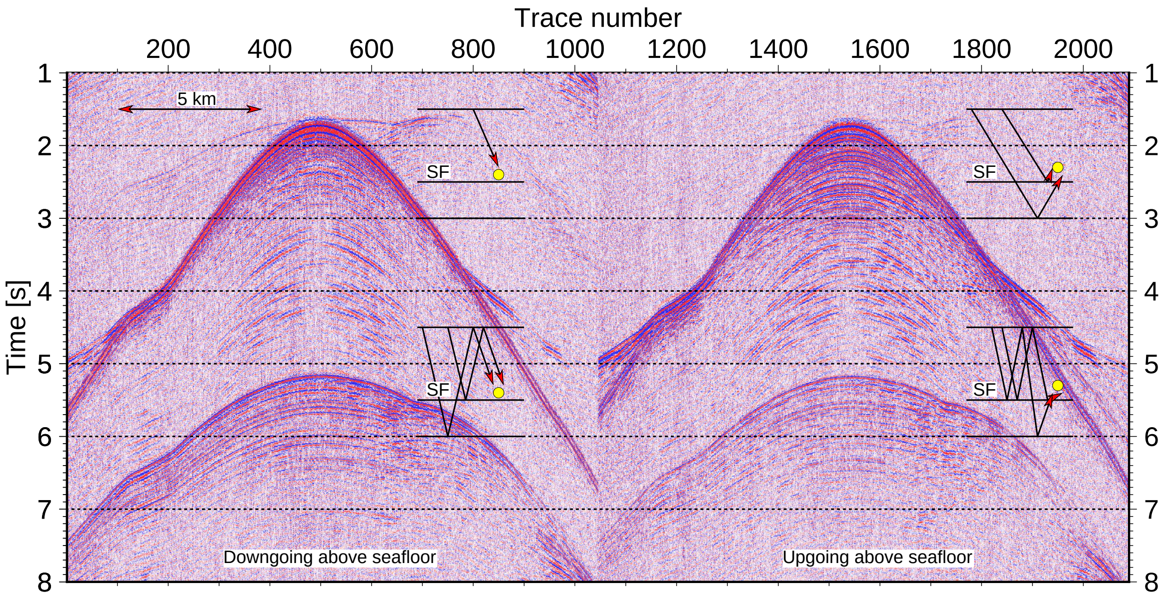

Figure 3.9: Down- and upgoing wavefields above seafloor recorded at OBS-35 on margin perpendicular line. Simple ray trace sketches are shown to indicate downgoing primary, multiples and upgoing primary, multiples. Yellow circle indicates location of OBS on the seafloor (SF).

removal of steep dips, we need to use a large aperture size because the dips are very large in the frontal ridge area. Hence, a migration aperture size of 85° was used in this study. Further, to avoid spatial aliasing of steep dips at high frequencies, a smaller trace spacing of 12.5 m was used in the migration.

The mirror-imaging migration code used in this study was developed by D. Klaeschen of IFM-GEOMAR, Kiel, Germany. Mirror migration assumes that the downgoing multiples are not recorded on the seafloor, but recorded as upgoing primaries at a virtual datum above the sea-surface with twice the thickness of the water column (Fig. 3.10). In a preliminary study, *Scherwath and Spence* (2011) applied this code to OBS data collected off Vancouver Island margin, to image sedimentary structures below a topographic frontal ridge near the deformation front. However, their results were limited in depth by a short trace length (7 s) and a small OBS spacing ($\sim 500 - 800$ m).

The mirror-imaging migration code requires a fine grid velocity model, which we obtained by simultaneously inverting travel times from wide-angle reflections and refractions recorded on the OBS data and vertical incidence reflections recorded on the SCS data (see *Yelisetti et al.* (2014), and Chapter 2). The final interval velocity model was re-gridded with a grid spacing of 12.5 m in both horizontal and vertical directions, and converted to RMS velocities (Fig. 3.11 and 3.12). The model is padded at the top so that the water layer is twice the thickness of the water column at the OBS, as required for mirror imaging. An average free surface elevation of 2200 m was used on the margin-parallel line since the water depth at the OBS positions on this line only varies slightly. However, four different velocity models with varying free surface elevations were used on the margin-perpendicular line to accommodate the rapid lateral changes in water depth at the OBS positions on this line.

Previous studies (e.g., *Dash et al.*, 2009; *Ronen et al.*, 2005) indicated that migration of upgoing wavefield (primaries) is not the best option, particularly for a sparse receiver geometry, since they provide poor illumination particularly in the shallow part of the image. In contrast, downgoing waves (multiples) provide wider illumination coverage, and they are also less susceptible to scattering and amplitude variations associated with near seabed anomalies. Hence they provide a better image of the subseafloor structures than the upgoing waves (primaries) which are more susceptible to inhomogeneous media just under the seabed. Alternatively, downgoing waves travel closer to vertical than primaries and hence they provide better illumination of the subseafloor structure than primaries. Therefore, we applied migration to the downgo-

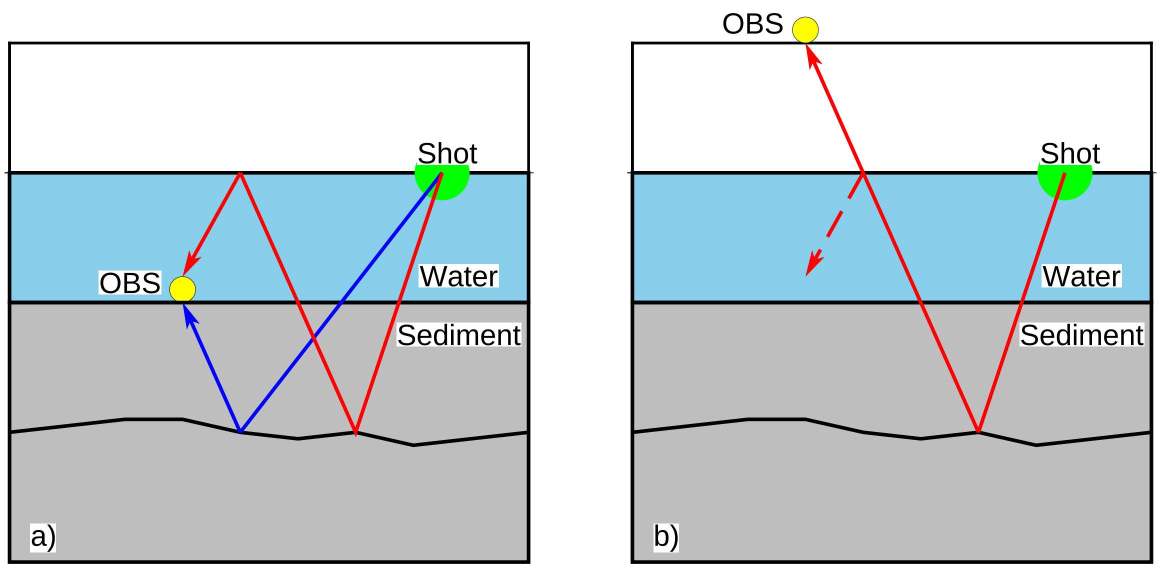

Figure 3.10: The principle of multiple migration. Upgoing primary (blue ray) and downgoing multiple signal (red ray) are shown in (a). Migration assumes that the downgoing multiples shown in (a) are not recorded on the seafloor, but recorded as upgoing primaries above the seasurface with twice the thickness of the water column as shown in (b).

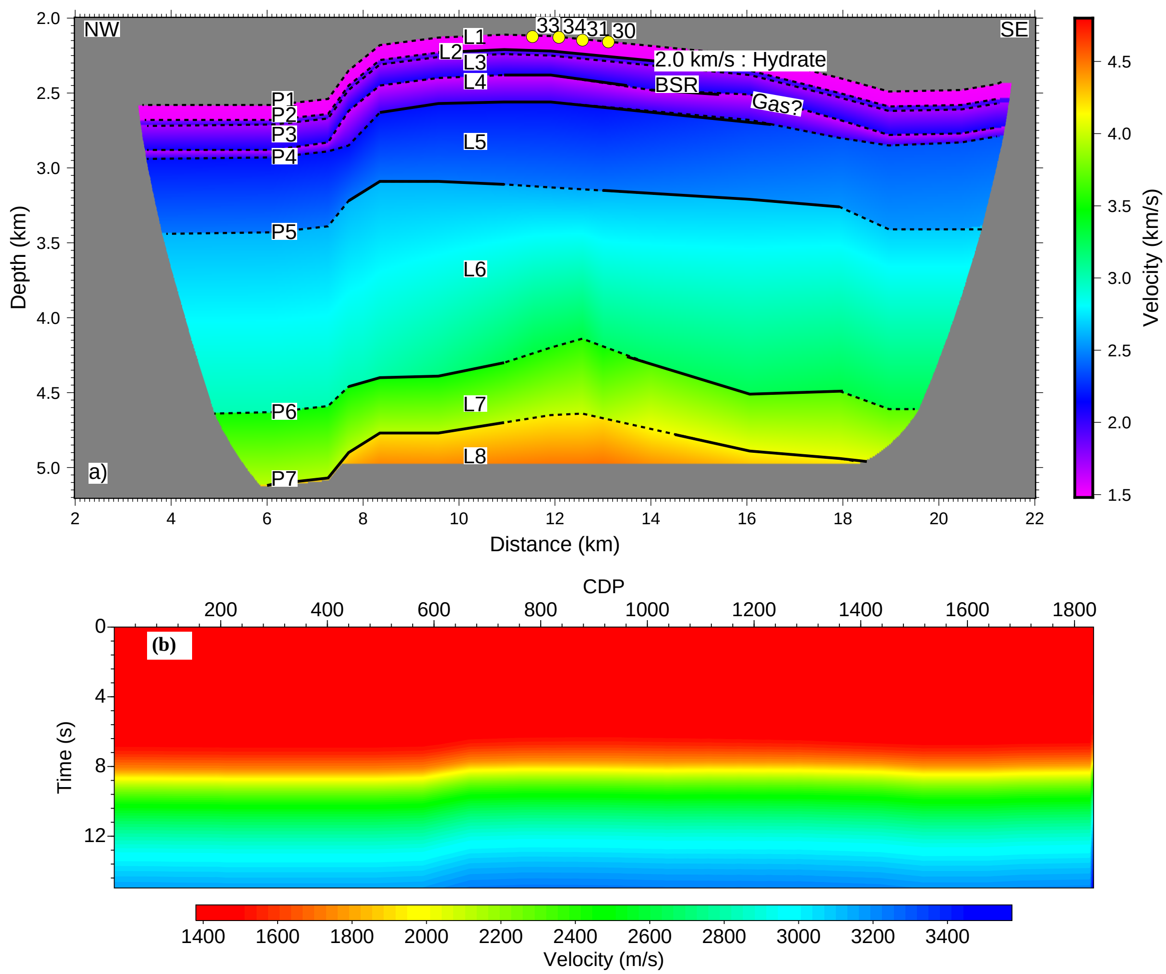

Figure 3.11: (a) Tomographic velocity model obtained using simultaneous inversion of travel times from wide-angle reflections, refractions and vertical incidence reflections along margin parallel line-4 (*Yelisetti et al.*, 2014). P1-P7 and L1-L7 indicate arrival names and layer numbers, respectively. Yellow circles indicate OBS positions on the seafloor. (b) RMS velocity field required for multiple imaging obtained from model derived in (a). Average water depth at OBS position is 4400 m. Trace spacing is 12.5 m.

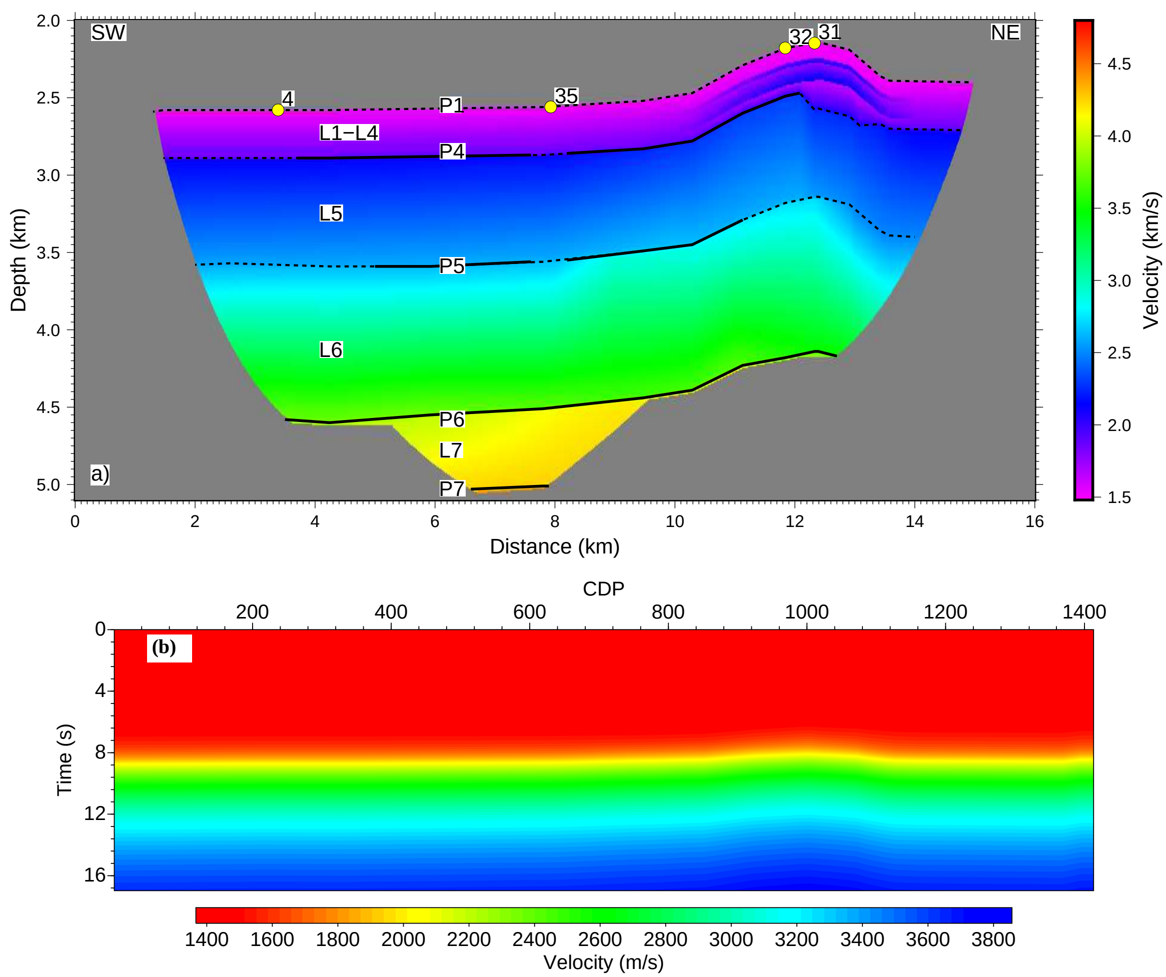

Figure 3.12: (a) Tomographic velocity model obtained using inversion of travel times from wide-angle refractions along margin perpendicular line-1 (*Yelisetti et al.*, 2014). P1-P7 and L1-L7 indicate arrival names and layer numbers, respectively. Yellow circles indicate OBS positions on the seafloor. (b) RMS velocity field required for multiple imaging obtained from model derived in (a). This model corresponds to water depth at OBS-04, which is $\sim$ 5200 m. Trace spacing is 12.5 m.

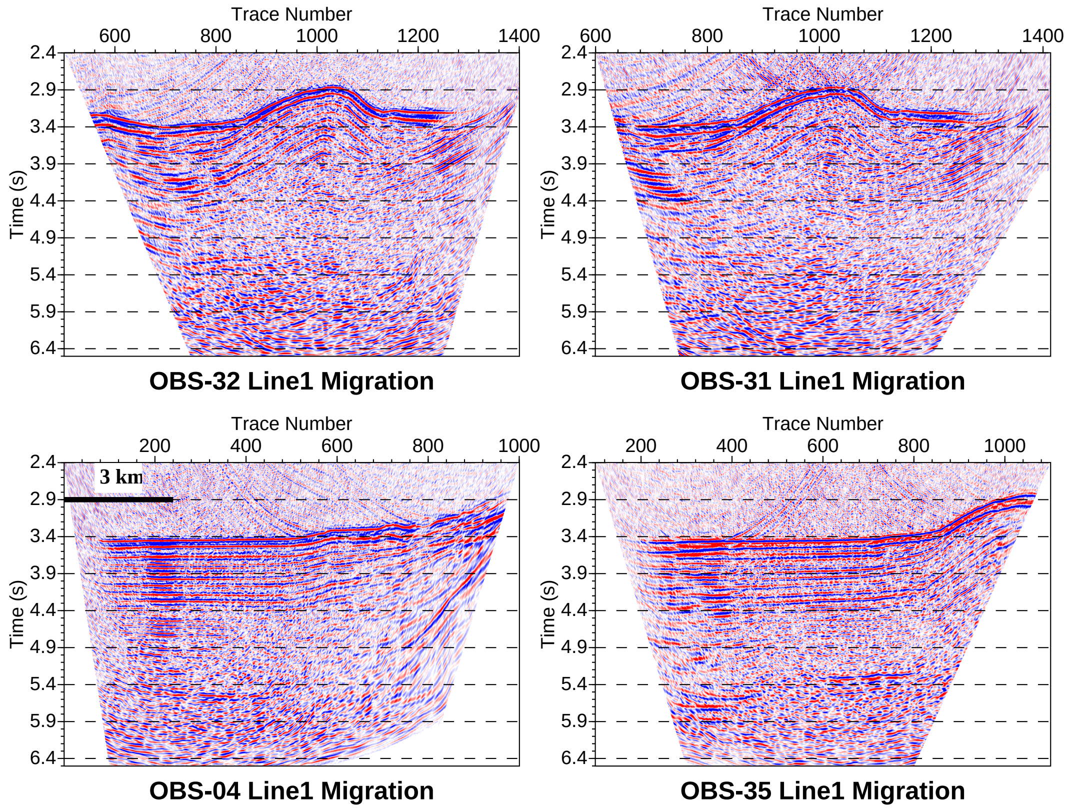

Figure 3.13: Migrated image of individual OBS's along margin perpendicular line-1 using downgoing wavefield above seafloor. Trace spacing is 12.5 m. Each OBS is able to image approximately 10.0-12.5 km.

ing wavefield above seafloor on both margin-parallel and margin-perpendicular lines. For the margin-perpendicular line, the individual migrated sections obtained using the downgoing wavefield above seafloor recorded on OBS's 4, 35, 32 and 31 are shown in Figure 3.13. Each OBS is able to image a horizontal distance of approximately $10 - 12.5$ km. The stacked image of the four individual migrations along this line is shown in Figure 3.14.

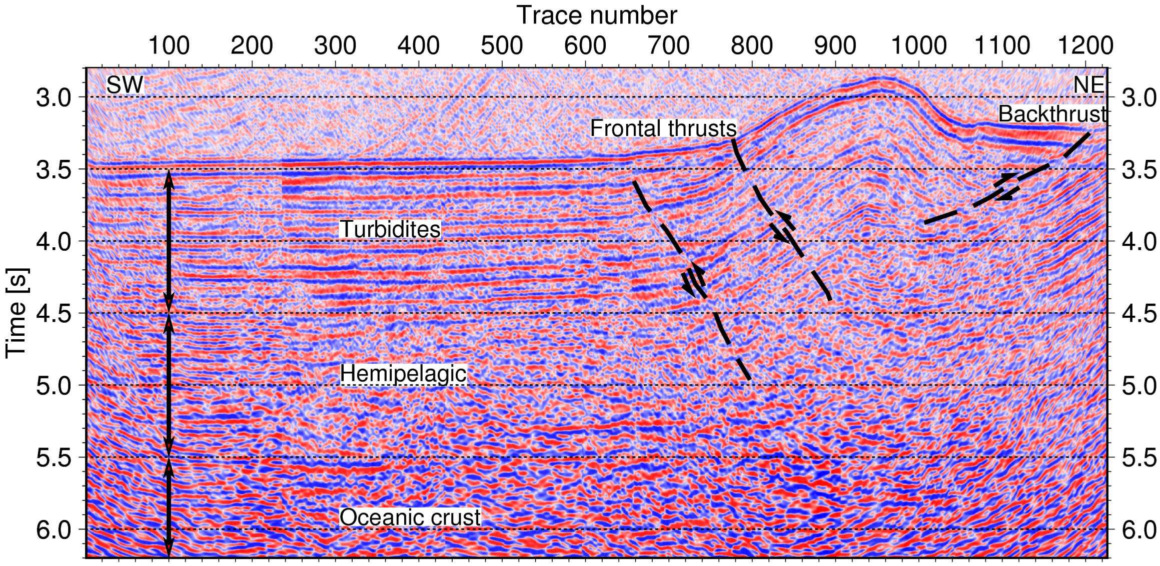

Figure 3.14: Migrated section along line-1 using downgoing waves above the seafloor with migration aperture of 85°. It is a stack of the four migrated images in Figure 3.13.

3.6 Mirror-imaging results

3.6.1 Comparision of mirror imaging with SCS image along margin-parallel line

OBS multiple-migrated stack section along the margin-parallel line using the downgoing wavefield above seafloor recorded on OBSs 33, 34, 31 and 30 is shown in Figure 3.15b for a migration aperture of 85°. A bandpass filter with frequencies $2-7-22-35$ Hz was applied to eliminate high frequency noise from the final migrated image. Migrated image of the SCS data along the same line is shown in Figure 3.15a for comparison with OBS image. A bandpass filter with frequencies $10-20-80-120$ Hz was applied to remove high frequency noise.

In general, the multiple-migration results indicate that several subsurface reflectors have higher amplitudes in the mirror image than in the single channel seismic image (Fig. 3.15). However, the SCS image has higher resolution, i.e. it has higher frequency content and resolves more closely-spaced reflections. But the OBS migration image has greater reflectivity at greater depths, and the reflectors are more continuous. Particularly, the seafloor is well imaged in the 10 km vicinity of the OBS's between CDP $650-1480$ (Fig. 3.15b). As well, the BSR is visible on migrated OBS image at ∼ 280 ms below the seafloor with polarity showing opposite (blue-red-blue) to that of seafloor reflection (red-blue-red). Below the BSR, the reflection amplitudes are enhanced and some structures are clearly evident which are not readily observed in the single-channel seismic data. Particularly beneath the ridge crest, the reflection amplitudes are very weak in the single channel image below the BSR depth between shot numbers 12550 and 13050 (Fig. 3.15a), while strong reflections are observed in the multiple-migrated image for trace numbers 800 to 1200 over times from 3.3 s to nearly 4.0 s.

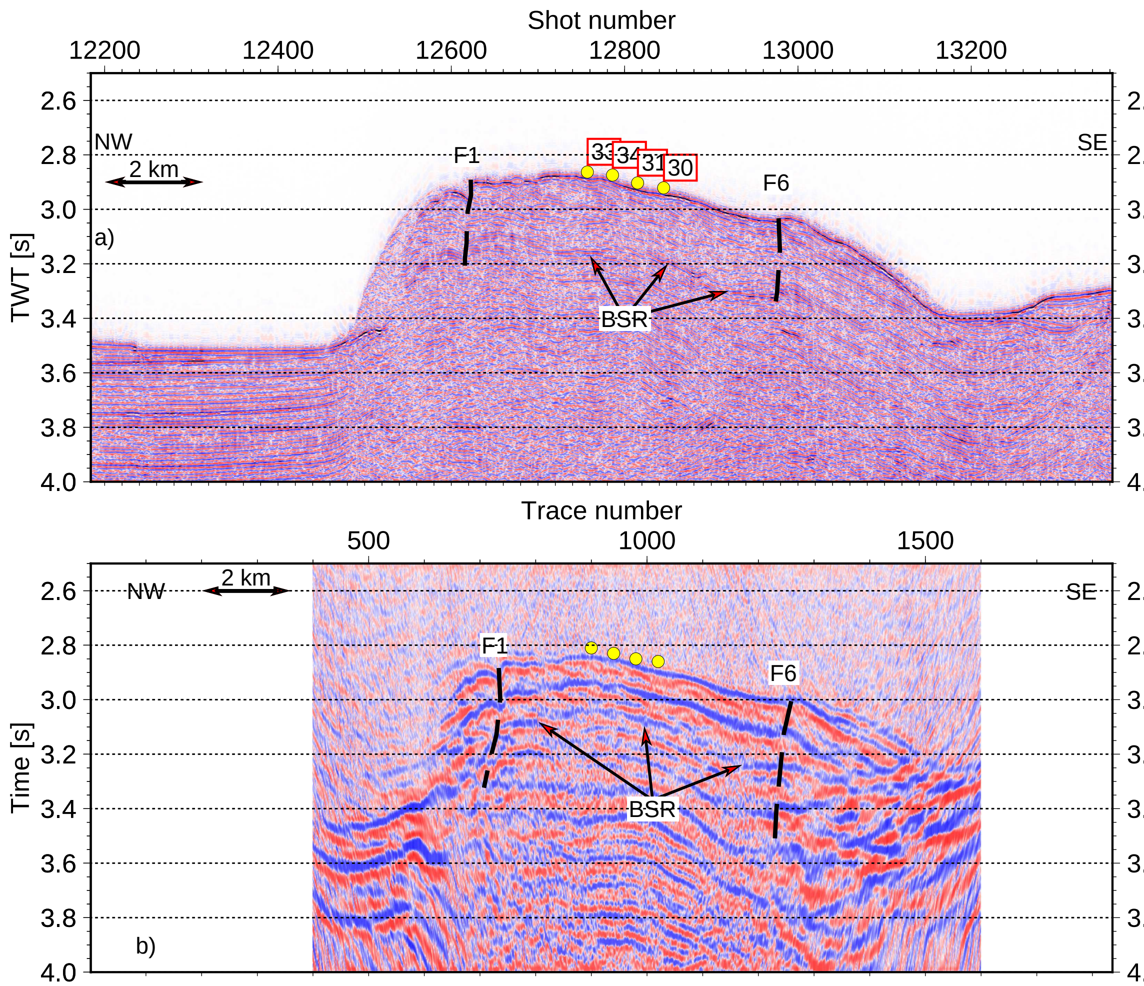

Figure 3.15: Comparision of a) Single channel and b) mirror imaging results along line-4 which passes through OBSs 33, 34, 31 and 30. Migration aperture of 85° is used in (b). Yellow circles indicate approximate location of OBS on the seafloor.

Major margin-perpendicular normal faults identified as F1 and F6 on the single-channel record (Fig. 3.15a) are clearly imaged in mirror image near trace number 710 and 1250, respectively (Fig. 3.15b). These faults extend from seafloor down to well below the BSR depth. Also, a strong and continuous reflector is seen at approximately 100 m below the seafloor (Fig. 3.15b), which possibly corresponds to a 30 m thick high velocity hydrate layer identified at the same depth from velocity modeling, as reported by *Yelisetti et al.* (2014) (Fig. 3.11a). However, the ridge flanks are not well imaged on this line because the multiple image deteriorates beyond a distance of approximately $5-7$ km on either side of the OBS position on the seafloor (Fig. 3.6, 3.7). Having an additional one or two OBSs at a larger separation of 5 km instead of the 500 m used on this line can extend the lateral coverage of the image.

3.6.2 Comparison of mirror imaging with SCS & MCS images along margin-perpendicular line

The migrated image obtained using the hydrophone component alone (Fig. 3.16b) looks very similar to the combined image obtained using both the hydrophone and geophone components (Fig. 3.14), which requires additional processing. The basic structures shown in both images (Fig. 3.14 and 3.16b) are independently confirmed by the single-channel and multi-channel images shown in Figure 3.16a,c. Figure 3.14 also shows strong reflections just beneath the ridge crest (between trace numbers $900-1000$ and $4-5$ s below the seafloor), which may be associated with the presence of fluids.

In contrast to the margin-parallel line, the images obtained along the margin perpendicular line are much better and show reasonable structures down to ~ 6.5 s below the seafloor (Fig. 3.16b). This is partially because of large receiver separation of 5 km between OBS's 4, 35 and 32 on this line. Secondly, the water depth is about 500 m greater in the Cascadia basin compared to the ridge top. Therefore, the mirror surface is ~ 1000 m higher on this line compared to the margin-parallel line. The longer travel time of ghosts associated with increase in mirror surface height provides deeper and wider illumination of the subsurface. The single-channel and multi-channel data were recorded down to 5 s, but no meaningful structures could be observed below 4 s.

The OBS multiple-migrated stack (Fig. 3.16b) provides a remarkable image that is significantly better than the migrated single-channel reflection section (Fig. 3.16a), even though both datasets were recordings of exactly the same set of airgun shots. Although its frequency content is lower than the SCS image, the OBS image shows deeper penetration, significantly improved reflectivity and lateral continuity as expected for lower frequencies. Reflector continuity even allows faults to be identified based on reflector offsets. Also, the core of anticline is well imaged from the OBS data, whereas it is poorly imaged from the SCS data. The identification of BSR is not very clear on this line, although a weak reflection signal is seen at ~ 280 ms below the seafloor.

The OBS mirror-imaging migration stack compares very favourably with the nearly-coincident multichannel reflection image (Fig. 3.16c). This is particularly remarkable because (i) the airgun array for the MCS data was larger than the size of the single airgun recorded on the OBSs and (ii) the MCS data contains higher fold (12) information than the OBS data. For example, the northeast flank of the ridge top is not well modelled in the MCS data, whereas using a large migration aperture, this portion of the ridge is well imaged in the OBS mirror image.

3.7 Interpretation and discussion

According to *Davis and Hyndman* (1989), the sedimentary section entering the Cascadia basin comprises 2.0 to 2.5 km rapidly deposited probably Pleistocene turbidites which are underlain by 0.8 to 1.0 km thick pre-Pleistocene hemipelagic deposits. On the multiple-migrated image, the sedimentary structure is uniform in the deep basin and strong reflections can be seen down to ~ 4.5 s below the seafloor (Fig. 3.16b); these are interpreted as the turbidite sequence. Below this depth, the sedimentary structure is mostly transparent and weak reflections are seen down to 5.5 s below the seafloor, which is interpreted as the hemipelagic sequence. As interpreted by *Yelisetti et al.* (2014), Layers L4 and L5 from the tomography velocity models (Fig. 3.11a and 3.12a) represent the upper turbidite sequence, whereas layers L6 and L7 are likely compacted accreted wedge sediments. They interpreted the sharp increase in velocity from 3.0 km/s to 3.8 km/s at the interface between L6 and L7 at 2 km below the seafloor as the boundary between the turbidites and the hemipelagic deposits (Fig. 3.11a and 3.12a). Some strong amplitude events are observed below 5.5 s depth on the OBS migrated image, which most likely represent reflections within or near the top of igneous oceanic crust. On the seaward side of the ridge crest on the OBS image, we interpret frontal thrusts which extend down to ~ 5 s below the seafloor. One of these thrust faults terminates just above the igneous oceanic crust, while the other fault is terminated by a seaward dipping sedimentary package, which could be

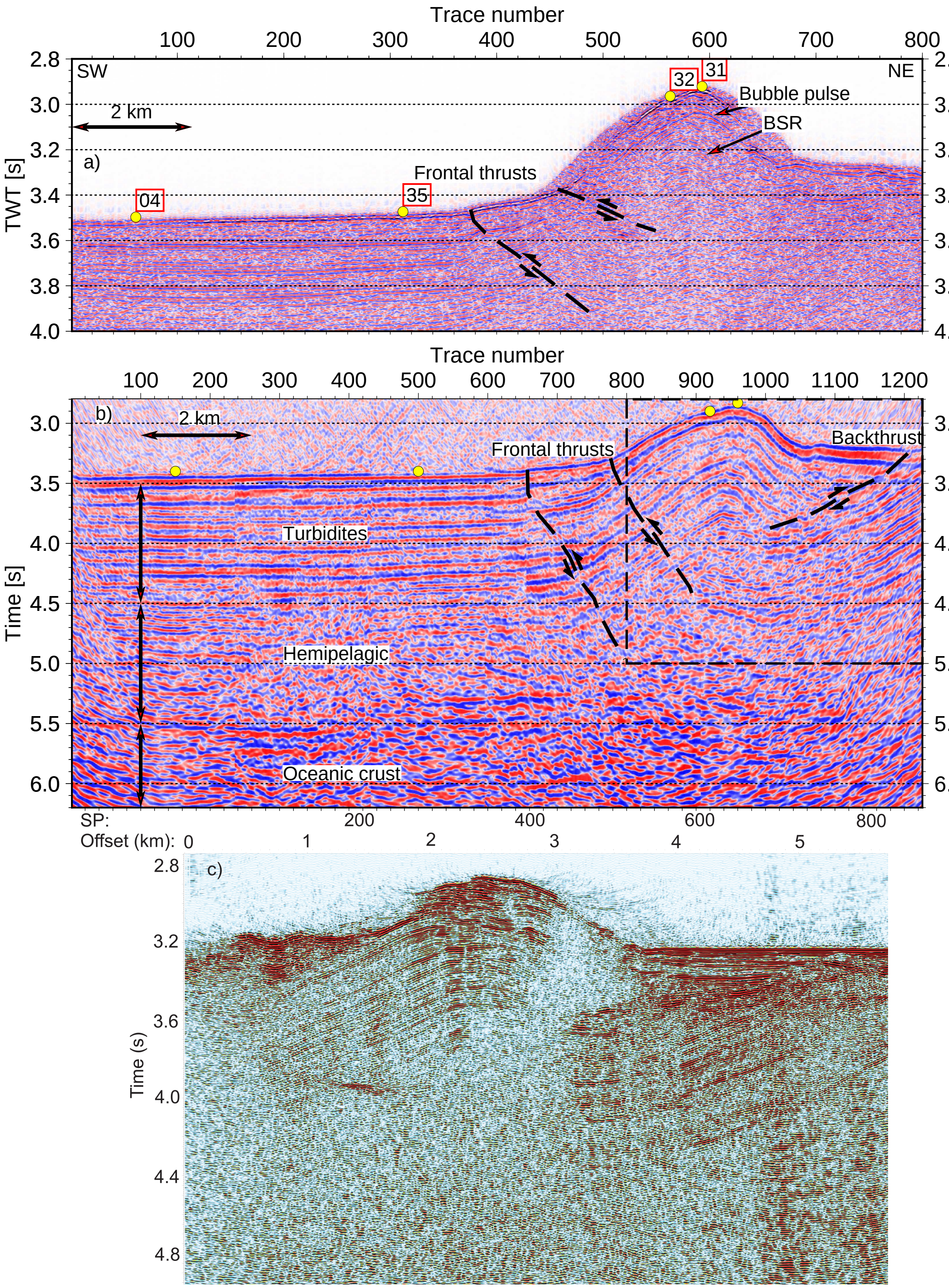

Figure 3.16: Comparision of a) single-channel and b) mirror imaging results along line-1 which passes through OBSs 4, 35, 32 and 31. Yellow circles indicate approximate location of OBS on the seafloor. c) Migrated image of multi-channel seismic line-395 which coincides approximately with line-1 of this survey. Approximate location of (c) is shown as black dashed rectangle in (b).

associated with the past position of the toe of accretionary complex (*Westbrook et al.*, 1994).

Perhaps the most significant feature observed on the OBS migrated image is the thrust-fold pattern identified on the landward side of the ridge crest (Fig. 3.16b). The incoming sedimentary sequence is folded and forms a landward-vergent frontal accreted ridge on top of a thick seaward-dipping sedimentary package. Furthermore, the seaward-dipping package acts as a backstop and the deformation is initiated at the foot of this package. The whole incoming Pleistocene sedimentary sequence is off-scraped rather than subducted, and uplifted above this pre-Pleistocene sedimentary section. Shortening in the overlying layers is accommodated by landward-dipping thrust planes. A backthrust that reaches nearly to the seafloor separates these two accreted sedimentary packages; this indicates that motion along the backthrust has continued until recent times. The thrust-fold pattern on the OBS image is consistent with the structure seen on the nearly coincident multi-channel seismic section (Fig. 3.16c) and on the single-channel seismic section (Fig. 3.16a), although the quality of the SCS section is too poor to make a detailed comparison. As well, these basic structures are even evident in the simple unmigrated NMO-corrected multiple arrivals from individual OBSs (Fig. 3.7a, b). These kinds of mixed-vergent structures are very rare and is observed in $< 0.5\%$ of modern convergent margins (*Gutscher et al.*, 2001).

The dual-vergent structure is observed for the first time on this margin, although small-scale seaward-dipping thrusts are occasionally observed on multichannel lines 89-03, 89-09 (*Spence et al.*, 1991b) and 85-04 (*Davis and Hyndman*, 1989). Variation in vergence is observed along the southern Cascadia margin. Off Oregon and Washington, landward-vergence is characterized by a deep decollement and coherent deformation across a broad continental slope, whereas seaward-vergence is characterized by a shallow decollement and intense deformation along a narrow slope (*MacKay et al.*, 1992). Most of the accretionary margins are characterized by seaward-vergent structures that are caused by high basal friction, whereas mixed-vergent structures are caused by basal shear stress approximately equal to zero (*Gutscher et al.*, 2001; *MacKay*, 1995). Landward-vergent structures are mainly caused by low basal shear stress and an arcward dipping decollement, which are primarily affected by changes in pore-fluid pressure. Multichannel seismic sections from 1985 and 1989 surveys on this margin indicate variations in deformation styles along the margin, which could be probably associated with localized variations in pore-fluid pressure (*Spence et al.*, 1991b). The dual-vergent structure observed here is probably related to horizontal compression associated with subduction and low shear stress resulting from over-pressure. Understanding the physical and mechanical properties of the basal layer at depth in this region is very essential as it has important implications for understanding natural hazards in the Cascadia margin.

3.8 Summary and conclusions

The mirror-imaging or multiple-migration technique is a powerful tool to image sub-surface structures. On a margin-perpendicular line across a frontal ridge on the North Cascadia margin, our results show that the mirror-image produced using a few widely-spaced OBSs is far superior to the single-channel reflection image collected simultaneously, and even better than a nearly coincident multichannel reflection image. The mirror-image is lower frequency than the reflection images, but it provides structure down to much greater depths (to the base of the sedimentary column on the incoming oceanic plate, at 3 km beneath the seafloor) and with much greater continuity. Our results also indicate that an OBS can image up to 5 km on either side of its seafloor position, in water depths of 2200 – 2600 m, and hence an OBS spacing of 5 km is sufficient to provide a two-fold migration stack. Furthermore, in our frontal ridge environment, the multiple migration image obtained using just the hydrophone component alone is equivalent to the image obtained using downgoing waves above the seafloor, which requires additional processing.

The high-quality multiple-migration image enables us to interpret structures not previously seen on the North Cascadia margin. Landward-dipping frontal thrusts are observed that are associated with a landward-vergent frontal accreted ridge. A backthrust that reaches up to seafloor is imaged, which probably indicates that the motion along this thrust has continued until recent times. A dual-vergent structure is observed for the first time on this margin, which could be related to horizontal compression associated with subduction and low basal shear stress resulting from over-pressure.

Chapter 4

Full waveform inversion of MCS data

A version of this chapter is intended for publication in Canadian Journal of Earth Sciences as: "Seismic velocity and attenuation structure beneath the Vancouver Island continental shelf using frequency domain visco-acoustic fullwaveform inversion of multichannel seismic data" by Subbarao Yelisetti and George D. Spence.

Author contribution: The author of this thesis is responsible for design of the research program, analysis of the data and composition of the manuscript. My supervisor, George Spence, provided guidance with the research plan, feedback and editorial supervision throughout the developement of this manuscript.

4.1 Introduction

At the Northern Cascadia margin off Vancouver Island, the Juan de Fuca plate is subducting beneath the North American plate at a convergence rate of 46 mm/year. As a result, sediments are scraped off from the downgoing plate and attached to the continental plate to form the accretionary wedge (*Hyndman et al.*, 1990). In southernmost Vancouver Island, major westerly trending faults partition the crust into two narrow zones the marine sedimentary Pacific Rim terrane and the ocean basaltic Crecent terrane, which were accreted to the margin in late Eocene time, between 55 and 42 Ma ago (*Hyndman et al.*, 1990). The Tofino forearc basin on the Vancouver Island continental shelf has a maximum width of about 60 km and a length of $\sim$ 200 km (Fig. 4.1) and contains up to 4 km of sedimentary rocks, which lie above the accretionary wedge basement, the Crescent terrane and the Pacific Rim terrane (*Hyndman et al.*, 1990). With up to 3 km of Miocene to Recent mudstones and minor sandstones, the Tofino basin comprises Paleogene to Neogene clastic rocks that have been penetrated by six exploratory wells drilled in the 1960s (*Shouldice*, 1971). Eocene sediments/volcanics were also encountered in four of these wells (*Shouldice*, 1971; *Narayan*, 2003). These volcanics are the source of the Prometheus magnetic anomaly (*Spence et al.*, 1991b). There is a magnetic anomaly high over the Crescent terrane and a low over the Pacific Rim terrane (*Hyndman et al.*, 1990). Beneath the eastern portion of the shelf, seismic reflection data indicate a localized thickening of the Tofino basin sediment section to more than 3 km, and this was interpreted as a fossil trench (*Hyndman et al.*, 1990). As a consequence of the great sediment thickness, a gravity anomaly low is observed over the fossil trench region (*Dehler and Clowes*, 1992).

Subduction of the Juan de Fuca plate beneath the North American plate has been the main tectonic driving force in the growth of the basin structure. The Tertiary strata beneath the continental shelf are relatively undeformed and form a wedge which thickens seaward along the west coast of Vancouver Island to the base of the continental slope. The observed faults, folds and unconformities in the basin indicate that the deformation increases southward from Brooks peninsula at the north end of Vancouver Island (*Tiffin et al.*, 1972). Anticlines and thrust faults which occur beneath the shelf edge are the result of intracrustal compression associated with the subduction process along the margin (*Yorath*, 1980). *Hyndman et al.* (1990) argue that these structures result from high pore pressures arising from horizontal tectonic shortening and fluid expulsion.

A series of multi-channel seismic (MCS) lines were collected across Tofino basin in 1985 and 1989 by the Geological Survey of Canada (Fig. 4.1). Interpretation of seismic reflection profiles, tomographic velocity models and biostratigraphic well data suggest that basement composition has largely controlled deformation of the overlying Tofino basin sediments. On migrated seismic sections, some thrust faults appear to penetrate close to the top of the subducting oceanic crust (*Spence et al.*, 1991b). The amount of displacement along the faults and style of deformation varies along the margin, which indicates localized variations of pore fluid pressure. 2D traveltime tomography of MCS first-arrival times (*Hayward and Calvert*, 2007) suggest that sediment deposition increased more rapidly in the later half of the Tofino basin history. According to this study, the development of the basin is related to the reactivation of

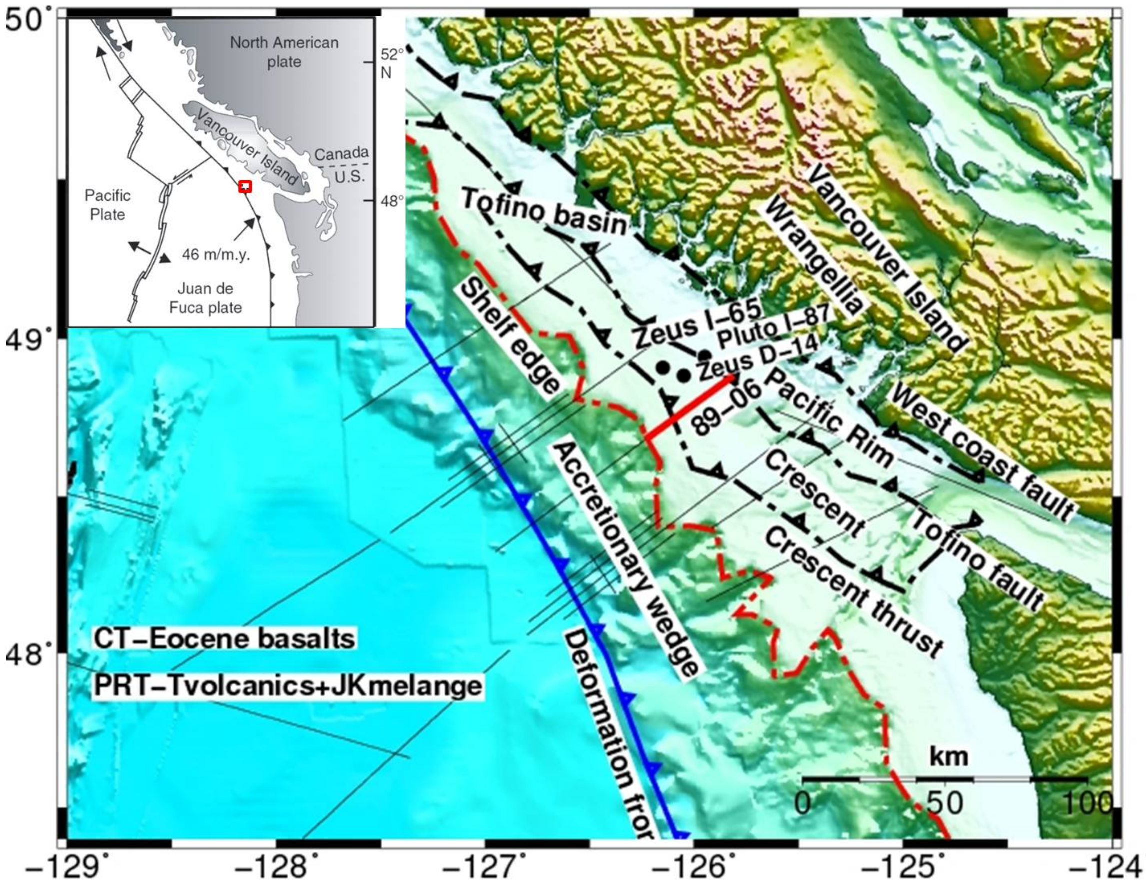

Figure 4.1: Location of the Tofino basin; dashed red line is the seaward margin of the basin. Thick solid red line indicates the location of multi-channel seismic reflection profile 89-06 used in the present study. Black lines indicate the location of other MCS lines on this margin. Black dash-dot lines indicate the surface location of landward dipping west-coast fault, Tofino fault and Crescent thrust. Inset shows the tectonic setting. (CT-Crescent terrane; PRT-Pacific Rim terrane; Solid circles- well locations).

the terrane-bounding Tofino fault. P-wave velocities derived from tomography show that anticlinal folds related to deformation of the accretionary wedge exhibit low velocities at the apex of the fold, whereas folds in sediments which overly the Crescent Terrane show a velocity pattern that more closely mimics the shape of the folds. The lower velocities at the apex of the fold are interpreted as the result of fracturing of older (Late Pliocene), more lithified sediments that contain fluids derived from deeper sediments and the accretionary wedge as opposed to overlying younger (Pleistocene to Holocene) sediments where the low-velocity is due to their lower burial depth.

Here, we apply the 2D frequency domain visco-acoustic full waveform inversion of *Pratt* (1999) to one of the marine MCS reflection lines (89-06, Fig. 4.1) on the

Vancouver Island continental shelf. A time migrated section of this line is shown in Figure 4.2. *Yuan et al.* (1996) applied 1D full waveform inversion to a small number of individual common-reflection-point gathers from several of the 1989 Geological Survey of Canada MCS lines located in the mid-slope region of the margin. Our study is the first 2D waveform tomography application to seismic data on this margin. We show that this technique can resolve significant structural details in MSC data that are not achievable with previously applied methods including 2D traveltime tomography of first arrivals. We also present the imaging challenges encountered while inverting structurally complex, noisy, short offset data devoid of low frequencies. However, the primary objective of this work is to further the study of the upper part of the Tofino basin by quantitatively imaging its structure. In particular, we aim 1) to obtain the detailed seismic velocity and attenuation structure of the Tofino fore-arc basin, 2) to understand the nature of deformation within Tofino basin sediments and 3) to understand the relationship between Tofino basin sediments and the underlying Crescent terrane and Pacific Rim terrane.

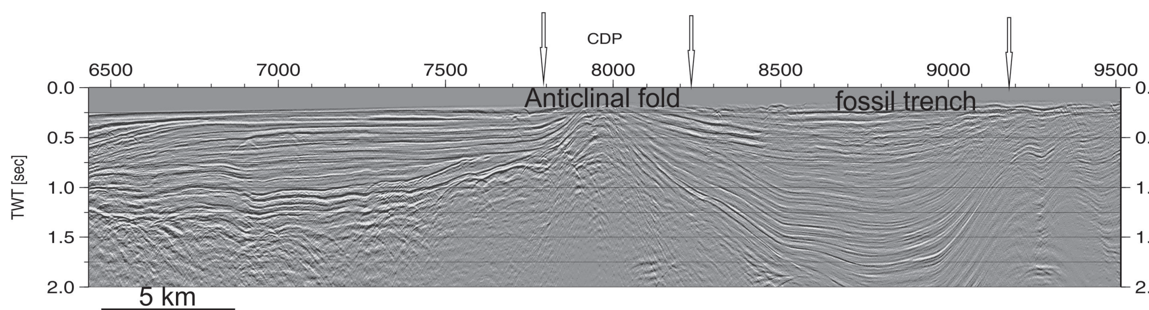

Figure 4.2: Time migrated seismic reflection section of line 89-06. Arrows indicate projected locations of 3 exploration wells shown in figure 4.20.

4.2 Theory

The first step in the application of full waveform inversion is the determination of a very good starting velocity model. We obtained this model by traveltime tomography of first arrivals on individual shot gathers, similar to the method applied by *Hayward and Calvert* (2007). However, we utilized the tomographic techniques of *Zelt and Smith* (1992) and *Zelt and Barton* (1998), rather than that of *Aldridge and Oldenburg* (1993) applied by *Hayward and Calvert* (2007). Thus, we first present an overview of the traveltime inversion methodology, and subsequently discuss some of the key theoretical considerations in the full waveform inversion method of *Pratt* (1999).

4.2.1 Traveltime tomography

The grid model (*Zelt and Barton*, 1998), which uses only first arrivals, is well-suited to use a large number of shot gathers, since it is a much more automated process than the block model (*Zelt and Smith*, 1992), where the structure must be specified layer-by-layer and reflector-by-reflector. The problem is that the automated approach in the grid model is not so suitable where there are rapid lateral changes in velocity (Fig. 4.3). In our initial application of the grid model, the inversion process would find the minimum traveltime residuals, but the residuals were still very large in these regions of large velocity change. By using the block model in a combined forward and inverse modelling approach, the flexibility in the model parametrization allowed us to obtain a better fit in these regions of high residuals (Figs. 4.4, 4.5). The block model was then gridded in a format appropriate for the grid model, and then used as a refined starting model in a final regularized inversion that used the full dataset of traveltime observations. The forward modeling is node-based while the inversion is cell-based. The regularization is a jumping method in which the constraints are applied to the model perturbation with respect to the starting model (block model). We carefully chose the smallest, flattest and smoothest perturbation constraints, which varied with depth. The model was held fixed above the seafloor bathymetric interface and new ray paths were calculated for each iteration based on the starting model.

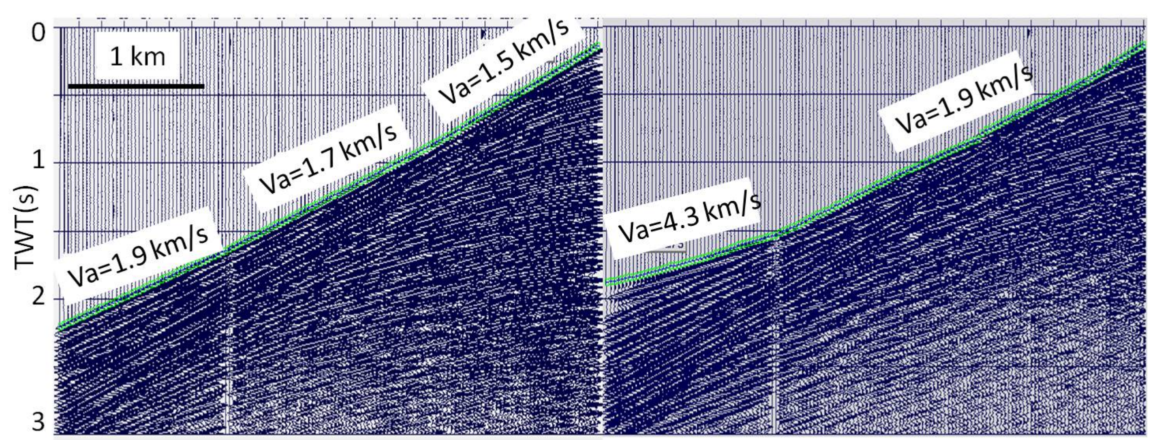

Figure 4.3: Shot gathers near CDP location 6710 and 7550 (see figure 4.2 for CDP locations) showing rapid lateral variation in apparent velocity. Green rectangles indicate travel time picks.

In traveltime tomography, the inversion is carried out by finding a model that predicts the measured arrival times, usually by iterative ray trace methods. The non-linear relation between travel time (T), velocity (v) and the slowness (s) is given by the Eikonal equation, which is a simple equation to predict the travel time for a given ray path (Γ) as the seismic energy propagates along rays.

$$T = \int_{\Gamma} \frac{1}{v}\, dl = \int_{\Gamma} s\, dl \tag{4.1}$$

In the forward problem, travel times are computed using a reference velocity model. The inverse problem tries to minimize the difference between the observed travel times (t_{obs}) and calculated travel times (t_{cal}) by updating the reference velocity model. The relation between the data residual vector (δt) and model perturbation (δm) is given by the following linear equation (*Hole*, 1992):

$$A\, \delta m = \delta t \tag{4.2}$$

where A is the partial derivative matrix of travel time with respect to the model parameters along the ray path, and

$$\delta t = t_{obs} - t_{cal} \tag{4.3}$$

However, the solution of an inverse problem is highly non-linear and is non-unique as the data contain errors and the problem is under-determined. This is controlled by regularizing the solution. Regularisation stabilizes ill-conditioned and singular inverse problems by incorporating prior information about the model in the inversion. Prior information can consist of estimates of model parameters or their derivatives, or can reflect the types of solution desired. The final solution is obtained by minimizing the objective misfit function (Φ) with respect to the model vector (m) as follows (*Zelt and Barton*, 1998):

$$\Phi(m) = \delta t^T C_d^{-1} \delta t + \lambda [m^T C_h^{-1} m + S_z m^T C_v^{-1} m] \tag{4.4}$$

where C_d is data covariance matrix and C_h and C_v are horizontal and vertical roughening matrices, respectively; S_z determines the relative importance of maintaining vertical versus horizontal smoothness. λ is the trade-off parameter that controls the relative importance of data and prior information, and provides the model with the least structure for a given data misfit. In general, we choose λ to give misfit to data of $\chi^2 = N$ (expected misfit for Gaussian errors). This applies the prior information subject to fitting data to a statistically appropriate level.

4.2.2 Full waveform inversion

Waveform tomography represents a more advanced approach, in which the whole waveform is used in the reconstructions. In general, the approach of waveform tomography represents an attempt to fully account for the complex interaction of the propagating wave and the target.

In the present study, traveltime tomography uses only first arrivals whereas waveform tomography uses reflections, refractions and diffraction events. Therefore, traveltime tomography is fundamentally limited in resolution and waveform tomography restores the missing resolution of traveltime tomography (*Williamson*, 1991; *Williamson and Worthington*, 1993). The resolution is of the order of first Fresnel zone width in traveltime inversion whereas it is of the order of wave length in waveform inversion. The high resolution comes from the fact that it uses not only the first arrivals, but also secondary arrivals.

We used the 2-D frequency domain visco-acoustic waveform tomography approach (*Pratt*, 1999). In the forward modeling, we compute the synthetic seismograms using the following frequency domain acoustic wave equation (constant density).

$$\nabla^2 u(x,\omega) + \frac{\omega^2}{c^2(x)}\, u(x,\omega) = -f(x,\omega) \tag{4.5}$$

where u is the wavefield vector (pressure or displacement) and f is the source vector. ω is the angular frequency and c is the wave velocity, which can be complex valued if the medium is attenuating.

The above wave equation is solved using a frequency domain finite difference method. The equation can be represented as follows.

$$S\,u = f \tag{4.6}$$

or

$$u = S^{-1} f \tag{4.7}$$

where S is a differencing matrix or impedance matrix.

The non-linear Born scattering equation which describes the interaction of the

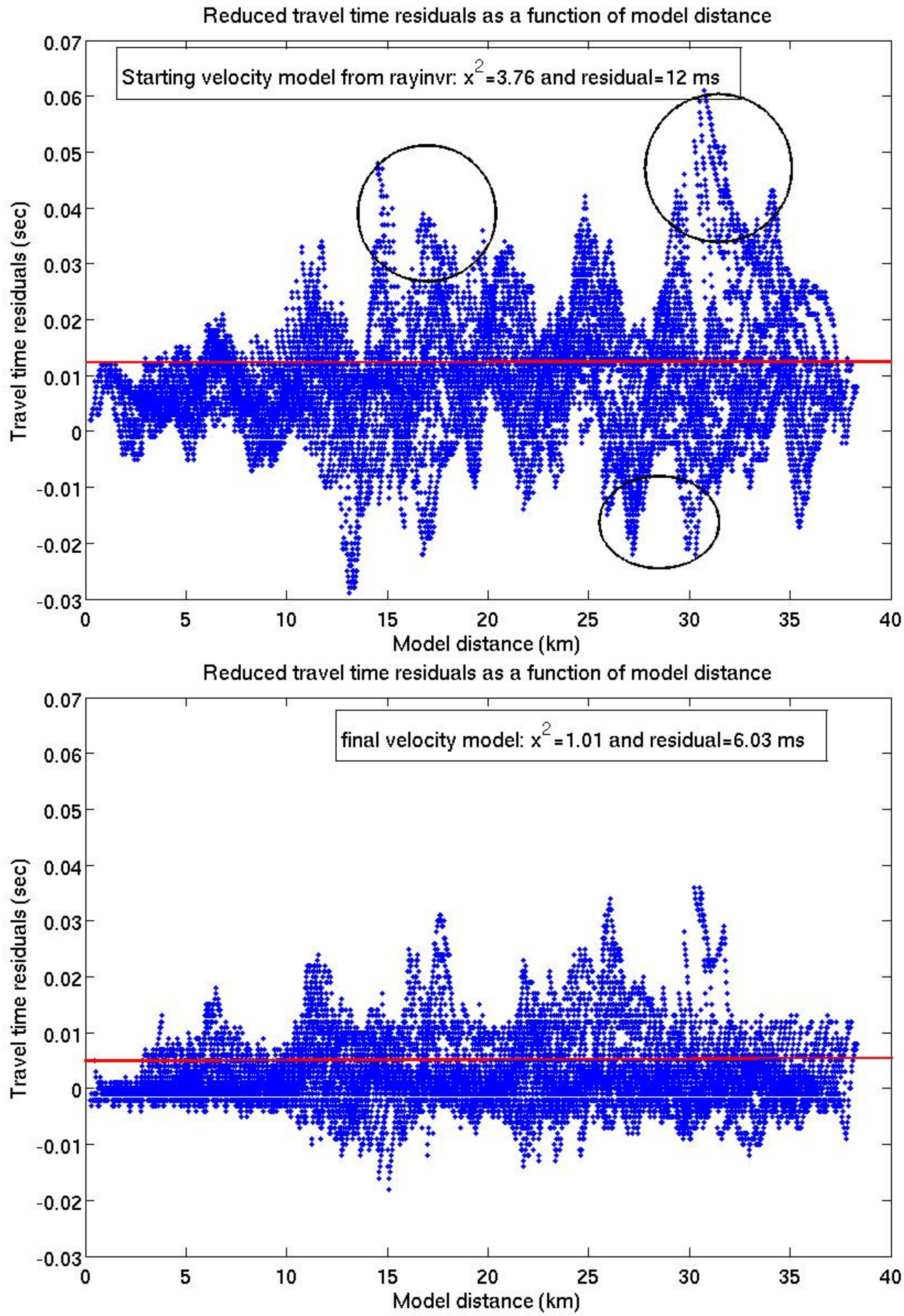

Figure 4.4: Travel time residual using block model (above) and fine grid model (below) showing the improvement in residuals using grid model. Red line indicates the average residuals. Black circles indicate high residuals in block model that were improved using grid model.

source wavefield with the scattering medium while traveling to the receiver is given by *Wu and Toksöz* (1987):

$$U(r_s, r_g) = -\omega^2 \int_V \delta s(r)\, G(r, r_s)\, G(r, r_g)\, dr \tag{4.8}$$

where $U(r_s, r_g)$ is scattered wavefield, ω is angular frequency, δs is scattering potential and G is free space Green's function.

The inversion modelling minimizes the misfit between observed waveforms and forward modeled waveforms by iteratively updating the model. The model perturbation (δm) is related to the data misfit (E) by the following equation (Newton method):

$$\delta m = -H^{-1} \nabla E \tag{4.9}$$

where H is Hessian matrix which contains the second derivatives of the misfit function. The misfit function is given by the sum of squared data residual errors. However, the Hessian matrix is very huge and often singular. Hence it is very difficult to invert. The conjugate gradient method is one of the most effective methods for the iterative inversion. It ignores the Hessian and uses the gradient of the misfit function directly to update the model as shown below.

$$m^{(k)} = m^{(k-1)} - \alpha^{(k-1)} \nabla E^{(k-1)} \tag{4.10}$$

where k is the number of iterations and α is the step length which is given by

$$\alpha = \frac{|\nabla E_m|^2}{|J \nabla_m E|^2} \tag{4.11}$$

where || represents the Euclidean length of the vectors and the *Fréchet* derivative matrix or the *sensitivity* matrix J is given by

$$J = \frac{\partial u}{\partial m} = -S^{-1} \frac{\partial S}{\partial m} u \tag{4.12}$$

The attenuation is introduced into the model using the complex velocity as a function of frequency and is given by

$$c(f) = c\left[1 + \frac{1}{\pi Q} \ln\left(\frac{f}{f_\circ}\right) - \frac{i}{2Q}\right] \tag{4.13}$$

(*Aki and Richards*, 1980), where f is the modeling frequency, Q is the quality factor,

c is the model velocity and $f_\circ$ is the base frequency at which no dispersion occurs in the medium.

4.3 Traveltime tomography method

4.3.1 Velocity models

The MCS data used in this study were acquired in 1989 using a 144-channel streamer with maximum offset of 3783 m (*Spence et al.*, 1991a). The shot spacing was 50 m and the airgun array (128.15 L) was towed at a depth of 10 m. The data were recorded for a time of 14 s at a sample interval of 4 ms. Preliminary results of MCS data processing are presented in Appendix C.

First arrival offsets are observed out to maximum offset, with maximum apparent velocities typically near 1.9 km/s but locally as large as 4.3 km/s. An example of the data is shown Figure 4.3. A starting model was carefully constructed by first modelling a subset (five shots spaced every 2 km along the model) of the travel times using a ray-tracing approach in a block model with interfaces. Later, travel times from every 5th shot (every 250 m) along the line were used for modeling. A total of 139 shots were placed along the model length, which is 38.5 km. Using the combination of forward modeling and damped-least squares inversion, we achieved a χ^2 of 3.76 and rms travel time residual of 12 ms, respectively (Fig. 4.6a).

The final model (Fig. 4.6b) was obtained in a tomographic inversion of first arrival travel times within a uniform velocity grid with a grid spacing of 25 m. Modelled travel times and observed travel times agreed with a travel time residual of 6 ms, which was equivalent to the picking error. The final fine grid model was subtracted from the block model to obtain the velocity anomaly model (Fig. 4.6c). Velocity perturbations as large as ± 240 m/s were observed in the final model (Fig. 4.6c).

Figure 4.4 shows the travel time residual plots using both the block model and the fine grid model. The large travel time residuals observed at $15-20$ km model distance and at $26-36$ km model distance (indicated by black circles in Fig. 4.4) from the block model were reduced using the fine grid model (Fig. 4.4, 4.5). Observed and calculated travel times using these two models were plotted as a function of model distance (Fig. 4.5a, b). Arrows in Figure 4.5 indicate significant improvement in travel time residuals for the fine grid model relative to the block model.

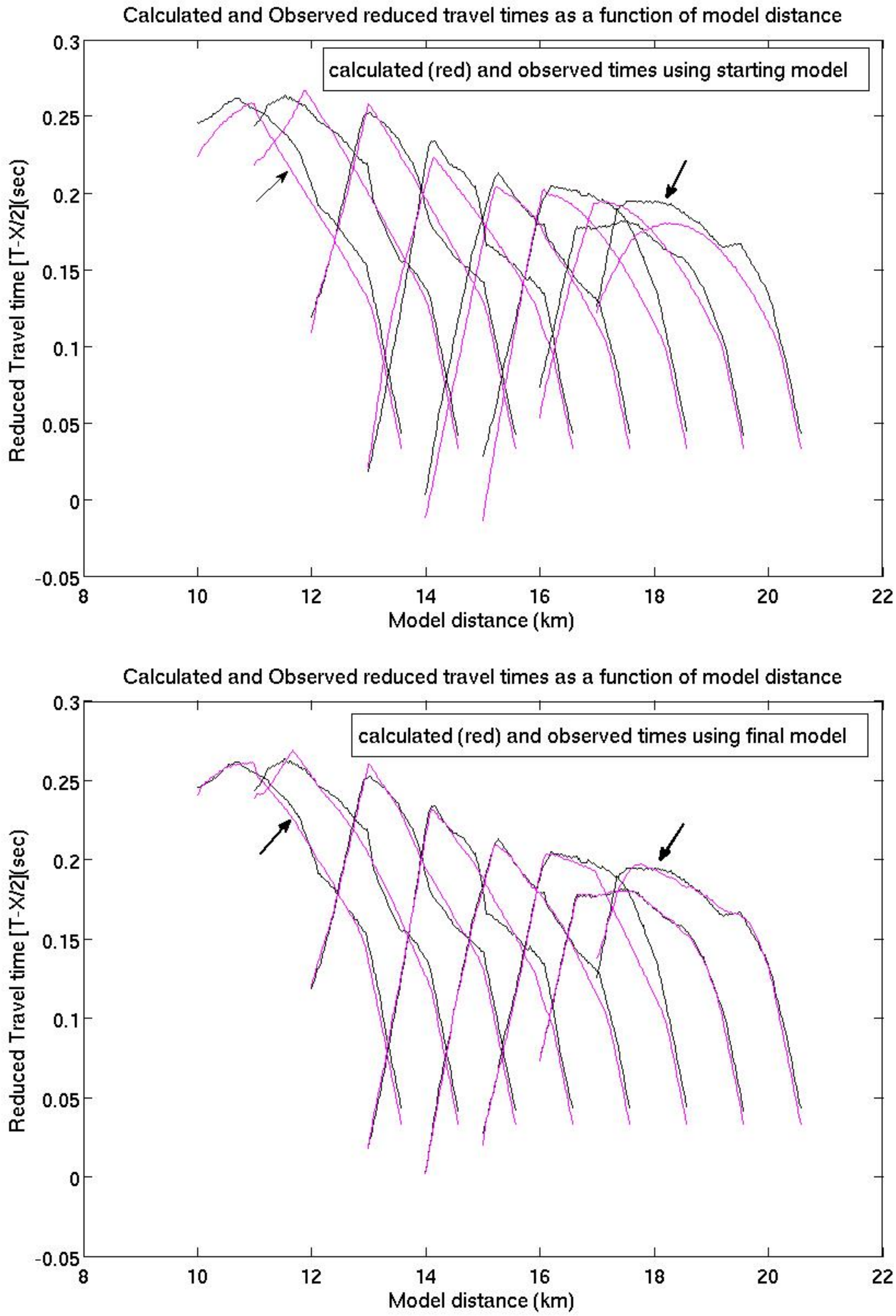

Figure 4.5: (a) Calculated and observed travel times using block model (above) and fine grid model (below) over model distance $8 - 22$ km. Black arrows indicate the locations of improvement in residuals using grid model.

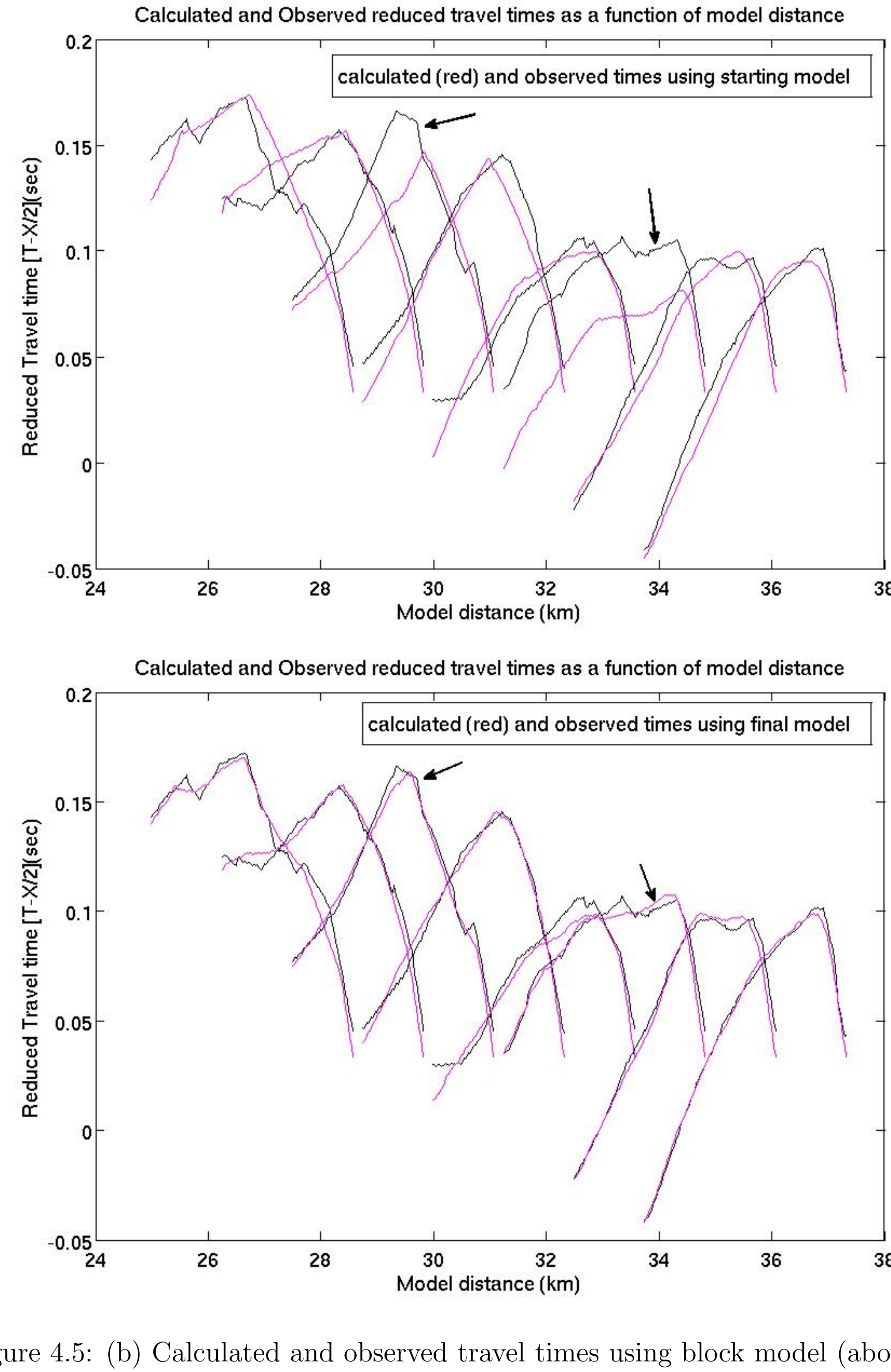

Figure 4.5: (b) Calculated and observed travel times using block model (above) and fine grid model (below) over model distance $24-38$ km. Black arrows indicate the locations of improvement in residuals using grid model.

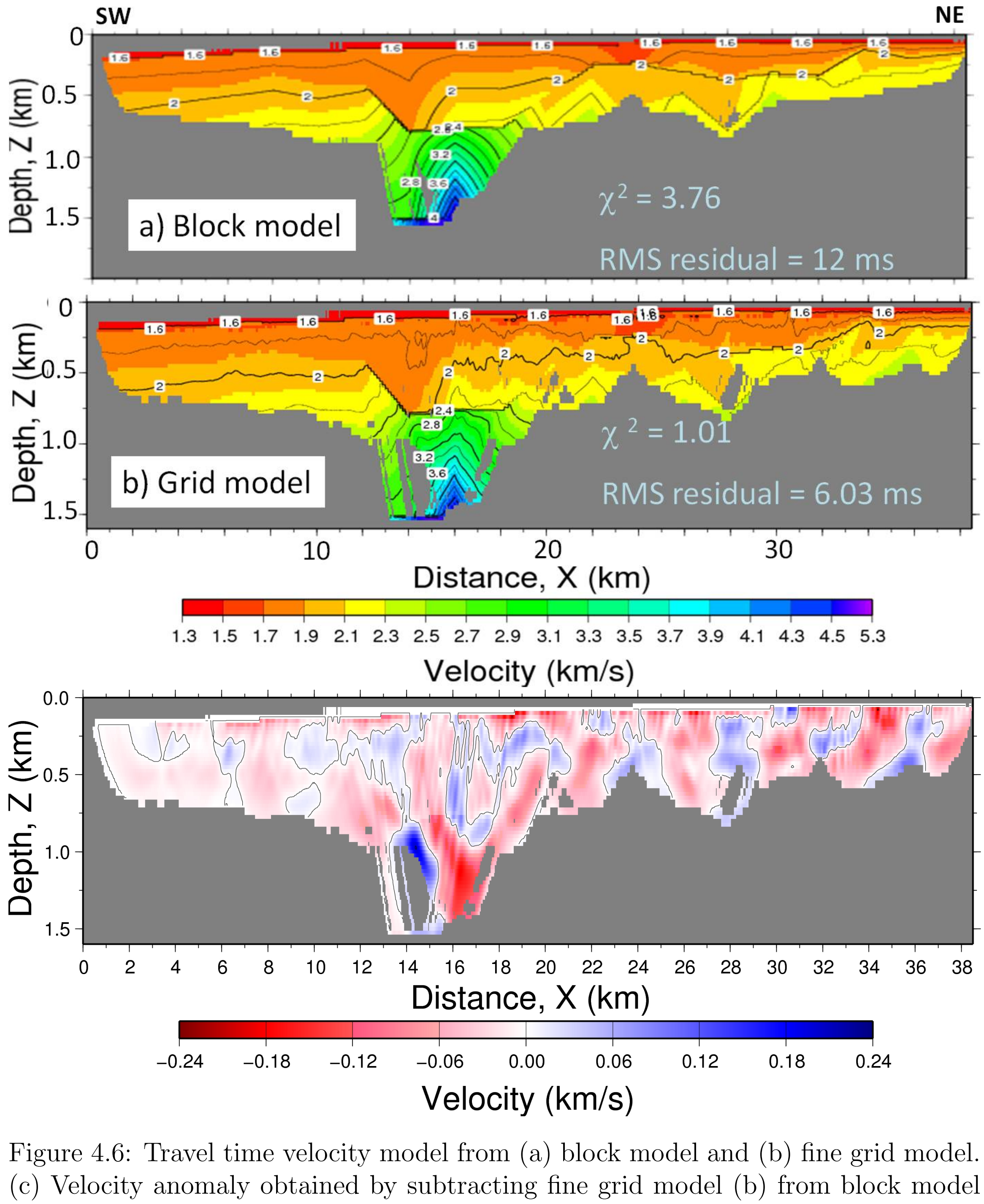

Figure 4.6: Travel time velocity model from (a) block model and (b) fine grid model. (c) Velocity anomaly obtained by subtracting fine grid model (b) from block model (a).

4.3.2 Corrugation tests

Corrugation tests were done to further assess the lateral resolution of the tomographic fine grid velocity model. We used a constant vertical velocity perturbation of 5% to the final velocity model and constant corrugation widths of 0.5 km, 1 km and 2 km. Then, we traced the rays through the perturbed model and calculated the travel times using forward modeling. With the final velocity model as a starting model, these calculated times were used for inversion to obtain the corrugated velocity model. Perturbations were then calculated by subtracting the final velocity model from the corrugated velocity model. The model was able to resolve structures with a lateral resolution of ~ 1 km to depths of $0.5 - 1$ km (Fig. 4.7). Anomalies of 0.5 km width are resolved only in the near surface (~ 250 m).

4.4 Waveform inversion strategy

We followed a waveform inversion strategy similar to that of *Takougang and Calvert* (2011). A typical shot gather showing the direct arrival, reflections and refractions is shown in Figure 4.8. The corresponding frequency spectrum is shown in Figure 4.9, which indicates the minimum available frequency for inversion of 6 Hz.

The starting velocity model derived from traveltime inversion was used in forward modelling to calculate modelled travel times. These are within $\frac{1}{2}$ cycle of the observed travel times (Fig. 4.10) indicating that the initial velocity model is of sufficient quality to carry out inversion. During the inversion, the starting velocity model was updated by iteratively minimizing the misfit between the forward modeled data and the field data. The gradient is computed by multiplying the forward propagated wavefield with the back-propagated data residual.

Prior to inversion, data preconditioning included low-pass filtering (up to 15 Hz), amplitude scaling to match modelled data with field data and time windowing. The goal of preconditioning is to organise the seismic data in a form that is suitable for waveform tomography. This implies that any aspect of the data that is not predicted by the 2-D acoustic propagation scheme, e.g. shear waves, coherent noise, shot-to-shot energy variations, amplitude discrepancy and bad traces, should be removed or corrected. Furthermore, amplitude variations in real data may arise from acoustic attenuation effects, poor instrument coupling, noise contamination, or elastic effects. Thus, the real data must be pre-processed so that its amplitude versus offset behaviour

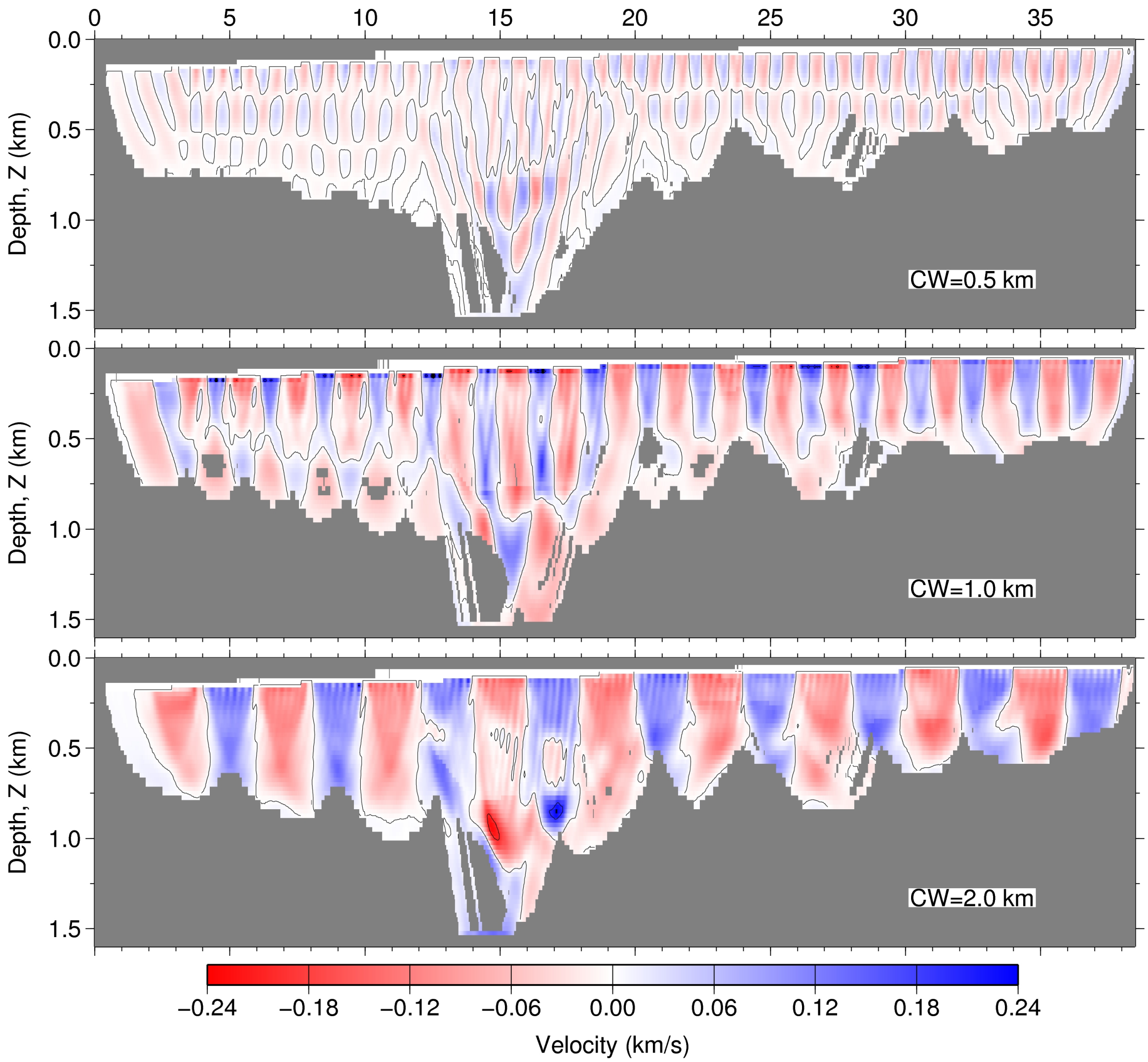

Figure 4.7: Corrugation models for vertical velocity perturbation of ±500 m/s with corrugation widths (CW) of 0.5 km, 1.0 km and 2.0 km.

matches that of the modelled first arrivals. In order to match the amplitudes of both the data sets, we followed a method proposed by *Brenders and Pratt* (2007), in which the observed data are multiplied by a simple exponential-decay function obtained from a linear regression of the log rms amplitudes as a function of offset. After scaling, the observed data are transformed into frequency domain for input to inversion.

4.4.1 Time windowing

A time window is commonly applied to the input data before extracting the frequency domain data. The main purpose of time windowing is to provide the algorithm at the

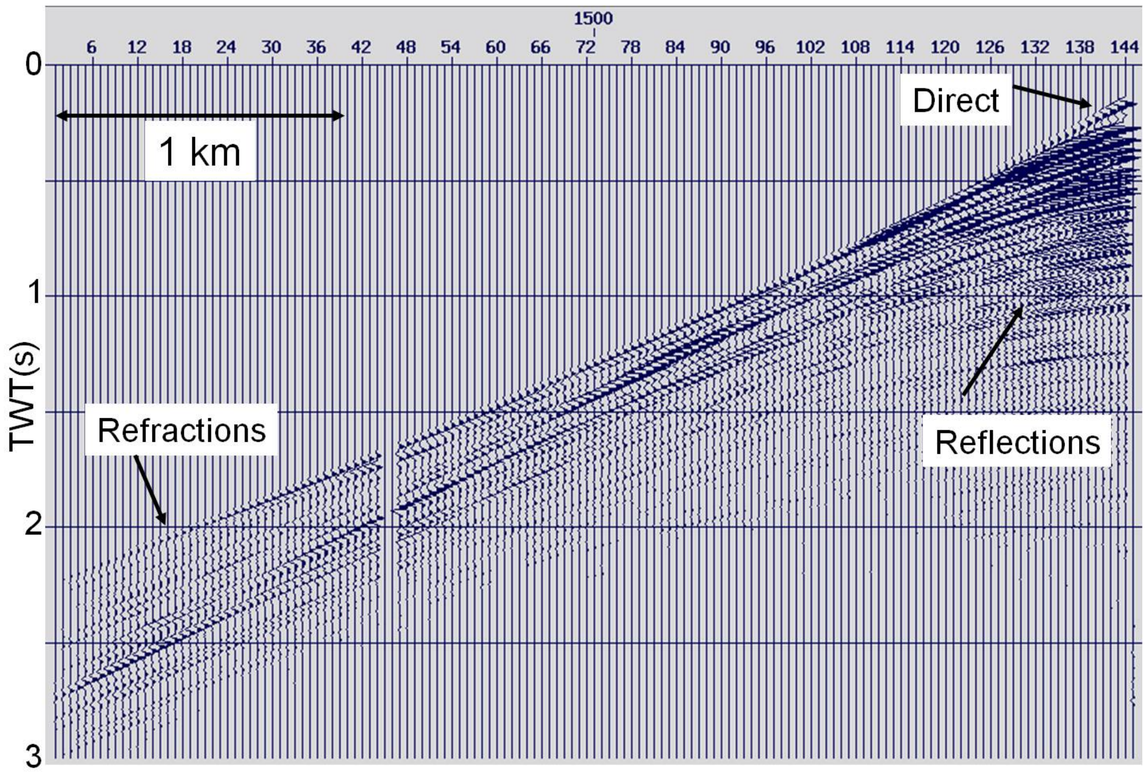

Figure 4.8: Raw shot gather 1500 (corresponds to model distance 4 km) showing the direct arrival, refraction and reflection events. Time window of 2 s after the first arrival is chosen for inversion.

early stage of the inversion with data that favor the contribution of first arrivals, direct and refracted energy, and exclude late arrivals, multiples and scattered energy that originate from outside the imaging plane. Early arrivals have a greater contribution to the reconstruction of low wavenumbers, and thus help to stabilize the inversion. The window size can be increased in the later stages of the inversion to include late arrivals (e.g., *Brenders and Pratt*, 2007). The choice of time window will influence the frequency interval used in the inversion. We used a window size of 2 s after the first arrival with maximum modelled time set to 2.5 s at a sample interval of 4 ms.

4.4.2 Time domain source signature

The source wavelet can be estimated using the procedures outlined in *Pratt* (1999) if it is not known prior to the inversion. The source signature is usually not updated while inverting for a new velocity model. The initial source wavelet was obtained from source inversion using the starting velocity model and a spike wavelet. The

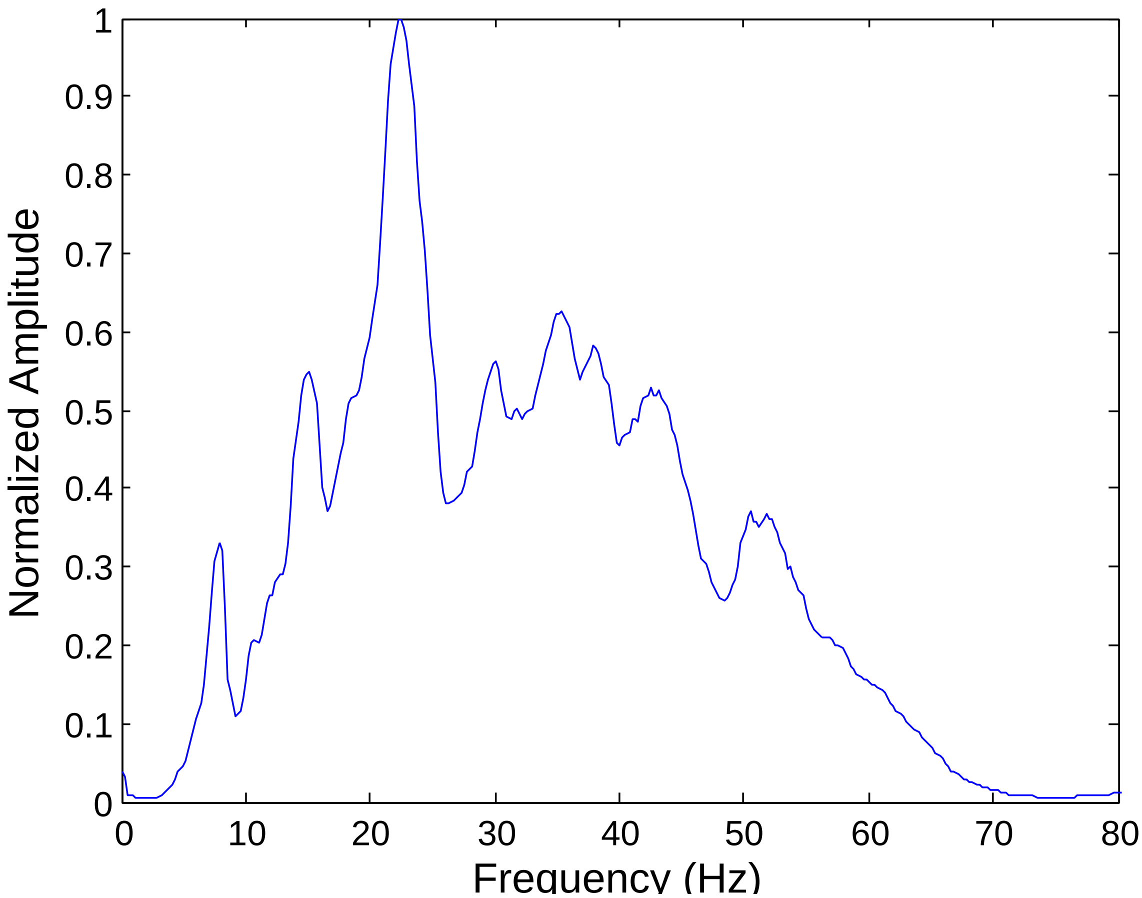

Figure 4.9: Amplitude spectrum corresponding to the shot gather shown in figure 4.8. Starting frequency of 6 Hz is used for inversion.

uniformity in estimated source signature (Fig. 4.11a) from shot-to-shot indicates the quality of the starting velocity model. For our final inversion we used the averaged source signature over all shots (Fig. 4.11b).

4.4.3 Frequency selection

There are currently no well-defined criteria for choosing frequencies in waveform tomography. The general methodology is based on the Nyquist sampling theorem (e.g., *Pratt et al.*, 2005). A frequency interval $\Delta f = \frac{1}{T_w}$ is needed to describe the data within the time window T_w. The spectrum of all frequencies within this interval for which the amplitudes are non-zero needs to be sampled. Frequencies within the spectrum are inverted sequentially rather than simultaneously, starting from low to high (*Takougang and Calvert*, 2011).

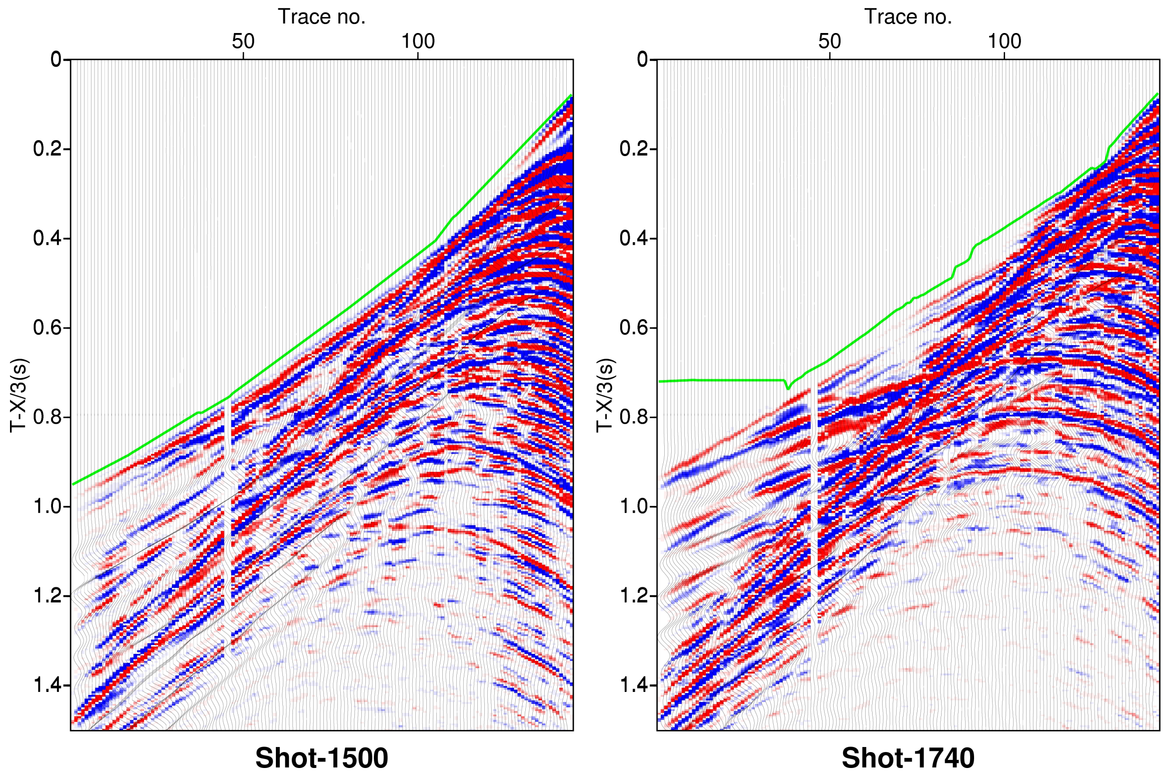

Figure 4.10: Raw data (colour) and synthetic data (wiggle) for shot 1500 and 1740 showing the match of first arrivals within half a wavelength. Synthetic data are calculated using the final traveltime inversion velocity model. Travel time picks (green line) are plotted for comparision.

Inversion was applied for a total of 21 frequencies between $6-14$ Hz with 0.4 Hz interval and five iterations per frequency. These frequencies were chosen based on the Nyquist sampling criterion to avoid aliasing and time wrap-around effects. Attenuation is set to zero (Q=infinity) for velocity inversion. We used a grid spacing of 12.5 m in both horizontal and vertical directions, which results in 3081 grid points in the horizontal direction and 161 grid points in the vertical direction. This fine grid interval was chosen based on the dominant frequency in the data, which is ~ 30 Hz. Therefore, the smallest wavelength that can be modelled is 50 m, assuming a minimum model velocity of 1500 m/s. These parameters satisfy the criterion of four grid points per wavelength that is required to obtain 95% accuracy in estimated numerical velocities.

Both amplitude and phase of the source function were updated at each iteration step. The gradient was filtered in the wave number domain using a 2D-bandpass filter in both horizontal and vertical directions. We used values of $0-3$ for K_x and

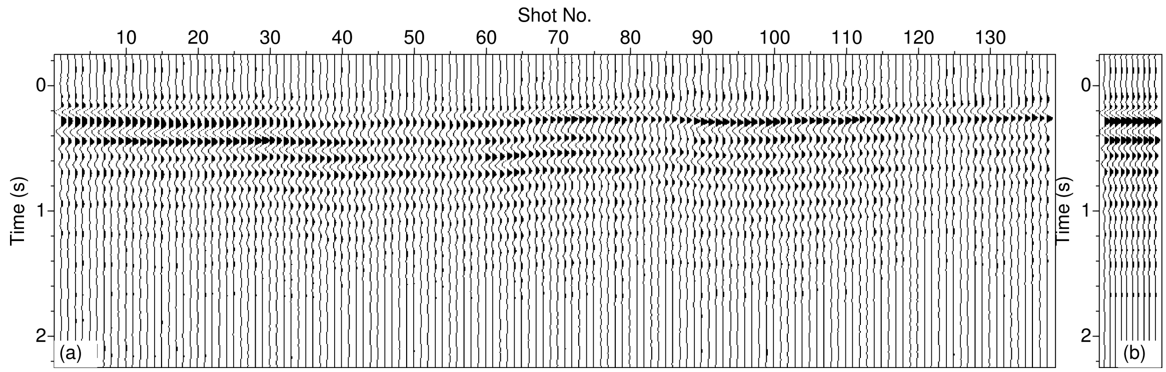

Figure 4.11: a) Source signature obtained using the final travel time inversion velocity model and b) average source signature over all shots.

$1.5 - 14$ for K_z. These numbers are calculated using the minimum model velocity and the dominant frequency present in the data.

4.4.4 Inversion for attenuation

Waveform inversion was applied, initially to obtain the acoustic velocity model. Later, using this velocity model, we simultaneously inverted for visco-acoustic velocity and attenuation models by using a complex velocity as a function of frequency (Eq. 4.13). Unlike acoustic velocity inversion, where the attenuation is set to zero, here we used a homogeneous attenuation model ($Q = 100$) as input with a grid spacing of 12.5 m in both horizontal and vertical directions. All other inversion parameters used here are same as the ones used for acoustic inversion. Furthermore, amplitude balancing of observed and forward modelled data is not required for attenuation inversion, since attenuation structure is recovered from the amplitude losses encountered due to variations in subsurface lithology and structure.

4.5 Properties of velocity model

The final velocity model obtained after $6 - 14$ Hz inversion is shown in Figure 4.12b. This clearly resolves more detailed structures compared to the starting velocity model shown in Figure 4.12a. The velocity perturbations relative to the starting velocity model are clearly shown in the difference model obtained by subtracting the initial model from the final model (Fig. 4.12c). Velocity anomalies as large as ±150 m/s are observed after the final iteration step.

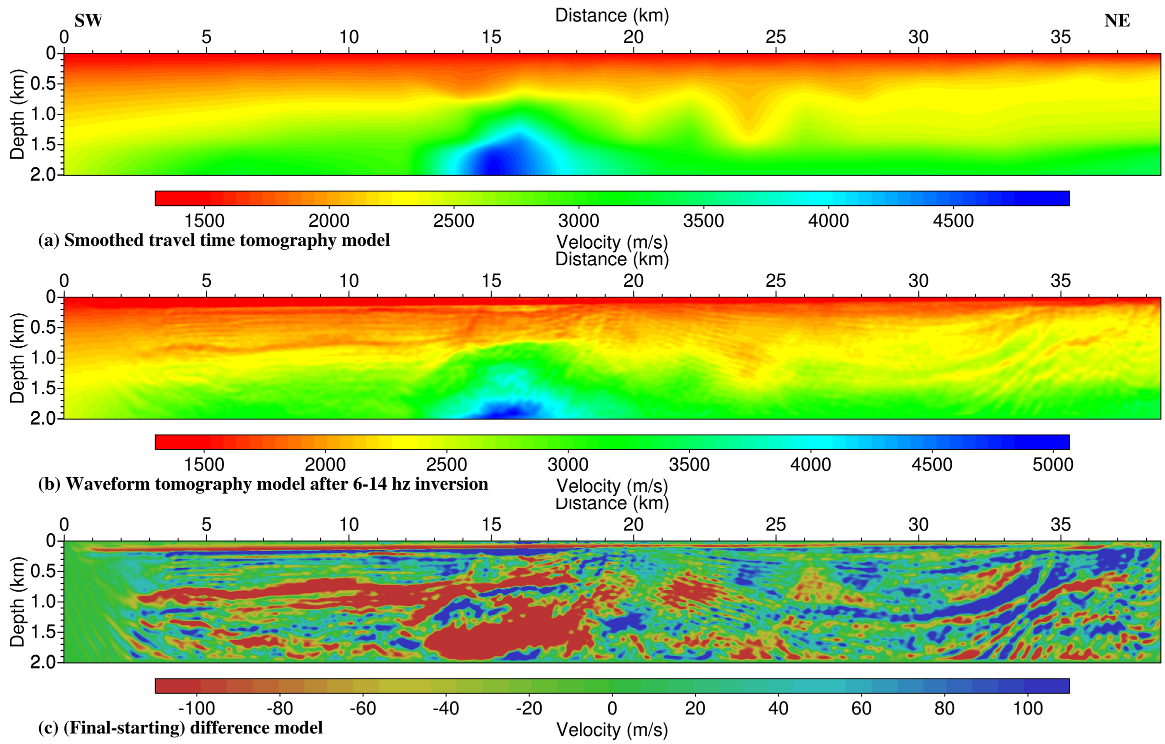

Figure 4.12: (a) Smoothed travel time inversion velocity model used as the starting model for the waveform inversion, (b) waveform inversion model after $6-14$ Hz inversion and (c) velocity anomaly model obtained by subtracting the initial model (a) from final model (b).

Figures 4.13a, b indicates the variation in objective function at each model iteration and relative reduction in objective function with respect to its previous update, respectively. Velocity perturbations as large as ± 150 m/s are observed in the initial stages of the inversion process, which are reduced to ± 10 m/s in the final stages of inversion (Fig. 4.13c).

The final velocity model from full waveform inversion indicates a prominent low-velocity zone between $2-14$ km model distance (Fig. 4.12b), which is not observed in the traveltime inversion model (Fig. 4.12a). To further assess this low-velocity zone, we computed synthetic shot gathers using the final velocity model. A sample of these shot gathers that pass through this low-velocity zone at model distance 6 km, 8 km and 10 km are shown in Figure 4.14. These are compared to observed shot gathers and to synthetic shot gathers from the traveltime inversion model. Clearly, there is a high degree of similarity between the raw shot gathers and those computed from the final velocity model; specifically, as highlighted in Figure 4.14, prominent reflections in the observed shot gathers are present in the final modelled shot gathers,

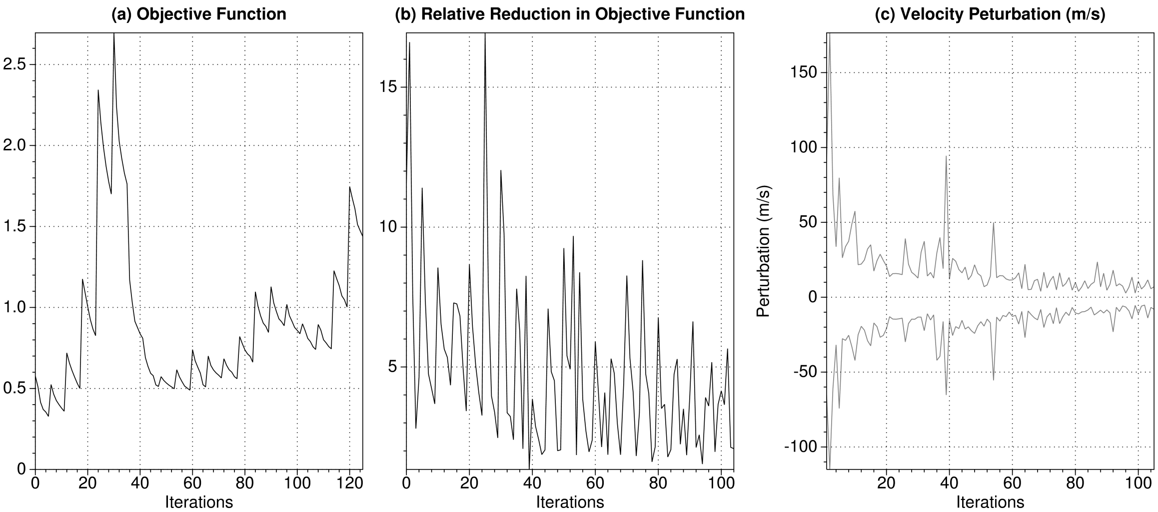

Figure 4.13: (a) Decrease in objective function, (b) relative reduction in objective function and (c) final velocity perturbation. A total of 21 frequencies were used in inversion.

but they are absent from gathers using the starting or traveltime inversion model. We confirmed that much of this reflectivity originates from the low-velocity zone by producing a model in which this low-velocity zone is removed from the final model, by smoothly interpolating structure from above and below the zone. Figure 4.15 shows the synthetic shot gathers with and without the low-velocity zone. The difference between these two sets of synthetic shot gathers are arrivals due to the low-velocity zone, and many of these correspond to reflections in the observed shot gathers. However, there is still a lot of reflectivity in the plot without the low-velocity zone in the near-offset depth range from $1.2 - 1.5$ s (Fig. 4.15b). Presumably, this comes from structure deeper than the low-velocity zone as opposed to the reverberations from the low-velocity zone shown in the difference plot (Fig. 4.15c).

To further assess our final velocity model, synthetic shot gathers are computed at model distance 14 km, 16 km and 18 km, where a prominent high velocity zone is observed at depths below ~ 1.0 km. These shot gathers are compared to observed shot gathers and synthetic shot gathers from traveltime inversion model (Fig. 4.16). Again, there is a high degree of similarity between the observed shot gathers and those computed from the final velocity model. The improvement, relative to the initial velocity model from traveltime inversion, is mainly in the near-offset half of the gathers, where the starting model gathers typically have too few reflections except for an overly prominent strong reflection indicated by yellow arrow in Figure 4.16.

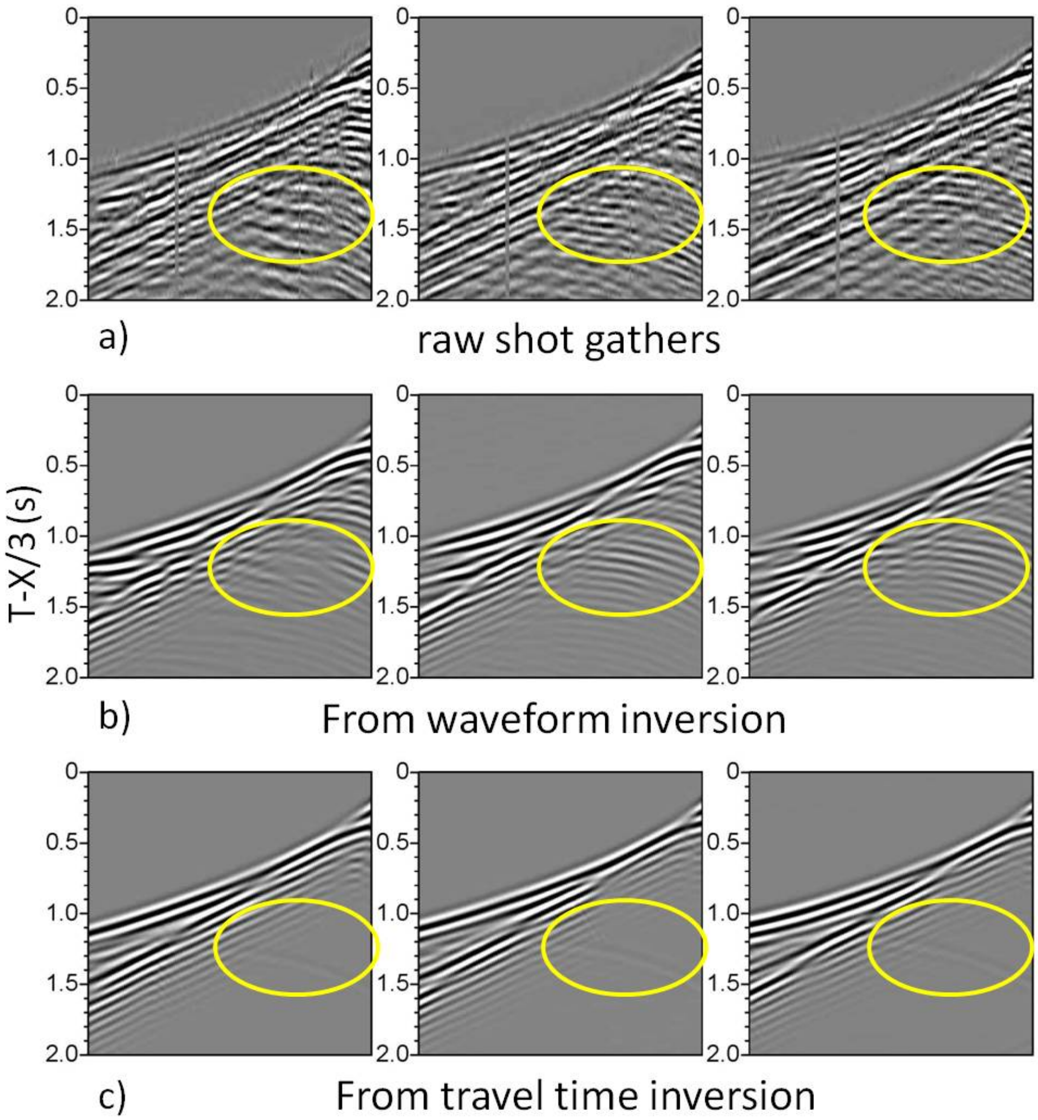

Figure 4.14: Shot gathers through the low velocity zone at model distance 6 km, 8 km, 10 km. a) observed shot gathers b) synthetic shot gathers using FWI velocity model c) synthetic shot gathers using travel time velocity model.

A common offset gather derived using the final velocity model is shown in Figure 4.17b, for offset 3308 m. The observed common offset gather for the same offset is shown in Figure 4.17a. Clearly, there is a high degree of similarity between the raw data and the predicted data. An anticlinal structure near trace number 55 and a shallow sub-basin between trace number 60 and 120 are well imaged.

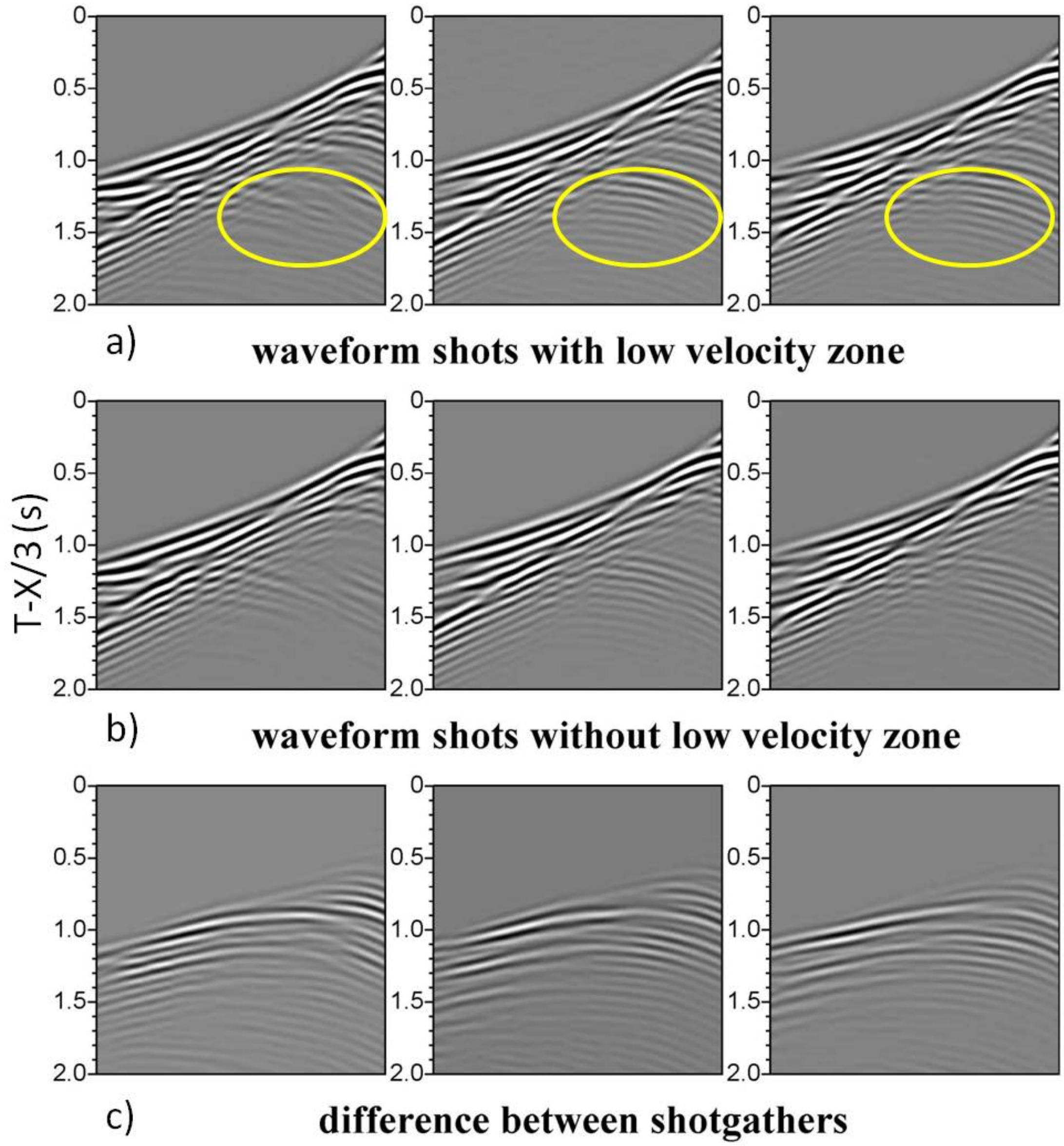

Figure 4.15: Synthetic shot gathers using FWI velocity model at model distance 6 km, 8 km, 10 km. a) with low velocity zone b) without low velocity zone c) difference between (a) and (b).

To see the overall quality of our model, we plotted the observed and modelled data in the frequency domain (Fig. 4.18) corresponding to a frequency of 6 Hz. We can clearly follow the phase information in these two data sets, which is not readily observed in the difference plot (Fig. 4.18c). This indicates that the final

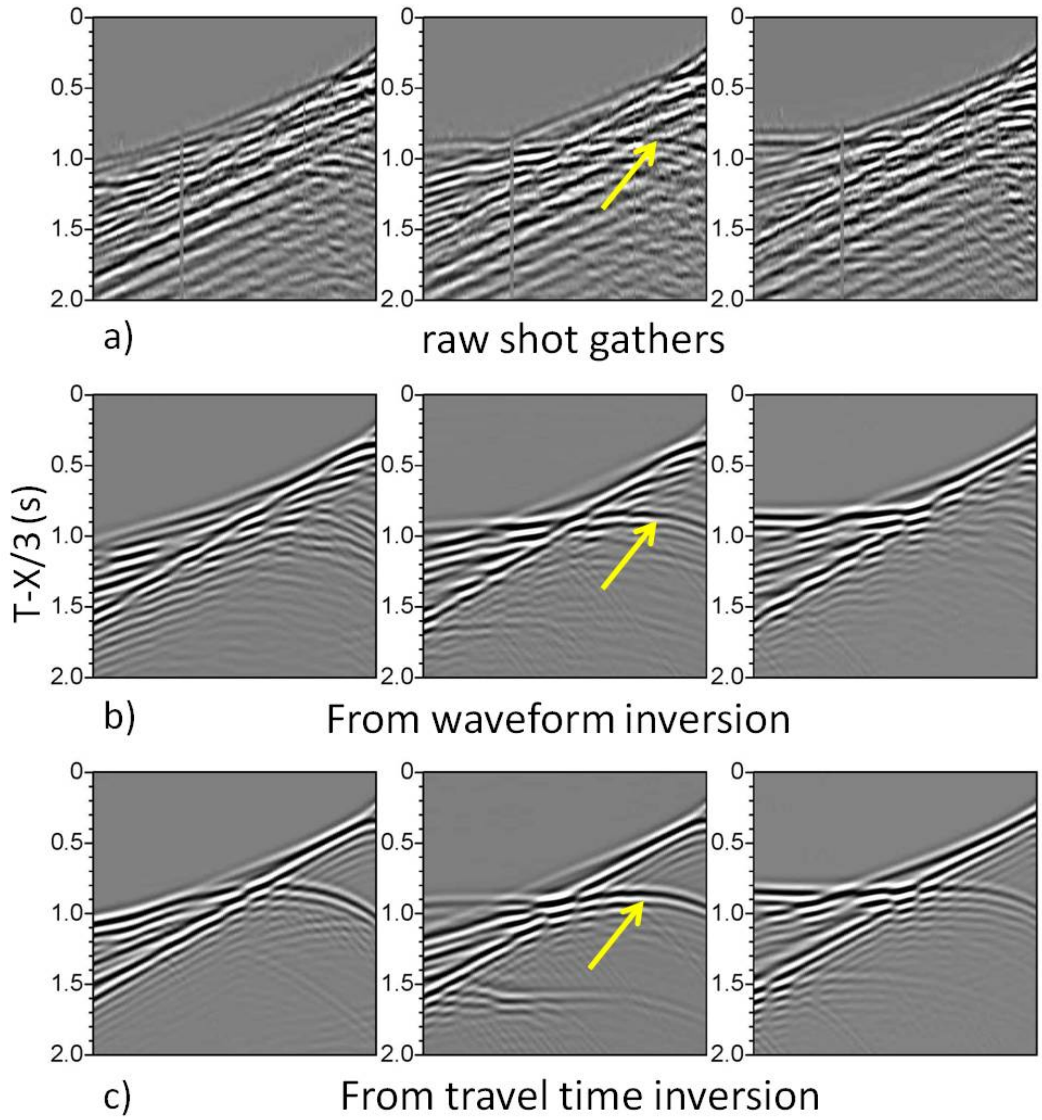

Figure 4.16: Shot gathers through the high velocity zone at model distance 14 km, 16 km, 18 km. a) raw shot gathers b) synthetic shot gathers using FWI velocity model c) synthetic shot gathers using travel time velocity model. Arrow indicates a reflector that corresponds to an apparent velocity of > 4 km/s.

velocity model incorporates most of the phase information that is contained in the data. However, strong amplitude anomalies are observed at the far-offset (receiver numbers $0-50$, Fig. 4.18c), which could be associated with mode conversion and elastic effects that are not included in the visco-acoustic inversion. These amplitude

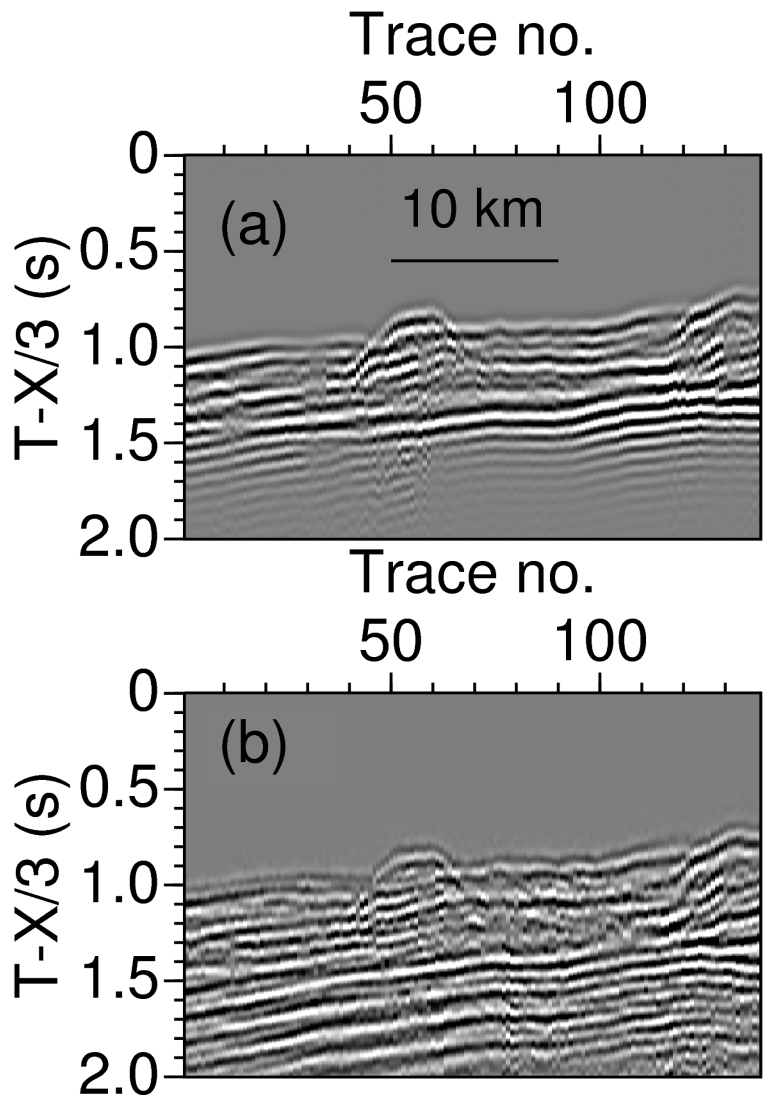

Figure 4.17: (a) Observed common offset gather low pass filtered to 14 Hz at offset 3308 m. Trace spacing is 250 m. (b) Common offset gather from visco-acoustic full-waveform inversion. A high degree of similarity exists between observed and modeled data, particularly in the shallow sediment section above 1.5 s.

anomalies could be improved using visco-elastic inversion.

4.6 Properties of attenuation model

The results of the visco-acoustic velocity and attenuation inversion models are shown in Figure 4.19. Seismic waves propagating into basement structures are strongly attenuated due to heterogeneity and mode conversion effects, which are not included

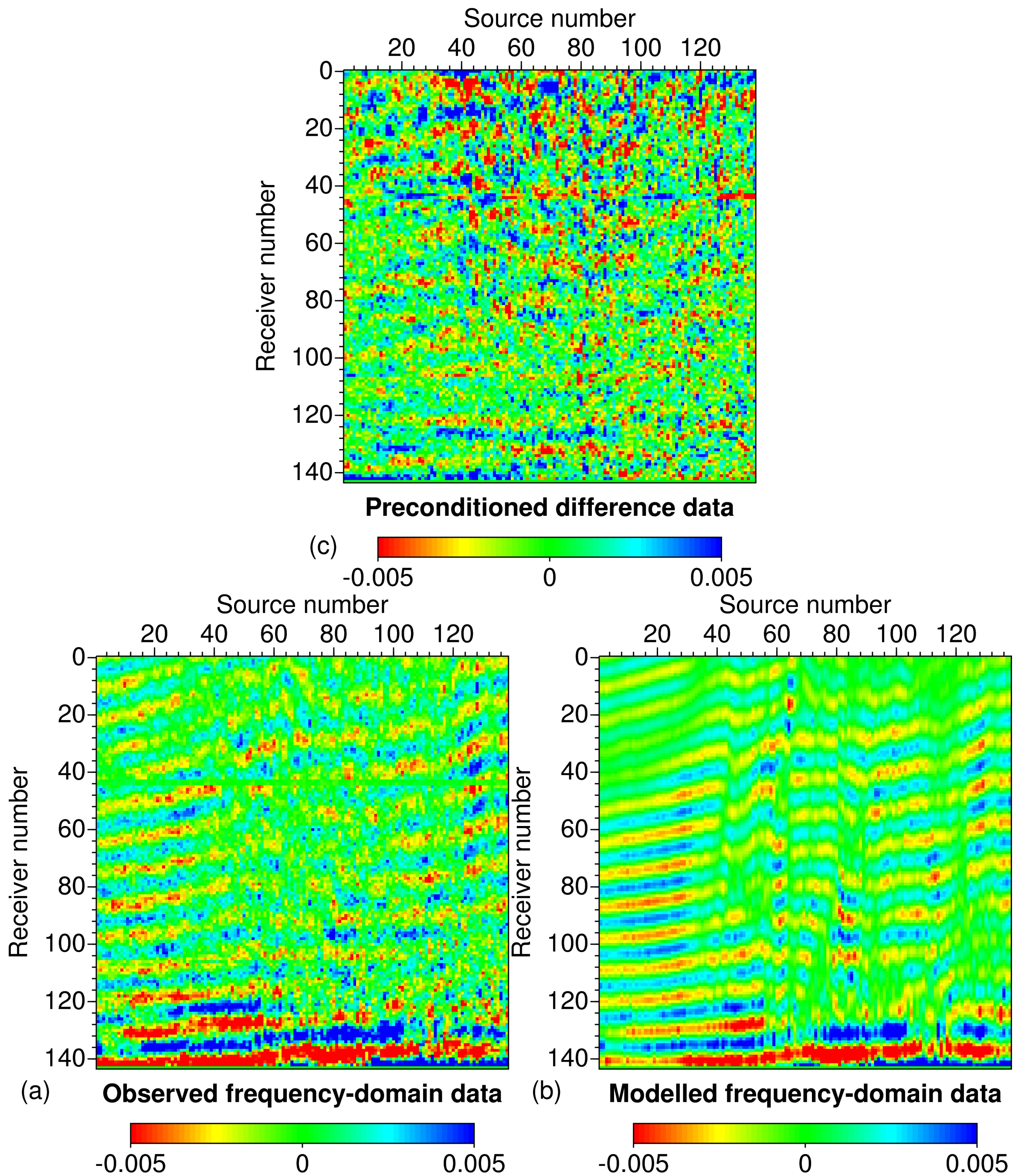

Figure 4.18: Model features in frequency domain. a) Observed data b) modelled data and c) difference between (a) and (b) corresponding to a frequency of 6 Hz. Note that small receiver numbers correspond to the far-offset range.

in the inversion (Fig. 4.17b, 4.19b). Hence the match between the raw data and predicted data is less accurate at depths below 1.5 s (Fig. 4.17b). After visco-acoustic inversion, the attenuation model is greatly improved from the initial homogeneous model with attenuation of 0.01. However, only slight improvements are noticed in the final visco-acoustic velocity model compared to the acoustic velocity model shown in Fig. 4.12b, which indicates that most of the waveform amplitude changes associated with sub-surface structural and lithological variations were incorporated into the recovered attenuation model, and phase changes are incorporated into the recovered velocity model. The final velocity model looks smoother compared to the attenuation model which exhibits greater variation in structure. This may be due to coherent noise, source-receiver coupling, and radiation patterns that affect amplitude of waveforms, but are not related to attenuation (*Takam Takougang and Calvert*, 2012).

4.7 Comparision with drill hole data

Sonic log velocities from three of the wells (Zeus-I65, Zeus-D14 and Pluto-I87) were used in the present study to compare with velocities from waveform inversion models (Fig. 4.20). Zeus-I65 was drilled on an anticline and penetrated through the top of the Crescent terrane, Zeus-D14 was drilled on the flank of an anticline and penetrated through volcanics, while Pluto-I87 was drilled on an anticlinal structure and penetrated through a thin gas bearing sand at depth (*Shouldice*, 1971). However, these wells were projected onto our line by 18 km, 10 km and 11 km, respectively. Highly smoothed log velocities are assigned velocity uncertainities of ± 200 m/s, ± 100 m/s and ± 150 m/s for Zeus-I65, Zeus-D14 and Pluto-I87 velocities, respectively. This large error of ± 200 m/s for a 500 m thick layer with an average velocity of 2 km/s would only result in a two-way travel time error of approximately ± 0.05 s. Comparison of the wells and the seismic profile illustrates that, despite possible errors involved in depth-to-time conversion and the lateral projection of the wells, meaningful correlations may be observed. Results indicate that waveform inversion velocities match reasonably well with the sonic log velocities (Fig. 4.20), down to the maximum modelled depth of ~ 2 km, which indicates the reliability of our inversion results. Seismic velocities at Zeus-D14 well in the depth interval $1.5 - 2.0$ km (Fig. 4.20) appear to be higher at the projected location of the well than at the well itself, which is 10 km from the seismic line. This discrepancy could be related to sub-surface structural variation along the margin.

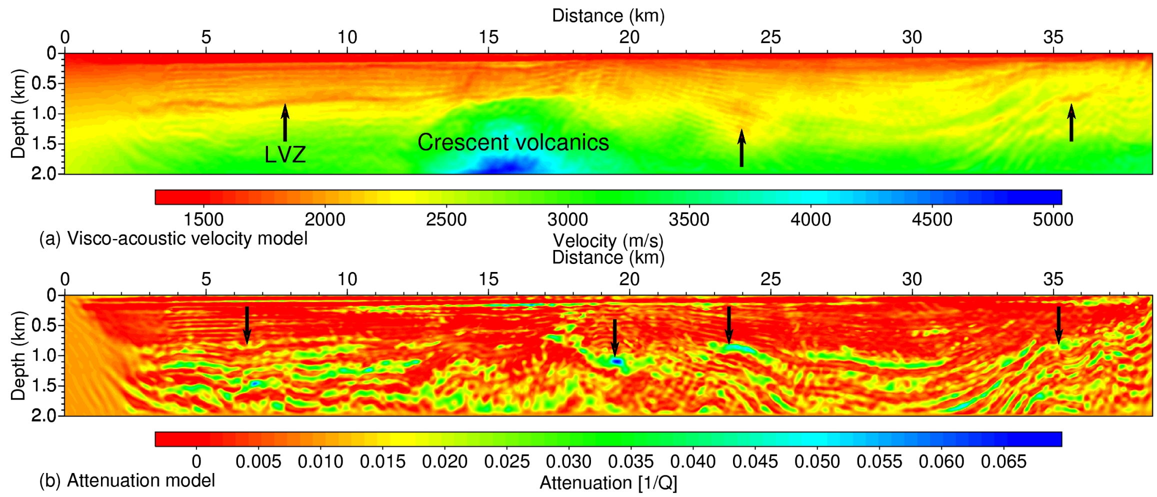

Figure 4.19: (a) Final visco-acoustic FWI velocity model after 6 − 14 Hz inversion and (b) Final attenuation model after 6 − 14 Hz inversion. Black arrows indicate localized zones low-velocity and high attenuation, respectively.

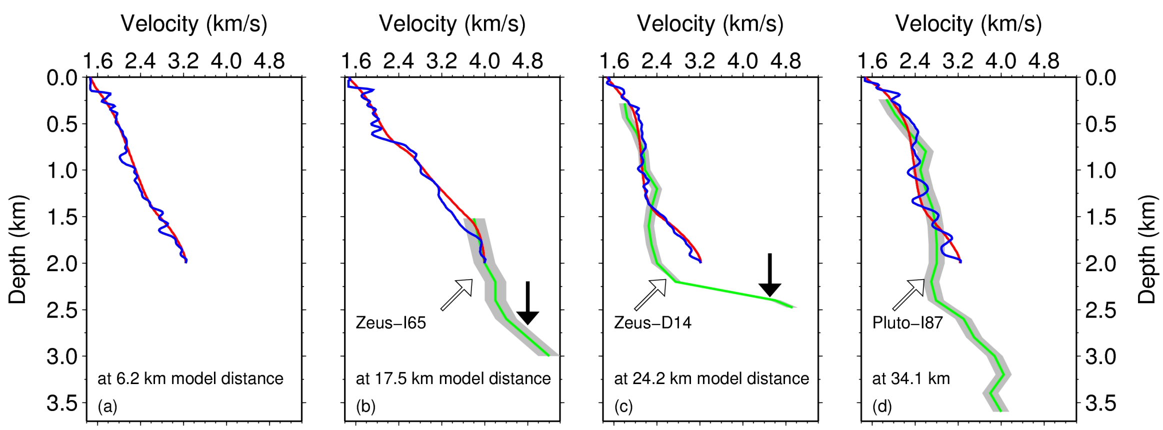

Figure 4.20: 1D-velocity profiles through starting model (red) and final model (blue) along with sonic log velocties (green). Uncertainty in sonic log velocities indicated in gray. Location of the 1D velocity profiles corresponding to sonic logs is shown in figure 4.2 as arrows. Solid black arrows indicate locations where Eocene volcanics were found in the Shell Canada exploratory wells.

4.8 Results and discussion

The final velocity model obtained from visco-acoustic inversion is converted to two-way travel time, assuming vertical incidence rays, for direct comparison with the migrated seismic stack section (Fig. 4.21b). The magnetic anomaly along this line is also plotted (Fig. 4.21a).

4.8.1 Velocity structure

Low-velocity zone (LVZ)

The most prominent feature of the final velocity model (Fig. 4.19a) is the low velocity zone in the southwestern portion of the line. It is observed within the accretionary prism sediments of the Tofino basin. The sediment velocities in this zone are ~ 200 m/s lower than the surrounding velocities at similar depths. The LVZ is observed between $\sim 600 - 1000$ m below seafloor (mbsf) and extends up to ~ 10 km in length. Superposition of the velocity model on the migrated seismic section indicates that this LVZ is associated with a strong seismic reflection (Fig. 4.21b). A LVZ is not observed in the previous studies (*Hayward and Calvert*, 2007) due to resolution limits imposed by conventional processing and traveltime tomography. We speculate that the LVZ is probably a consequence of high pore pressures arising from fluid expulsion from accretionary wedge sediments beneath the Tofino basin (*Calvert and Clowes*, 1991). *Hayward et al.* (2003) also observed a LVZ in association with high fluid pressures at the Barbados accretionary prism based on the vertical seismic profile observations. Shell exploratory wells also show high fluid pressure (lithostatic gradients) in the Tofino basin beneath the continental shelf (*Shouldice*, 1971; *Hyndman et al.*, 1990). Alternatively, the LVZ could be due to over-pressured gas in this potential hydrocarbon environment (*Shouldice*, 1971). Lithology changes associated with a high porosity layer could also cause the observed LVZ.

The LVZ identified here is associated with a gas migrating pathway (indicated by a black arrow in Fig. 4.21b) that reaches up to seafloor at $\sim 14 - 15$ km model distance. Another localized LVZ is identified on the northeast portion of the section at 750 m below the seafloor near $35 - 36$ km model distance (indicated by a black arrow in Fig. 4.19a). It is observed below a broad anticlinal feature and is associated with strong reflections as seen from the seismic section (Fig. 4.21b). This feature is associated with high attenuation (Fig. 4.19b) and may be associated with gas migration from below.

Crescent terrane

A high velocity feature occurs between ~ 12 and 18 km, over which seismic velocities rapidly increase downward from 2000 m/s to 2500 m/s at 750 m depth and then uniformly to 5000 m/s at 2000 m depth (Fig. 4.19a). This is interpreted as the shallowest occurrence of volcanic Crescent terrane. The location of Crescent terrane beneath the shelf is also marked by a magnetic high (Fig. 4.21a and *Spence et al.* (1991b). However, the magnetic high occurs $\sim$ 5 km landward of the shallowest occurrence of the volcanic Crescent terrane. This indicates that the Crescent terrane is highly fractured where it is shallow or otherwise demagnetised. An anticlinal fold or diapiric feature (between 1722 km model distance, Fig. 4.21b) is observed $\sim 2-3$ km landward of the shallowest Crescent terrane, and is likely associated with the landward dipping Tofino fault that forms the top boundary of Crescent terrane.

Pacific Rim terrane

Sediment velocities within the shallow shelf generally increase landwards (Fig. 4.21b). This landward increase may be associated with the general compressional environment at the time of emplacement of the Crescent and Pacific Rim terranes. Lateral changes in velocity are better seen by subtracting the final FWI velocity model from average 1D-velocity profile of final model (Fig. 4.21c). As a specific example, velocities in the northeastern portion of the model (between 32 and 38 km model distance) are about $\sim$ 600 m/s higher than average velocities just to the west. This may be associated with a possible deeper transition to the Pacific Rim terrane.

4.8.2 Attenuation structure

The low velocity zone indicated in the previous section, and other localized low velocity zones, (black arrows in Figure 4.19a) are associated with high values of attenuation. Some of these zones are close to faults or folds, so the low velocity and high attenuation may be due to elevated fracture porosity. Attenuation values as high as $0.03 - 0.06$ are observed at depths below 1 km, which probably indicates increased clay content and the presence of mineralized fluids (*Malinowski et al.*, 2011). In the mid-shelf region where an anticlinal structure is present, shallow high velocities ($3-5$ km/s) coupled with high attenuation values (> 0.03) were observed at depths below $\sim$ 1 km. These high velocity and high attenuation (low Q) values indicate the presence of Crescent volcanics. Alternatively, the high attenuation may also be due to scattering and elastic effects that are not included in the visco-acoustic inversion. The landward-dipping Tofino fault that separates the Crescent terrane from Pacific Rim terrane (Fig. 4.1) is tentatively identified as a thin layer with high attenuation values (Fig. 4.21b).

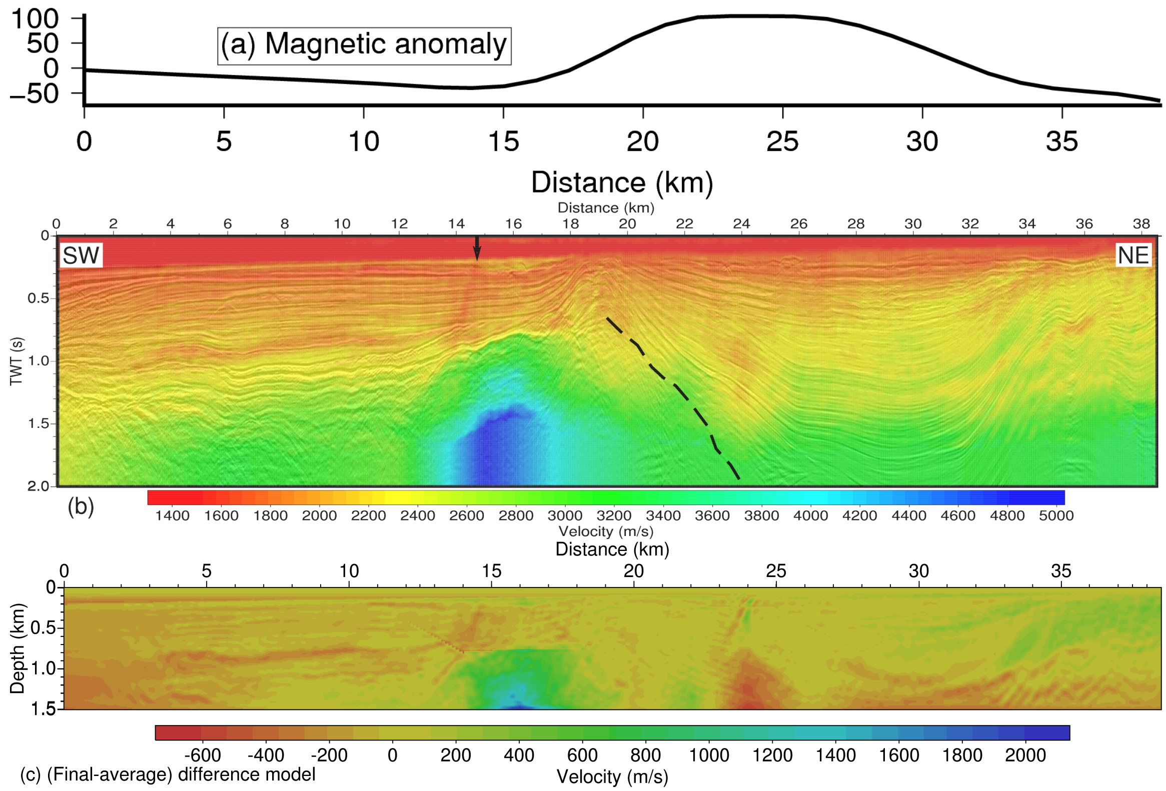

Figure 4.21: (a) Variation of magnetic anomaly along the line, (b) Final velocity model superimposed on migrated seismic section and (c) Final velocity model minus the average 1D-velocity model. Black arrow indicates gas migration pathway and black dashed line indicates approximate location of Tofino fault.

4.9 Interpretation

In general the modelled velocities can be summarised in to three layers. (i) Average velocities of up to 2 km/s in the shallow sediment section ($500 - 1200$ m) correspond to interbedded sediments with muddy siltstone/silty mudstone. This is represented by mostly red-yellow in the velocity colour scale (Fig. 4.21b). (ii) Below this, the velocities of up to 3.2 km/s are observed in the depth interval that is represented by mostly greens in the velocity colour scale, which corresponds to mudstone. (iii) The blues in the velocity colour scale indicate > 4 km/s which corresponds to Eocene volcanics.

Seismic velocities are > 4 km/s below ~ 1.5 km depth near Zeus-I65 well, which indicate the presence of Eocene volcanics at this depth. However, seismic data at Zeus-D14 do not permit us to identify the top of massive volcanics, which may be observed at $2.2 - 2.5$ km sub-surface depth based on the velocities observed at Zeus-

I65 and attenuation results. Similarly, seismic velocities at $\sim 1.0-2.0$ km sub-surface depth near Pluto-I87 well indicate wiggles with velocity undulations as large as ± 200 m/s. These could be related to alternate layers of fluid or gas saturation associated with bending-related faulting (*Takam Takougang and Calvert*, 2012).

The thickness of the sediment fill increases towards fossil trench region and then decreases over the Pacific Rim terrane (Fig. 4.21b). This fossil trench region (*Hyndman et al.*, 1990) is bounded by the basement highs of the Crescent terrane and the Pacific Rim terrane. The sediment structures show steep dips at the western edge of the Pacific Rim terrane as opposed to gentle dips observed over the Crescent basement high. Comparision of this line with other seismic lines along the margin indicates that the fossil trench region has its greatest thickness along this line and that sediment deformation varies along the margin (*Spence et al.*, 1991b; *Hayward and Calvert*, 2007).

Sediment velocities closely follow the shape of the diapiric feature observed at $18-20$ km model distance. This is in contrast to the south where the sediment velocities decrease in the core of the anticline on multichannel lines 85-01 and 89-02 (*Hayward and Calvert*, 2007), which indicates the structural variation along the margin. Furthermore, the sediment velocities are smoother and less deformed over the accreted wedge on the southwestern portion of the line compared to the northeast where the sediments are more deformed (greater folding and faulting) indicating that the deformation increases landward.

4.10 Conclusions

This study shows that with proper data preconditioning and a good inversion strategy, waveform tomography of relatively short-offset streamer data can be used to image geological features in the shallow subsurface above ~ 1.5 km depth. Specifically, the application of waveform tomography to seismic reflection data from the Tofino basin has enabled the identification of a prominent low velocity zone (associated with high attenuation) in the basin sediment section at a depth of $800-900$ m over a lateral distance of ~ 10 km. The low velocity zone could be associated with (a) lithology changes associated with a high porosity layer, (b) fluid over-pressure, and (c) over-pressured gas in this potential hydrocarbon environment. High seismic velocities ($\sim 4-5$ km/s) at depths of $1.5-2.0$ km, coupled with high attenuation values, enabled the identification of the top boundary of the Eocene volcanic Crescent terrane. In general, sediment seismic velocity increase landward, likely indicating the over-consolidation of shelf sediments. Furthermore, the sharp increase sediment velocity at $\sim$ 10 km west of Vancouver Island indicates the underlying transition to the Pacific Rim terrane. High attenuation values ($0.03 - 0.06$) were observed at depths below 1 km. These probably indicate increased clay content and the presence of mineralized fluids. Velocity and inelastic attenuation models derived in this study may provide background or regional seismic trends that are useful to hydrocarbon exploration industry for planning of possible new seismic exploration in Tofino basin.

Chapter 5

Conclusions and future directions

In this dissertation, seismic imaging and inversion methods were used to obtain the detailed subsurface structure of the Vancouver Island continental margin from Cascadia basin to the shelf region. The first part of this thesis was focussed on traveltime inversion of OBS and SCS data collected over a frontal ridge near the decollement; it aimed to image the submarine slope failure feature observed from multibeam bathymetry data and to examine the possible link of gas hydrate occurrence to slope failure. In the second part of the dissertation, mirror imaging was applied to hydrophone and vertical geophone components of the OBS data set to obtain a multiple migrated stack section. The last part of this dissertation was focussed on obtaining detailed seismic velocity and attenuation models of the Vancouver Island continental shelf using seismic traveltime inversion and full waveform inversion. The results of this thesis contribute to a better understanding of natural hazards such as tsunamis and earthquakes in this region. The results also provide background structural information in Tofino basin for a better understanding of sediment deformation and the nature of basement structures, and this may be useful for possible future exploration of oil and gas in this region.

5.1 Traveltime inversion of OBS data to image frontal ridge slope failure

In the first part, reflection and refraction travel times from single channel and ocean bottom seismometer data from the frontal ridge region were inverted to obtain 2D seismic velocity models (Fig. 2.8) along margin-parallel and margin-perpendicular lines, where a slope failure was observed from the bathymetry data. Both seismic and bathymetic data showed the presence of normal faults (Fig. 2.14), which have seafloor scarps as large as 40 ± 5 m and extend down to the BSR. These faults disrupt the BSR with vertical displacements as large as 40 m. Two of these faults coincide with the sidewalls of the slump indicating that the lateral extent of the slump is controlled by these faults.

Tomographic velocity estimates obtained in this study are comparable to previous results based on MCS and OBS data as well as sonic log velocities from IODP X311 in this region. Velocity models indicate the occurrence of a BSR at a depth of $\sim 265-275$ m below the seafloor, which matches reasonably well with the theoretically predicted BSR depth. The velocity structure below the BSR indicates a landward increase in sediment velocity from Cascadia basin towards the deformation front and then a decrease on the landward side of the ridge crest. This probably indicates sediment over-consolidation and horizontal compression as a result of ongoing subduction, as the sediments are scraped off, deformed, and compressed in the process of frontal ridge formation.

The velocity models obtained in this study also show high velocities of $2.0 - 2.1$ km/s at shallow depths of ~ 100 m beneath the ridge crest. Hydrate concentration estimates using effective medium modelling based on these P-wave velocities showed gas hydrate concentrations of up to $\sim 40\%$ of the pore space, which is in good agreement with the IODP X311 drilling results from the adjacent frontal ridge. This high velocity layer which occurred on both the Slipstream and Orca ridges on this margin was interpreted as a gas hydrate layer. Analysis of multi-beam bathymetry data showed that the glide plane occurs at a depth of $\sim 100 \pm 10$ m beneath the seafloor, which closely matches the depth of the high velocity hydrate layer. Shear wave velocity estimates based on rock physics modelling show substantial increase in S-wave velocity from 367 m/s to 501 m/s at this depth.

This is the first study to show that the glide plane matches with a shallow gas hydrate layer at ~ 100 m depth. This is in contrast to an adjacent frontal ridge where the depth of the glide plane occurs at approximately the same depth as the BSR (Fig. 2.13). These two results indicate different scenarios of slope failure in the frontal ridge area. In one case, the contrast in sediments strengthened by hydrate to that of non-hydrated sediments above is responsible for the slope failure, while in other case, the contrast between hydrated sediments above to that of gas saturated sediments below is what causing the slope failure. In either case, the contrast in sediment strength due to the presence of hydrates promoted the slope failure or at least it made the process easier. Volume estimates based on multi-beam bathymetry data showed that the amount of material removed during the failure (~ 0.33 km^3) is in close agreement with the amount of material present as debris (~ 0.24 km^3) on the seafloor. These estimates also indicate that the mass failures on this margin are approaching the size of others that have generated large tsunamis (e.g., 1998 Papua New Guinea, $1-3$ km^3), indicating the societal significance of this study.

5.2 Multiple imaging of OBS data to image faults and vergence structures

The second part of this thesis deals with the multiple migration of few widely spaced OBSs using both hydrophone and vertical geophone data. Our results for the first time showed that this technique can be used to image the downgoing oceanic crust at $\sim 5-6$ km beneath the seafloor in water depths ranging from $2.0-2.5$ km in the frontal ridge region of the northern Cascadia margin. The depth of penetration is much greater in the OBS migrated image compared to the coincident single-channel and nearly coincident multichannel images even though the size of the airgun used for OBS and SCS data is smaller than the one used for MCS data acquisition. Results also show that, in these water depths, an OBS can image up to 5 km on either side of its position on the seafloor and hence an OBS spacing of 5 km is sufficient to provide a two-fold migration stack.

The multiple migrated image shows that the sedimentary structure in the Cascadia basin is very uniform and strong reflections are imaged down to 4.5 s below the seafloor which probably corresponds to the base of the turbidite sequence (Fig. 3.16). Below this depth, weak and transparent reflections are seen down to 5.5 s, which may indicate the hemipelagic sediment sequence. Strong amplitude reflections from the top of the igneous oceanic crust are observed below 5.5 s depth.

The multiple migrated image clearly shows the continuity of reflectors which enabled us to identify faults based on reflector offsets. Landward dipping frontal thrusts and a seaward dipping backthrust were imaged from the OBS migration. The backthrust separates landward dipping frontal accreted ridge sediments from seaward dipping sedimentary package; it extends upward to near the seafloor, indicating that the motion along this fault has continued until recent times. Our results for the first time revealed a dual-vergence structure on the northern Cascadia margin, which could be associated with fluid flow variations resulting from subduction and low basal shear stress resulting from over-pressure and has important implications for understanding megathrust earthquakes on this margin.

5.3 Full waveform inversion of MCS data to image basement structures beneath the shelf

In the last part of this thesis, frequency domain visco-acoustic full waveform inversion was applied to multichannel seismic data off the Vancouver Island margin to obtain detailed seismic P-wave velocity and attenuation models beneath the continental shelf. This is the first 2D waveform inversion study on this margin. The anelastic velocity and attenuation models derived in this study are useful to understand sediment deformation within Tofino basin and its relationship with underlying accreted terranes. 1D velocity-depth profiles obtained from the 2D models match reasonably well with the projected sonic log velocities to depths of up to 2 km beneath the seafloor.

The results indicate a prominent low-velocity zone (LVZ) in the Tofino basin sediment section where the velocities are approximately 200 m/s lower than the background velocities (Fig. 4.19). This LVZ extends over a lateral distance of 10 km at a depth of about $800 - 900$ m and is associated with high attenuation values. This LVZ could be caused by over-pressured sediments or corresponds to lithology changes associated with a high porosity layer. Alternatively, this could be a result of over-pressured gas saturated sediments. In general, high seismic attenuation values ($0.03 - 0.06$) are observed below 1 km depth, which indicates the increased clay content and the presence of mineralized fluids.

Shallow high seismic velocities of $4 - 5$ km/s are observed in the mid-shelf region which probably corresponds to the shallowest occurrence of the volcanic Crescent terrane (Fig. 4.21). Crescent terrane is also marked by a magnetic high $\sim 2 - 3$ km landward of its shallowest occurrence. This indicates that the Crescent terrane is highly fractured or otherwise demagnetised where it is shallow. An anticlinal feature is observed in the mid-shelf region and is associated with the landward dipping Tofino fault that is delineated by a thin layer of high attenuation values. The landward increase in sediment velocity in the shallow sediment section indicates the compressional regime associated with the emplacement of Crescent and Pacific Rim terranes. Finally, a sharp increase in sediment velocity is observed about 10 km west of the Vancouver Island, which indicates the underlying transition to the Pacific Rim terrane.

5.4 Future directions

Based on the results obtained in this thesis for the three projects that were under investigation, several recommendations can be made for each project for future studies.

5.4.1 Frontal ridge slope failure

1. In the present study, we only have two perpendicular refraction lines. More data is required to do 3D inversion which is essential to get the detailed subsurface structure of the frontal ridge area. This will also help to identify the downdip extent of the gas hydrate stability zone, which is critical to understand the dynamics of the gas hydrate system in this region.

2. Site U1326 of the IODP X311 was drilled in the vicinity of the Orca slide region. No such measurements exist for the Slipstream slide. Therefore, more such drilling sites are required to understand the lateral extent and the thickness of the shallow high velocity layer in the frontal ridge area. Drilling to depths well below the gas hydrate stability zone will also be useful to obtain a better reference velocity-depth profile.

3. Fluids play an important role in the construction of accretionary frontal ridges. More work is needed to verify fluid flow along faults. This could be achieved by measuring fluid expulsion rates at seafloor scarps on the ridge crest. Overpressure resulting from hydrate dissociation or an earthquake would lead to slope failure. Therefore, long-term monitoring of pore-pressure and permeability using borehole observatories would help to analyse the slope stability. Furthermore, heatflow probe measurements are required to understand the migration of hot fluids through fault conduits that are responsible for the BSR uplift.

4. Shear wave velocity analyses using travel times recorded on horizontal components of OBSs which is currently underway (T. He, personal communication) will provide additional constraints on the seismic velocities pertaining to gas

hydrates. Seafloor compliance measurements, which are sensitive to the presence of gas hydrate, show an increase in shear moduli. Frequency variation of seafloor compliance provides better estimates of subsurface physical properties and gas hydrate distribution in the frontal ridge region (*Willoughby et al.*, 2008).

5. Salinity measurements using spontaneous potential logs and electromagnetic induction instruments at fault (F1) down to BSR depth and at locations where there is no hydrate found would help to understand hydrate formation mechanism in the frontal ridge area.

6. Comparison of Slipstream slide with adjacent slides in the frontal area and similar slope failure events around the world would help to understand the failure mechanisms better. Furthermore, 2D and 3D finite element based fluid flow simulations including gas hydrate would provide useful information about the overpressure generated as a result of gas hydrate dissociation due to bottom water warming and tectonic driven fluid flow. These models would further help to predict gas migration pathways, and provide clues about regional slope failure of the frontal ridges on this margin.

5.4.2 Multiple migration of OBS data

1. This study shows that an OBS spacing of 5 km is optimal to obtain a two-fold stack. Therefore, for the same length shot line, more receivers at a smaller spacing provide a larger fold stack, and perhaps improve the image further.

2. The airgun source used in this study was 120 cu. in. Bolt airgun. The data obtained using this airgun is dominated by a strong bubble pulse which occurred at every 100 ms interval and was difficult to remove using conventional processing techniques. Having a bigger airgun source with less bubble pulse effects (e.g. using a GI gun) would enhance the S/N ratio and provide deeper signal penetration depth. Larger trace lengths would also enable us to detect secondary multiples (occurs at 5 times the seafloor reflection) which carry even more useful information and provide wider coverage than primary signal and first-order multiple alone.

3. The multiple imaging technique is still in the developmental stage. Recent studies, for example, joint least-squares inversion of upgoing and downgoing

wavefields (*Wong et al.*, 2010), least-squares reverse time migration/inversion of downgoing waves (including higher order multiples) (*Wong et al.*, 2011), linearized full wave inversion of primaries and multiples (*Wong et al.*, 2012a), joint imaging with streamer and OBS data (*Wong et al.*, 2012b), show that multiple imaging provides improved subsurface structural image with less migration artifacts, enhanced amplitude along the true reflectors and suppressed crosstalk from the image. However, most of these methods were tested only on synthetic 2D data sets. Application of joint inversion of primaries, multiples and streamer data to field 3D data sets from complex regions such as frontal ridge area is challenging and computationally intensive, but provide better structural images of the subsurface.

4. Our results for the first time showed dual-vergence structure on the northern Cascadia margin. This could be associated with fluid flow and has important implications for understanding earthquakes on this margin. Therefore, drilling at the location where the dual-vergence structure is observed could provide clues about rheological and mechanical properties of the subsurface. This will also be a useful test for contrasts in sediment properties and deformation between landward and seaward vergent sections of the accretionary prism.

5.4.3 Continental shelf seismic analysis

1. The 2D frequency domain visco-acoustic full waveform inversion applied in this study is the first of its kind on this margin. The demonstrated reliability and resolution of the P-wave velocity and attenuation models obtained for the Vancouver Island continental shelf by the full waveform inversion suggests that this technique could be applied to other MCS lines on this margin. Integrating results from all the lines may be useful for understanding the regional tectonics of this margin.

2. The high resolution velocity and attenuation models obtained in this study show structures down to 2 km beneath the seafloor. The depth of penetration is limited by the relatively short offsets present in the data. Using a large streamer would provide large offsets that enable identification of deeper basement structures and also provide clues about the deeper occurrence of faults such as the Tofino fault and Crescent thrust and the deeper boundary between the Crescent

and the Pacific Rim terranes.

3. The lowest frequency available for inversion in this study is 6 Hz. Low frequencies are crucial to obtain low wave-number information from the data. They penetrate deeper and provide information about long wavelength features. More importantly, low frequencies are crucial for successful convergence of the non-linear inversion process. Therefore, it is recommended to have low frequencies while collecting the data for the application of full waveform inversion. This could be achieved by using variable depth sreamers (for example, see *Soubaras and Dowle* (2010); *Kneller et al.* (2014)), where the source signal is characterized by sharp, clean wavelets with large bandwidth. As well, estimating source signature during data acquisition would minimize potential errors coming from using modelled source signature.

4. The low velocity zone identified in this study could be related to over-pressured sediments or corresponds to lithology changes associated with a high porosity layer or it may be the result of over-pressured gas saturated sediments in this potential hydrocarbon environment. Therefore, drilling through the LVZ is not only useful to understand the cause of the LVZ, but is also useful to understand the local tectonics of this region. Furthermore, amplitude variation with offset analysis may also provide clues about the LVZ.

5. In this study we used the visco-acoustic wave equation. However, use of this equation is limited to areas where the velocity gradients are smooth. When large velocity gradients are present, the full visco-elastic wave equation provides better results. This would also enable inversion for other elastic parameters such as density and shear wave velocity. However, use of this equation is very challenging because it is highly computationally intensive and highly non-linear, which requires a robust inversion approach (e.g., *Mulder and Plessix*, 2008; *Brossier et al.*, 2009b). An alternative approach is to use the visco-acoustic wave equation but correct for amplitude differences between observed and predicted waveforms produced by large velocity gradient as suggested by *Chapman et al.* (2010).

6. In this study we provide qualitative and realistic resolution analysis of our model results. However, a more quantitative analysis is required to understand the parameter uncertainties arising from the inversion process.

Appendix A

OBS relocation

Primary details of the OBS relocation process are presented in chapter 2 as part of the manuscript. Additional details of this process are presented in this section. These were excluded from the OBS paper presented in chapter 2 in order to reduce the length of the manuscript. The relocation program (obsloc.m) uses direct arrival times recorded on OBSs, water velocity profile (Fig. A.1) and deployment coordinates of OBS position. As mentioned in chapter 2, for a given OBS, it positions the OBS at each node within the uniform grid, and calculates the distance to each shot. Since water velocity is known and for each shot the observed direct arrival traveltime is measured, the corresponding true shot-receiver distance can be calculated. The routine then sums the total distance residual (calculated node-distance minus true distance) over all shots for that given OBS position, and the minimal distance residual gives the best position. Relocated OBS position for OBS-04 calculated using this program is shown in Fig. A.2. Variation of distance residuals with shot number for each OBS position is shown in Fig. A.3. The final OBS drifts for all OBSs from their deployment positions are shown in table A.4, which indicates average OBS drifts of 50 m with an average residual error of 12 m. Relocated OBS positions are projected onto a straight line (Fig. A.5) prior to traveltime inversion for easy interpretation.

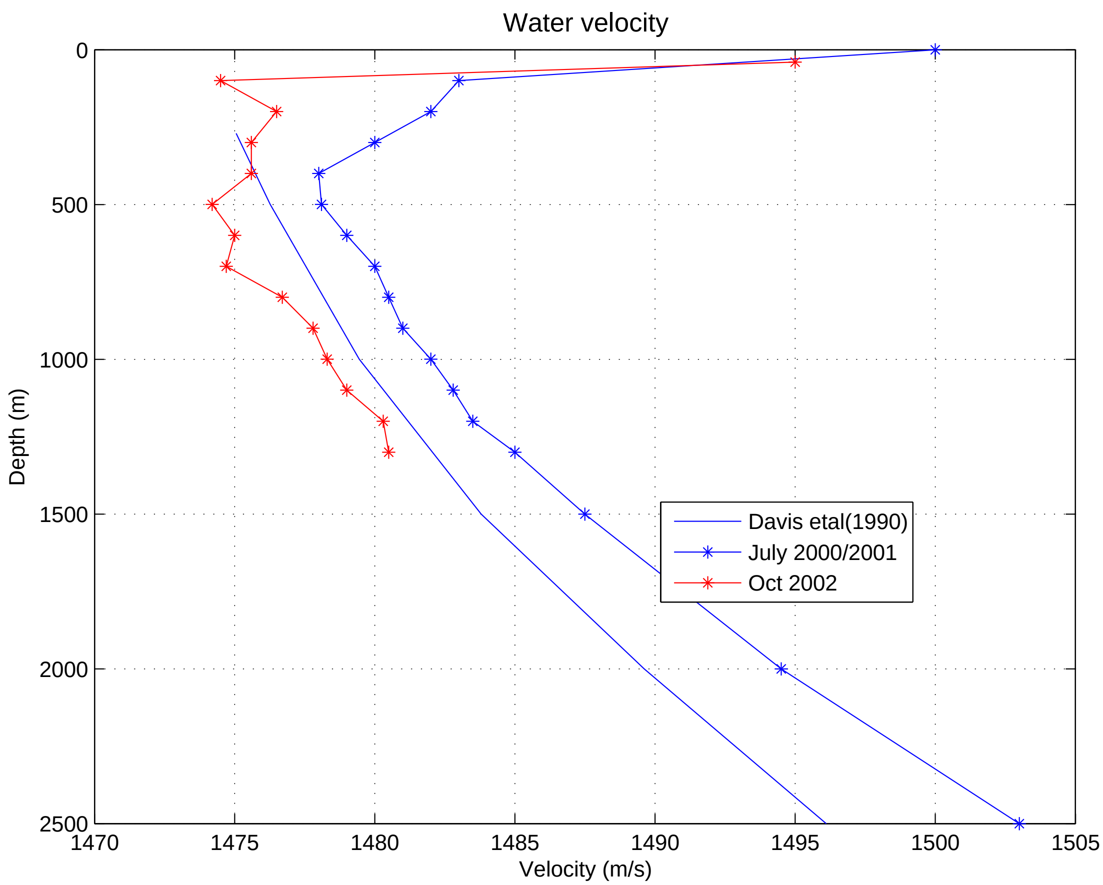

Figure A.1: Velocity-depth profiles from velocimeter (stared lines) at location near center of Bullseye vent (*Spence et al.*, 2003). Results from *Davis et al.* (1990) are also plotted for comparison. Velocity profile from July cruise is used for OBS relocation in this study. We extrapolated the values below 1300 m depth.

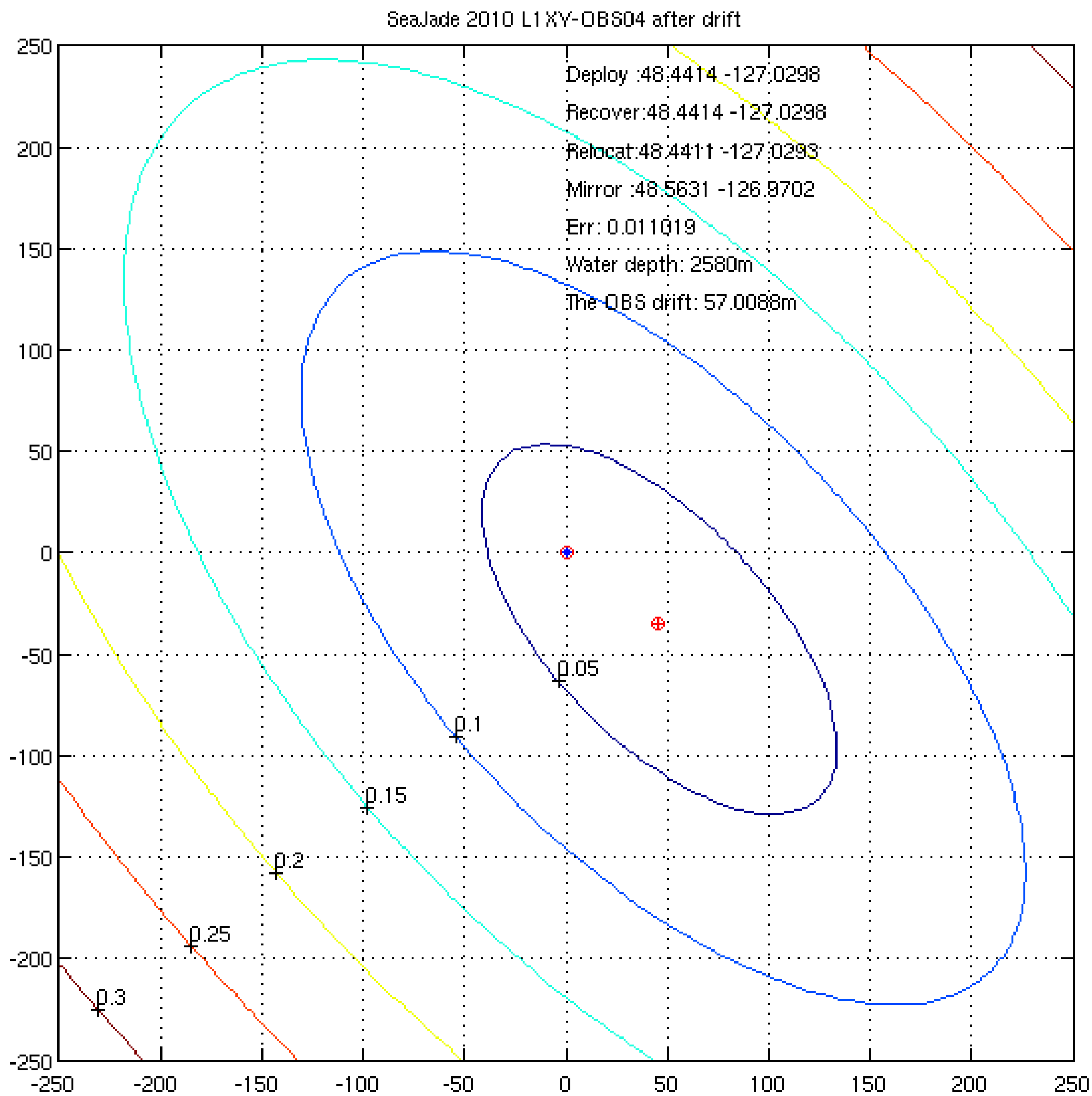

Figure A.2: Re-located position of OBS-04. The relocated position is a red circle-cross located at the minimum distance residual (11.0 m) with a drift of 57 m in the south-east direction. The initial position of OBS based on deployment and recovery location is indicated by a blue star. R.M.S. contour interval is 50 m. The OBS drift distance is the total distance the OBS was moved from the deployment location.

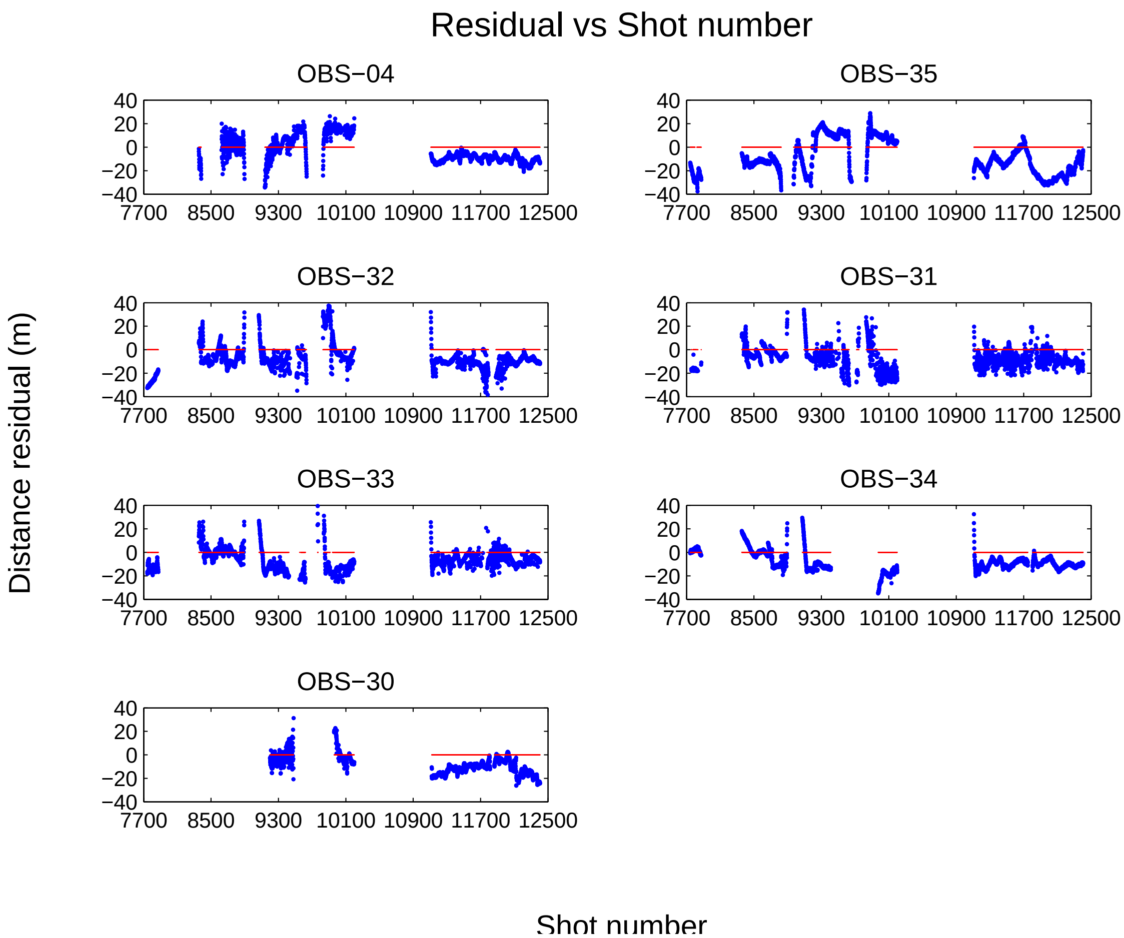

Figure A.3: Distance residual for each shot relative to the OBS position after inversion. Red line corresponds to the residual value of zero. Gaps in the data indicate the location of OBS and loops or transit during data acquisition. Direct arrival times corresponding to these gaps are not used in inversion as they provide least constraint on the OBS position.

OBS ##	OBS drift(m)	Distance residual(m)	Water depth(m)			Drift direction
			Deployment	Relocated	Difference	
04	57.0	11.0	2579.3	2579.4	0.1	SE
35a	49.5	16.6	2561.0	2559.8	1.2	SE
32	63.2	12.9	2177.5	2178.1	0.6	SSE
31	79.1	11.5	2145.0	2146.8	1.7	NE
33a	43.0	10.3	2120.4	2123.9	3.5	SW
34a	41.2	11.5	2126.1	2128.5	2.3	SSE
30	55.0	11.9	2156.5	2158.7	2.1	E

Figure A.4: Distance residual and drift from its deployment position for each OBS position after inversion. The average drift and residuals for these OBSs are 50 m and 12 m respectively. Direction of drift is also indicated.

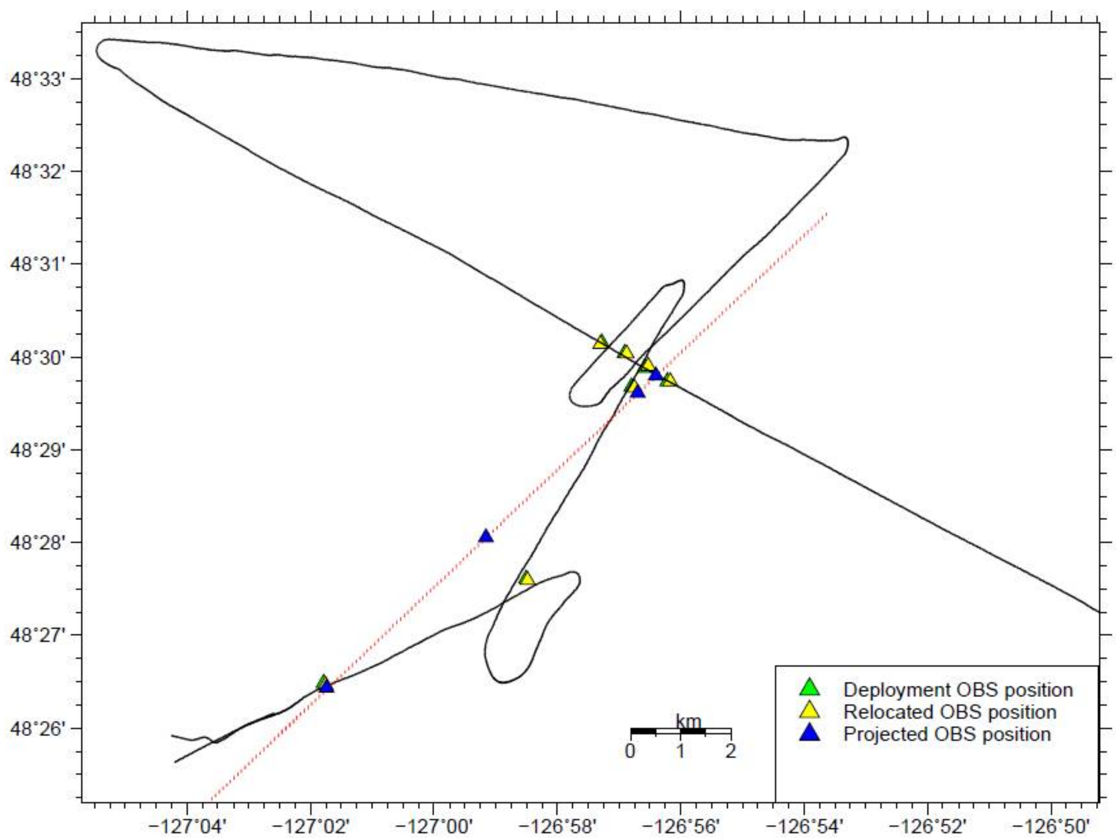

Figure A.5: OBS deployment and relocated positions. Black line indicates the ship track. Prior to traveltime inversion, shot and relocated obs positions are projected onto a straight line (red dotted line) that fits through the shot locations, while keeping the shot-receiver distance intact.

Appendix B

Origin of potential double BSR and relation to sea-level change and bottom water temperature effect

As disscussed in Chapter 2, a discontinuous BSR is visible on the margin-parallel single-channel seismic line (line-4a) crossing Slipstream Ridge. Additionally, some prominent reflection-packages interpreted to be anomalous BSR reflections (labelled BSR_a as indicated by arrows in Fig. 2.14a, are significantly shallower than the theoretical BSR curve (Fig. 2.14a), which assumes a geothermal gradient of $0.06\,^{\circ}C/m$. One possible cause of a shallower BSR is a bottom warming pulse produced by ocean warming at the end of the Last Glacial Maximum (LGM).

On the northwest side of the section of line-4a (SP 12620-12700), two distinct reflector packages are interpreted as a possible double BSR (Fig. 2.14a). The distance between the double reflectors is 35 ± 3 m. We speculate that the shallower reflector represents upward migration of the BSR produced mostly by bottom water warming since the LGM, with the amount reduced slightly by the associated increase in water depth.

The LGM on this margin occurred at $\sim 15,000$ years before present when the Cordilleran Ice Sheet (CIS) reached its maximum thickness. Therefore, considering that sea-level was ~ 120 m lower during the last glacial maximum (*James et al.*, 2009; *Dyke*, 2004; *Booth et al.*, 2004) and bottom water temperature was reduced by $\sim 4\,^{\circ}C$ (*Westbrook et al.*, 1994) during this period, the BGHSZ is expected to have been ~ 63 m deeper than present day conditions. These results are comparable to a recent study by N. *Scholz* (2014). However, the observed difference in the depths between the theoretical BSR and the BSR_a reflector-packages is smaller than 63 m. For an upward migration of the BGHSZ by 35±3 m, our results indicate that a bottom water temperature increase of $\sim 2.34\,^{\circ}$C in addition to a sea-level rise of 120 m would be required. In a similar tectonic environment, *Bangs et al.* (2005) observed $20-40$ m difference between the double reflectors beneath Hydrate Ridge on the southern Cascadia margin, and interpreted it to be caused by a bottom water temperature rise of $\sim 1.75-2.25\,^{\circ}$C with a coincident sea-level rise of 120 m. These results suggest that the upward migration of the base of the gas hydrate stability field may have increased the hydrate concentration in the region above it by releasing methane to migrate upward. The upward migration behaviour of the hydrate stability zone is further discussed below.

In general, the pressure change associated with sea-level change is instantaneous. However, the temperature change at the seafloor requires considerable time to reach the BGHSZ. In principle, the time required for the migration of thermal pulse to the BGHSZ can be calculated using *Louden and Wright* (1989) relation, which describes temperature (T) as a function of depth (z) below the seafloor and time (t), and is given by

$$T_z = T_\circ + z\left(\frac{\partial T}{\partial z}\right) + dT * erfc\left(\frac{z}{2\sqrt{d*t}}\right) \tag{B.1}$$

Fig. B.1 shows the effect of a bottom water temperature change (dT) assuming an initial seafloor temperature of $T_\circ = 0\,^{\circ}$C and present day temperature of $2.34\,^{\circ}$C. Geothermal gradient of $0.06\,^{\circ}$C/m and thermal conductivity of $1.1\,W/(m.K)$ were used. Thermal diffusivity (d) is $3.6\,x\,10^{-7} m^2/s$, calculated using results from *Hyndman et al.* (1979); however, uncertainties on this parameter may be large. Fig. 15 indicates that the BGHSZ rises quickly initially, followed by a slow rise to the equilibrium position. For example, it requires $\sim$ 5000 years to migrate up by 15 m and requires $\sim 20,000$ years to migrate up by 27 m from its initial position, assuming that the initial conditions used in this estimation are realistic and represent the actual scenario before failure. Therefore, the BGHSZ does not approach stability for at least $5,000-10,000$ years after the LGM. Thus, the bottom water temperature change that is required to shift the BGHSZ had to occur at least $5,000-10,000$ years ago (*Bangs et al.*, 2005). A general problem with a change of the BGHSZ from bottom-warming and pressure changes from sea level rise during the Holocene is that it should uniformly occur along the margin, if not at least across the Slipstream Ridge. However, the observed "double BSR" only occurs over a short fragment of the Slipstream Ridge and is especially apparent where the slope failure has occurred. Thus, it is possible that other factors have contributed to the depth changes in the BGHSZ.

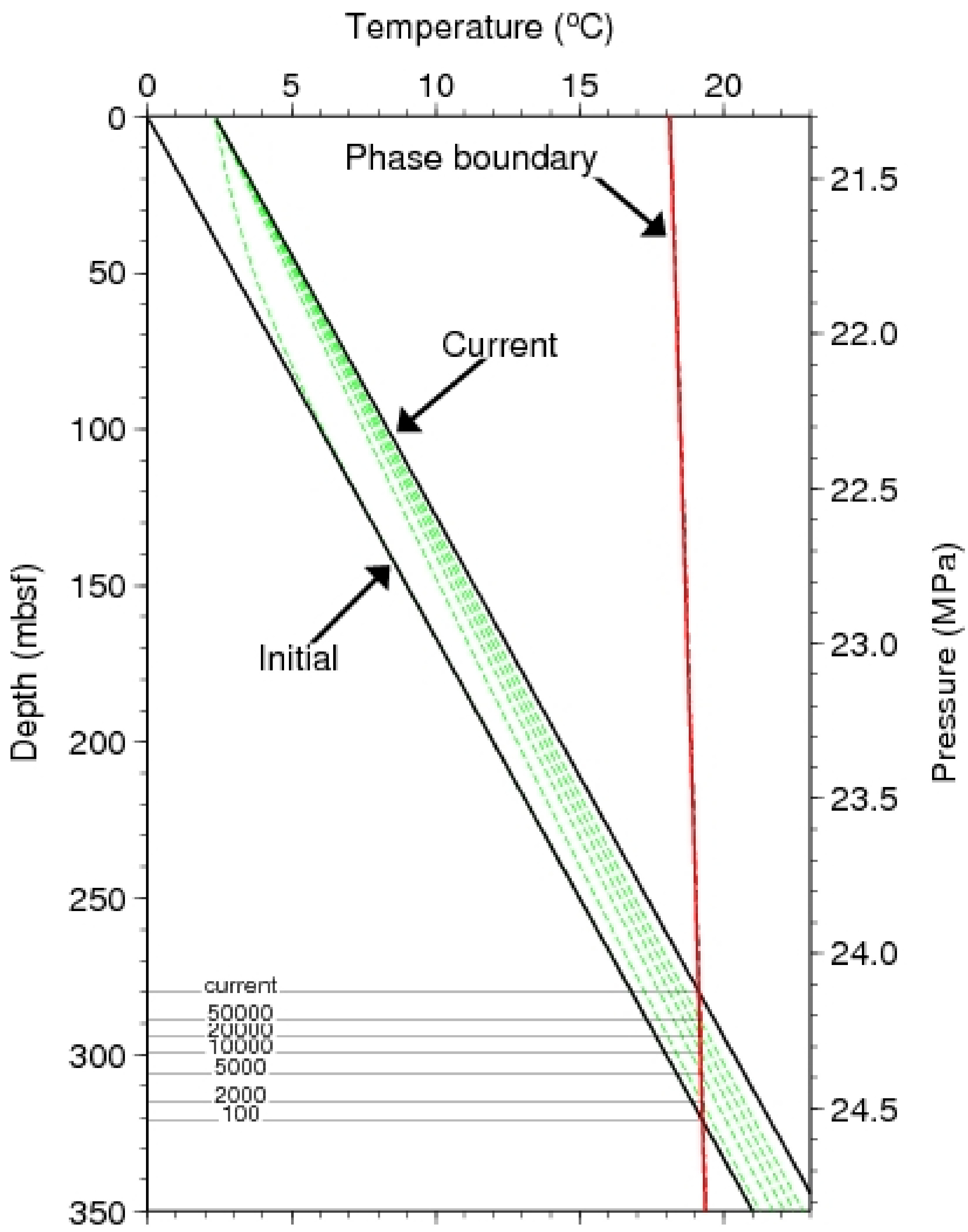

Figure B.1: Thermal evolution of the sediment column for a seafloor temperature change of 2.34 °C (based on relations in *Louden and Wright*, 1989). Red line indicates the theoretical phase boundary curve.

Appendix C

MCS data processing and full waveform inversion

C.1 MCS data processing results

Preliminary processing results of the MCS data used in chapter 4 are presented in this section. The data processing includes assigning geometry to the field data, Common Depth Point (CDP) sorting, spherical divergence correction, band pass filtering, FK-filetring to remove the low frequency noise, normal move out (NMO) velocity analysis, stacking and migration. An example of a semblance spectrum corresponding to CDP location 8431 is shown in Fig. C.1. Constant velocity gathers are averaged over five adjacent CDPs. Near offset reflections are flattened by choosing the appropriate NMO velocity; however, far-offset reflections are obscured by the strong presence of linear noise (Fig. C.1). Stacking velocities derived from velocity analysis are converted to interval velocities using Dix equation (*Dix*, 1952) (Fig. C.2). Smoothed interval velocities are then superimposed on migrated seismic section (Fig. C.3). Smoothed interval velocities derived from NMO velocity analysis are used as input to traveltime inversion, which subsequently used as starting velocity model for full waveform inversion. Tomographic velocities are compared to NMO interval velocities at selected CDP locations (Fig. C.3).

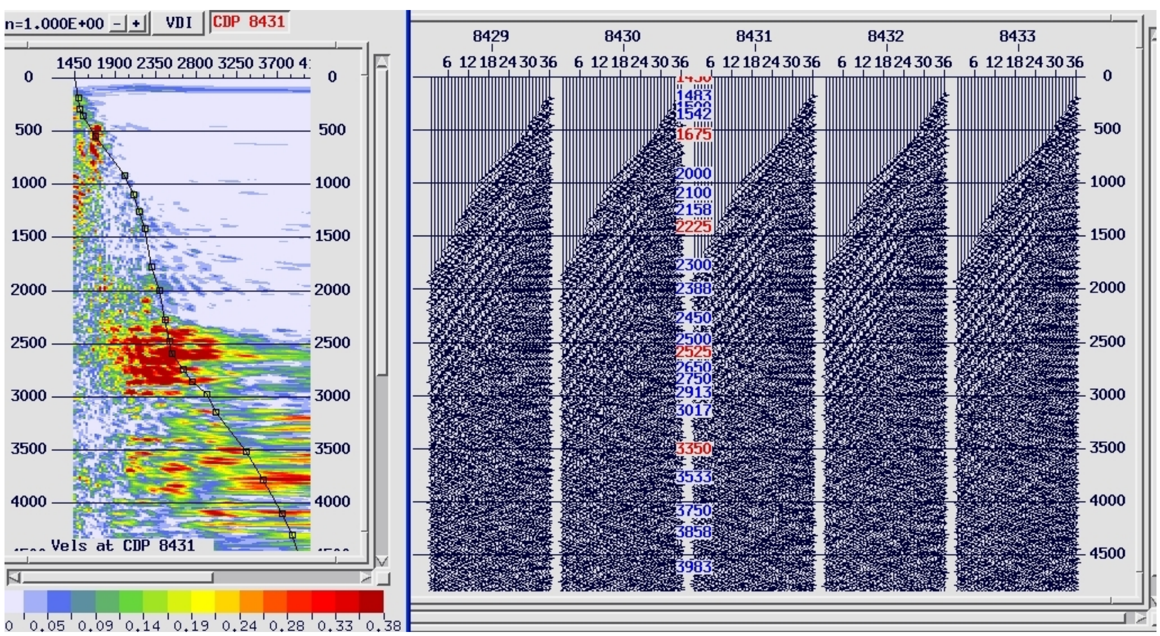

Figure C.1: Semblance velocity analysis at CDP 8431.

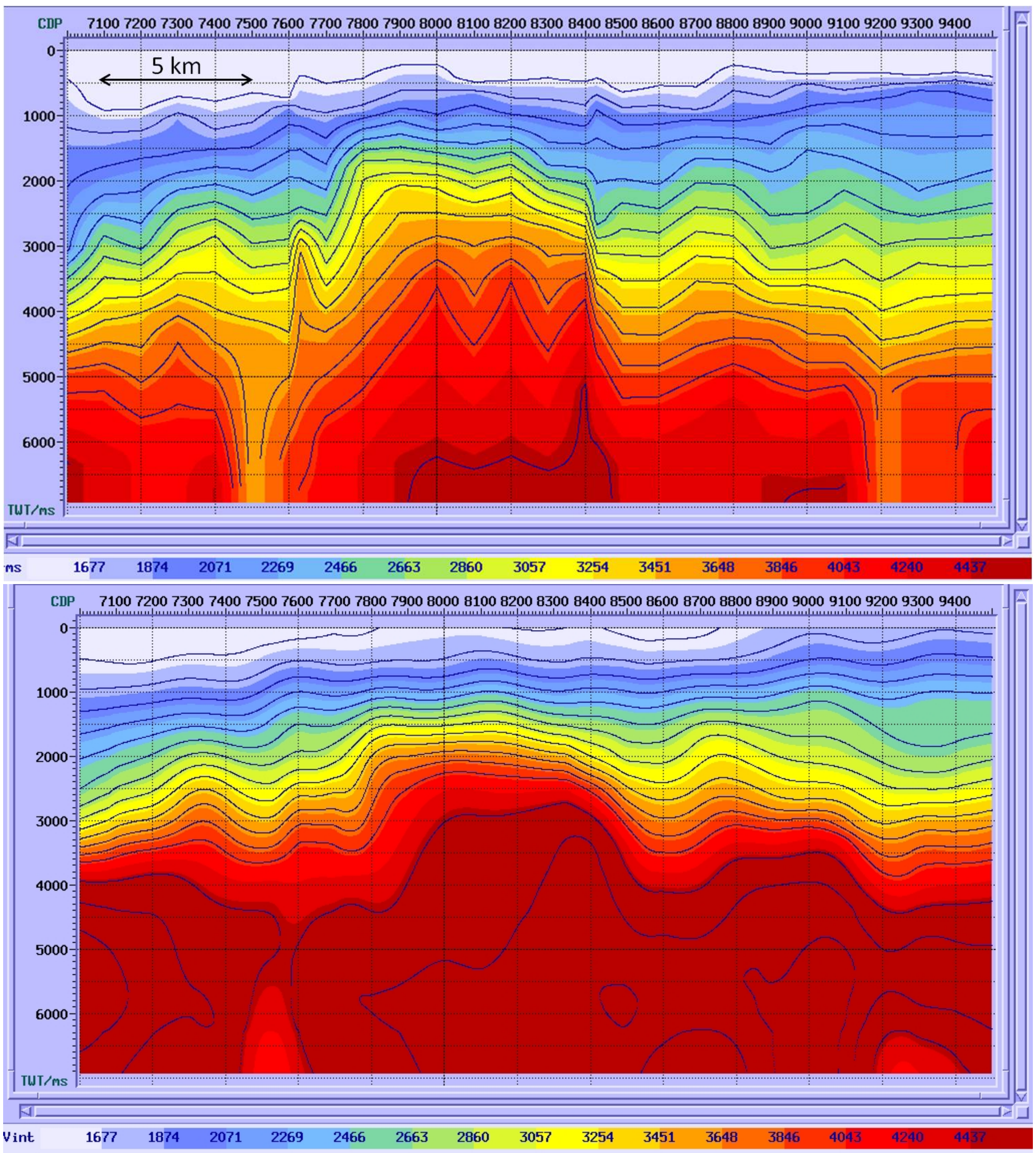

Figure C.2: Stacking velocities (above) derived from seismic data processing are converted to interval velocities (below) using Dix equation (*Dix*, 1952).

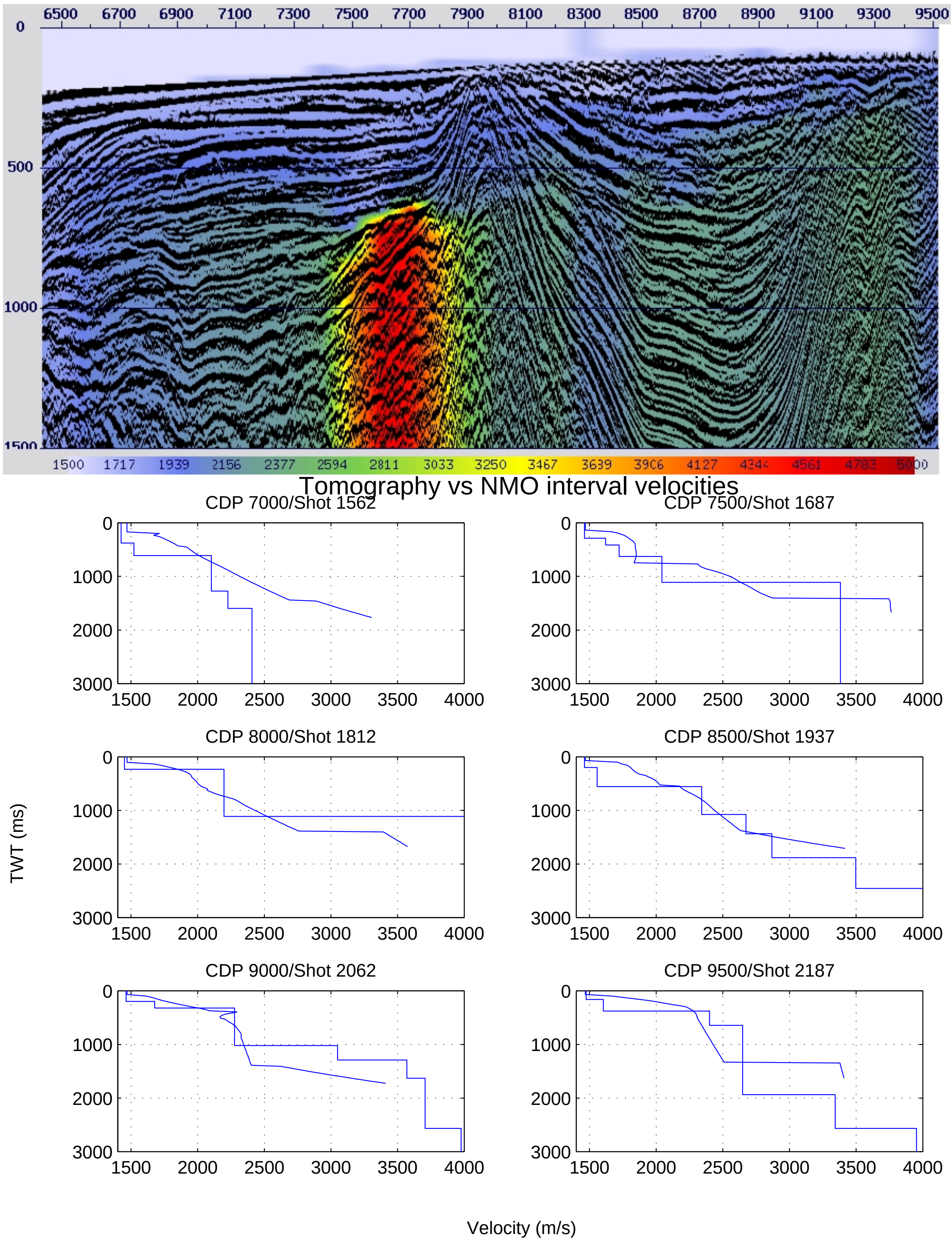

Figure C.3: (above) Smoothed interval velocities derived from seismic data processing are superimposed on migrated seismic section. (below) Comparison of traveltime inversion velocities (smoothed line) with interval velocities (staircase line) from NMO velocity analysis at every 500 CDPs along the model. CDP spacing is 12.5 m.

C.2 Full waveform inversion results

Primary results of full waveform inversion are presented in Chapter 4. Additional details of this application are presented in this section. Particularly, inversion results using logarithmic residuals (*Shin and Min*, 2006) and logarithmic phase only residuals (*Brenders and Pratt*, 2007) are presented in this section (Fig. C.4). Furthermore, results using starting frequency of 7.2 Hz are shown in Fig. C.5. These results show the importance of low frequencies that are crucial to obtain the high resolution structures beneath the seafloor. Low frequencies also provide information about long wavelength features in the subsurface. These results further help to assess the sensitivity and resolution analysis of our model.

C.3 Computational time

Computational time required for full waveform inversion used in this study are presented below. This depends on the acquisition geometry, number of node points in the finite difference grid, number of frequencies and iterations used in the inversion. In this study, we used 138 shots with 1527 receivers placed along the model length although only 144 receivers are active. The finite difference grid consists of 3081 x 161 grid points. We inverted one frequency at a time for a total of 21 frequencies with five iterations per frequency.

On a GNU/Linux cluster with 32-bit kernel (Intel(R) Xeon(R) CPU E5420 @ 2.50GHz, 8.3 Gb RAM, 8 cores), acoustic inversion took about 25 hours to invert for velocity structure using a single core, which is about 15-20 min per frequency / iteration. Inverting for both velocity and attenuation using visco-acoustiv inversion required about 50 hours of computational time.

The computational time for forward modelling took about one hour using one core at a time. Using parallel computing, it only took about 10 min using all 8 cores.

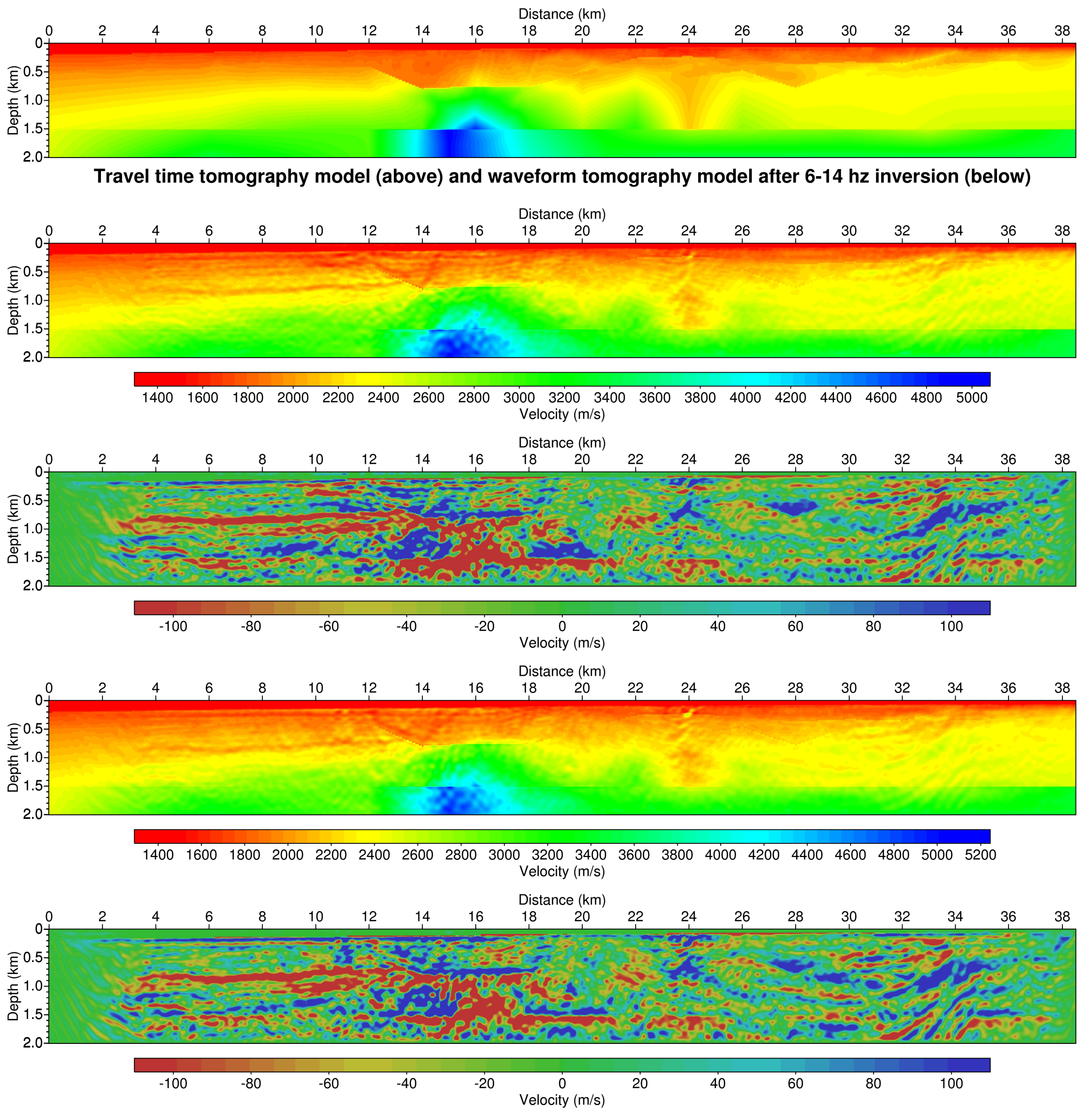

Figure C.4: (a) Starting velocity model from travel time inversion. (b) FWI velocity model after 6-14 Hz inversion using logarithmic phase only residuals (*Brenders and Pratt*, 2007), and (c) difference between (b) and (a). (d) FWI velocity model after 6-14 Hz inversion using logarithmic residuals (*Shin and Min*, 2006), and (e) difference between (d) and (a).

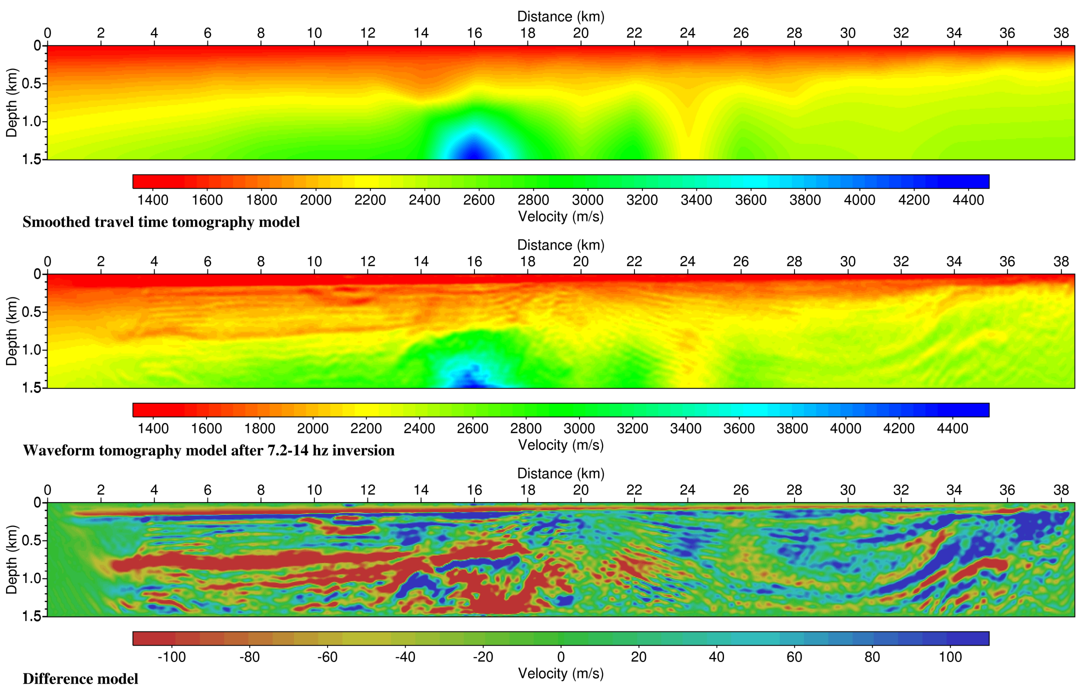

Figure C.5: (a) Starting velocity model from travel time inversion. (b) FWI velocity model after 7.2-14 Hz inversion and (c) difference between (b) and (a).

Bibliography

Aki, K., and P. Richards (1980), Quantitative Seismology: Theory and Methods, *WH Freeman & Co.*

Aldridge, D. F., and D. W. Oldenburg (1993), Two-dimensional tomographic inversion with finite-difference traveltimes, *Journal of Seismic Exploration*, *2*(3), 257–274.

Andersen, K. K., N. Azuma, J.-M. Barnola, M. Bigler, P. Biscaye, N. Caillon, J. Chappellaz, H. B. Clausen, D. Dahl-Jensen, H. Fischer, et al. (2004), High-resolution record of Northern Hemisphere climate extending into the last interglacial period, *Nature*, *431*(7005), 147–151.

Arnulf, A., A. Harding, S. Singh, G. Kent, and W. Crawford (2012), Fine-scale velocity structure of upper oceanic crust from full waveform inversion of downward continued seismic reflection data at the Lucky Strike Volcano, Mid-Atlantic Ridge, *Geophysical Research Letters*, *39*(8).

Audet, P., M. G. Bostock, N. I. Christensen, and S. M. Peacock (2009), Seismic evidence for overpressured subducted oceanic crust and megathrust fault sealing, *Nature*, *457*(7225), 7678, doi:10.1038/nature07650.

Audet, P., M. G. Bostock, D. C. Boyarko, M. R. Brudzinski, and R. M. Allen (2010), Slab morphology in the Cascadia fore arc and its relation to episodic tremor and slip, *Journal of Geophysical Research*, *115*, doi:10.1029/2008jb006053.

Bangs, N. L. B., R. J. Musgrave, and A. M. Trehu (2005), Upward shifts in the southern Hydrate Ridge gas hydrate stability zone following postglacial warming, offshore Oregon, *Journal of Geophysical Research*, *110*(B3), doi:10.1029/2004jb003293.

Barnes, C., M. Charara, and T. Tsuchiya (2008), Feasibility study for an anisotropic full waveform inversion of cross-well seismic data, *Geophysical Prospecting*, *56*(6), 897–906.

Barr, F. J., and J. I. Sanders (1989), Attenuation of water-column reverberations using pressure and velocity detectors in a water-bottom cable, in *1989 SEG Annual Meeting*, Society of Exploration Geophysicists.

Berndt, C., J. Mienert, M. Vanneste, and S. Bünz (2005), Gas hydrate dissociation and sea-floor collapse in the wake of the Storegga Slide, Norway, *Norwegian Petroleum Society Special Publications*, *12*, 285–292.

Bleibinhaus, F., J. A. Hole, T. Ryberg, and G. S. Fuis (2007), Structure of the California Coast Ranges and San Andreas Fault at SAFOD from seismic waveform inversion and reflection imaging, *Journal of Geophysical Research: Solid Earth (1978–2012)*, *112*(B6).

Booth, D. B., K. G. Troost, J. J. Clague, and R. B. Waitt (2004), The Cordilleran Ice Sheet, *Quaternary Period in the United States*, *1*, 17–43.

Bostock, M., R. Hyndman, S. Rondenay, and S. Peacock (2002), An inverted continental Moho and serpentinization of the forearc mantle, *Nature*, *417*(6888), 536–538.

Brandon, M. T. (1985), Deformational processes affecting unlithified sediments at active margins: A field study and a structural model., *Dissertation Abstracts International Part B: Science and Engineering*, *45*(11), 174.

Brenders, A., and R. Pratt (2007), Full waveform tomography for lithospheric imaging: results from a blind test in a realistic crustal model, *Geophysical Journal International*, *168*(1), 133–151.

Brenders, A. J. (2011), Strategies For Waveform Tomography of Long-offset, 2-D Exploration Seismic Data, Ph.D. thesis, University of Western Ontario.

Brossier, R., S. Operto, and J. Virieux (2009a), Seismic imaging of complex onshore structures by 2D elastic frequency-domain full-waveform inversion, *Geophysics*, *74*(6), WCC105–WCC118.

Brossier, R., S. Operto, and J. Virieux (2009b), Two-dimensional seismic imaging of the Valhall model from synthetic OBC data by frequency-domain elastic full-waveform inversion, in *SEG, Expanded Abstracts*, vol. 28, pp. 2293–2297.

Brown, H., W. Holbrook, M. Hornbach, and J. Nealon (2006), Slide structure and role of gas hydrate at the northern boundary of the Storegga Slide, offshore Norway, *Marine Geology*, *229*(3-4), 179–186.

Bünz, S., and J. Mienert (2004), Acoustic imaging of gas hydrate and free gas at the Storegga Slide, *Journal of Geophysical Research*, *109*(B4), doi:10.1029/2003jb002863.

Calkins, J. A., G. A. Abers, G. Ekstrm, K. C. Creager, and S. Rondenay (2011), Shallow structure of the Cascadia subduction zone beneath western Washington from spectral ambient noise correlation, *Journal of Geophysical Research*, *116*(B7), doi:10.1029/2010jb007657.

Calvert, A. (1996), Seismic reflection constraints on imbrication and underplating of the northern Cascadia convergent margin, *Canadian Journal of Earth Sciences*, *33*(9), 1294–1307.

Calvert, A., and R. Clowes (1991), Seismic evidence for the migration of fluids within the accretionary complex of western Canada, *Canadian Journal of Earth Sciences*, *28*(4), 542–556.

Calvert, A. J. (2004), Seismic reflection imaging of two megathrust shear zones in the northern Cascadia subduction zone, *Nature*, *428*(6979), 163–167.

Calvert, A. J., L. A. Preston, and A. M. Farahbod (2011), Sedimentary underplating at the Cascadia mantle-wedge corner revealed by seismic imaging, *Nature Geoscience*, *4*(8), 545548, doi:10.1038/ngeo1195.

Canals, M., G. Lastras, R. Urgeles, J. Casamor, J. Mienert, A. Cattaneo, M. De Batist, H. Haflidason, Y. Imbo, J. Laberg, and et al. (2004), Slope failure dynamics and impacts from seafloor and shallow sub-seafloor geophysical data: case studies from the COSTA project, *Marine Geology*, *213*(1-4), 972, doi:10.1016/j.margeo.2004.10.001.

Chapman, C., J. Hobro, and J. Robertsson (2010), Elastic corrections to acoustic finite-difference simulations, in *2010 SEG Annual Meeting*, Society of Exploration Geophysicists.

Chen, M.-A. P. (2006), Northern Cascadia marine gas hydrate: Constraints from resistivity, velocity, and AVO, MSc thesis, University of Victoria, Victoria.

Choi, Y., D.-J. Min, and C. Shin (2008), Two-dimensional waveform inversion of multi-component data in acoustic-elastic coupled media, *Geophysical Prospecting*, *56*(6), 863–881.

Claypool, G. E., and I. Kaplan (1974), The origin and distribution of methane in marine sediments, in *Natural gases in marine sediments*, pp. 99–139, Springer.

Clennell, M., P. Henry, M. Hovland, J. S. Booth, W. J. Winters, and M. Thomas (2000), Formation of natural gas hydrates in marine sediments: Gas hydrate growth and stability conditioned by host sediment properties, *Annals of the New York Academy of Sciences*, *912*(1), 887–896.

Clowes, R., M. Brandon, A. Green, C. Yorath, A. S. Brown, E. Kanasewich, and C. Spencer (1987), LITHOPROBE-southern Vancouver Island: Cenozoic subduction complex imaged by deep seismic reflections, *Canadian Journal of Earth Sciences*, *24*(1), 31–51.

Collett, T. S., and J. Ladd (2000), 19. Detection of gas hydrate with downhole logs and assessment of gas hydrate concentrations (saturations) and gas volumes on the Blake Ridge with electrical resistivity log data, in *Proceedings of the Ocean Drilling Program. Scientific results*, vol. 164, pp. 179–191, Ocean Drilling Program.

Dash, R., G. Spence, R. Hyndman, S. Grion, Y. Wang, and S. Ronen (2009), Wide-area imaging from OBS multiples, *Geophysics*, *74*(6), Q41–Q47.

Dash, R. K. (2007), Crustal structure and marine gas hydrate studies near Vancouver Island using seismic tomography, Ph.D. thesis, School of Earth and Ocean Sciences, University of Victoria.

Davis, D., J. Suppe, and F. Dahlen (1983), Mechanics of fold-and-thrust belts and accretionary wedges, *Journal of Geophysical Research: Solid Earth (1978–2012)*, *88*(B2), 1153–1172.

Davis, E., and R. Hyndman (1989), Accretion and recent deformation of sediments along the northern Cascadia subduction zone, *Geological Society of America Bulletin*, *101*(11), 1465–1480.

Davis, E., R. Hyndman, and H. Villinger (1990), Rates of fluid expulsion across the Northern Cascadia Accretionary Prism: Constraints from new heat row and multichannel seismic reflection data, *Journal of Geophysical Research: Solid Earth (1978–2012)*, *95*(B6), 8869–8889.

De Batist, M., J. Klerkx, P. Van Rensbergen, M. Vanneste, J. Poort, A. Y. Golmshtok, A. A. Kremlev, O. M. Khlystov, and P. Krinitsky (2002), Active hydrate destabilization in Lake Baikal, Siberia?, *Terra Nova*, *14*(6), 436–442.

Dehler, S., and R. Clowes (1992), Integrated geophysical modelling of terranes and other structural features along the western Canadian margin, *Canadian Journal of Earth Sciences*, *29*(7), 1492–1508.

Dessa, J.-X., and G. Pascal (2003), Combined traveltime and frequency-domain seismic waveform inversion: a case study on multi-offset ultrasonic data, *Geophysical Journal International*, *154*(1), 117–133.

Dillon, W., W. Danforth, D. Hutchinson, R. Drury, M. Taylor, and J. Booth (1998), Evidence for faulting related to dissociation of gas hydrate and release of methane off the southeastern United States, *Geological Society, London, Special Publications*, *137*(1), 293–302.

Dix, C. H. (1952), *Seismic prospecting for oil*, Harper.

Dyke, A. S. (2004), An outline of North American deglaciation with emphasis on central and northern Canada, *Developments in Quaternary Sciences*, *2*, 373–424.

Enkin, R. J., T. S. Hamilton, M. Riedel, and J. Pohlman (2010), Gravity driven slumps and turbidites from the frontal ridge of Cascadias accretionary wedge Canada: controls from deglacial sedimentation, tectonics, and gas hydrates, AGU.

Fink, C., and G. Spence (1999), Hydrate distribution off Vancouver Island from multifrequency single-channel seismic reflection data, *Journal of Geophysical Research: Solid Earth (1978–2012)*, *104*(B2), 2909–2922.

Foucher, J.-P., H. Nouzé, and P. Henry (2002), Observation and tentative interpretation of a double BSR on the Nankai slope, *Marine Geology*, *187*(1), 161–175.

Ganguly, N., G. Spence, N. Chapman, and R. Hyndman (2000), Heat flow variations from bottom simulating reflectors on the Cascadia margin, *Marine Geology*, *164*(1-2), 53–68.

Gao, F., G.-l. Fradelizio, A. Levander, G. Pratt, C. Zelt, et al. (2005), Seismic velocity, Q, geological structure and lithology estimation at a ground water contamination site, *75th SEG, Expanded Abstracts*, pp. 1561–1564.

Gao, F., A. Levander, C. Zelt, et al. (2006), An Iterative Approach For Geophysical Diffraction Tomography: Implication For True Amplitude Migration, in *2006 SEG Annual Meeting*, Society of Exploration Geophysicists.

Gholami, Y., R. Brossier, S. Operto, V. Prieux, A. Ribodetti, J. Virieux, et al. (2011a), Two-dimensional acoustic anisotropic (VTI) full waveform inversion: the Valhall case study, in *SEG Technical Program Expanded Abstracts*, vol. 30, p. 2543.

Gholami, Y., R. Brossier, S. Operto, A. Ribodetti, J. Virieux, et al. (2011b), Acoustic VTI full waveform inversion: sensitivity analysis and realistic synthetic examples, in *SEG Technical Program Expanded Abstracts*, pp. 2465–2470.

Godfrey, R. J., P. Kristiansen, B. Armstrong, M. Cooper, and E. Thorogood (1998), Imaging the Foinaven ghost, in *68th annual international meeting, SEG, expanded abstracts*, vol. 17, pp. 1333–1335.

Goldfinger, C., C. H. Nelson, and J. E. Johnson (2003), Holocene earthquake records from the Cascadia subduction zone and northern San Andreas Fault based on precise dating of offshore turbidites, *Annual Review of Earth and Planetary Sciences*, *31*(1), 555–577.

Grion, S., R. Exley, M. Manin, X. Miao, A. Pica, Y. Wang, P. Granger, and S. Ronen (2007), Mirror imaging of OBS data, *first break*, *25*(11).

Gutscher, M.-A., D. Klaeschen, E. Flueh, and J. Malavieille (2001), Non-Coulomb wedges, wrong-way thrusting, and natural hazards in Cascadia, *Geology*, *29*(5), 379–382.

Haacke, R. R., G. K. Westbrook, and M. S. Riley (2008), Controls on the formation and stability of gas hydrate-related bottom-simulating reflectors (BSRs): A case study from the west Svalbard continental slope, *Journal of Geophysical Research*, *113*(B5), doi:10.1029/2007jb005200.

Haeckel, M., E. Suess, K. Wallmann, and D. Rickert (2004), Rising methane gas bubbles form massive hydrate layers at the seafloor, *Geochimica et Cosmochimica Acta*, *68*(21), 4335–4345.

Hannigan, P. K., J. R. Dietrich, P. J. Lee, and K. G. Osadetz (1998), Petroleum resource potential of sedimentary Basins on the Pacific margin of Canada, *Tech. rep.*, Geological Survey of Canada, Open File (6,814).

Haq, B. U. (2003), Climatic impact of natural gas hydrate, in *Natural Gas Hydrate*, pp. 137–148, Springer.

Hayward, N., and A. J. Calvert (2007), Seismic reflection and tomographic velocity model constraints on the evolution of the Tofino forearc basin, British Columbia, *Geophysical Journal International*, *168*(2), 634–646, doi:10.1111/j.1365-246x.2006.03209.x.

Hayward, N., G. K. Westbrook, and S. Peacock (2003), Seismic velocity, anisotropy, and fluid pressure in the Barbados accretionary wedge from an offset vertical seismic profile with seabed sources, *Journal of Geophysical Research*, *108*(B11), doi:10.1029/2001jb001638.

Helgerud, M. B., J. Dvorkin, A. Nur, A. Sakai, and T. Collett (1999), Elastic-wave velocity in marine sediments with gas hydrates: Effective medium modeling, *Geophysical Research Letters*, *26*(13), 2021–2024.

Hobro, J., T. Minshull, and S. Singh (1998), *Tomographic seismic studies of the methane hydrate stability zone in the Cascadia Margin, in Henriet, J.-P.and Mienert, J. eds., Gas Hydrates: Relevance to World Margin Stability and Climate Change*, vol. 137, pp. 133–140, Geological Society of London.

Hobro, J., T. Minshull, S. Singh, and S. Chand (2005), A three-dimensional seismic tomographic study of the gas hydrate stability zone, offshore Vancouver Island, *Journal of Geophysical Research*, *110*(B9), doi:10.1029/2004jb003477.

Hobro, J. W. D. (1999), Three-dimensional tomographic inversion of combined reflection and refraction seismic travel-time data, Ph.D. thesis, Department of Earth Sciences, University of Cambridge.

Holbrook, W. S. (2001), Seismic studies of the Blake Ridge: Implications for hydrate distribution, methane expulsion, and free gas dynamics, *Natural gas hydrates*, pp. 235–256.

Hole, J. (1992), Nonlinear high-resolution three-dimensional seismic travel time tomography, *Journal of Geophysical Research: Solid Earth (1978–2012)*, *97*(B5), 6553–6562.

Hornbach, M. J., W. S. Holbrook, A. R. Gorman, K. L. Hackwith, D. Lizarralde, and I. Pecher (2003), Direct seismic detection of methane hydrate on the Blake Ridge, *Geophysics*, *68*(1), 92–100.

Hornbach, M. J., L. L. Lavier, and C. D. Ruppel (2007), Triggering mechanism and tsunamogenic potential of the Cape Fear Slide complex, US Atlantic margin, *Geochemistry, Geophysics, Geosystems*, *8*(12).

Hsu, S., C. Tsai, C. Ku, and J. Sibuet (2009), Flow of turbidity currents as evidenced by failure of submarine telecommunication cables, in *Intern Conf on Seafloor Mapping for Geohazard Assessment, Extended Abs, Rendiconti online, Societ Geologica Italiana*, vol. 7, pp. 167–171.

Hyndman, R., and G. Spence (1992), A seismic study of methane hydrate marine bottom simulating reflectors, *Journal of Geophysical Research: Solid Earth (1978–2012)*, *97*(B5), 6683–6698.

Hyndman, R., and K. Wang (1993), Thermal constraints on the zone of major thrust earthquake failure: The Cascadia subduction zone, *Journal of Geophysical Research: Solid Earth (1978–2012)*, *98*(B2), 2039–2060.

Hyndman, R., C. Yorath, R. Clowes, and E. Davis (1990), The northern Cascadia subduction zone at Vancouver Island: Seismic structure and tectonic history, *Canadian Journal of Earth Sciences*, *27*(3), 313–329.

Hyndman, R., G. Spence, R. Chapman, M. Riedel, and R. Edwards (2001), Geophysical studies of marine gas hydrate in northern Cascadia, *Natural gas hydrates*, pp. 273–295.

Hyndman, R. D. (2013), Downdip landward limit of Cascadia great earthquake rupture, *Journal of Geophysical Research: Solid Earth*, *118*(10), 5530–5549, doi: 10.1002/jgrb.50390.

Hyndman, R. D., and E. E. Davis (1992), A mechanism for the formation of methane hydrate and seafloor bottom-simulating reflectors by vertical fluid expulsion, *Journal of Geophysical Research: Solid Earth (1978–2012)*, *97*(B5), 7025–7041.

Hyndman, R. D., E. E. Davis, and J. A. Wright (1979), The measurement of marine geothermal heat flow by a multipenetration probe with digital acoustic telemetry and insitu thermal conductivity, *Marine Geophysical Researches*, *4*(2), 181–205.

James, T., E. J. Gowan, I. Hutchinson, J. J. Clague, J. V. Barrie, and K. W. Conway (2009), Sea-level change and paleogeographic reconstructions, southern Vancouver Island, British Columbia, Canada, *Quaternary Science Reviews*, *28*(13-14), 1200–1216.

Jeong, W., H.-Y. Lee, and D.-J. Min (2012), Full waveform inversion strategy for density in the frequency domain, *Geophysical Journal International*, *188*(3), 1221–1242.

Katzman, R., W. S. Holbrook, and C. K. Paull (1994), Combined vertical-incidence and wide-angle seismic study of a gas hydrate zone, Blake Ridge, *Journal of Geophysical Research: Solid Earth*, *99*(B9), 17,975–17,995.

Kayen, R. E., and H. J. Lee (1991), Pleistocene slope instability of gas hydrate-laden sediment on the Beaufort sea margin, *Marine Georesources & Geotechnology*, *10*(1-2), 125–141.

Keen, C., and R. Hyndman (1979), Geophysical review of the continental margins of eastern and western Canada, *Canadian Journal of Earth Sciences*, *16*(3), 712–747.

Kelley, D., and J. Delaney (2005), Vancouver Margin Mapping cruise TN-175, November 7-14, *Tech. rep.*, University of Washington.

Kneller, E., L. Zekian, T. Coleou, J. Coulon, and Y. Lafet (2014), Benefits of Broadband Seismic Data for Reservoir Characterization-Santos Basin, Brasil., in *76th EAGE Conference and Exhibition-Workshops*.

Koh, C. A., E. D. Sloan, A. K. Sum, and D. T. Wu (2011), Fundamentals and applications of gas hydrates, *Annual Review of Chemical and Biomolecular Engineering*, *2*, 237–257.

Kvenvolden, K. A. (1993), Gas hydratesgeological perspective and global change, *Reviews of Geophysics*, *31*(2), 173–187.

Kwon, T.-H., and G.-C. Cho (2012), Submarine Slope Failure Primed and Triggered by Bottom Water Warming in Oceanic Hydrate-Bearing Deposits, *Energies*, *5*(12), 28492873, doi:10.3390/en5082849.

Lailly, P. (1983), The seismic inverse problem as a sequence of before stack migrations, in *Conference on inverse scattering: theory and application*, pp. 206–220, Society for Industrial and Applied Mathematics, Philadelphia, PA.

Levander, A., C. Zelt, and W. Symes (2007), 1.08 - Crust and Lithospheric Structure Active Source Studies of Crust and Lithospheric Structure, in *Treatise on Geophysics*, edited by G. Schubert, pp. 247 – 288, Elsevier, Amsterdam, doi: http://dx.doi.org/10.1016/B978-044452748-6.00014-6.

Lopez, C. (2008), Seismic velocity structure associated with gas hydrate at the frontal ridge of northern Cascadia margin, MSc thesis, University of Victoria, Victoria.

Lopez, C., G. Spence, R. Hyndman, and D. Kelley (2010), Frontal ridge slope failure at the northern Cascadia margin: Margin-normal fault and gas hydrate control, *Geology*, *38*(11), 967–970.

Louden, K., and J. Wright (1989), Marine heat flow data: A new compilation of observations and brief review of its analysis, *Handbook of seafloor heat flow.CRC, Boca Raton, FL*, pp. 3–67.

MacKay, M. E. (1995), Structural variation and landward vergence at the toe of the Oregon accretionary prism, *Tectonics*, *14*(6), 1309–1320.

MacKay, M. E., G. F. Moore, G. R. Cochrane, J. Casey Moore, and L. D. Kulm (1992), Landward vergence and oblique structural trends in the Oregon margin accretionary prism: Implications and effect on fluid flow, *Earth and Planetary Science Letters*, *109*(3), 477–491.

Malinowski, M., S. Operto, and A. Ribodetti (2011), High-resolution seismic attenuation imaging from wide-aperture onshore data by visco-acoustic frequency-domain full-waveform inversion, *Geophysical Journal International*, *186*(3), 1179–1204.

Malinverno, A., M. Kastner, M. Torres, and U. Wortmann (2008), Gas hydrate occurrence from pore water chlorinity and downhole logs in a transect across the northern Cascadia margin (Integrated Ocean Drilling Program Expedition 311), *Journal of Geophysical Research*, *113*(B8), B08,103.

Martin, V., P. Henry, H. Nouze, M. Noble, J. Ashi, and G. Pascal (2004), Erosion and sedimentation as processes controlling the BSR-derived heat flow on the Eastern Nankai margin, *Earth and Planetary Science Letters*, *222*(1), 131–144.

Maslin, M., N. Mikkelsen, C. Vilela, and B. Haq (1998), Sea-level–and gas-hydrate–controlled catastrophic sediment failures of the Amazon Fan, *Geology*, *26*(12), 1107–1110.

Matsumoto, R., H. Tomaru, and H. Lu (2004), Detection and evaluation of gas hydrates in the eastern Nankai Trough by geochemical and geophysical methods, *Resource geology*, *54*(1), 53–67.

McCrory, P. A., J. L. Blair, F. Waldhauser, and D. H. Oppenheimer (2012), Juan de Fuca slab geometry and its relation to Wadati-Benioff zone seismicity, *Journal of Geophysical Research*, *117*(B9), doi:10.1029/2012jb009407.

Mienert, J., M. Vanneste, S. Bünz, K. Andreassen, H. Haflidason, and H. P. Sejrup (2005), Ocean warming and gas hydrate stability on the mid-Norwegian margin at the Storegga Slide, *Marine and Petroleum Geology*, *22*(1), 233–244.

Milkov, A. V. (2004), Global estimates of hydrate-bound gas in marine sediments: how much is really out there?, *Earth-Science Reviews*, *66*(3), 183–197.

Monger, J., R. Price, and D. Tempelman-Kluit (1982), Tectonic accretion and the origin of the two major metamorphic and plutonic welts in the Canadian Cordillera, *Geology*, *10*(2), 70–75.

Mora, P. (1987), Nonlinear two-dimensional elastic inversion of multioffset seismic data, *Geophysics*, *52*(9), 1211–1228.

Mulder, W., and R.-E. Plessix (2008), Exploring some issues in acoustic full waveform inversion, *Geophysical Prospecting*, *56*(6), 827–841.

Muller, J. (1977), Evolution of the Pacific Margin, Vancouver Island, and adjacent regions, *Canadian Journal of Earth Sciences*, *14*(9), 2062–2085.

Narayan, Y. (2003), A new Cenozoic foraminiferal biostratigraphy, paleoecology (biofacies) and strontium isotope study of Shell Canada exploration wells from the Tofino Basin, offshore Vancouver Island, Master's thesis, University of Victoria, Victoria, British Columbia. 288. p.

Nedimović, M. R., R. D. Hyndman, K. Ramachandran, and G. D. Spence (2003), Reflection signature of seismic and aseismic slip on the northern Cascadia subduction interface, *Nature*, *424*(6947), 416–420.

Nicholson, T., M. Bostock, and J. Cassidy (2005), New constraints on subduction zone structure in northern Cascadia, *Geophysical Journal International*, *161*(3), 849–859.

Nisbet, E. G., and D. J. Piper (1998), Giant submarine landslides, *Nature*, *392*(6674), 329–330.

Nur, A., G. Mavko, J. Dvorkin, and D. Galmudi (1998), Critical porosity: A key to relating physical properties to porosity in rocks, *The Leading Edge*, *17*(3), 357–362.

Operto, S., J. Virieux, J.-X. Dessa, and G. Pascal (2006), Crustal seismic imaging from multifold ocean bottom seismometer data by frequency domain full waveform tomography: Application to the eastern Nankai trough, *Journal of Geophysical Research: Solid Earth (1978–2012)*, *111*(B9).

Pacal, E. E. (2012), Seismic Imaging with Ocean-bottom Nodes (OBN): New Acquisition Designs and the ATLANTIS 4C OBN Survey, Ph.D. thesis, University of Houston.

Paull, C. K., W. Ussle, and W. S. Borowski (1994), Sources of Biogenic Methane to Form Marine Gas Hydrates In Situ Production or Upward Migration? a, *Annals of the New York Academy of Sciences*, *715*(1), 392–409.

Plessix, R.-É., and Q. Cao (2011), A parametrization study for surface seismic full waveform inversion in an acoustic vertical transversely isotropic medium, *Geophysical Journal International*, *185*(1), 539–556.

Popescu, I., M. De Batist, G. Lericolais, H. Nouzé, J. Poort, N. Panin, W. Versteeg, and H. Gillet (2006), Multiple bottom-simulating reflections in the Black Sea: potential proxies of past climate conditions, *Marine Geology*, *227*(3), 163–176.

Pratt, R., Z.-M. Song, P. Williamson, and M. Warner (1996), Two-dimensional velocity models from wide-angle seismic data by wavefield inversion, *Geophysical Journal International*, *124*(2), 323–340.

Pratt, R., F. Hou, K. Bauer, and M. Weber (2005), Waveform tomography images of velocity and inelastic attenuation from the Mallik 2002 crosshole seismic surveys, *Bulletin-Geological Survey of Canada*, *585*, 122.

Pratt, R. G. (1990), INVERSE THEORY APPLIED TO MULTI-SOURCE CROSS-HOLE TOMOGRAPHY. PART 2: ELASTIC WAVE-EQUATION METHOD, *Geophysical Prospecting*, *38*(3), 311–329.

Pratt, R. G. (1999), Seismic waveform inversion in the frequency domain, Part 1: Theory and verification in a physical scale model, *Geophysics*, *64*(3), 888–901.

Pratt, R. G., and M. Worthington (1990), Inverse theory applied to multi-source cross-hole tomography. Part 1: acoustic wave-equation method, *Geophysical Prospecting*, *38*(3), 287–310.

Pratt, R. G., C. Shin, and G. Hick (1998), Gauss–Newton and full Newton methods in frequency–space seismic waveform inversion, *Geophysical Journal International*, *133*(2), 341–362.

Ramachandran, K., S. Dosso, G. Spence, R. Hyndman, and T. Brocher (2005), Forearc structure beneath southwestern British Columbia: A three-dimensional tomographic velocity model, *Journal of Geophysical Research: Solid Earth (1978–2012)*, *110*(B2).

Ravaut, C., S. Operto, L. Improta, J. Virieux, A. Herrero, and P. Dell'Aversana (2004), Multiscale imaging of complex structures from multifold wide-aperture seismic data by frequency-domain full-waveform tomography: application to a thrust belt, *Geophysical Journal International*, *159*(3), 1032–1056.

Riddihough, R. (1977), A model for recent plate interactions off Canada's west coast, *Canadian Journal of Earth Sciences*, *14*(3), 384–396.

Riddihough, R. D., R P; Hyndman (1991), *Modern Plate Tectonic Regime of the Continental Margin of western Canada*, Geological Survey of Canada, Geology of Canada Series no. 4, 1991; p. 437-455.

Riedel, M., G. Spence, N. Chapman, and R. Hyndman (2001), Deep-sea gas hydrates on the northern Cascadia margin, *The Leading Edge*, *20*(1), 87–109.

Riedel, M., T. Collett, M. Malone, and the Expedition 311 Scientists (2006a), Expedition 311 summary, in *Riedel, M., Collett, T.S., Malone, M.J., and the Expedition 311 Scientists, Proc. IODP, 311: Washington, DC (Integrated Ocean Drilling Program Management International, Inc.). doi:10.2204/iodp.proc.311.101.2006*, vol. 311.

Riedel, M., I. Novosel, G. D. Spence, R. D. Hyndman, R. N. Chapman, R. C. Solem, and T. Lewis (2006b), Geophysical and geochemical signatures associated with gas hydraterelated venting in the northern Cascadia margin, *Geological Society of America Bulletin*, *118*(1-2), 23–38.

Riedel, M., A. Trhu, and G. Spence (2010a), Characterizing the thermal regime of cold vents at the northern Cascadia margin from bottom-simulating reflector distributions, heat-probe measurements and borehole temperature data, *Marine Geophysical Researches*, *31*(1-2), 1–16.

Riedel, M., T. S. Collett, and M. Malone (2010b), Expedition 311 synthesis: scientific findings, in *In Riedel, M., Collett, T.S., Malone, M.J., and the Expedition 311 Scientists, Proc. IODP, 311: Washington, DC (Integrated Ocean Drilling Program Management International, Inc.). doi:10.2204/iodp.proc.311.213.2010*, vol. 311.

Riedel, M., G. Spence, and cruise participants (2014), Cruise Report 2010005PGC, SeaJade, Seafloor Earthquake Array - Japan Canada Cascadia Experiment, Ocean bottom seismometer deployment and active-source airgun refraction and reflection program, CCG Vessel John P. Tully, 30 June - 10 July, 2010, Geological Survey of Canada Open File Report 7558., *Tech. rep.*, Geological Survey of Canada.

Ronen, S., L. Comeaux, X.-G. Miao, et al. (2005), Imaging downgoing waves from ocean bottom stations, in *2005 SEG Annual Meeting*, Society of Exploration Geophysicists.

Rothwell, R., J. Thomson, and G. Kähler (1998), Low-sea-level emplacement of a very large Late Pleistocene megaturbiditein the western Mediterranean Sea, *Nature*, *392*(6674), 377–380.

Scherwath, M., and G. Spence (2011), Mirror-Imaging Processing of Ocean Bottom Seismometer Data, *Tech. rep.*, Geological Survey of Canada Pacific, Sidney.

Scholz, N. (2014), Submarine landslides offshore Vancouver Island, British Columbia and the possible role of gas hydrates in slope stability, PhD thesis, University of Victoria, Victoria.

Schuemann, T., M. Whiticar, and K. Rohr (2010), Petroleum resource potential of tofino basin, *Tech. rep.*, University of Victoria and Ministry of Eanergy, Mines and Petroleum Resources.

Sears, T. J., P. J. Barton, and S. C. Singh (2010), Elastic full waveform inversion of multicomponent ocean-bottom cable seismic data: Application to Alba Field, UK North Sea, *Geophysics*, *75*(6), R109–R119.

Shin, C., and D.-J. Min (2006), Waveform inversion using a logarithmic wavefield, *Geophysics*, *71*(3), R31–R42.

Shipley, T. H., M. H. Houston, R. T. Buffler, F. J. Shaub, K. J. McMillen, J. W. Ladd, and J. L. Worzel (1979), Seismic evidence for widespread possible gas hydrate horizons on continental slopes and rises, *AAPG bulletin*, *63*(12), 2204–2213.

Shipp, R. M., and S. C. Singh (2002), Two-dimensional full wavefield inversion of wide-aperture marine seismic streamer data, *Geophysical Journal International*, *151*(2), 325–344.

Shouldice, D. (1971), Geology of the western Canadian continental shelf, *Bulletin of Canadian Petroleum Geology*, *19*(2), 405–436.

Singh, S. C., and T. A. Minshull (1994), Velocity structure of a gas hydrate reflector at Ocean Drilling Program site 889 from a global seismic waveform inversion, *Journal of Geophysical Research: Solid Earth (1978–2012)*, *99*(B12), 24,221–24,233.

Singh, S. C., T. A. Minshull, and G. D. Spence (1993), Velocity structure of a gas hydrate reflector, *Science*, *260*(5105), 204–207.

Sirgue, L., O. Barkved, J. Dellinger, J. Etgen, U. Albertin, and J. Kommedal (2010), Thematic Set: Full waveform inversion: the next leap forward in imaging at Valhall, *First Break*, *28*(1728), doi:10.3997/1365-2397.2010012.

Sloan, E. (1998a), Physical/chemical properties of gas hydrates and application to world margin stability and climatic change, *Geological Society, London, Special Publications*, *137*(1), 31–50.

Sloan, E. D. (1998b), *Clathrate Hydrates of Natural Gases, Revised and Expanded*, CRC Press.

Sloan, E. D. (2003), Fundamental principles and applications of natural gas hydrates, *Nature*, *426*(6964), 353–363.

Smithyman, B., R. G. Pratt, J. Hayles, and R. Wittebolle (2009), Detecting near-surface objects with seismic waveform tomography, *Geophysics*, *74*(6), WCC119–WCC127.

Song, Z.-M., P. R. Williamson, and R. G. Pratt (1995), Frequency-domain acoustic-wave modeling and inversion of crosshole data: Part II-Inversion method, synthetic experiments and real-data results, *Geophysics*, *60*(3), 796–809.

Soubaras, R., and R. Dowle (2010), Variable-depth streamer–a broadband marine solution, *First Break*, *28*(12).

Spence, G., R. Hyndman, S. Langton, E. E. Davis, and C. Yorath (1991a), Marine multichannel reflection survey across the northern Cascadia accretionary prism, *Tech. rep.*, Geological Survey of Canada, Open file report, 2391.

Spence, G., T. Minshull, and C. Fink (1995), 9. SEISMIC STUDIES OF METHANE GAS HYDRATE, OFFSHORE VANCOUVER ISLAND, in *Proceedings of the Ocean Drilling Program, Scientific Results*, vol. 146, edited by W. G. M. R. Carson, B. and E. Suess.

Spence, G., W. Wood, and R. Coffin (2003), DTAGS2: Deep Towed SSeismic and Piston Coring for Gas Hydrates Offshore Vancouver Island, Cruise PGC02-08: 30 Sep - 14 Oct 2002, *Tech. rep.*, Center for Earth and Ocean Research, University of Victoria.

Spence, G., R. Haacke, and R. Hyndman (2010), *Geophysical characterization of gas hydrates*, vol. 14, chap. Seismic indicators of natural gas hydrate and underlying free gas, pp. 39–71, SEG Geophysical Developments Series.

Spence, G. D., and R. D. Hyndman (2001), The challenge of deep ocean drilling for natural gas hydrate, *Geoscience Canada*, *28*(4).

Spence, G. D., R. Clowes, and R. Ellis (1985), Seismic structure across the active subduction zone of western Canada, *Journal of Geophysical Research: Solid Earth (1978–2012)*, *90*(B8), 6754–6772.

Spence, G. D., R. D. Hyndman, E. E. Davis, and C. J. Yorath (1991b), *Seismic structure of the northern Cascadia accretionary prism: Evidence from new multichannel seismic reflection data*, *in R. Meissner, L. Brown, H. -J. Durbaum, W. Franke, K. Fuchs and F. Seifert eds., Continental Lithosphere: Deep Seismic Reflections, Geodynamics series*, vol. 22, pp. 257–263, Wiley-Blackwell, doi:10.1029/gd022p0257.

Spiess, V., and cruise participants (2001), Report and preliminary results of R/V Sonne Cruise SO149, Victoria - Victoria, 16.8. - 16.9.2000. Berichte, Fachbereich Geowissenschaften, Universitat Bremen, No. 179, 100 pages, Bremen, 2001., *Tech. rep.*, University of Bremen.

Synolakis, C. E., J.-P. Bardet, J. C. Borrero, H. L. Davies, E. A. Okal, E. A. Silver, S. Sweet, and D. R. Tappin (2002), The slump origin of the 1998 Papua New Guinea tsunami, *Proceedings of the Royal Society of London.Series A: Mathematical, Physical and Engineering Sciences*, *458*(2020), 763–789.

Taber, J. J., and S. W. Smith (1985), Seismicity and focal mechanisms associated with the subduction of the Juan de Fuca plate beneath the Olympic Peninsula, Washington, *Bulletin of the Seismological Society of America*, *75*(1), 237–249.

Takam Takougang, E., and A. Calvert (2012), Seismic velocity and attenuation structures of the Queen Charlotte Basin from full-waveform tomography of seismic reflection data, *Geophysics*, *77*(3), B107–B124.

Takougang, E. M. T., and A. J. Calvert (2011), Application of waveform tomography to marine seismic reflection data from the Queen Charlotte Basin of western Canada, *Geophysics*, *76*(2), B55–B70.

Tarantola, A. (1984), Inversion of seismic reflection data in the acoustic approximation, *Geophysics*, *49*(8), 1259–1266.

Tarantola, A. (1988), Theoretical background for the inversion of seismic waveforms including elasticity and attenuation, *Pure and Applied Geophysics*, *128*(1-2), 365–399.

Tiffin, D., B. Cameron, and J. Murray (1972), Tectonics and depositional history of the continental margin off Vancouver Island, British Columbia, *Canadian Journal of Earth Sciences*, *9*(3), 280–296.

Vigh, D., and E. W. Starr (2008), 3D prestack plane-wave, full-waveform inversion, *Geophysics*, *73*(5), VE135–VE144.

Virieux, J., and S. Operto (2009), An overview of full-waveform inversion in exploration geophysics, *Geophysics*, *74*(6), WCC1–WCC26.

Vogt, P. R., and W.-Y. Jung (2002), Holocene mass wasting on upper non-Polar continental slopesdue to post-Glacial ocean warming and hydrate dissociation?, *Geophysical Research Letters*, *29*(9), 55–1–55–4.

von Huene, R., and D. W. Scholl (1991), Observations at convergent margins concerning sediment subduction, subduction erosion, and the growth of continental crust, *Reviews of Geophysics*, *29*(3), 279–316.

Wang, K., and Y. Hu (2006), Accretionary prisms in subduction earthquake cycles: The theory of dynamic Coulomb wedge, *Journal of Geophysical Research*, *111*(B6), doi:10.1029/2005jb004094.

Wessel, P., W. H. F. Smith, R. Scharroo, J. Luis, and F. Wobbe (2013), Generic Mapping Tools: Improved Version Released, *Eos, Transactions American Geophysical Union*, *94*(45), 409–410, doi:10.1002/2013EO450001.

Westbrook, G. K., B. Carson, R. J. Musgrave, and et al. (1994), Proceedings of the Ocean Drilling Programme, Initial Reports, *Tech. Rep. Leg 146 Part 1*, College Station, TX.

Williamson, P. (1991), A guide to the limits of resolution imposed by scattering in ray tomography, *Geophysics*, *56*(2), 202–207.

Williamson, P. R., and M. Worthington (1993), Resolution limits in ray tomography due to wave behavior: Numerical experiments, *Geophysics*, *58*(5), 727–735.

Willoughby, E. C., K. Latychev, R. N. Edwards, K. Schwalenberg, and R. D. Hyndman (2008), Seafloor compliance imaging of marine gas hydrate deposits and cold vent structures, *Journal of Geophysical Research*, *113*(B7), doi:10.1029/2005jb004136.

Wong, H., T. Ldmann, B. Baranov, B. Karp, P. Konerding, and G. Ion (2003), Bottom current-controlled sedimentation and mass wasting in the northwestern Sea of Okhotsk, *Marine Geology*, *201*(4), 287305, doi:10.1016/s0025-3227(03)00221-4.

Wong, M., B. Biondi, S. Ronen, et al. (2010), Joint least-squares inversion of up-and down-going signal for ocean bottom data sets, in *SEG Technical Program Expanded Abstracts*, pp. 17–22.

Wong, M., S. Ronen, B. Biondi, et al. (2011), Least-squares reverse time migration/inversion for ocean bottom data: A case study, in *2011 SEG Annual Meeting*, Society of Exploration Geophysicists.

Wong, M., B. Biondi, S. Ronen, et al. (2012a), Imaging with multiples using linearized full-wave inversion, in *SEG Technical Program Expanded Abstracts 2012*, pp. 1–5, Society of Exploration Geophysicists.

Wong, M., S. Ronen, B. Biondi, et al. (2012b), Joint imaging with streamer and OBN data, in *2012 SEG Annual Meeting*, Society of Exploration Geophysicists.

Woodward, M. J. (1992), Wave-equation tomography, *Geophysics*, *57*(1), 15–26.

Wu, R.-S., and M. N. Toksöz (1987), Diffraction tomography and multisource holography applied to seismic imaging, *Geophysics*, *52*(1), 11–25.

Xu, W., and C. Ruppel (1999), Predicting the occurrence, distribution, and evolution of methane gas hydrate in porous marine sediments, *Journal of Geophysical Research-Solid Earth*, *104*(B3), 5081–5095.

Yelisetti, S., G. D. Spence, and M. Riedel (2014), Role of gas hydrates in slope failure on frontal ridge of northern Cascadia margin, *Geophysical Journal International*, *199*(1), 441–458, doi:10.1093/gji/ggu254.

Yilmaz, Ö. (2001), *Seismic data analysis*, vol. 1, Society of Exploration Geophysicists Tulsa.

Yorath, C. (1980), The Apollo structure in Tofino basin, Canadian Pacific continental shelf, *Canadian Journal of Earth Sciences*, *17*(6), 758–775.

Yorath, C., A. Green, R. Clowes, A. S. Brown, M. Brandon, E. Kanasewich, R. Hyndman, and C. Spencer (1985), Lithoprobe, southern Vancouver Island: Seismic reflection sees through Wrangellia to the Juan de Fuca plate, *Geology*, *13*(11), 759–762.

Yu, J. (2004), Enhancing Illumination Coverage of VSP Data by Crosscorrelation Imaging Condition, *Tech. rep.*, University of Utah.

Yuan, T., G. D. Spence, and R. D. Hyndman (1994), Seismic velocities and inferred porosities in the accretionary wedge sediments at the Cascadia margin, *Journal of Geophysical Research: Solid Earth*, *99*(B3), 4413–4427.

Yuan, T., R. Hyndman, G. Spence, and B. Desmons (1996), Seismic velocity increase and deep-sea gas hydrate concentration above a bottom-simulating reflector on the northern Cascadia continental slope, *Journal of Geophysical Research: Solid Earth (1978–2012)*, *101*(B6), 13,655–13,671.

Yuan, T., G. Spence, R. Hyndman, T. Minshull, and S. Singh (1999), Seismic velocity studies of a gas hydrate bottom-simulating reflector on the northern Cascadia continental margin: Amplitude modeling and full waveform inversion, *Journal of Geophysical Research: Solid Earth (1978–2012)*, *104*(B1), 1179–1191.

Zatsepina, O. Y., and B. Buffett (1998), Thermodynamic conditions for the stability of gas hydrate in the seafloor, *Journal of Geophysical Research: Solid Earth (1978–2012)*, *103*(B10), 24,127–24,139.

Zelt, C. A., and P. J. Barton (1998), Three-dimensional seismic refraction tomography: A comparison of two methods applied to data from the Faeroe Basin, *Journal of Geophysical Research: Solid Earth (1978–2012)*, *103*(B4), 7187–7210.

Zelt, C. A., and R. B. Smith (1992), Seismic traveltime inversion for 2D crustal velocity structure, *Geophysical Journal International*, *108*(1), 16–34.

Zykov, M. M. (2006), Three-dimensional travel time tomography of the gas hydrate area offshore Vancouver Island based on OBS data, Ph.D. thesis, School of Earth and Ocean Sciences, University of Victoria.

Zyla, T. (2012), Tracking methane bubble plumes on the northern Cascadia margin, BSc thesis, University of Victoria, Victoria.